Development of ecological concretes by recycling locally available by-products from the aluminum industry

Thèse

Thi Hang Tran

Doctorat en génie civil
Philosophiæ doctor (Ph. D.)

Québec, Canada

Development of ecological concretes by recycling locally available by-products from the aluminum industry

Thèse

Thi Hang Tran

Sous la direction de :

Luca Sorelli, directeur de recherche
David Conciatori, codirecteur de recherche

Résumé

Les émissions élevées de carbone dues à la production de ciment sont l'un des problèmes les plus critiques pour la durabilité du béton. Au cours des dernières décennies, l'utilisation d'ajouts cimentaires (SCMs) dans le béton est devenue très courante pour produire un béton durable. En outre, la demande mondiale croissante d'infrastructures entraîne aujourd'hui une surexploitation des ressources naturelles. En raison de la disponibilité limitée et variables des SCMs dans les régions, il existe aujourd'hui un besoin urgent d'explorer des SCMs qui sont disponibles localement pour la production d'un béton durable.

Chaque année, 1,5 million de tonnes de brasques usées (SPL) sont générées comme déchets par les fonderies d'aluminium primaire dans le monde. Après traitement, le SPL devient un matériau inerte, appelé LCLL-ash dans cette étude. Les LCLL-ash sont riches en aluminium et en silice, ce qui leur confère des caractéristiques pour remplacer le ciment dans le béton.

Tout d'abord, les LCLL-ash sont broyées à la même taille que les particules de ciment. 10 à 20% en masse du ciment, composant la pâte de ciment, est remplacé par le LCLL-ash broyée. Une petite quantité d'anhydrite synthétique (autre sous-produit lié à l'industrie de l'aluminium) est également ajoutée dans certains mélanges. Comme pour les bétons conventionnels, les résultats présentés montrent que la LCLL-ash a, au début, un effet de nucléation et une faible réaction pouzzolanique, tandis que la LCLL-ash change les produits d'hydratation avec l'apparition d'une nouvelle phase AFm-CO_3 et la formation accrue d'ettringite par rapport à la pâte pure. Un niveau de remplacement optimisé de 10% de ciment a pu être atteint sans affecter les propriétés micromécaniques.

Deuxièmement, une étude préliminaire sur l'effet de la LCLL-ash calcinée à haute température (800ºC et 1000ºC) sur l'hydratation des pâtes de ciment est réalisée. La partie du ciment remplacée par la LCLL-ash calcinée est de 20% en masse et le *e/c* est de 0.485. La LCLL-ash calcinée a changé les produits d'hydratation avec la formation de la phase AFm-CO_3 et retarde la vitesse d'hydratation du ciment. Cependant, la chaleur générée par l'hydratation et la teneur en hydrates dans le ciment LCLL-ash calciné sont inférieures à celles du ciment LCLL-ash. On peut conclure que la calcination n'a pas amélioré de manière significative la réaction pouzzolanique du ciment LCLL-ash. Ceci est probablement lié à l'hétérogénéité de la LCLL-ash, entraînant un changement de sa composition chimique.

Troisièmement, pour mieux comprendre l'effet des fillers minéraux sur les mélanges de BFUP, nous avons mené une campagne expérimentale large et complète au niveau de la pâte de ciment et du béton. Le ciment a été remplacé par des fillers minéraux issus de l'industrie de la pierre (poudre de granite, poudre de calcaire) et post-consommés (poudre de verre) qui sont disponibles localement au Québec. Les résultats obtenus permettent une meilleure compréhension de l'effet du remplacement du ciment Portland et de la fumée de silice par 10-40% de charges minérales sur les propriétés à l'état frais du béton, la cinétique d'hydratation, le retrait endogène et les propriétés mécaniques. L'effet du remplacement du liant par des fillers minéraux a également été vérifié à l'échelle du BFUP.

Enfin, une formule LCLL-BFUP a été développée avec succès en optimisant la densité de compaction du mélange sur la base du modèle de compaction des particules (CIPM). La substitution du ciment par la LCLL-ash était de 6% et 12% de la masse. Les résultats montrent que la LCLL-ash retarde le pic d'hydratation maximum du clinker par rapport au mélange de référence. Cependant, la LCLL-ash aide à diminuer le retrait endogène, réduisant ainsi les fissures précoces. De plus, la substitution jusqu'à 12% de la masse du ciment par de la LCLL-ash est possible pour produire un BFUP répondant aux exigences de la norme canadienne (120 MPa). De plus, le mélange de BFUP développé a une teneur en ciment inférieure à 550 kg/m^3, ce qui permet de réduire le coût et les émissions de CO_2 du BFUP.

Mots clés: Béton fibré à ultra-hautes performances, sous-produits, ajouts cimentaires, brasques usées, ciment, filler minéral, production d'aluminium primaire, bas *e/c*, retrait endogène, CIPM, compaction des particules.

Abstract

The high carbon emissions due to cement production is one of the most critical issues for fostering concrete sustainability. In the last decades, supplementary cementitious materials (SCMs) in concrete have become very common to produce sustainable concrete. Moreover, today, the growing worldwide demand for infrastructures is causing over-exploited natural material sources. Concerned by the limited availability of SCMs and their regional variation, there is today an urgent need for exploration of alternative SCMs which are locally available in the production of durable concrete.

Every year 1.5 million tons of spent pot lining (SPL) are generated as waste from the primary aluminum smelters worldwide. After treatment, SPL becomes an inert material called LCLL-ash in this study. LCLL-ash is rich in aluminum and silica content which will be a potential property to replace cement in concrete.

Firstly, ground LCLL-ash as the fineness of cement is replaced cement partially on the paste systems at 10 and 20% wt. A small amount of synthetic anhydrite (other by-products related to the aluminum industry) is also added in some mixes. As for normal concretes, the presented results show that LCLL-ash has a nucleation effect and low pozzolanic reaction at an early age, whereas LCLL-ash changes the hydration products with the presence of AFm-CO_3 and more ettringite compared to the neat paste. An optimized replacement level of 10% cement could be achieved without affecting the micromechanical properties.

Secondly, a preliminary study on the effect of calcined LCLL-ash at high temperatures (800^{o}C and 1000^{o}C) on the hydration of cement pastes is carried out. The replacement cement by grind-(calcined) LCLL-ash is 20% wt. and *w/b* of 0.485. Calcined LCLL-ash has changed the hydration production with the formation of the AFm-CO_3 phase and delays the hydration of cement. However, the heat of hydration and the hydrates content in calcined LCLL-cement are lower than that of LCLL-cement. It can conclude that calcination did not significantly improve the pozzolanic reaction of LCLL-ash. This is possibly related to the heterogeneity of LCLL-ash, leading to changing its chemical composition.

Thirdly, to better understand the effect of mineral fillers on UHPC mixtures, we carried out a wide and comprehensive experimental campaign at the cement paste and concrete scales. In particular, cement was replaced by mineral fillers from the stone industry (granite powder, limestone powder) and post-

consumer (glass powder) which are locally available in Quebec. The presented results show a better understanding of the effect of replacing Portland cement and silica fume with 10-40% of mineral fillers on fresh concrete properties, hydration kinetics, autogenous shrinkage, and mechanical properties. The effect of replacing binders by mineral fillers was also verified at the UHPC scale.

Finally, an LCLL-UHPC formulation was successfully developed by optimizing the packing density of the mixture based on the compaction-interaction packing model (CIPM). The substitution of cement by LCLL-ash was 6% and 12% wt. The result shows that LCLL-ash delays the maximum hydration peak of clinker compared to the reference mix. However, LCLL-ash helps decrease the autogenous shrinkage, reducing the early-age cracking. Moreover, the substitution of up to 12% wt. of cement by LCLL-ash is possible to produce UHPC to meet the requirement of Canadian standard UHPC (120 MPa). Furthermore, the developed UHPC mixture has a cement content of less than 550kg/m^3, resulting in lower cost and embodied CO_2 emission of UHPC.

Keywords: Ultra-high-performance concrete, by-products, supplementary cementitious materials, treated spent pot lining, cement, mineral fillers, primary aluminum production, low *w/c*, autogenous shrinkage, CIPM, packing density.

Table of Contents

List of figures

List of tables

List of abbreviations

A	Sodium aluminum hydrate
C-A-S-H	Calcium aluminate silicate hydrate
CH	Calcium hydroxide
CIPM	Compaction-interaction packing model
C-S-H	Calcium silicate hydrate
DDM	Double Danish Modeling
E	Ettringite
GBFS	Granulated blast furnace slag
GGBFS	Ground granulated blast furnace slag or GGBFS
Hc	Calcium hemicarbonaluminate
HPC	High-performance concrete
LCL&L	Low Caustic Leaching and Liming
Mc	Calcium monocarbonaluminate
NSC	Normal strength concrete
OPC	Ordinary Portland cement
PSD	Particle size distribution
RH	Relative humidity
SCMs	Supplementary cementitious materials
SF	Silica fume
TGA	Thermogravimetric analysis
UHPC	Ultra-high performance concrete
w/b	Water-to-binder ratio
w/c	Water-to-cement ratio
w/f	Water-to-fine ratio
XRD	X-ray Diffraction

To my father and my mother!

« A dream is only a dream until you decide to make it real »
---Harry Styles---

Acknowledgment

Firstly, I would like to express my sincere thank to my supervisor Professor Luca Sorelli for allowing me to pursue my PhD research at the Laval University, Canada. Thank you for your positive spirit, support, and encouragement during my research. Thank you for your ideas in introducing me to the sustainable development of engineering. Besides research, he is a very kind and very optimistic person. It is impressive to me to learn a lot from your knowledge and experiences.

Appreciations are expressed to my co-supervisor, Professor David Conciatori, for your encouragement and assistance. Thank you for the weekly meetings in our group where I can communicate with my colleagues and share my research advancement with others. Special thanks for organizing the social activities each semester, a refreshing and relaxing time after school.

Thanks are extended to the jury members: Professor Ahmed Soliman, Professor Ahmed El Refai and Professor Houshang Darvishi Alamdari, for the fruitful discussion and the valuable suggestions for bringing out the best of my doctoral thesis.

Special thanks to my colleagues Zhao Chen, and Jessy Frech Baronet for training me to use and analyze the results from the CSM indentation. Thanks to my colleague Mahdiar Dargahi for precious support, contribution, and teamwork to make the new nanoindenter Alemnis work. Thanks to my colleague David Bouchard for your valuable advice and discussions on my experimental works. Thanks to Dr. Ousmane Ahmat Hisseine for your fruitful discussion and strategy for writing a professional science article.

I would like to thank the support of the NSERC CRD grant program and the CRITM consortium. I also thank Rio Tinto and Cement Quebec Inc. for financing this project. My sincere thanks to Mr. Laurent Birry from Rio Tinto, Mr. Martin Beaulieu of Cement Quebec, Prof. Claudiane Ouellet-Plamondon and Prof. Willam Wison for their expert advice during the project. I also thank the professors and all technicians of the Civil Engineering Department and all the faculty staff I have interacted with.

Sincere thanks to my colleagues for the beautiful moments and the fun we have shared: Truong Thanh Nguyen, Fahime Sokhangou, Xuande Chen, Duc Anh Tran, Victor Brial, Samaneh Khani, Alicia Dupuit, Rodolfo Castillo Araiza. My PhD life can’t fill joy without guys.

I am very grateful to my family members and friends who always support me during this journey. Special thanks to my dear parents, who always love and support me unconditionally. My parents had always concerned me when I decided to pursue study abroad. Finally, I am very grateful to my husband, who open a new chapter of my life in Canada. Thanks for your love, patience, and always encouraging me.

Quebec, April 2022 Thi Hang Tran

Foreword

This doctoral thesis is part of a large collaborative project between two universities ÉTS Montreal and Laval Université, and two industrial partners (Cement Quebec Inc. and Rio Tinto) under the NSERC CRD research program framework starting from January 2018 to April 2022. The realization of this thesis is under the supervision of Professor Luca Sorelli and co-supervision of Professor David Conciatori —Department of Civil and Water Engineering, Laval Université. This manuscript is presented in the form of a thesis by inserting articles. The fundamental part of this thesis consists of three articles are presented in chapters 2, 4 and 5, as follows:

Chapter 2 / Article 1

Hang Tran, Victor Brial, David Conciatori, Claudiane Ouellet-Plamondon, Luca Sorelli, « *Understanding the Microstructure Changes Of Concretes Recycling Treated Spent Pot Lining From Primary Aluminum Production* », Cement and concrete composites, under review.

Chapter 4 / Article 2

Hang Tran, David Bouchard, Ousmane Ahmat Hisseine, Luca Sorelli, «*A Multiscale Approach to Develop Ecological UHPC With High-Volume of Recycled Mineral Fillers*», Cement and concrete research, under review.

Chapter 5 / Article 3

Hang Tran, David Bouchard, Victor Brial, Thomas Sanchez, Ousmane Ahmat Hisseine, David Conciatori, Claudiane Ouellet-Plamondon, Luca Sorelli, «*Developing Sustainable Ultra-High-Performance Concrete with Aluminum Production Wastes*», Construction and Building Materials, under review.

As the first author, I have mainly contributed to preparing such manuscripts in conceptualization, and discussion, carrying out the most significant part of the comprehensive experimental campaign, including several techniques, writing, reviewing, and editing. Prof. Sorelli contributed to discussing, conceptualizing, and reviewing. The co-authors Prof. Sanchez and Dr. Ousmane contributed to specific parts of the above articles, e.g., helping me implement the CIPM model or the Double Danish hydration analysis, respectively. Mr. Bouchard contributed to help in measuring the packing density of the

systems. Mr. Brial contributed to cement paste sample preparation with LCLL-ash and chemical analysis of LCLL-ash by XRD with Rietveld method. Prof. Ouellet-Plamondon and Prof. Conciatori contributed to the rise in funding and article editing, especially for the French part.

Introduction

Industrial problem

Concrete is the most widely used construction material on the planet, with approximately two cubic meters per person [1]. The production of cement for the construction industry is one of the main sources of global CO_2 emissions, which represents every year 5-8% of global CO_2 emissions [2,3]. Note that about 0.84 tons of CO_2 are liberated per ton of cement produced, which is due mainly to the clinkerization of cement. Given the relationships between life cycle characteristics and CO_2 use, the emission of CO_2 can be assessed for environmentally friendly concrete production [4]. This has given the concrete industry a strong incentive to become considerably "greener" about concrete. The cement and concrete industries are under increasing pressure to produce concrete with a low environmental impact and sustainable development. In a landmark work, Mindess et al. [5], discussed the most promising strategies to improve the sustainability of concrete, listing the most effective ones, which are essentially as follows [6]:

- replacement of as much as to cement as possible with supplementary cementitious materials (SCMs);
- lowering the amount of concrete required to support loads by employing high strength concretes;
- increasing the durability of concrete to provide a longer service life and lower maintenance costs.

Today, it is well accepted that substituting SCMs for a portion of the cement in concrete production is probably the most effective way of decreasing CO_2 emissions and energy consumption. Most SCMs are industrial by-products or natural pozzolans such as fly ash from coal-fired power plants, ground-granulated blast furnace slag from iron production and silica fume from the ferrosilicon industry, calcined clay, and rice husk ash. These SCMs serve to preserve environmental resources and enhance the performance, durability, and cost of concrete. The replacement of Portland cement with SCMs has become the focus of attention of research for at least the past two decades [7–10]. The practice of using SCMs is already a widely adopted industrial practice. For example, in the US, SCMs are usually added directly to concrete production rather than blended with clinker. Over 60% of ready-mixed

concrete contains SCMs as a substitute for a portion of the Portland cement [11]. The demand for cement and concrete still significantly increases worldwide, rising from 3.6 billion tons in 2011 [12] to 5.8 billion tons by 2050 [13]. Thus, the supply of current SCMs will not be enough to satisfy the rising cement demand. Also, the availability of conventional by-product SCMs varies regionally; for instance, the amount of fly ash will decrease since coal-fired power plants are being phased out for environmental protection purposes in several countries [14]. Therefore, there is an urgent need to explore alternative SCMs and their performance in concrete.

Ultra-high-performance concrete (UHPC) is a new class of concrete that has been under development in recent decades and provides new potentials for enhancing construction sustainability. UHPC is pushing the limits of concrete industry thanks to outstanding compressive strength, excellent tensile strength and unprecedented durability. More important, UHPC allows extending service life and reducing construction maintenance costs as more durable and impermeable material [15,16]. Moreover, it is possible to reduce the construction volume in structural elements which take fully advantage of UHPC compressive strength. Because of these advantages, UHPC technology is spreading in various bridge construction and rehabilitation applications [17–20]. However, commercially available UHPC mixes have often a high cement content (e.g., more than 900 kg/m^3) and fibers content (e.g., 1-3% by volume), leading to the increase cost of UHPC compared to conventional concrete. Therefore, it pushes the researchers to develop eco-friendly UHPC for wider engineering application. UHPC mix design is characterized by very low water-to-cement ratio (*w/c*), which causes a very low capillary porosity and a significant percentage of unreacted clinker which is residually left in the microstructure. Interestingly, previous studies disclosed that the cement hydration degree is only about 40-60% in UHPC [21–23]. A promising option to address sustainability concerns related to reducing environmental impact and reducing the cost of UHPC is to replace unhydrated cement part with SCMs or mineral fillers. Moreover, the use of locally available SCM is more efficient to reduce the transport cost and create local circular economy loops.

In Canada, the aluminum industry produces 2.9 million tons of aluminum per year, and each ton of aluminum generates about 25 kg of spent pot lining (SPL) [24]. In particular, SPL is a waste material generated from the primary aluminum smelters. Figure 0-1 shows the aluminum production and amount SPL generated from the top aluminum producers in the world. It shows that the production of about 64 million tonnes of aluminum generated approximately 1.4 million tonnes of SPL from top global

aluminum producing countries in the world in 2018 [25]. Thus, disposing of SPL is a challenge for the aluminum industry in the world because SPL is listed as a hazardous waste since it contains toxic and leachable elements such as cyanide and fluoride as well as its hydro-reactivity generating explosive gases [24,26–28]. Therefore, SPL must be treated before proceeding to its landfill. SPL is separated into two parts, the first cut is rich in carbon material from the cathode, and the second cut is rich in vitrified refractory.

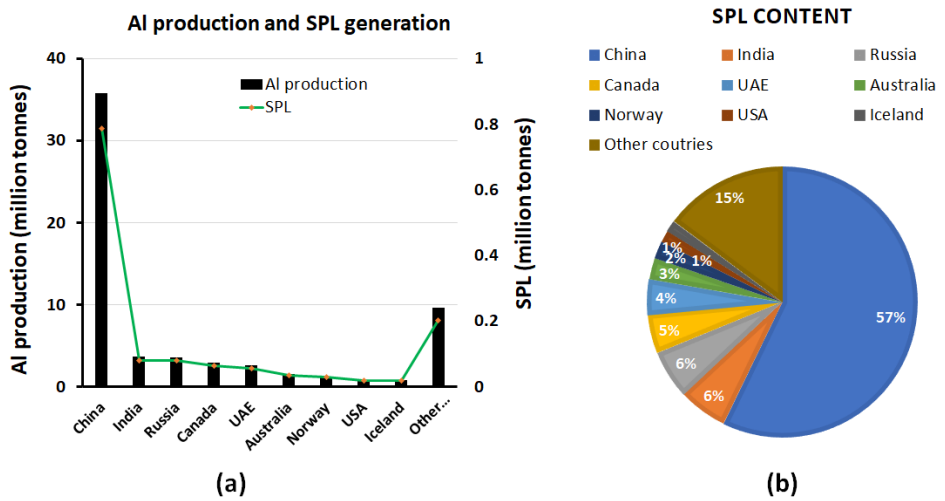

Figure 0-1. SPL generated by the top aluminum producing countries in 2018 [25].

About 80 kT of SPL is produced annually in Canada, especially about 20 kt of SPL from Rio Tinto (RT) [29]. In the early 1990s, RT has developed, at the Arvida Research and Development Centre (ARDC; Jonquière, Québec), the hydrometallurgical process called “Low Caustic Leaching and Liming” (LCL&L), which extracts fluorides and cyanides to product inert by-products with high potential for valorization [30]. After treating by the LCL&L process, the second cut of SPL is called “LCLL-ash”. LCLL-ash is rich in alumina, silica, and sodium content, which can be used to replace partially cement in concrete production.

Research problem

LCLL-ash contains high silica and alumina compared to Portland cement. Thanks to its chemical composition, LCLL-ash has the potential to be used in concrete production as SCM or mineral fillers. However, the use of these local by-products from the aluminum industry in concrete is still limited in the open literature. The effect of LCLL-ash on the cement paste properties is today unknown.

Moreover, LCLL-ash is a fine powder that would be potentially employed as mineral filler in the development of UHPC. Methods based on particle packing density have been recently developed to introduce mineral fillers in sustainable concrete [31,32]. The effect of replacing the cement with LCLL-ash in UHPC is unexplored. Moreover, the use of mineral fillers may allow to reduce cement in UHPC mixes and reduce the autogenous shrinkage, which is often vital in UHPC as a direct consequence of the high cement and silica fume content. Indeed, autogenous shrinkage occurs in the first days after mixing and can cause potential cracks at early ages [33,34]. Therefore, using mineral fillers may be an efficient solution to mitigate the autogenous shrinkage of UHPC by using less binder.

This thesis will address the following research questions:

- Can we efficiently recycle LCLL-ash in concrete as SCM or mineral filler? How does LCLL-ash change the microstructure properties of the cement paste?

- If LCLL-ash is not reactive, can calcination improve the reactivity of LCLL-ash? Does calcined LCLL-ash undergo pozzolanic reactions creating additional Calcium-Silicate-Hydrates (C-S-H)?

- Can we employ LCLL-ash as a mineral filler to replace the unreacted part of cement in UHPC mixes? How do mineral filler changes the properties of cement paste at a low water-to-cement ratio?

- How much LCLL-ash can be used to replace cement in UHPC while maintaining mechanical properties? Does LCLL-ash reduce the early-age autogenous shrinkage of UHPC?

The overall novelty of this thesis is the development of sustainable concrete by replacing cement by treated by-product from the aluminum smelter — LCLL-ash, which is massively and readily available in Quebec. This could have several benefits. Firstly, this allows producing more environmentally friendly concretes. Secondly, this use would be a sustainable solution to avoid disposing of LCLL-ash in a landfill. Finally, LCLL-ash can be used as partial replacement cement as mineral fillers in high-strength concrete, lowering their cost.

Objectives

This thesis aims to study the feasibility of the use of LCLL-ash in concrete. The detailed objectives are as follows:

1. Characterize the chemo-micromechanical properties of the new constituent phases of cement pastes with LCLL-ash.

2. Study effect of calcined LCLL-ash at different temperatures on hydration kinetic and hydration production of cement paste.

3. Study the effect of mineral fillers on UHPC at an early age in terms of fresh concrete properties, hydration kinetic, and autogenous shrinkage.

4. Optimize the LCLL-ash content in replacement cement in eco-friendly UHPC production.

Organization of the thesis

The thesis comprises five chapters.

The introduction section explains the industrial problem and research problem involving the concrete industry and LCLL-ash — treated by-products from primary aluminum production.

The brief literature survey is presented in chapter 1, which is deepened in each chapter. This section presents the introduction of cement chemistry, the supplementary cementitious materials, LCLL-ash, ultra-high performance concrete (UHPC), and Eco-friendly UHPC.

The following four main chapters are presented in the form of the article. The summary of the four chapters is shown in Table 0-1.

Chapter 2 presents the chemo-mechanical properties of the cement paste system incorporating LCLL-ash with a constant water-to-binder (*w/b*) ratio of 0.35. LCLL-ash was ground to the fineness of cement and used to partially replace cement at a dosage of 10% and 20% by mass. Some of the mixes were also added a small amount of synthetic anhydrite (AH) — other by-products related to the aluminum sector. The new hydrated products were found in LCLL-cement paste. Moreover, the cement pastes with 1.25% of AH and 10% LCLL enhanced the mechanical property at 28 days.

Chapter 3 shows the preliminary results on the effect of calcined LCLL-ash at a different temperature on the hydration of the cement paste system with *w/b* equal to 0.485. LCLL-ash was grinded and calcinated at 800^{o}C and 1000^{o}C. Then calcined LCLL-ash replaced cement at 20% by mass. The new hydrated products were found in both systems with calcined and non-calcined LCLL-ash. The hydration kinetic measured by isothermal calorimetry did not show the pozzolanic reaction of calcined LCLL-ash.

Chapter 4 presents a comprehensive study on the effect of recycled mineral fillers (granite powder, limestone powder and glass powder) on UHPC. Firstly, cement paste systems were fabricated by replacing silica fume and Portland cement at different levels from 0% to 40% by volume while keeping a low water-to-fine (*w/f)* ratio of 0.20. At the concrete level, the most promising cement paste with mineral fillers was employed to develop Eco-UHPC, of which compressive strength and electrical bulk resistivity were characterized. The results show that the newly developed UHPC-filler formulations were successfully attempted while remaining compressive strength of 100–110 MPa and exhibiting a significant reduction of autogenous shrinkage.

Chapter 5 presents the development of substainable UHPC incorporating LCLL-ash without treatment (no grinding and non-calcination). LCLL-ash replaced cement in UHPC mixtures at a dosage of 6% and 12% by mass. The new LCLL-UHPC formulations were then designed by particle packing optimization—Compaction-Interaction Packing Model (CIPM). Afterward, a multi-technique experimental and analytical approach was employed to assess the key features of the developed LCLL-UHPC, including fresh concrete properties, hydration kinetic, autogenous shrinkage, and mechanical properties. The results showed that LCLL-ash is a promising mineral filler that can enable producing low-CO_2 UHPCs.

Finally, the main findings are summarized in conclusion section, and the recommendations for future outlook are also proposed.

Table 0-1. Summary of chapters 2, 3, 4 and 5.

Chapter	Tille	Research question	Methods
2	The Microstructure Signature of Cement Pastes Recycling Treated Spent Refractory Lining from Aluminum Production	• What are the microstructure phases of cement pastes with LCLL-ash? • Whare the changes o the properties of cement paste with LCLL-ash?	• X-ray diffraction (XRD) • Thermogravimetric analysis (TGA) • Wavelength-dispersive spectroscopy • Scanning electron microscopy (SEM) • Microindentation
3	(Chapter) Preliminary investigation of the hydration in cement paste with calcined refractory waste from the primary aluminum smelters	• Does calcined LCLL has pozzolanic reactivity in a cement paste system?	• XRD • TGA • Isothermal calorimetry
4	Understanding The Effect of Recycled Mineral Fillers on Ultra-High Performance Concretes	• How do mineral fillers affect the microstructure properties of cement pastes and mortars at very low water-to-fines (w/f) ratios?	• Mini-slump test • Isothermal calorimetry • TGA • Autogenous shrinkage • Microindentation • Compressive strength • Electrical resistivity test
5	Developing Sustainable Ultra-High-Performance Concrete with Aluminium Production Wastes	• Can we use the LCLL-ash as mineral fillers in UHPC? • What is the effect of LCLL-ash on UHPC-performance?	• Optimized mix design by CIPM model • Mini-slump test • Isothermal calorimetry • XRD • SEM • Autogenous shrinkage • Microindentation • Compressive strength

Chapter 1. Literature review

1.1. Historic of concrete

Concrete is the most widely used substance in the world after water, environ 2 m^3 per person per year. Concrete is first used in the Roman Empire [35]. The Roman concrete consists of broken bricks, rocks, hydraulics binders, natural pozzolana, ground brick and water. After that, concrete became well-known in 1824 with the introduction of Portland cement [36]. Reinforced concrete is concrete with an embedded reinforcement developed in 1849. The most common material used as reinforcement is steel. The advantage of reinforced concrete is that it enhances the tensile stresses and the compression loads. With the increase of using high-strength concrete for construction, high-performance concrete (HPC) is developed in the 1980s. The compressive strength of HPC is from 45-100 MPa. In 1994, the Ultra-high performance concrete (UHPC) was first coined and became a hot research topic for researchers. UHPC is an innovative cementitious material that exhibits an excellent compressive strength of over 150 MPa and high durability [37].

Table 1-1. Ingredient proportion of three types of concrete [38]. NSC: normal strength concrete, HPC: high-performance concrete, UHPC: ultra-high-performance concrete.

Composition	NSC	HPC	UHPC
Cement [kg/m^3]	350-375	350-500	700-1500
Silica fume [kg/m^3]	-	150-250	175-375
Water-to-cement ratio [-]	0.4-0.6	0,3-0,35	0,16-0,2
Water [kg/m^3]	150-200	150-160	160-230
Superplasticizer [kg/m^3]	-	3,5-10	10-45

Table 1-2. Properties of three types of concrete [38]. NSC: normal strength concrete, HPC: high-performance concrete, UHPC: ultra-high-performance concrete.

Properties	NSC	HPC	UHPC
Compressive strength [MPa]	20-40	50-100	120-250
Tensile strength [MPa]	1-3	3-6	7-15
Elastic Modulus [MPa]	25-35	35-40	50-60
Porosity [%]	14-20	10-13	1.5-5
Diffusion Chloride [m^2/s]	2.10−11	2.10−12	2.10−14

1.2. Portland cement

1.2.1. Hydration of Portland cement

Ordinary Portland cement (OPC) is the most commonly used type of cement globally. OPC is the main ingredient of cement paste, mortar and concrete. It is produced by grinding Portland cement clinkers and a limited amount of gypsums. The raw material of limestone, marl and a small addition of iron are burnt at 1450ºC. The main component of class OPC clinker is alite (C_3S, 60-50% by weight), belite (C_2S, 10-20% by weight), tricalcium aluminate (C_3A, 5-10% by weight) and calcium aluminate ferrite (C_4AF, 3-8% by weight) [39].

OPC is a hydraulic material. When OPC is mixed with water, it causes a series of chemical hydration reactions and causes to set. The setting can take several hours, and the paste hardens in several weeks, resulting in progressive stiffness, strength, shrinkage and creep behavior of concrete. The reactions between major phases and water usually occur at the same time but a different rate. These reactions are influenced by several factors such as temperature, fineness of cement, the concentration of elements, the water-cement ratio, the presence of additives, etc.[40]. The chemical reaction of pure cement compounds may be summarized as follows [40]:

Calcium silicates

Alite is the main clinker phase of OPC, and it is responsible for the initial set and early strength development (before 28days). As soon as C_3S makes contact with water, several ions start dissolving from the C3S grain surface, leading to a large amount of heat being released [41]. Initially, Calcium silicate hydrate (C-S-H) gel has started to precipitate around the C_3S grain, while solid calcium

hydroxide (CH) is not precipitated due to a poisoning of the surface of the CH nuclei by silicate ions [40]. CH starts to precipitate until the concentration of CH is higher enough to overcome the poisoning effect.

Belite is the second most abundant clinker in OPC, and belite contributes effectively to concrete strength development after 28 days. It usually reacts 30% in the first 28 days and 90% in one year [42]. Belite (C_2S) reacts with water in a similar way compared to alite at a slow rate.

The following chemical equation illustrates [40] :

$$2C_3S + 5.6H \rightarrow C_3S_2H_3 + 2.6CH \quad (1.1)$$

$$2C_2S + 3.6H \rightarrow C_3S_2H_3 + 0.6CH \quad (1.2)$$

In reality, the Ca/Si ratio in the C-S-H is not a constant entity, and it varies for different types of cement [41]. It is typically in the range of 1.57 to 2.1. For example, Bentz [43] modified the hydration of their cement as follows:

$$C_3S + 5.3H \rightarrow C_{1.7}SH_4 + 1.3CH \quad (1.3)$$

$$C_2S + 4.3H \rightarrow C_{1.7}SH_4 + 0.3CH \quad (1.4)$$

It is noted that the index provided below each compound indicates their respective volume stoichiometries in the hydration reactions.

Aluminates

Tricalcium aluminate hydrates most rapidly and causes the rapid setting time, and usually, gypsum is added to control this unexpected fast setting. As a result, a large amount of heat is released and contributes to early strength. The ettringite (AFt) needles are first present, and after a period of a few hours, the AFt may become unstable and convert to monosulfate (AFm) form with additional aluminate or ferrite after depletion of free calcium sulphate in the cement paste [44]. On the other hand, AFt has a higher ration S/Ca ratio than AFm. The following chemical equations illustrate the formation of ettringite and monosulfate (AFm), which are the most common type of AFt and AFm, respectively.

$$C_3A + 3C\underline{S}H_2 + 26H \rightarrow C_6A\underline{S}_3H_{32} \quad (1.5)$$

$$C_6A\underline{S}_3H_{32} + 2C_3A + 4H \rightarrow 3C_4A\underline{S}H_{12} \quad (1.6)$$

Ferrite is an impure form of tetracalcium aluminoferrite (C4AF), in which the Al/Fe ratio may differ from 1. It reacts similarly to the C_3A, and it contributes very little to strength. The reaction rate is generally low and decreases with the Fe/Al ratio [41]. The hydration products are also AFt and AFm, with Al_3^+ partially replaced with Fe_3^+ [45]:

$$C_4AF + 3C\underline{S}H_2 + 30H \rightarrow C_6(A,F)\underline{S}_3H_{32} + (A,F)H_3 + CH \quad (1.7)$$

1.2.2. Cement hydration kinetic

Hydration reactions are the fundamental aspect responsible for cementitious material behavior. During hydration reactions, clinker phases transform to give different hydrates, resulting in space bridging between the grains and increasing the solid volume fraction in the cement paste. Silicate phases react to form calcium hydroxide (CH) and calcium silicate hydrate (C-S-H), whereas Aluminate and Ferrite hydration leads to the precipitation of the so-called aluminoferrite hydrates.

Through a typical heat evolution curve Figure 1-1, the hydration of Portland cement can be characterized by four stages: (I) Pre-induction period, (II) induction stage, (III) acceleration stage and (IV) post-acceleration stage.

a. Pre-induction and induction period

It is also called the initial dissolution period. Once cement contact with water, cement immediately reacts, and C_3A is the most rapid active phase and then forms ettringite phase. The evolution of these phenomena slows down rapidly and then followed by a period of low reactivity, known as the dormant stage (or induction period). Different theories have been proposed to explain the mechanisms occurring during the induction period, which are the membrane of protective layer theory or the delayed nucleation and growth theory [46]. The dormant stage will not exceed 5 hours. At this stage, cement grains remain plastic stage. The time at the end of this stage is generally related to the initial set of the cement.

b. Acceleration and post-acceleration period

The main peak of hydration can be observed at this period, in which the rate of reaction accelerates strongly and reach a maximum rate at the end of stage III. The main peak generally refers to the

massive precipitation of hydrated calcium silicate and portlandite from C_3S. Cement paste (or concrete) temperature increased rapidly during this period. Kurdowski [44] described this mechanism as the transport of ions to and from the surface of the anhydrous particle through a gradually thickening shell that forms around the anhydrous core. These shells may reach a thickness of 0.5 μm to 1.0 μm after 8-10 hours of hydration.

The final setting time generally occurs before the paste shows the maximum rate of heat development. The post-acceleration stage (IV) slows down gradually due to the decline in the amount of yet unreacted grains. The thickness of the hydrate layer that covers unhydrated particles increases, and the surface area of the unhydrated part decreases. The C-S-H phase continues to be formed, and the relative contribution of C_2S to this process increases with time.

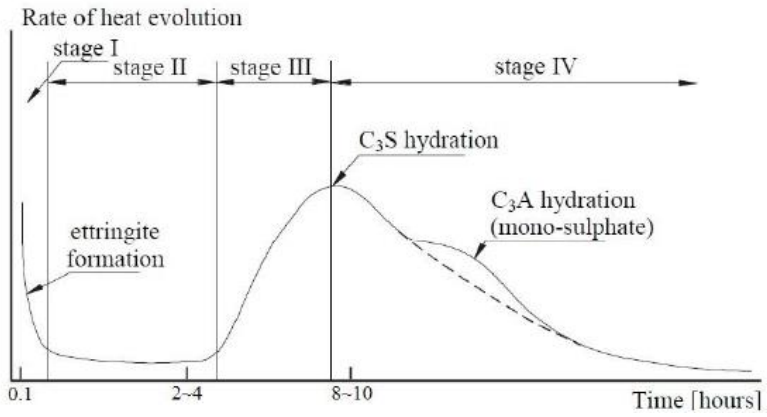

Figure 1-1. Rate of heat evolution during the hydration of Portland cement [47].

1.2.3. Development of microstructure in hydrating cement paste

When cement contact with water, cement grains are separated individually by water. As mentioned previously, C_3A is the most active phase during the pre-induction period of hydration. At this stage, the cement grains are covered with an aluminum-rich gel and short ettringite rods (Figure 1-2a). After this stage, C_3S starts to react. The “outer” C-S-H formed on the ettringite needles. Next, the second hydration of C_3A produces the longer ettringite needles and the beginning of “inner” C-S-H formation. The morphology of C-S-H gel at this stage is different, which shows as honeycomb [48] or long fiber [49]. The calcium hydroxide precipitates as a crystalline from the solution into an empty pore. It looks like a hexagonal plate-like shape, as shown in Figure 1-2. Ettringite has a crystalline or needle with a

length up to 10μm and 0.25μm in diameter. The C-S-H formation and CH crystalline continuously form in which the solid phase increase rapidly (Figure 1-2c) until the cement paste hardens.

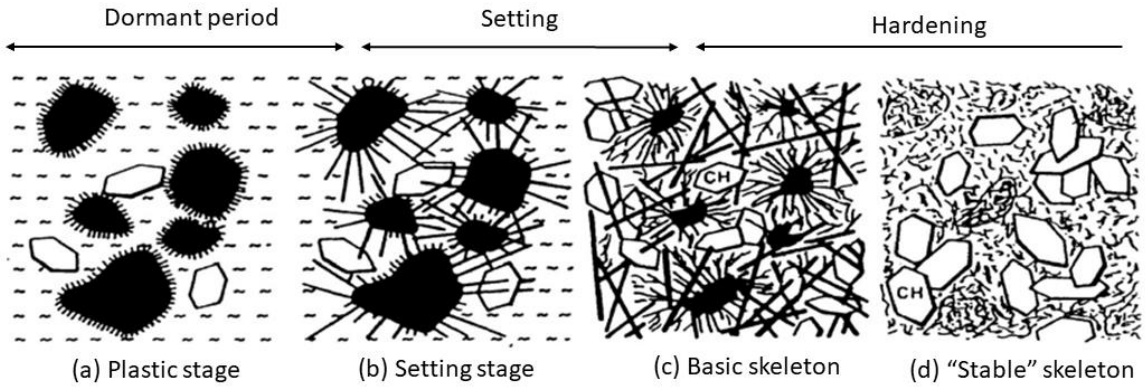

Figure 1-2. Formation of reaction products and build-up of microstructure [49].

1.3. Calcium-silicate-hydrates (C-S-H)

The C-S-H occurs after the dormant stage (Figure 1-3) as C_3S start reacting. C-S-H is the main hydration product in Portland cement system, and it contributes significantly to the physical, chemical and mechanical properties. Figure 1-5 shows the SEM image of typical C-S-H morphology. The solid structure of C-S-H, based on tobermorite, is composed of a complex layer of Ca and O atoms in contact on both sides with silica chains (as illustrated in Figure 1-3) [50–52]. C-S-H has a composition of ~1.5-1.9 $CaO.SiO_2.nH_2O$, which the water molecules, n, depend on the relative humidity and temperature. The Ca/Si and Al/Si atomic ration of the C-S-H gel present in cement paste is 1.7-2.1 and 0.05-0.1, respectively [41].

Scrivener [53] employed the backscattered electron (BSE) image to distinguish IP and OP, while Richard et al [54] used transition electron microscopy (TEM) to recognize them. The C-S-H is classified as "inner" Ip and "outer" Op C-S-H, defined as those formed in space initially occupied by clinker grains and by water, respectively, [55,56], as shown in Figure 1-4. By means of nitrogen sorption tests, Jennings et al. [57] discovered the existence of two types of C-S-H with different densities: low-density (LD) C-S-H with a density of 1.44 g/cm^3 and high-density (HD) C-S-H a density of 1.75 g/cm^3.

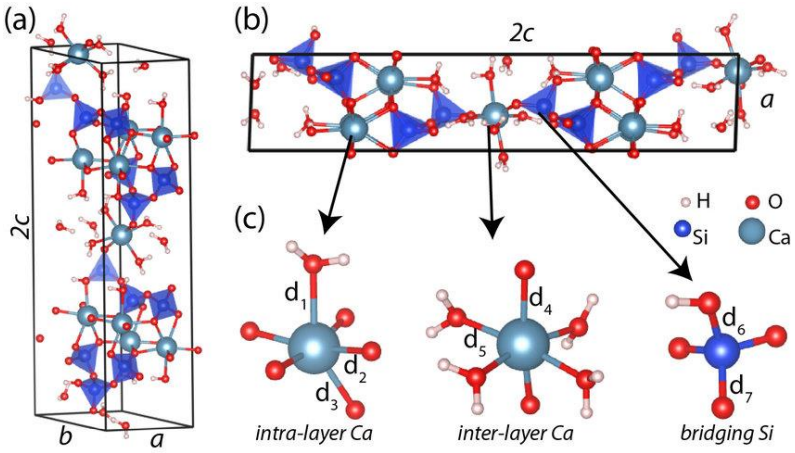

Figure 1-3. Model C-S-H structure represented by 14Å tobermorite in (a) perspective and (b) side view. (c) Bonding geometries of intra-layer Ca, inter-layer Ca and bridging Si. O, H, Si and Ca atoms are shown with red, white, blue and light blue spheres using a ball-and-stick model [52].

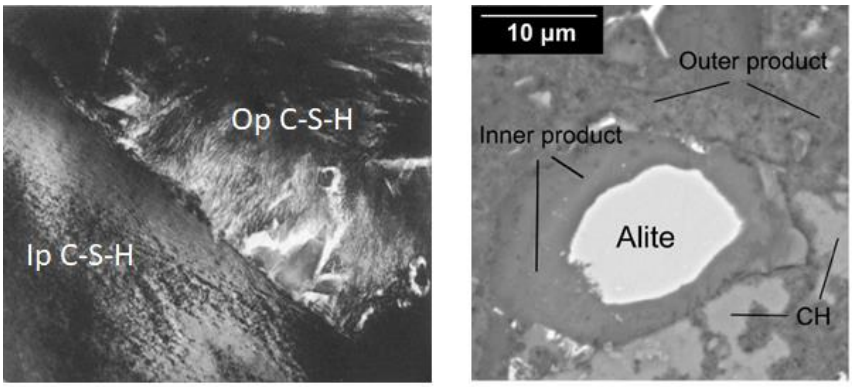

Figure 1-4. (a) A typical TEM image showing an Ip C-S-H and Op C-S-H of a paste hydrated for 3 months (w/c=0.4, 20ºC) [55], (b) Backscattered electron (BSE) image of a CEM I cement hydrated under distilled water for (b) 90 days (at 20°C w/c = 0.4) [56].

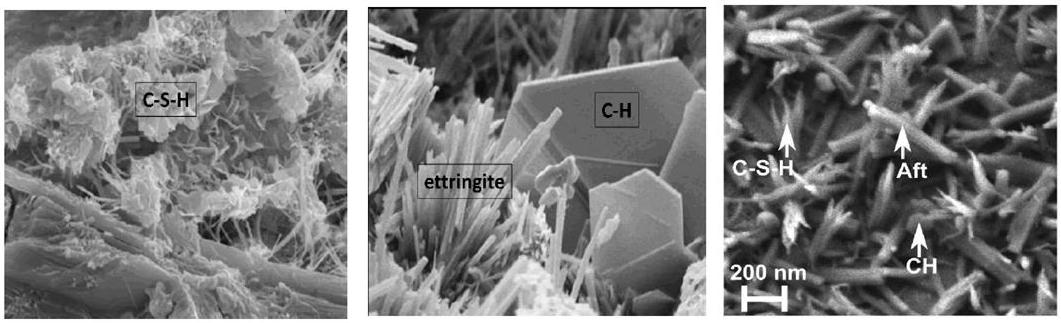

(a) (b) (c)

Figure 1-5. SEM image of (a) C-S-H, (b) platy crystals of Portlandite CH and needle-like ettringite Aft and (c) of clinker surface [58,59].

1.4. Calcium-aluminate-silicate-hydrates (C-A-S-H)

In the presence of SCMs, the Ca/Si ratio is generally lower than in neat paste, while the Al/Si is expected to increase with alumina-silicate SCM such as slag, fly ash and especially calcined clays [60–64]. Richardson [65] has reported "fibrillar-like" or "foil-like" morphologies for outer C-A-S-H, with a foil-like morphology only observed for Ca/Si atomic ratios at or below 1.5. The Al/Si ratio of C-A-S-H is from 0.11 to 0.34 for the system with slag, measured by nuclear magnetic resonance (NMR). Interestingly, the poor crystalline C-A-S-H was found in the ancient Roman marine concrete [66] that was immersed in seawater for 2000 years. This concrete is made with a high volume of fine-grained volcanic ash. During the hydration, the crystalline C-A-S-H is formed, and it contributed to the long-term durability of the ancient Roman concrete.

Wilson et al [67] investigate the C-(A)-S-H (with or without aluminate) phase properties on systems with 30% replacement by fly ash and 50% replacement by slag by coupling the nanoindentation and quantitative energy-dispersive spectroscopy (QEDS) technique. The chemo-mechanical properties of C-(A)-S-H shows in Table 1-3. As can be seen, the Ca/Si and Al/Ca atomic ratio in the system with 50S (50% slag) is higher than that in the system with 30FA (30% fly ash).

Table 1-3. The chemo-mechanical properties of C-(A)-S-H phase in the system with fly ash and slag, employed by coupling nanoindentation and QEDS technique. Indentation Modulus M, Indentation Hardness H, Si/Ca atomic ratio, (Fe+Al)/Ca atomic ratio, and S/Ca atomic ratio are indicated.

Systems	M (GPa)	H(GPa)	Si/Ca (at.)	(Fe+Al)/Ca (at.)	S/Ca (at.)
OPC	28.1±3.8	0.85±0.17	0.47±0.04	0.06±0.02	0.05±0.03
30FA	28.6±4.2	0.87±0.19	0.57±0.07	0.15±0.03	0.06±0.03
50S	26.2±2.6	0.78±0.13	0.60±0.04	0.11±0.02	0.04±0.01

1.5. Calcium carboaluminate phase

Calcium carboaluminate phase or AFm-CO_3 phase (including calcium monocarboaluminate Mc and calcium hemicarboaluminate Hc) is formed with the presence of the carbonate content in the mix [68,69]. In an ordinary Portland cement without limestone, C_3A and C_4AF will react quickly with calcium sulphate to form ettringite (AFt). Upon depletion of SO_4^{2-}, remaining C_3A and C_4AF will react with ettringite to form monosulphate or hydroxy-AFm solid solution [70]. In the presence of limestone, this reaction is modified. Calcium monocarboaluminate is immediately formed, and the transformation of monosulfoaluminate to monocarboaluminate occurs at 28 days [71], as shown in Figure 1-6.

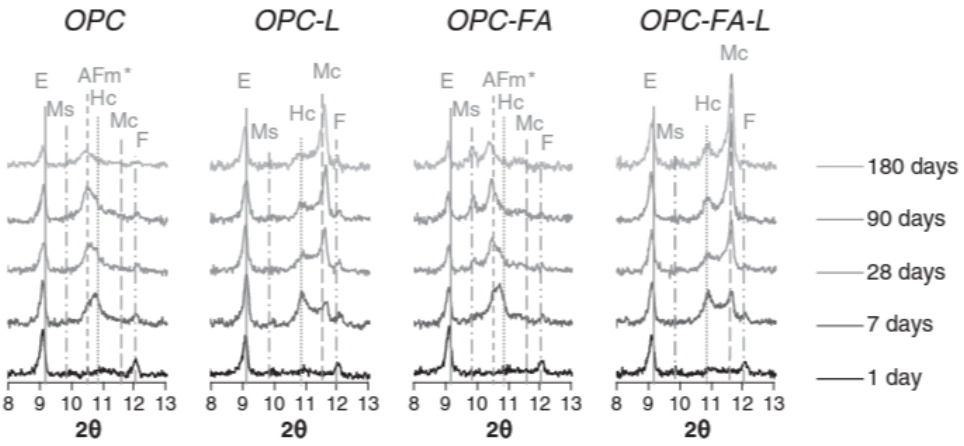

Figure 1-6. X-ray diffraction patterns for the different tested blends at 1, 7, 28, 90 and 180 days. The main peaks of ettringite (E), monosulphate (Ms), possibly a sulphate and carbonate containing hydroxy-AFm (AFm), hemicarbonate (Hc), monocarbonate (Mc) and ferrite (F) are indicated. (OPC: cement, L: limestone, FA: fly ash) [71].*

Interestingly, Wang et al. [72] found that in the Portland-limestone cement with alumina-rich pozzolan, monocarboaluminate Mc formed at a low limestone replacement level while hemicarboaluminate Hc occurred at high substitution levels. Moreover, AFm- CO_3 formation significantly increases the solid

volume of hydrates due to lower densities than the C-S-H, portlandite, and calcite. Consequently, it can help in the reduction of the pore volume, volume stability and chloride resistance [72,73]. AFm-CO_3 is more pronounced in the Limestone calcined clay cement (LC3), which is a family of multicomponent cement that incorporate limestone and calcined kaolinitic clays replacing up to 50% of the conventional OPC [63,74,75] (as shown in Figure 1-7).

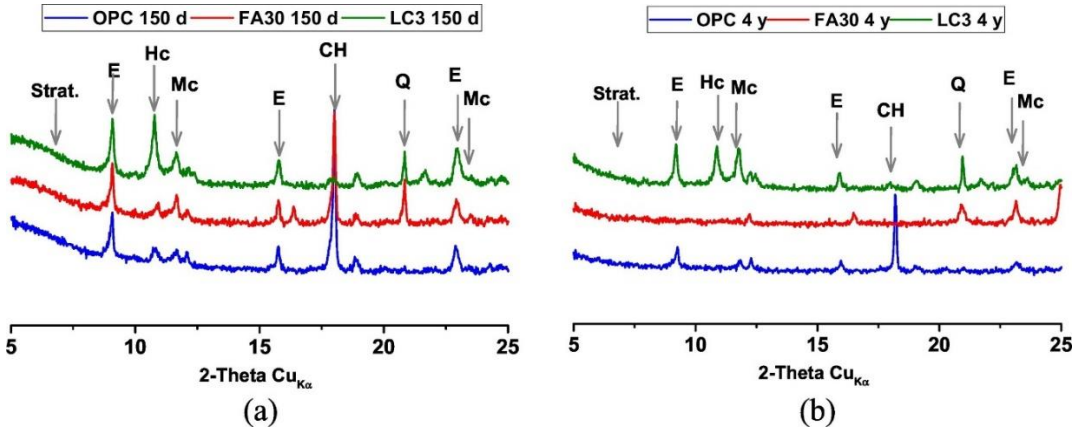

Figure 1-7. X-ray diffractograms of hydrated cement paste at (a) 150 days and (b) 4 years (E: ettringite, Ms: monosulphate , Hc: hemicarbonate, Mc: monocarbonate, Q: quartz, CH: Portlandite, strat.: Stratlingite and F: ferrite are indicated. (OPC: cement, L: limestone, FA: fly ash).

1.6. Supplementary cementitious materials (SCMs)

The demand for the infrastructure expansion for concrete causes the over-exploited natural material sources. Nowadays, the utilization of supplementary cementitious materials (SCMs) in concrete has become very common to produce sustainable concrete. Using SCMs employment in concrete offers not only to enhance the mechanical properties and durability of concrete but also benefits in terms of reduction of carbon dioxide, natural source preservation and waste management. SCMs commonly used meet the requirement of ASTM C618, including Class C and F fly ash—from a coal-fired power plant, ASTM C989 ground-granulated blast-furnace slag (GGBFS) — from iron production, ASTM C1240 silica fume—from ferrosilicon industry and other industrial by-products or natural pozzolanas such as calcined clay, metakaolin, and rice husk ash.

SCMs can partially replace cement in concrete through three different mechanisms (i) a physical mechanism known as filler effect, (ii) the latent hydraulic reactivity, and (iii) a chemical mechanism is known as a pozzolanic reaction.

(i) Filler effect

Finely ground mineral fillers or fine powder influenced the rate of reaction in cementitious materials in the early hydration [76]. The acceleration can be contributed by several mechanisms: (i) the dilution of cement content, which provides relatively more space for the formation of hydrates from the clinker hydration [77], (ii) the heterogeneous nucleation of C-S-H is enhanced due to extra surface provided by fine filler, acting as additional nucleation sites [58,76] and (iii) ion sorption/exchange effects, which means the sorption of several ions on the C-S-H drive force for continuing hydrate growth [78,79]. Among these, the nucleation site (or seeding effect) effect is perhaps the most important mechanism that might affects the hydration kinetic of Portland cement. An example from [58], fine ground limestone accelerates the hydration of C_3S by providing an extra surface for nucleation. At an early age, Figure 1-8 indicates during the hydration, the surface of C_3S and limestone is covered by hydrates. Obseverly, C-S-H precipitates more on limestone surface after 3 hours of hydration than on alite grain (Figure 1-8b). The filler effect of SCMs mainly depends on some critical parameters, such as particle size, crystallography, etc.

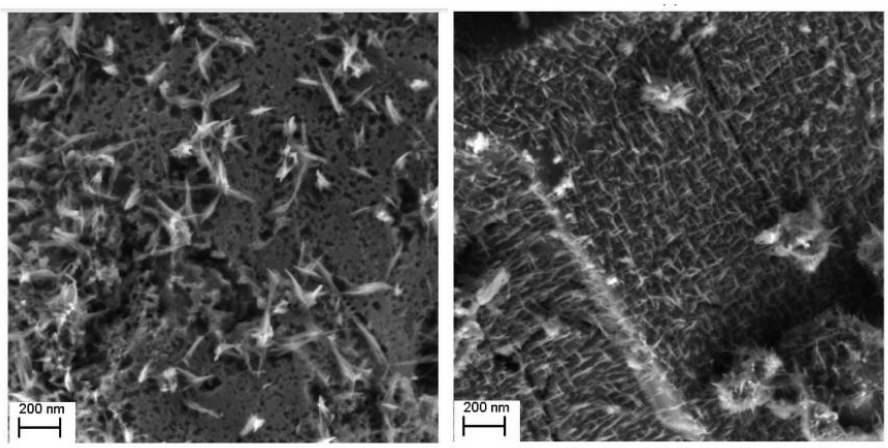

Figure 1-8. Example SEM images of the surface: (a) C_3S grain and (b) limestone grain, for the mix of 60% C_3S and 40% limestone after 3 hours of hydration [58].

(ii) Latent hydraulic reaction

Cement having latent hydraulic properties is produced from ground granulated blast furnace slag (GGBFS or slag). GGBFS is produced by grinding granulated blast furnace slag (GBFS), which is an industrial by-product generated from iron and steel production. GGBFS is commonly used as a partial replacement for Portland cement in mortar or concrete production. The hydration of clinker occurs with

a contact of water (hydrolytic attack) while hydration of GGBFS appears due to the reaction of glass dissolution by hydroxyl attack [80]. The reaction rate of slag cement is slower than Portland cement. Slag needs an activator to activate; thus, cement plays an important role as an activator to provide calcium hydroxide (($Ca(OH)_2$) to react with the active aluminum (Al) and silicon (Si) ions that are liberated from the glassy substance [81]. In addition, $Ca(OH)_2$ also acts mostly for pH activation.

The latent hydraulic property of GGBFS causes a lower early-age strength of concrete with GGBFS. However, the compressive strength significantly increases after 28 days. Addelli et al. [80] investigated the pozzolanic reactivity of GGBFS on mortar with 0-80% replacement level. The results show that the early-age strength of mortar is lower than the reference, while at 28 days or beyond, the compressive strength grows rapidly and exceeds the strength of reference with up to 40% of replacement.

(iii) Pozzolanic effect

SCMs contribute to the hydration reaction at a later age through the reaction with $Ca(OH)_2$ released by the hydration of OPC to form a second C-S-H (II) [7]. Thus, $Ca(OH)_2$ is consumed by the reaction of SCMs and the reaction of SCMs on blended cement mainly gave the same hydration products. For example, the reaction of siliceous pozzolanic SCM as silica fume (S) leads to the formation of C-S-H as follows: $S + 1.7CH + 2.3H \rightarrow C_{1.7}SH_4$. However, for aluminosilicate SCMs as metakaolin, also calcium aluminate hydrates will appear, for instance, monosulfoaluminate in the case of availability of calcium sulfate. With the presence of calcium carbonate (CC) in the blended cement, calcium carbo-aluminate hydrates form instead of monosulfoaluminate, and the balance sulfate will precipitate as ettringite [10].

The second C-S-H and other hydration products will fill the pore space and further reduces the porosity. This leads to an increase long-term strength and durability of concrete. These SCMs include fly ash, metakaolin (MK), and agricultural residue ashes, such as rice husk ash (RHA). Duan et al. [82] found that the compressive strength of concrete incorporating metakaolin increase gradually and improve the pore microstructure of concrete. Antoni et al. [64] reported that the 15% blended cement (10% MK + 5% limestone) indicated higher strength than the neat cement reference mortar at all ages. Madandoust et al. [83] investigated the mechanical properties and durability of RHA concrete (from 0-30% replacement level). The results showed that the lower compressive strength at early age while the

strength increased to 96% at 90 days and became slighter greater than the reference concrete at 360 days. This phenomenon can be explained by the pozzolanic reaction of RHA.

1.7. Mineral fillers

One of the most effective ways to enhance construction sustainability is to develop effective concrete mixtures with less ordinary Portland cement [84]. However, the source of SCMs (such as fly ash or slag) is limited and not available in all countries [85]. However, new potential powder materials may be employed as mineral fillers, e.g., mineral fillers coming from stone quarry wastes produced by crushing rock. As discussed by Taylor [41], for *w/c* below 0.38, complete hydration of the cement will not occur. In fact, a portion of cement will remain unhydrates and thus serve as a reinforcing filler. Thus, in high- or ultra-high performance concrete with high content of cement and low *w/c* ratio, cement clinker is a rather expensive filler material. In a landmark work, Bentz et al. [86] studied the possibility of replacing the coarser fraction of cement which does not react in low water-to-cement systems, as an inert filler. They predicted the hydration and compressive strength by cement hydration and microstructure development model (CEMHYD3D). The water-to-solid (*w/s*) mass ratio was 0.25 to 0.3, where solid was defined as cement plus mineral fillers. The results indicated that the predicted compressive strength of systems with fillers slightly reduced compared to the neat system. Afterwards, Bentz [87] carried out experimental works to valid the previous hypothesis on High Strength Concrete with a compressive strength of 78 MPa. The replacement of "coarse" cement particles replaced by inert fillers at *w/s* ratio of 0.3. The fine cement (<30 μm) was blended with coarse limestone in paste and mortar systems. The results show that the expected compressive strength loss in the filled system in mortars after 7 days was consistent with model predictions, and no significant reduction in strength was detected at 56 days. Bentz et al. [88–90] applied Power's model to study total capillary porosity in limestone-filled cement pastes for a *w/s* in the range of 0.30 to 0.35. The results on high strength concrete with a compressive strength of 78 MPa concluded that it is possible to replace cement with limestone around 15% to obtain a paste with a similar or better gel-space ratio of about 0.9. Moreover, the replacement of about 10% cement with limestone at *w/c* = 0.3 produced a mortar with a reduction of the autogenous shrinkage and chloride diffusion.

1.8. Spent pot lining

1.8.1. Spent pot lining generation

In primary aluminum production, alumina is extracted from metallic aluminum by electrolytic reduction in Hall-Héroult cells, which is shown in Figure 1-9. In this process, a large quantity of electrical current enters the cell through carbon anodes. It passes through the electrolyte bath before being collected by carbon cathodes at the bottom of the cell. The electrolyte is essentially a solution that contains alumina (Al_2O_3) dissolved in cryolite (Na_3AlF_6), held in temperatures around 960° C [91]. The molten fluoride-containing salts and sodium impregnate the carbon cathode lining. Consequently, the cell fails after 5-8 years of operation, and the carbon cathode pot lining is removed by recycling of iron and aluminum pieces.

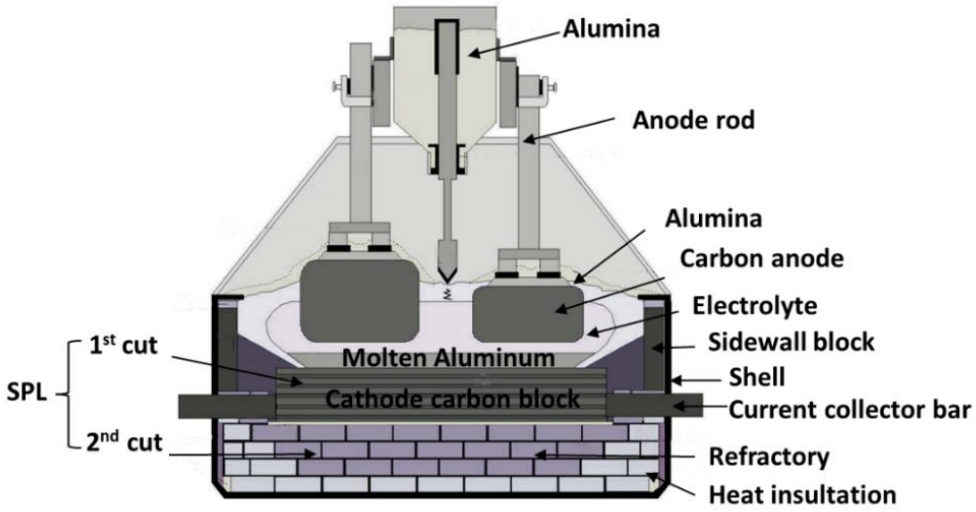

Figure 1-9. Schematic of the main features of a Hall-Héroult aluminum reduction cell [92].

The remaining waste materials are called spent pot lining (SPL). SPL can separate into parts (i) first cut- a carbon-rich fraction constituted of old cathode and (ii) second cut-mainly refractory brick part with a non-carbon fraction (as shown in Figure 1-10.). The composition of the SPL varies depending on the technologies. As can be seen in Figure 1-11, it can be observed that SPL contains cyanides, fluorides and some metals (Al and Na), which are toxic as leaching into water and react with water to explosive gases. Therefore, SPL is listed as hazardous material [25]. Dealing with SPL disposal has become a significant concern of aluminum manufacturers as disposing of SPL into the environment is

not permitted. About 22 kg of SPL is generated per ton of aluminum produced. In 2018, producing 64 million tonnes of primary aluminum generated approximately 1.4 million tonnes of SPL in the worldwise [25]. Roughly 80 kT of SPL is produced in Canada per year, with about 20 kt coming from Rio Tinto (RT) [29]. Demand for aluminum is expected to grow significantly to 2040 [93]. This means that it will also lead to increased SPL generation. In other words, the challenge of managing SPL will continue to be intensive in the future.

(a) (b)

Figure 1-10. (a) Demolition of SPL [92], (b) SPL after breaking up [94].

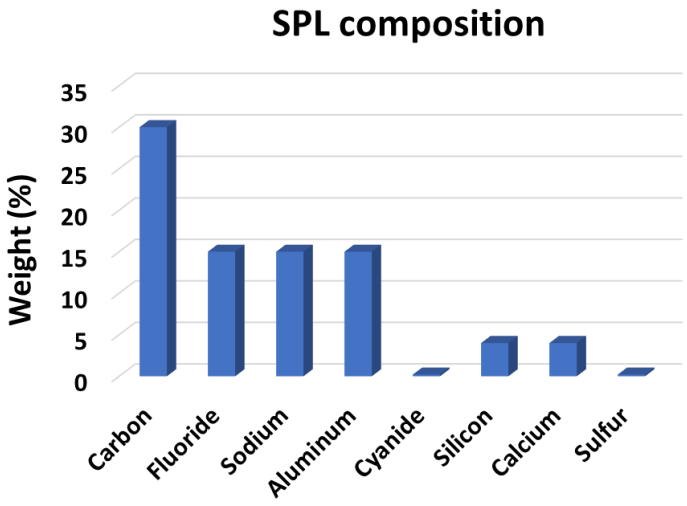

Figure 1-11. Chemical composition of SPL [92].

Table 1-4. Summarized SPL treatment and processes [25].

Process	Company-Owner	Procedure and outcome	Outcome
Pyro-metallurgical	Alcoa (Reynolds) Gum Springs	Crushed and mixed with limestone and sand Rotary kiln at 1000°C	Landfilling dry at a hazardous waste site
	RT (Comalco) COMTOR	Extract cyanides in the pre-treatment reactor	A soluble caustic for cement kiln and alumina plant
	Alcoa of Australia	Ground SPL and react with oxygen and natural gas in an Ausmelt reactor at 1300°C	To make AlF_3-reused
	Nova Pb	Rotary kiln at 1000°C	Calcifrit (high fluoride) & Calcicoke (high C)
	Regain Process	Destruction of simple cyanide to deactivate SPL	To more accessible to transport, but still hazardous
Hydro-metallurgical	Rio Tinto Alcan-LCL&L Process	Total extract of the leachable fluorides and cyanides	A safety treated SPL residue

1.8.2. Spent pot lining treatment

Before re-using SPL by a third party, it has to undergo partial or total detoxification. There are many SPL treatment and processing solutions available. However, some of the processes have been developed to the pilot stage but then stopped at an industrial scale [25]. To date, pyro-metallurgical or hydro-metallurgical processes are the most used in the world. A summary of these processes is summarized in Table 1-4. As can be seen, the treatment to extract toxic elements of SPL is very specific and complex, and their chemical composition of treated SPL will also be different between each process. Therefore, the comparison between these treated SPL is out of the scope of this work. We focus on the hydro-metallurgical treatment explained below as the one industrially implemented in Quebec.

1.8.3. LCLL-ash

In the early 1990s, Rio Tinto developed an innovative process - hydrometallurgical process - called Low Caustic Leaching and Liming (LCL&L) process in Jonquière, Quebec, Canada. The LCL&L process will convert SPL into inert by-products. The plant treats 80 kt of SPL annually and has treated more than 700 kt of SPL since 2008. To date, the unique facility that uses the LCL&L procedure to treat SPL is in Jonquière, Quebec.

The SPL is firstly crushed and then water leached in a low caustic solution to neutralize the hydro-reactivity and put the fluorides and cyanides into the solution, as shown in Figure 1-12. After that, the solid component is filtered to produce an inert residue. After this water leaching stage, the second cut is treated to produce LCLL-ash. Approximately 10 kt per year of LCLL-ash is produced in this plant [92]. The mean particle size of LCLL-ash is approximately 20 µm. LCLL-ash has a high content of alumina and silica, which can be a potential material to replace partial cement in concrete production.

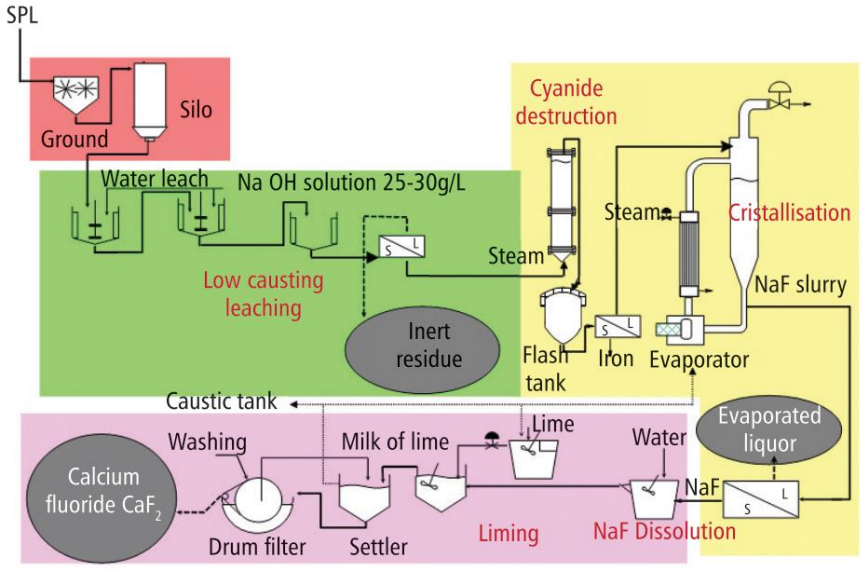

Figure 1-12. LCL&L process diagram [95] .

1.9. Ultra-high performance Concrete (UHPC)

1.9.1. Introduction

Ultra-high performance concretes (UHPCs) are a new class of cementitious composites that has been developed more than 30 years of academic and industrial research to achieve the following properties [96–100]. Undoubtedly, UHPCs have become a breakthrough in several civil engineering and architectural applications, e.g., bridge infrastructure, retrofitting techniques, etc. [96,101–105]:

- **Compressive strength between 150 and 250 MPa** [99,106,107], which is almost comparable to those of steel fibers and allows reducing the structural size. Figure 1-13a compares the compressive behavior of UHPCs with a Normal Concrete in terms of a stress-strain relationship. The compressive strength and ultimate deformation of UHPCs is significantly greater than conventional concrete with a factor of magnitude between 5 and 10. Notably, the compressive strength of UHPCs is comparable to the yield strength of structural steel;

- **A ductile tensile behavior** that confers an unprecedented *crack resistance* with respect to previous concrete composites. UHPCs exhibit a strain hardening concrete, which means that the tensile "material law" (i.e., the stress-strain relationship of the material under tension) has an ascending branch, as shown in Figure 1-13b. Such ductile tensile response is due to multiple micro-cracks, which grow simultaneously before their coalescence into a large crack at large deformation. Figure 1-13.b shows an example of multiple microcracks occurring in a UHPC sample under tensile loading, which is not visible to the naked eye as they have a micrometer size [108].The same figure compares the tensile response of UHPCs and conventional concrete showing a plateau at a stress of about 12 MPa with deformation at the peak load of about 0.15% [109–113]. Note that the tensile strength is of the order of 10-15 MPa, which is 10 times less than the compressive strength. The area underneath the tensile stress-strain relationship is also called *fracture energy*, i.e., the energy needed to create a crack in the material. The UHPCs fracture is about 20–30 kJ/m^2, which is more than 100 times that of a Normal Concrete (NC). Figure 1-13.a shows the tensile behavior of an UHPCs in more detail;

- **Nearly zeros permeability and chloride diffusion** guarantee exceptional durability to UHPCs structures [98]. Notably, even when microcracks may occur, e.g., under serviceability states for non-pre-stressed structures, UHPCs exhibits still very low permeability until a critical deformation threshold [114–116].

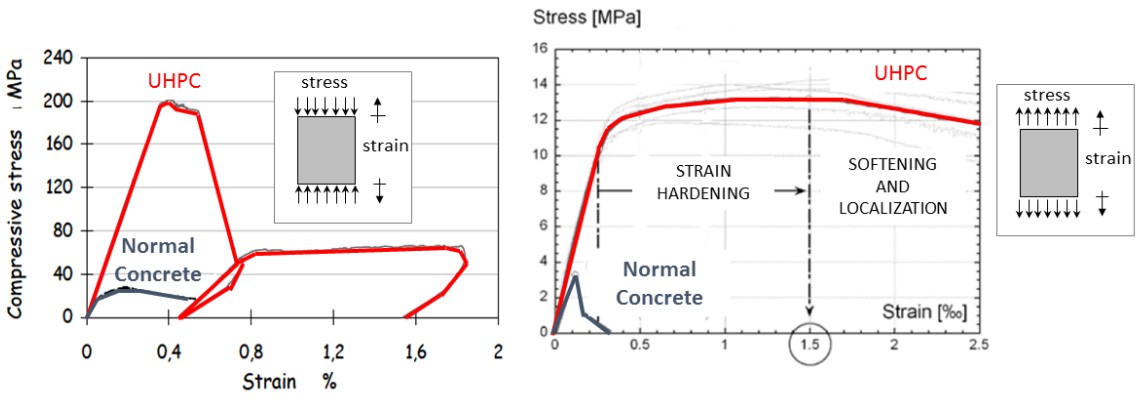

(a) (b)

Figure 1-13. Comparison of an UHPC and Normal Concrete: (a) Compressive behavior [101]; (b) Tensile behavior [117].

Figure 1-14a compares different beam solutions with the same maximum moment. Clearly, the use of UHPC allows reduction of the weight from about 500 kg/m down to 140 kg/m for concrete structures, and it provides a solution comparable to the steel structure. As shown in Figure 1-14a, the thickness of UHPC is thinner than normal strength UHPC to meet the sustain loads. Thus, UHPC can offer new possibilities of reduced-weight structures and new designs of structures for better aesthetics. Also, UHPC is eliminated using coarse aggregates to improve the granular packing density (Figure 1-14b) leading to a denser interfacial transition zone of microstructure and increasing the long-term durability of UHPC.

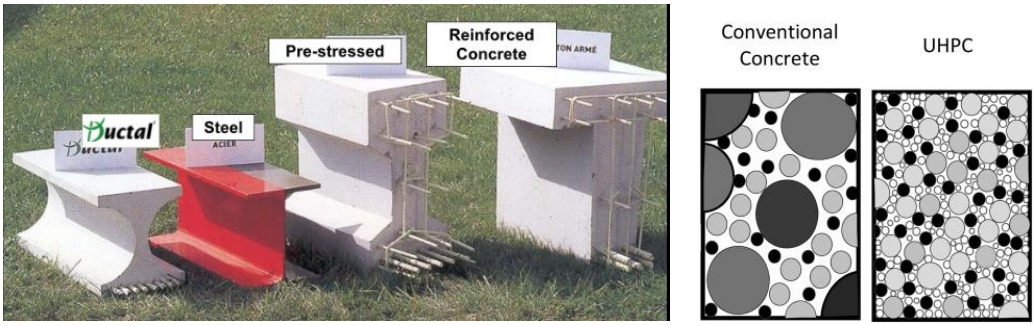

Figure 1-14. (a) Comparison of beam with same moment resistant: (i) Reinforced UHPCs (ii) steel beam; (iii) Pre-stressed concrete; (iv) Reinforced concrete [118], (b) Compare between the conventional concrete versus UHPC [119].

Because of its exceptional properties, structures made with UHPC will have much longer service life with lower maintenance and repair costs over time compared to NSC or HPC structures [120]. According to Aïtcin [121], the Quebec Ministry of Transportation calculated that the initial cost of a 55 MPa bridge was 8% less than that of a 35 MPa bridge without taking into account a more extended

service life. UHPC became commercially available in the United States since 2000. Favorite constructions of UHPC can be seen as structural repairs, bridge deck overlays, and architectural works. For example, Figure 1-15 presents some constructions applied to UHPC materials.

(a) (b) (c)

Figure 1-15. (a) UHPC overlay on a bridge, USA, (b) Fondation Louis Vuitton, Paris, France, (c) Pedestrian bridge in Sherbrook, Canada.

1.9.2. Ingredients

Binder

UHPC contains a relatively high amount of cement content compared to that used in conventional concrete or high-performance concrete, in the range of 600-1200 kg/m^3 [122]. Silica fume (SF) is the second essential binder element in UHPC. SF has a high pozzolanic reaction that reacts with Portlandite from cement to produce additional C-S-H, enhancing the strength properties of UHPC. SF can improve the workability of UHPC in filling voids between cement and fine aggregate [122,123]. Silica fume content is from 15% to 35% by mass of cement in UHPC formula [124,125]. It should be highlighted that only about 20% of total silica fume hydrates, given the extremely low *w/c* environment [126]. Thus, UHPC strength from silica fume would rather come from the unreacted silica fume that contributes to reducing the final porosity and increasing the packing density of the matrix microstructure. The cost of UHPC is higher than that of traditional concrete, likely due to high binder content. For example, NC is sold at \$130/m^3, and the cost of commercially available UHPCs escalates to the range of \$750–\$1,400/m^3 in Europe and \$1,000–\$2,620/m^3 in North America [127–130].

Fine aggregates

UHPC eliminates coarse aggregates to improve the interfacial transition zone (ITZ) between the cementitious matrix and aggregate. Furthermore, ITZ defects reduce overall matrix porosity and

improve mechanical properties [131]. The fine aggregates are likely quartz sand or natural sands. These fine aggregates can also reduce the paste thickness of UHPC. An optimum sand-to-cement ratio is reported as 1.4 for a quartz sand size of 0.8 mm [132].

Steel fibers

Adding steel fiber to UHPC can enhance the ductility of UHPC [37]. The workability of UHPC mixture can be affected by the addition of steel fibers. The most common size of steel fiber is 13 mm in length and 0.2 mm in diameter. However, 6 mm long and 0.15 mm diameter steel fibers can be used up to 10% by mixture volume [133]. Steel fibers account for up to 50% of UHPC costs. More than 45% of UHPC cost is attributed to powders [129]. Richard et al. [134] recommended using 2% by mixture volume of steel fibers for an economical and workable UHPC mixture.

Water-to-binder (*w/b*) ratio

UHPC is characterized by a very low *w/b* ratio. As the *w/b* ratio drops, the distance between adjacent binder particles reduces, implying that the hydrates of one particle must shrink to reach the hydrates of surrounding particles. It also improves the hydration of the product and densifies the microstructure of the UHPC, resulting in increased mechanical strength and durability of the product [119,135]. An optimum *w/b* ratio of 0.18-0.25 was found in a previous study [22,23,136] to ensure spread flow and achieve maximum relative density.

Superplasticizer

Due to the very low *w/b* ratio, the workability of UHPC can be improved by adding a superplasticizer (SP) to the mixture. SP had been used as critical chemical admixtures for concrete [137]. The molecules are adsorbed onto particles, which are subsequently physically separated by steric and/or electrostatic forces opposing their attractive forces [138,139]. The amount of SP needed depends on the consistency of the materials in the combination as well as the type of SP used. Polycarboxylic ethers (PCEs), a new generation of superplasticizers created in the 1980s, can reduce water by up to 40% [140,141]. The effects of PCE-type SP on the fresh behavior of cementitious materials are found as adsorption, rheological behavior and retardation hydration effect [139,141]. Wille et al. [132] suggest that SP dosage of 1.4-2.4% by cement weight.

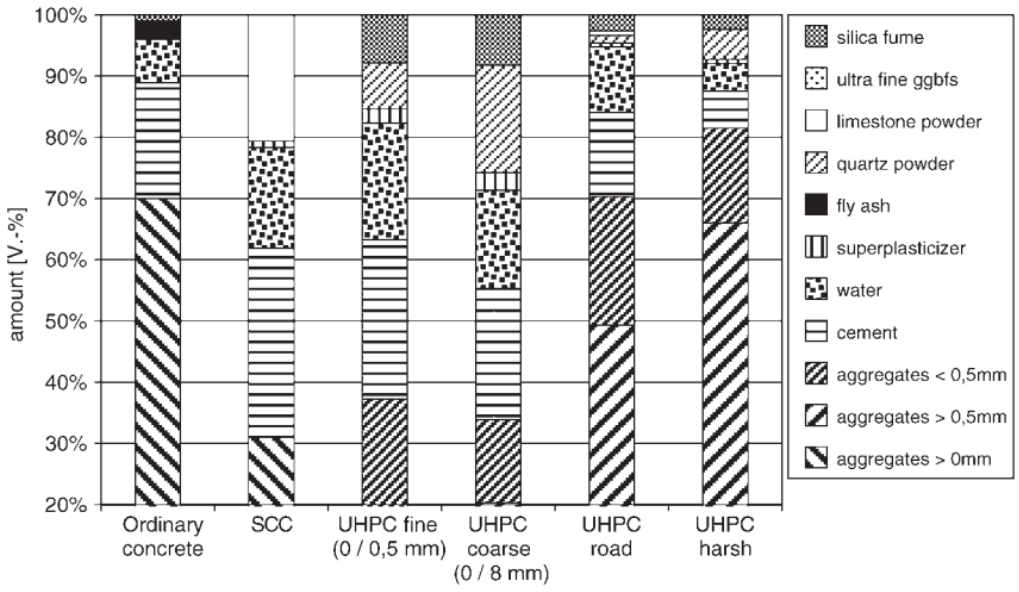

Figure 1-16. Comparison of mix compositions for normal-strength, high-strength and various UHPCs [142].

Figure 1-16 compares the composition (by volume) of a normal-strength concrete, a high strength concrete, a self-compacting concrete (SCC) and different UHPCs with sand inclusions of different maximum sizes. Note that normal UHPC mix designs include a large amount of binders (cement + silica fume)[1] and no coarse aggregate (i.e., sand with a diameter larger than 0.5 mm). That is, common UHPC employs only fine sand for two reasons: (i) to assure the rheological property at the fresh state [143]; (ii) the difference in thermal and mechanical properties between aggregate and cementitious matrix is one of the main reasons for the micro cracking in the interface zone, and that the length of the micro cracks is proportional with the grain size of aggregates [144].

[1] *Really, UHPCs should literally be considered as a mortar as the maximum sand size is less than 2 mm.*

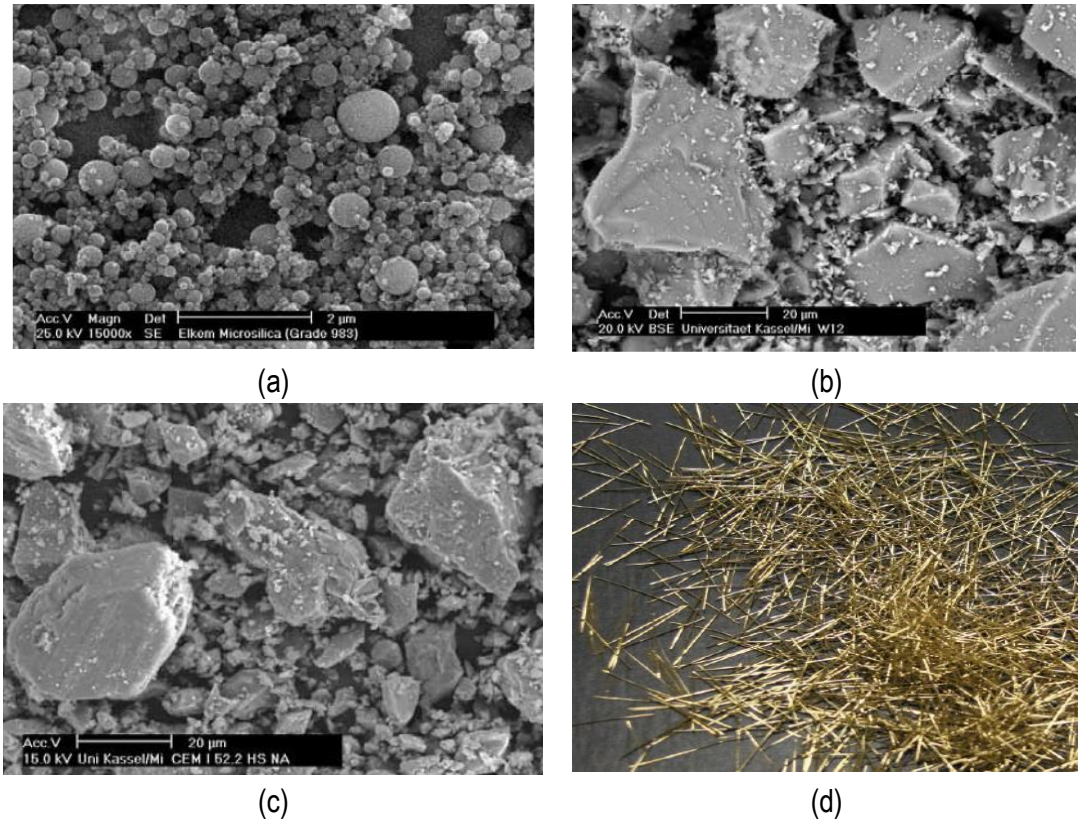

Figure 1-17. Examples of (a) micro-silica particles with a size of 0.01-1 μm; (b) quartz sand with a diameter between 1-100 μm; (c) cement clinker grains with a size 0.1-100 μm; (d) steel micro-fibers with a length of about 12 mm and diameter of 0.2 mm.

1.9.3. Mix design method

The UHPC mix design has been optimized in a twofold manner:

1. By **maximizing the packing density** of the microstructure with the use of very fine minerals, quartz powder and silica fume so that the micrometer pores and defects are nearly absent [97,99]. Figure 1-18.a schematically illustrates the maximization of the packing density of an UHPCs is by the optimal choice of the size distribution of particles (powder quartz, sand, silica fume, and cement);

2. by adding an **efficient steel micro-fiber reinforcement** which maximizes the composite toughness (i.e., the dissipated energy). The fiber reinforcement has been optimally designed to assure that the fibers pull out simultaneously without breaking from the cement matrix. Figure 1-18.b shows the distribution of the steel micro-fiber (at a fiber volume content V_f = 2%) inside a UHPC by tomography.

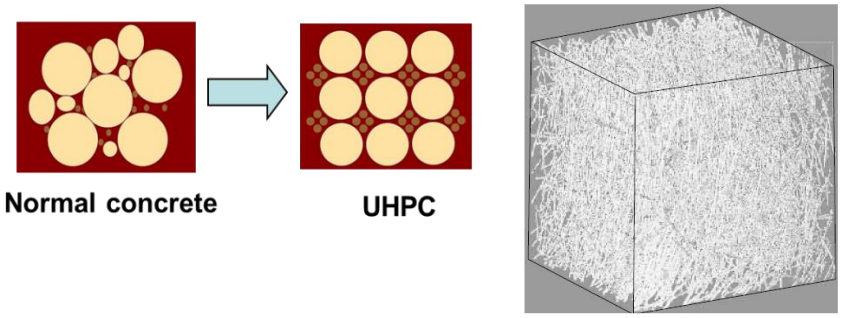

(a) (b)

Figure 1-18. (a) Example of the UHPCs microstructure optimization by maximizing the packing density with an optimal size distribution of the particles; (b) View of the steel fiber distribution (at the volume content of 2%) within an UHPCs by tomography [101].

The size distribution of ultrafine particles[2] has been optimized to maximize the packing density. Figure 1-19.a shows an example of the optimal size distribution of the ultrafine particles (cement, silica fume, quartz powder, sand). As illustrated in Figure 1-19b, this packing optimization causes an increase in strength but also significantly reduces the amounts of water and superplasticizer required for the rheological flowability. The effect of the packing density on the compressive strength is shown in Figure 1-19.a which shows the relationship between the compressive strength and the density: the greater the packing density, the greater the density, the greater the compressive strength. Notably, heat treatment can further affect the packing density increasing the compressive strength, as shown in Figure 1-19b.

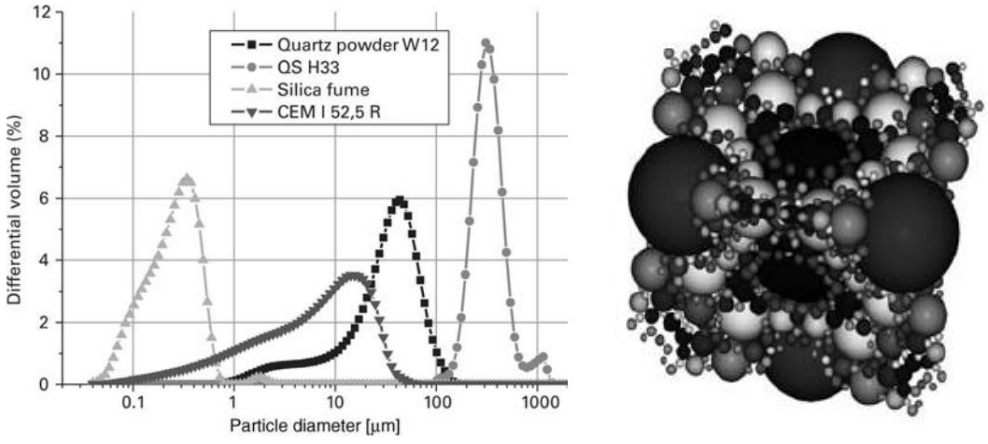

(a) (b)

Figure 1-19. (a) Example of optimal size distribution for ultra fine particles in UHPCs mix design; (b) Optimum packing [142].

[2] *ultrafine particles cement, quartz, powder, silica fume plus further inert or reactive fine fillers if required*

Particle packing density

The method for designing the concrete mixtures is particle packing density to obtain a compact mixture by selecting the appropriate size and proportion of particulate materials. In considering packing, smaller particles should be employed to fill the voids between the large particles, resulting in a lower porosity throughout the entire skeleton. The concept of packing density is introduced to evaluate the arrangement of the granular mixture. The packing density of granular mixtures can be defined as the volume of solid per total bulk volume.

With the advent of novel concrete types, such as high-performance concrete (HPC), self-consolidating concrete (SCC), and ultra-high-performance concrete (UHPC), particle-size optimization has reignited attention in recent decades [158]. The packing density of concrete has been shown to be one of the most critical factors impacting its performance (increasing strength, reducing permeability, and reducing porosity in the transition zone). The increase in aggregate packing density can increase the workability of concrete at the same *w/b* or increase the strength of concrete by reducing *w/b* at given workability for a fixed paste volume. However, a higher packing density is preferred; the maximum packing density does not necessarily guarantee a workable concrete mixture [159].

Particle packing models

Particle packing models are based on mathematical equations that specify how different-sized particles interact geometrically. The analytical particle packing models are used to calculate the theoretical packing density of a mixture. The calculation is based on the particle size distribution and packing density of the various particle groups present in the mixture. It is noted that we should consider the interaction between the particles: wall effect — this effect occurs close to a wall or close to a large particle and loosening effect — this effect appears when the small particles are too large to fit in between the voids or between the large particles, as shown in Figure 1-20.

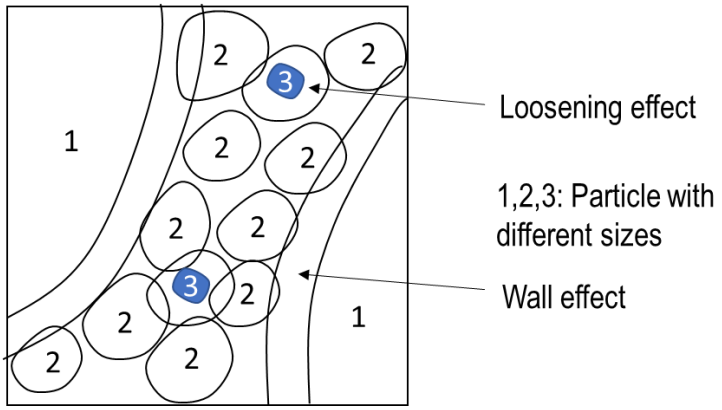

Figure 1-20. Wall and loosening effects in a ternary system of granular mixture [160].

Several common particle packing models are developed and employed. De Larrard and Sedran [158,161,161,162] proposed different approaches to design concrete, such as the Linear Packing Density Model (LPDM), and Solid Suspension Model (SSM) and Compressive Packing Model (CPM). Fennis [163] developed the compaction-interaction packing model (CIPM) based on the CPM method [160]. The CIPM take into account the interaction due to the surface forces like van der Waals forces for very fine particle (≤ 125 µm), which are necessary for UHPC. Hajiesmaeili et al. [100] applied the CIPM model to design Ultra-High Performance Fiber Reinforced Concrete with 50% clinker replacement by limestone. Therefore, the CIPM will be selected in this study to optimize the packing density of granular mixtures of UHPC.

Compaction-interaction packing model

The CPM [160] considers geometrical characteristics (loosening and wall effects) as well as compaction energy to predict the packing density of a mix having n monosized classes. Fennis used Eq.(1.8) to calculate the actual packing density Φ for the monosized class.

$$K = \sum_{i=1}^{n} \frac{\varphi_i / \varphi_i^*}{1 - \varphi_i / \varphi_i^*} \tag{1.8}$$

$$\frac{\varphi_i}{\varphi_i^*} = \frac{r_i \Phi}{\beta_i \left(1 - \sum_{j=1}^{i-1} \left[1 - b_{ij}\left(1 - 1/b_j\right)\right] r_i \Phi - \sum_{j=i+1}^{n} \left[a_{ij} \beta_j / \beta_j\right] r_i \Phi\right)} \tag{1.9}$$

K = Compaction index depends on the compaction energy applied to the mixture

β_i : virtual packing density of size class i, as in Eq.(1.9)

$$\beta_i = \alpha_i(1+\frac{1}{K}) \tag{1.10}$$

α_i = Experimentally determined packing density of class i for a prescribed packing process and K value, as shown in Table 1-5.

The components of UHPC are in a wide range of particle sizes, which are not monosized without interaction. Then, the actual packing density Φ is obtained by solving the *Eq.* (1.11):

$$K = \sum_{i=1}^{n} \frac{\sum_{k=1}^{M} \frac{\varphi_{k,i}}{\beta_{k,i}}}{\sum_{k=1}^{M} \varphi^*_{k,i} / \beta_{k,i} - \sum_{k=1}^{M} \varphi_{k,i} / \beta_{k,i}} \tag{1.11}$$

Where,

$$\varphi_{k,i} = p_k . r_{k,i} . \Phi \tag{1.12}$$

$$\varphi^*_{k,i} = \beta_{k,i} . p_k \left[1 - \left[\sum_{j=1}^{i-1} \left[1 - b_{ij}(1 - 1/\beta_{k,i} \right] \right] r_{k,j} \Phi + \sum_{J=i+1}^{n} a_{ij} r_{k,j} \Phi / \beta_{k,j} \right] \tag{1.13}$$

In which

Φ = Actual packing density of the mixture with k materials

p_k = Volume fraction of material k

$r_{k,i}$ = Volume fraction of material k in class i

$\beta_{k,i}$ = Virtual packing density of material k in class i (Eq.(1.11))

$$\beta_{k,i} = \alpha_{k,i}(1+\frac{1}{K}) \tag{1.14}$$

$\alpha_{k,i}$ = Experimentally determined packing density of class material k in class i

The geometrical interaction between size classes is represented by a_{ij} — the loosening effect and b_{ij} —the wall effect, as is shown in Eq. (1.12) and Eq.(1.13) , respectively.

$$a_{ij}=\begin{cases}1-\dfrac{\log_{10}(d_i/d_j)}{w_{0,a}} & \log_{10}(d_i/d_j)>w_{0,a}\\ 0 & \log_{10}(d_i/d_j)\le w_{0,a}\end{cases},\quad w_{0,a}=\begin{cases}w_a\times L_a & \mathrm{d}_j<25\mu m\\ w_a & \mathrm{d}_j\ge 25\mu m\end{cases} \tag{1.15}$$

$$b_{ij}=\begin{cases}1-\dfrac{\log_{10}(d_i/d_j)}{w_{0,b}} & \log_{10}(d_i/d_j)>w_{0,b}\\ 0 & \log_{10}(d_i/d_j)\le w_{0,b}\end{cases},\quad w_{0,b}=\begin{cases}w_b\times L_b & \mathrm{d}_j<25\mu m\\ w_b & \mathrm{d}_j\ge 25\mu m\end{cases} \tag{1.16}$$

Where,

d_i and d_j are the diameter of size class i and class j, respectively

d_c is the transition diameter in the CIPM below which compaction-interaction is taken into account

$w_{0,a}$ and $w_{0,b}$ are the functions for maximum range of loosening effect and wall effect respectively.

w_a and w_b are the constants denoting the maximum range of loosening effect and wall effect, respectively.

L_a and L_b are constants (L_a =1.5 and L_b =0.2).

Table 1-5. K values for various packing processes [163].

Packing process	Methods	K value
Dry	Pouring	4.1
	Rodding	4.5
	Vibration	4.75
	Vibration + compression of 10 kPa	0
Wet	Smooth thick paste	6.7
	Proctor test	12
Virtural	-	∞

Packing density measurements of the components

For the powders larger than 125 μm, the particles are weighed in a container with a known volume. Packing density is calculated by dividing the weight of the particles in a unit volume by the specific gravity of the particles.

For the powders smaller than 125 μm, to measure the packing density of the fine powder more accurately, the water demand method based on mixing energy has been used [164]. The liquid demand of the mix is determined as the liquid (water and superplasticizer) at which maximum mixing power is measured. The packing density $\alpha_{i\_\exp}$ of each material can then be calculated as follows: $\alpha_{i\_\exp} = V_p / (V_P + V_L)$, where V_p is the volume of powder, and V_L is the total added liquid solution until reaching the maximum power consumption.

1.9.4. Autogenous shrinkage

Autogenous shrinkage is more pronounced in UHPC than in conventional concrete. While the contribution of autogenous shrinkage to the total long-term deformations in concretes with a high *w/b* ratio can be as low as 5–10% [165], it can reach up to 50% in low *w/b* concretes [166]. A high autogenous shrinkage is easily observed in the first day after mixing, which might generate a micro-crack of UHPC [33,34]. Due to a low *w/c* ratio and high amount of cement and silica fume, the early-age autogenous shrinkage is due to capillary depression caused by the hydration in the porous network and the latter is caused by evaporation of pore water to the surrounding. When the surface tension increases exceed the capacity of the fresh concrete, autogenous shrinkage is manifested [167].

Autogenous deformation is measured according to the ASTM C1698 — applying for cement paste and mortar — by using the sealed corrugated tubes test, as shown in Figure 1-21. The autogenous deformation was zeroed at the final setting time measured as described in ASTM C403. Figure 1-21 presents the sealed autogenous shrinkage of 6 commercial UHPCs for 7 days. As can be seen, while the autogenous shrinkage of U-D and U-F is lowest after 7 days, U-C and U-E exhibit high deformation excessing 800 με.

Figure 1-21. A corrugated PE-mold and a 425 mm reference bar according to the ASTM C1698.

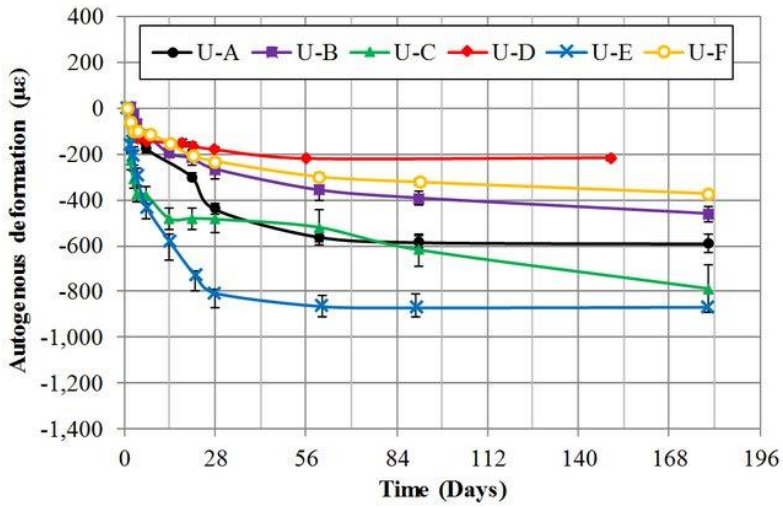

Figure 1-22. Autogenous shrinkage was measured by a sealed corrugated tube test of 6 commercial UHPCs [15].

Therefore, it is important to mitigate the autogenous shrinkage of UHPC. Several solutions can reduce autogenous shrinkage in UHPC, such as: adding fibers [168], adding admixtures (shrinkage-reducing admixtures, SRA, or expansive admixture, EA [169], the superabsorbent polymer [170], using industrial by-products (fly ash [171]) or agricultural waste [33,172]. Soliman et al.[168] replaced cement up to

12vol.% by wollastonite microfibers, resulting in the reduction in total shrinkage (both dry and autogenous shrinkage) by about 16% compared to that of the control mixture at 7 days.

1.9.5. Eco-friendly UHPC

Due to a very low water-to-cement (*w/c*) ratio of UHPC, only part of cement was hydrated. It is reported that about 45–60% of cement hydrates [22,23,136]. Consequently, the unhydrated cement plays the role of an expensive and high-CO2 filler—thereby making UHPC less cost-effective. Several significant efforts on partial replacement of cement with SCMs/fillers are one of the promising solutions to produce affordable UHPC with less environmental impact. In fact, SCMs/fillers are by-products and are considered as waste materials and sent to landfills. Thus, the recycling waste in construction would benefit the environment by lowering landfills for these industrial wastes, as well as the impact of global warming caused by the energy consumption and gas emissions associated with cement manufacture. Moreover, it would improve the workability and comparable strength compared to conventional concrete. Also, it would reduce the cost of concrete production by reducing the cement content. The commonly SCMs/fillers used UHPC include fly ash [173,174], slag [175–177], limestone powder [178,179], rice husk [33,180,181], granite powder [182,183] and glass powder [184,185].

Chapter 2. The Microstructure Signature of Cement Pastes Recycling Treated Spent Refractory Lining from Aluminum Production

2.1 Résumé

L'utilisation de sous-produits industriels disponibles localement comme d'ajouts cimentaires (SCMs) et fillers minéraux est essentielle pour réduire le carbone incorporé du béton. S'appuyant sur nos récents travaux sur la réactivité des brasques usées traités, appelés LCLL-ash, comme matériaux cimentaires, cette étude vise à mieux comprendre les changements de microstructure des pâtes de ciment incorporant des déchets de fonderie d'aluminium, tels que les LCLL-ash et l'anhydrite synthétique ($CaSO_4$).

Tout d'abord, la poudre fine de LCLL-ash a été utilisée pour remplacer partiellement le ciment dans les pâtes de ciment avec un rapport eau/liant (e/l) constant de 0.35. Les pâtes de ciment ont été caractérisées par une approche à techniques multiples. Les résultats de l'analyse de diffraction des rayons X (XRD) sur les pâtes de ciment et des LCLL-ash ont montré une modification des produits d'hydratation avec la présence de la phase carbo-aluminate. Les résultats de l'analyse thermogravimétrique (TGA) ont indiqué que les pâtes contenant de la LCLL-ash avaient des teneurs plus élevées en C-S-H, ce qui suggère que la LCLL-ash a un léger effet de nucléation. Les micrographies au microscope électronique à balayage (MEB) ont montré que la pâte de ciment contenant 10% de LCLL-ash favorise une microstructure plus dense grâce à l'effet filler. La spectroscopie dispersive en longueur d'onde (WDS) a montré que la LCLL-ash augmentait également le rapport Ca/Si de la phase intermixe C-S-H. Enfin, la microindentation a montré que l'addition de sulfate de calcium avec 10% de LCLL-ash a amélioré les propriétés mécaniques à 28 jours. En conclusion, une conception optimale du mélange pour une pâte de ciment avec 10% de ciment remplacé par la LCLL-ash avec une empreinte carbone réduite a été réalisée.

Mots-clés: remplacement du ciment, pâte de ciment, brasques usées traités, microstructure, microindentation, phases d'hydratation, sous-produits.

2.2 Abstract

The use of locally available industrial by-products as supplementary cementitious materials and mineral fillers is key for reducing the embodied carbon of concrete. Fostering our recent work on the reactivity of treated spent pot lining (SPL), called LCLL-ash, as cementitious materials, this study aims to better understand the microstructure changes of cement pastes incorporating aluminum smelter wastes, such as LCLL-ash and synthetic anhydrite ($CaSO_4$).

Firstly, fine powder LCLL-ash was used to partially replace cement in cement pastes with a constant water-to-binder ratio of 0.35. The cement pastes were characterized by a multiple-technique approach. The X-ray diffraction analysis (XRD) results on the LCLL ash-cement pastes showed a modification of the hydrated products with the presence of the carbo-aluminate phase. The thermogravimetric analysis (TGA) results indicated that the pastes containing LCLL-ash increased C-S-H contents, suggesting that LCLL-ash has a slight nucleation effect. The scanning electron microscopy (SEM) micrographs showed that the cement paste with 10% LCLL-ash favors a denser microstructure with a filler effect. The Wavelength-dispersive spectroscopy (WDS) showed that LCLL-ash also increased the Ca/Si ratio of the C-S-H phase intermix. Finally, microindentation showed that the addition of calcium sulfate addition with 10% LCLL-ash enhanced the mechanical property at 28 days. Conclusively, an optimal mix design for cement pastes with 10% of cement replaced by LCLL-ash with reduced carbon imprint was achieved.

Keywords: cement replacement, cement paste, treated spent pot lining, microstructure, microindentation, hydration phases, by-products.

2.3 Introduction

The use of industrial by-products as supplementary cementitious materials (SCM) or mineral fillers to reduce the cement content in concrete is a promising strategy to reduce its critical contribution to worldwide carbon emissions [186]. In particular, the recycling of industrial by-products which are locally available allows for reducing the environmental impact of transport [187].

Several SCMs, such as silica fumes, fly ashes, and ground blast-furnace slag, have been employed to recycle industrial by-products by replacing more than 50% of cement content [188–191]. In general, SCMs improve not only the ecological imprints of concrete, but they can also enhance its durability, e.g., mitigating the risk of alkali-reaction [191–193]. However, the performance of concretes containing

SCMs is affected by many factors, such as their chemical composition mineralogical and physical properties [180,194,195]. One of the major limitations to the use of SCMs is the transport cost and the development of new sources which are locally available is of great interest today. As an example, glass powder recycled from the glass bottle industry is today used as supplementary cementitious materials in concrete [67]. Furthermore, industrial by-products can act as mineral fillers and are efficiently employed to favor cement hydration and develop concretes with a low water-to-cement ratio [6,196].

Canada is the fourth-largest aluminum producer worldwide with nearly 3 million tons of primary aluminum produced each year thanks to the low cost of electrical power [197]. Aluminum is fabricated by the Hall-Héroult electrolysis process, involving the electrolysis of alumina, dissolved in liquid cryolite a molten salt acting as electrolyte [29]. Spent pot lining (SPL) is a hazardous waste generated from aluminum electrolysis cells. Considering that each ton of aluminum products generated about 22 kg of SPL, about 35 kt of SPL is generated per year by Rio Tinto in Canada. However, it is not possible to landfill SPL due to the high levels of leachable cyanides and fluorides [24]. SPL is made of two parts: (i) the 1st cut is rich in carbonaceous materials; (ii) the 2nd cut is rich in vitrified refractory. The carbon part has caloric value and can be used as a fuel substitute mixed with coal. Thanks to the fluoride content, the addition of SPL in the raw meal decreases the clinkerisation temperature by 20°C to 100°C according to the SPL replacement percentage [198]. This allows to reduce the fossil fuels consumption up to 4% and reduce the overall CO_2 emissions by 1% [198]. It is also possible to utilize SPL without treatment as a raw material in the cement kiln in the cement plant or as an additive in steelmaking is the most common as done in Europe, China, Brazil, Russia and South Africa [199,200]. The utilization of SPL in the cement industry provides a saving in fuel as it offers the solution to ecological problems created by the disposal of SPL waste [199]. Previous studies have shown that SPL has the potential for mineral additives in cement formulation [201]. However, the sodium content in SPL is an issue as cement manufacturers do not want to have extra sodium to avoid the durability concerns of concrete due to the alkalis silica reactions [202,203].

SPL can be treated by a hydrometallurgical process called “Low Caustic Leaching and Liming” (LCL&L) to extract toxic elements, including leachable cyanides and fluorides. Treated SPL is an inert by-product with a limited amount of Na and F content than untreated SPL with a high potential for valorization [30]. By treating only refractory bricks (2nd cut) separately from the carbon part (1st cut), an industrial by-product herein called LCLL-ash is produced. For instance, about 20 kt of LCLL-ash per year produced

at the SPL treatment plant in Jonquiere (Quebec) could be recycled in concrete production. The reuse of treated SPL or LCLL-ash in concrete can reduce the landfilling and the aluminum producer's environmental impact.

Previous studies employed SPL as supplementary cementitious materials by using lab-treated SPL [201,204,205]. In particular, Glass Frit (GF) resulted from a thermal treatment (pyrometallurgical process) followed by grounding it to the fineness of cement and mixing it in mortar and concrete by partial replacement of cement. Their results showed that GF had a remarkable pozzolanic potential for improving both rheological and mechanical properties of concrete after 28 days, which showed the reactivity behavior similar to slag [201,204]. In addition, Laldji et al.[205] showed that GF had low chloride ion permeability and excellent resistance to freezing and thawing.

Very recently, Brial et al. [206] studied the reactivity of LCLL-ash as supplementary cementitious materials by using the Rilem R^3 pozzolanic test [207]. The results showed that the LCLL-ash acts as an inert addition similar to quartz powder due to the presence of silicate phases, such as albite and/or nepheline. Interestingly, due to the high amount of reactive alumina in calcinated LCLL-ash, new hydrates phases may be at stake, such as carbo-aluminate phases and ettringite. However, the presence of phases containing alumina leads to hydro-reactivity (gas expansion), which is a complex phenomenon dependent on many factors, such as temperature, chemistry, and pH. However, this study is limited to solution reactivity tests and compression tests on standardized mortar with only 20% cement replacement by LCLL-Ash without any synthetic anhydrite.

Furthermore, synthetic anhydrite ($CaSO_4$) is another solid industrial by-product of aluminum smelters. For instance, in Quebec, it is produced by a fluoride plant (Jonquiere, Quebec) by using BUSS technology. Aluminum fluoride is an important additive for aluminum smelters. In particular, anhydrite is produced in the gasifier where the spat fluor (CaF_2) and sulfuric acid (H_2SO_4), react to produce hydrofluoric acid (HF), according to the following reaction:

$$CaF_2(s) + H_2SO_4(l) \rightarrow 2HF(g) + CaSO_4(s) \quad (1.17)$$

At the gasifier exit, synthetic anhydrite is neutralized with lime (CaO). It consists of more than 95% $CaSO_4$, reduced amounts of CaF_2, $CaCO_3$ and SiO_2, and other trace elements. Its $CaSO_4$ purity, well above 90%, is comparable to that of a geological deposit [208]. Synthetic anhydrite has a bulk density of 1.4 g cm^{-3}, and a fine particle size where 80% of the particles have a size less than 6.4 mm. About

80-110 kt of anhydrite is produced per year. This product is valorized in several applications, such as drying agent, as raw material instead of gypsum ($CaSO_4$*nH_2O) for cement plants, for floor screed (self-leveling) and also as fertilizer for agriculture.

In the knowledge of the authors, there is no data available in the open literature on the effect of treated SPL on the microstructure features of a cement paste. This work aims to further investigate the effects of replacing cement with LCLL-ash on the chemo-mechanical properties of a cement paste by means of a multiple technique methodology, which combines X-ray diffraction (XRD), scanning electron microscopy (SEM), Wavelength-dispersive spectroscopy (WDS), thermogravimetric analysis (TG/DTA), and micro-indentation. In particular, we investigated different replacements of cement up to 20% by grinded LCLL-ash. Furthermore, the addition of a small amount of anhydrite by-products is also investigated.

2.4 Research significance

Driven by the urgency of fighting climate changes, concrete industries, and renewable energy solutions by 2030-2050 will significantly reduce available quantities of SCMs for concrete [209]. For example, the coal plants in Canada will no longer be used by 2030 [14], and concrete producers want to use more fly ash in concrete [210], resulting in the scarcity of fly ash. Considering that the worldwide use of concrete is increasing due to population growth, there is a strategic need to seek alternative sources of SCMs or mineral fillers. The partial replacement of cement by the aluminum by-products will contribute to an effective circular economy solution for countries with a major production of aluminum, such as China, Europe, Asia, North America and Latin America. Moreover, developing locally available LCLL-cement will reduce landfilling aluminum waste and cost of concrete.

2.5 Materials and methods

2.5.1 Materials

A commercially ordinary Portland cement (OPC) type GU with estimated Bogue phase composition of 51.2% C_3S, 16.2% C_2S, 6.7% C_3A, 11.0% C_4AF and a Na_2O of 0.25% was used. LCLL-ash was supplied by Rio Tinto SPL treatment plant (Jonquiere, Canada). Synthetic anhydrite ($CaSO_4$) was used as a mineral admixture, and was supplied by Rio Tinto AlF3 plant (Jonquiere, Canada). The LCLL-ash was dried and grinded by means of the laboratory vibrating cup mill type Pulverized 9 at a speed of 1000 rpm. The particle size distribution (PSD) was measured by Mastersizer 2000 laser diffraction

spectrometry of a dilute particle suspension in isopropyl alcohol. Figure 2-1 shows the particle size distribution of LCLL and cement. Figure 2-2 illustrates the SEM micrographs of cement, LCLL-ash and anhydrite.

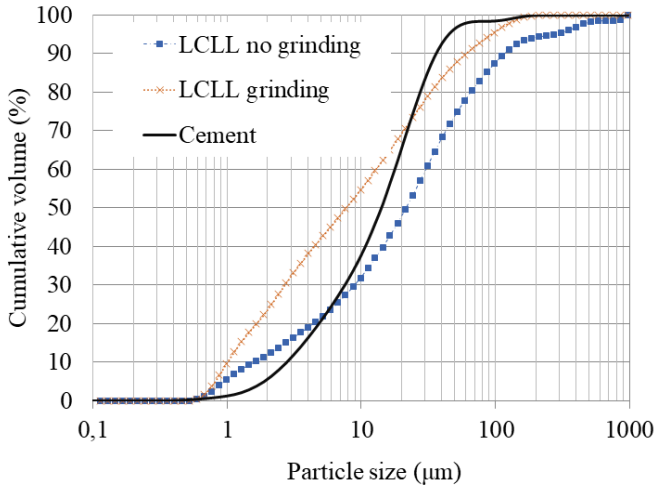

Figure 2-1. PSD of cement and LCLL-ash.

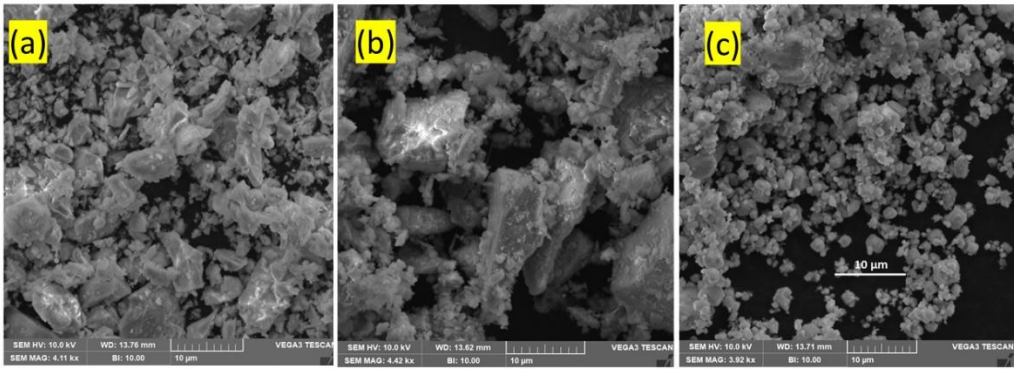

Figure 2-2. SEM micrographs of (a) cement, (b) LCLL-ash, and (c) anhydrite.

While the particles of cement and LCLL-ash are characterized by irregular shapes and sharp edges, anhydrite grains are quite spherical. The chemical composition of LCLL-ash, and cement were determined by X-ray fluorescence spectrometer (ZSX Primus II). The specific surface area of LCLL-ash was measured by BET method by using Micromeritics Tri STAR II. Table 2-1 shows the chemical and physical properties of LCLL-ash, and cement, respectively. The compositions of LCLL-ash are mainly SiO_2, Al_2O_3 and Fe_2O_3. A high content of the alkali content can be found in LCLL-ash, which is approximately 8% in weight of sodium oxide. Figure 2-3 shows the X-ray diffraction analysis of LCLL-

ash measured by X-ray diffraction (PANanlytical). LCLL-ash is mainly composed of crystalline phases such as corundum, nepheline, albite, anorthite and some amount of graphite [211]. The anhydrite (AH) granulometry was not investigated as it rapidly reacts with water.

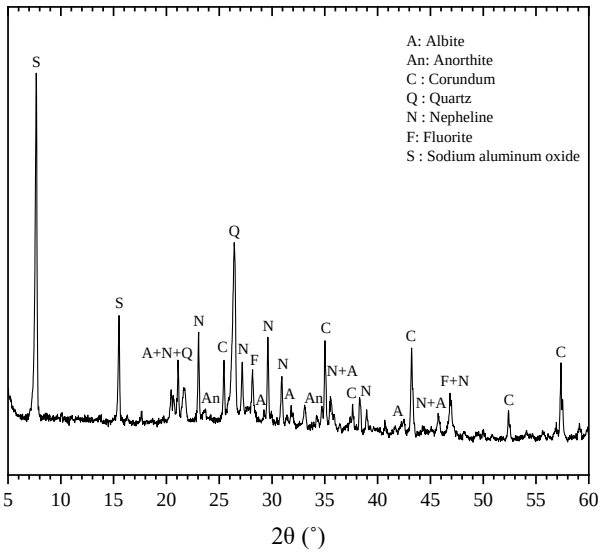

Figure 2-3. X-ray diffraction patterns of LCLL-ash.

2.5.1 Mix formulation and curing

Table 2-2 summarizes the mix-design series with different replacement percentages of cement at 0%, 10% and 20% by weight (wt.) with LCLL-ash. A small amount of anhydrite (AH) was also added in some mix-design (1.25% and 2.5% by wt. of cement). The material code corresponds to the percentage of cement replacement by LCLL-ash and anhydrite (Table 2-2). The cement pastes samples prepared with a water-to-binder ratio (*w/b*) of 0.35 were poured into cylindrical specimens with a size of 25 mm in diameter and 150 mm in height. After a cure of 24 h at room temperature, the specimens were demolded and cured in saturated limewater tank at an environmental temperature of 20°C ± 3°C. The hydration of the specimen was stopped at the desired ages by immersing them in isopropanol (1:1 by volume) for 7 days. According to the previous results [212,213], isopropanol exchange was employed to stop hydration for investigating the microstructure phase assemblage. Subsequently, the samples were conserved in a desiccator with soda lime to prevent carbonation for the analysis.

Table 2-1. Chemical properties (wt.%) and physical properties of cement and LCLL-ash.

	Cement	LCLL-ash
Chemical properties (wt.%)		
CaO	60.20	3.04
SiO_2	19.13	37.18
Al_2O_3	4.80	36.29
Fe_2O_3	3.60	7.37
SO_3	3.80	0.07
MgO	2.6	0.38
TiO_2	0.23	0.73
Na_2O	0.25	8.23
P_2O_5	0.19	0.12
K_2O	1.1	0.77
Mn_2O_3	0.07	-
Physical properties		
LOI	1.92	5.72
Specific gravity (g/cm^3)	3.09	2.72
Blaine's fineness (m^2/kg)	395	-
Surface area m^2/g (BET)	-	4.6

Table 2-2. Mix proportion in mass.

Name of samples	Cement [%]	LCLL-ash [%]	Anhydrite [%]	*w/b* [-]	*w/c* [-]
Control	100.00	/	/	0.35	0.35
10LCLL	90.00	10	/	0.35	0.38
10LCLL-1.25AH	88.75	10	1.25	0.35	0.39
20LCLL	80.00	20	/	0.35	0.43
20LCLL-2.5AH	77.50	20	2.50	0.35	0.45

2.6 Specimen preparation and experimental details

2.6.1 X-ray diffraction

X-ray diffraction (XRD) was employed to observe the formation of crystalline hydrates and non-reacted raw materials in hydrated pastes at different curing days. An X-ray diffraction analysis of the materials was performed using Philips X'pert APD operating at a tube voltage of 40 kV, a tube current of 40 mA, and using Cu K∝ radiation. About 3g of hydrated paste was crushed and finely grinded using a mortar and a pestle. Then, the sample should be immersed in 100 mL of isopropanol immediately after crushing for 10 min. The grinded powders were dried for 10 min in a ventilated oven at 40 ± 5 °C. The analyses were performed within an angle range of 5-70° 2 theta. The step width was set at 0.02, and the scan rate was 2°/min.

2.6.2 Thermogravimetric analysis

Thermogravimetric analysis (TGA) (Netzch STA 449 F3 Jupiter) was used to measure the mass loss upon heating the sample. For each test, about 40 mg of powder were taken in a ceramic crucible without lid. The heating ramp varied between 50 °C and 950 °C with a heating rate of 20°C/min. The test was done under a nitrogen atmosphere at a flow rate of 50 mL/min.

Then, the amount of CH and C-S-H can be estimated from the TG curve, using the tangential method [145], using the following equation [146]:

$$CH\,(\%) = \Delta WL_{CH}\,(\%)\ \mathrm{x}\ \frac{MW_{CH}}{MW_{H}}\mathrm{x}100\ (\%) \tag{2.1}$$

$$C-S-H\,(\%) = \Delta WL_{C-S-H}\,(\%)\ \mathrm{x}\ \frac{MW_{C-S-H}}{2.1MW_{H}}\mathrm{x}100\ (\%) \tag{2.2}$$

where ΔWL_{CH} , ΔWL_{C-S-H} is the percentage TG mass loss during 400-500 °C and 150-400 °C which should exclude AFm peak [145], MW_{CH} , MW_{C-S-H} and MW_{H} are the molecular weight of CH, C-S-H gel, and water, respectively. The chemical formula of C-S-H is taken as $C_{1.7}$ SH_4, some part of the 4 moles of water has already been lost below 150 °C [146]. The equilibrium composition of C–S–H is thus taken as $C_{1.7}$ $SH_{2.1}$ as given in [41], which explains the division by 2.1 used in in Eq. 2.2.

2.6.3 Scanning Electron Microscopy

Scanning electron microscopy (SEM) was carried out to study the microstructure of the blended cement pastes. The employed Scanning electron microscopy (SEM) instrument was the commercial brand Tescan Vega3. The samples were cut into 3 mm thick slices by a diamond saw. The slice was then impregnated with low viscosity epoxy under a vacuum. The impregnated sample was cured at 40°C for 24 h. The specimens were glued on metallic discs and polished with Anamet perforated polishing cloths installed on Ultrapol automatic polishing machine, applying an oil-based diamond suspension of different particle sizes (6 µm and 1 µm) for 1 h each. Before testing, the sample was coated with carbon to avoid electrical charges on the surface sample.

2.6.4 Wavelength Dispersion Spectroscopy

The electron probe micro-analyzer is a microbeam equipped with wavelength dispersive spectrometers (WDS). WDS is to characterize materials based on x-rays emitted from the solicited specimen because of interaction between the sample being analyzed and an electron beam. WDS analysis classifies emitted X-rays based on their wavelengths and offers spatial resolutions in the micrometer range depending on the electron beam energy and sample density [147]. It is worthy to note that WDS is a quantitative technique to measure chemical elements within a probed material spot. To avoid charging during high-vacuum chamber, the samples were coated with a thin layer of carbon. The WDS was measured by using a EPMA Cameca SX-100. The polished sections (the same sample preparation for SEM) were examined at an accelerating voltage of 15 kV and a dwell time of 0.04 seconds. The beam size is approximately 1 to 2 µm, based on previous work [148]. The grid of 20x20 points spaced by 3 µm was performed.

2.6.5 Micro-indentation test

For the sample preparation, the sample surface was cut into ideal size by 25 mm in diameter and 5 mm in thickness at the middle portion. The surface was polished by using the same machine in section 2.3.3, according to a well-established procedure [149–151], such as: (i-iv) the coarse polishing using different grit sizes (400, 600, 800 then 1200) was employed during 15 min for each paper; (v-vi) after that, oil-based diamond suspension (6 µm and 1 µm) were used during 15 min and 30 min, respectively. Between each polishing step, specimens were cleaned with isopropanol for 3 min in an ultrasonic bath to remove any debris.

For micro-indentation test, the penetration depth h_{max} should be chosen to be large enough to assure a homogenous response while considering that the probed volume is about 5-10 times of h_{max} [152,153]. In this study, the maximum applied load is 10 N, and the holding force is 300 seconds before unloading for creep investigation. A matrix of 10 x 10 indents was performed on each sample with an inter-distance of 500 µm (to avoid interaction between indented areas). The indentation tests were carried out by using a MCT CSM Instruments Indentation Tester. The indentation method consists of applying a load into the surface of the sample with a rigid indenter, typically a Berkovich diamond, with different phases: (i) loading phase; (ii) holding phase at constant load; (iii) unloading phases. The indentation modulus (M) and the contact area Ac needed to estimate the indentation hardness (H) are estimated by the initial slope of the load (P) vs. penetration depth (h) curve in the unloading branch (Figure 2-4). Based on continuum mechanics analysis of the P-h curve [154], the indentation properties (H and M) are defined by the following relations:

$$H \overset{def}{=} \frac{P_{\max}}{A_c} \tag{2.3}$$

$$M \overset{def}{=} \beta \frac{\sqrt{\pi}}{2} \frac{S}{\sqrt{A_c}} \tag{2.4}$$

where Pmax is the maximum load applied; Ac is the projected area of the indenter; and $S = (dP/dh)h=h_{max}$ is the initial slope of the unloading branch of the P-h curve; β is a coefficient accounting for the slip on the indenter surface and can be extrapolated from the indentation depth h using the Oliver and Pharr method [155].

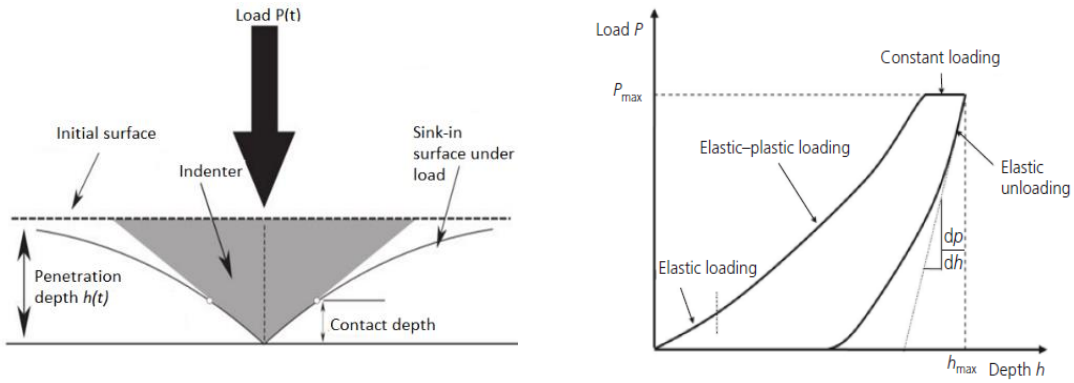

(a) (b)

Figure 2-4. A schematic view of the indentation load-displacement curve (a) sectional view of the physical parameter under load (b) load-deflection curve [149].

One of the major advantage of microindentation is the ability of rapidly measuring the logarithmic basic creep of a cement paste [149,151,156]. For modeling indentation creep of cementitious materials, Vandamme et al. [151] proposed the logarithmic contact creep compliance equation as :

$$L(t) = \frac{1}{M(t)} = \frac{1}{M_0} + \frac{1}{C}\ln\left(1 + \frac{t}{\tau}\right) \tag{2.5}$$

where C is the contact creep modulus C and τ is the characteristic time. The contact creep modulus (C) is further defined as follows [150,157]:

$$C = \frac{P_{\max}}{2x_1\sqrt{A_c / \pi}} \tag{2.6}$$

where x1 can be estimated by fitting the increase of indentation depth h(t) under constant loading by $\Delta h(t) = x_1 \ln\left(x_2 t + 1\right)$ .The contact creep modulus C is today widely employed to measure the logarithmic creep rate of a cement paste and can be reasonably used to predict the long-term deflection of structures [156].

2.7 Results and discussions

2.7.1 Hydration products by XRD

XRD allows a qualitative identification of the different crystalline phases composing the cement paste microstructure. Figure 2-5 shows the XRD patterns of hardened cement pastes with and without LCLL-ash at 28 days. The main hydration products were ettringite (E) and portlandite in addition to mineral components such as unreacted clinker phases and unreacted LCLL-ash. The pattern of ettringite and ferrite is visible for all tested samples at 9.1° 2θ and 12.2° 2θ, respectively. Moreover, anhydrite addition systems (10LCLL-1.25AH and 20LCLL-2.5AH) show a broader ettringite peak. This is attributed to a quickly dissolving of calcium sulfate, which then reacted with calcium aluminates during the early hydration to form more ettringite [214,215]. The main LCLL-ash crystalline phases, such as sodium aluminate oxide ($NaAlO_2$) at 7.9° 2θ and quartz at 26.4° 2θ, are still clearly present in all LCLL-ash blended cement pastes, particularly in samples that have higher contents of LCLL-ash in the mixture, due to its hydraulic properties.

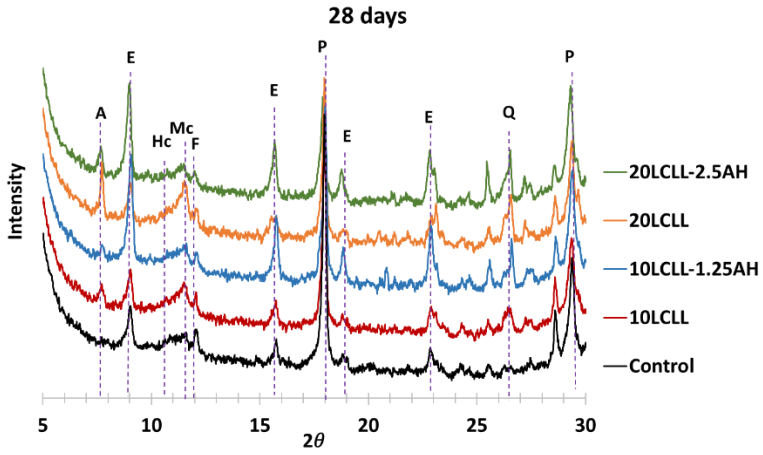

Figure 2-5. X-ray diffraction patterns of pastes at 28 days. Mc—monocarboaluminate, P—portlandite, E—ettringite, F—Ferrite, Hc—hemicarboaluminate, Q—quartz, A— Sodium aluminate oxide

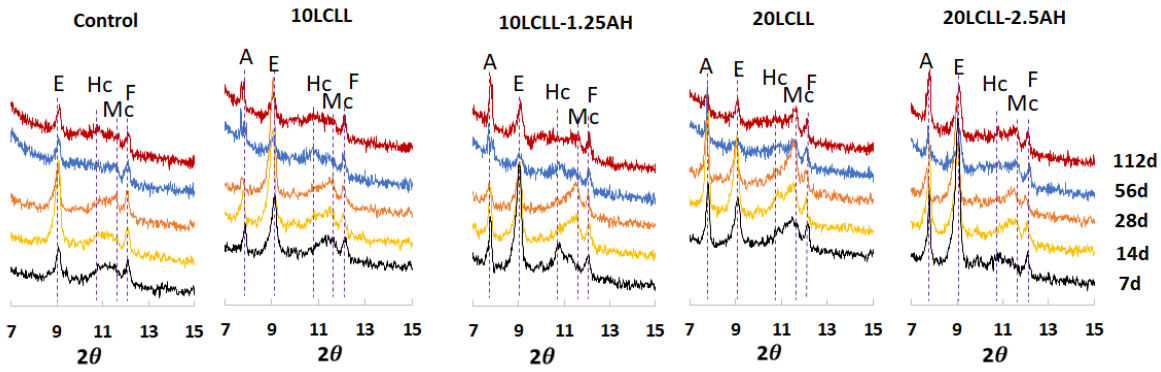

Figure 2-6. X-ray diffraction patterns of all investigated samples at difference days: Mc—monocarboaluminate, Hc—hemicarboaluminate, E—ettringite, F—Ferrite, A — Sodium aluminate oxide.

Figure 2-6 shows the XRD patterns of hydrated cement pastes at different curing days. As observation in samples with 10% and 20% substitution, the formation of AFm phase assigned as hemicarbonate peak (that is, calcium hemicarboaluminate hydrate, Hc) is detected at 7 days and 14 days, respectively, but it seems to level off after 14 days, whereas the monocarbonate peak (that is, calcium monocarbonaluminate hydrate, Mc) grows over time until 112 days. More interestingly, the intensity of Mc peak increases with the increase of LCLL-ash content (10LCLL and 20LCLL). This can explain by two possibilities: (i) owing to the reactive alumina from LCLL-ash and the CH and calcite in the binder to form Mc [214,216,217]; (ii) AFm is mainly formed by the reaction of CO_2 with CAH, similar phenomena of hydration of metakaolin-cement [218]. The ferrite phase was identified over 112 days in this study.

2.7.2 Hydrate content by TGA

TGA analysis aims at estimating the content of Portlandite and C-S-H of the cement pastes. thermogravimetric curves of hydrated cement paste samples at 7 and 28 days of hydration. Derivative thermogravimetric (DTA/DTG) curves were also plotted from TG data to identify the exact boundaries of phases presented in the hydrated sample. Four endothermic phases are observed. The first one is related to the evaporation of absorbed surface moisture in the range of 30-110°C. The second observed range is 110-400°C showing the dehydration of calcium aluminate hydrate and calcium silicate hydrate. The hydrates decomposition, between 400 and 500°C, corresponds to the CH dehydration during hydration. The final range corresponds to the decarbonation of calcium carbonate (600-800°C). It is noted that the intensity of the first peak is more pronounced for 10LCLL-1.25AH and

20LCLL-2.5AH systems. Therefore, it is possible to assign these peaks to the presence of ettringite and AFm phases. These phases are formed by adding sulfate in anhydrite or carbonate in LCLL-ash, which corroborates data of XRD results.

Figure 2-8 shows the estimated content of C-S-H and CH at 7 days and 28 days, respectively, in terms of the total mass and mass normalized to the cement mass. As for the cement paste (control), the C-S-H and CH contents increase over time due to C_3S and C_2S hydration as expected.

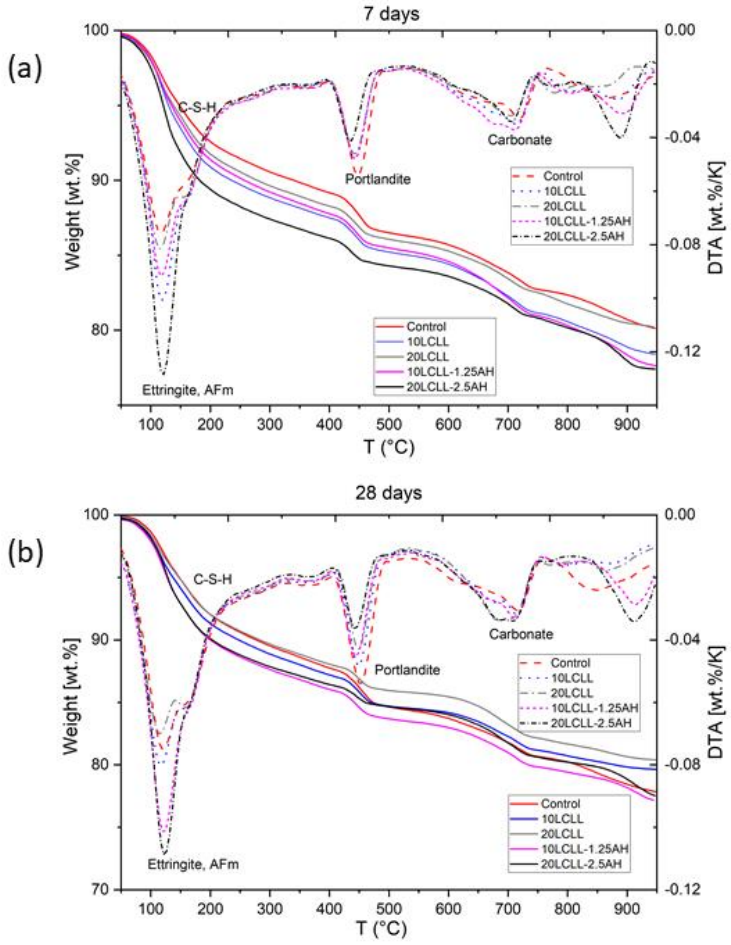

Figure 2-7. DTA/ TG curves of hydrated cement paste samples at (a) 7 days and (b) 28 days.

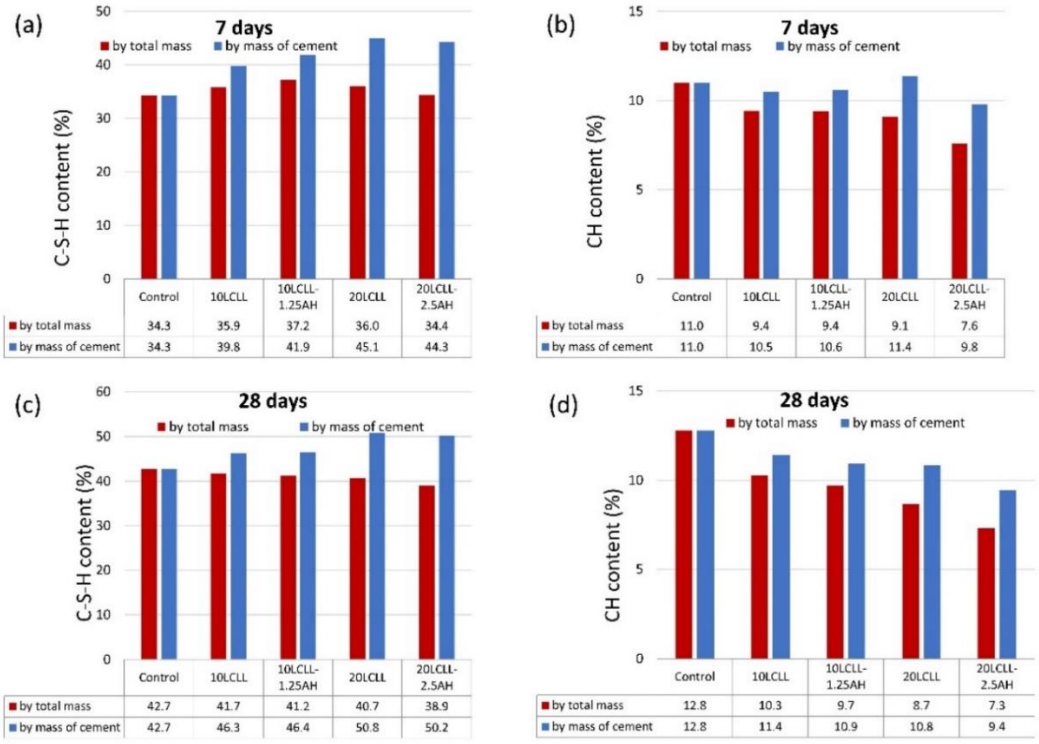

Figure 2-8. C-S-H content at (a) 7 days and (c) 28 days and CH content at (b) 7 days and (d) 28 days as determined from the TG curves.

As for the cement pastes with LCLL-ash in Figure 2-8a, C-S-H content at 7 days in the control sample is lower than that of the paste containing LCLL-ash, i.e., the C-S-H increase from 34% to 45% by mass of cement by adding 20% of LCLL-ash, which is an increase of about 32%. This can be attributed to different possible reasons, such as (i) the nucleation effect of LCLL-ash particles (ii) the dilution of cement particles by replacing LCLL-ash in cement paste, when the water-to-cement increases, there is more space for the formation of hydrates of cement; (iii) the formation of other hydrates phases, such as carbo-aluminate (e.g., Hc and Mc) and ettringite might have been included in the estimated content of C-S-H as difficult to separate their thermo-gravimetric effects. At a later hydration stage (28 days in Figure 2-8c), the increase in amount of C-S-H by mass of cement due to LCLL-ash addition is about 18% (i.e., the C-S-H increase from 43% to 51% by mass of cement by adding 20% of LCLL-ash), which is less important than the gain at 7 days.

Based on the TGA estimation, the CH in LCLL-ash systems reduces with the increase of LCLL-ash content, at both 7 days and 28 days, as shown in Figure 2-8b and Figure 2-8d. Note that the amount

of CH content by mass of cement in LCLL-ash systems at 28 days is lower than that of control paste due to the lower content of cement (Table 2-2). The fact that CH reduces by adding LCLL-ash may indicate that the reason of the aforementioned increase of C-S-H content is due to additional rich-aluminate hydrates.

2.7.3 Microstructure texture by SEM

Figure 2-9 shows SEM micrographs of the hardened pastes at 28 days. The microstructure of cement paste with LCLL-ash particles appears different from that of the control sample, which show a denser morphology. This can be explained by the filler effect of LCLL-ash particles during the hydration of cement [87,88]. However, 20LCLL shows to be more porous than the control, which is perhaps due to the dilution effect. The few micro-crack observed are likely due to dehydration under vacuum or autogenous shrinkage [219]. Furthermore, both unreacted clinkers and unreacted LCLL-ash particles are still visibly embedded in the cement paste matrix (as shown in Figure 2-9b and 9c).

2.7.4 Phase distribution by WDS chemical analysis

WDS analysis aims at describing the phase distribution and microstructure heterogeneity. The WDS spot quantitative analysis was performed on the Control and 10LCLL samples to better understand the effect of LCLL-ash particles on the chemical properties of the blended cement paste. Figure 2-10 shows the WDS spot contour of the 10LCLL sample at 28 days. As an observation, the areas with a high level of Ca and Si are residual clinker. The LCLL-ash particles are rather heterogeneous in elemental compounds and non-uniform sizes. For example, the particle with a high concentration of Al, Na, Si, and O on the mapping can be associated with albite, accounting for about 20% of LCLL-ash [206].

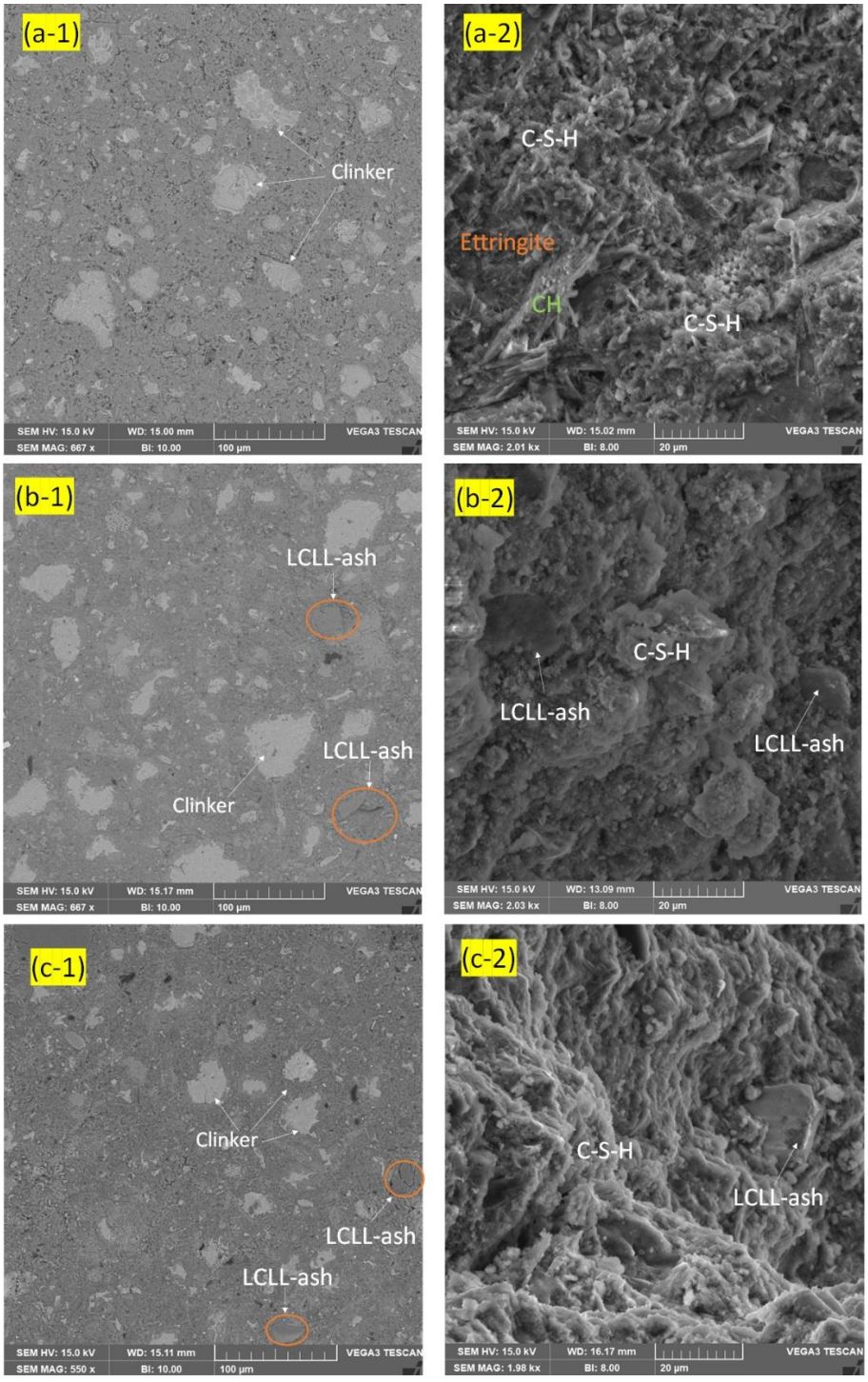

Figure 2-9. BSE images of 28-day curing. (a) Control; (b) 10LCLL; and (c) 20LCLL.

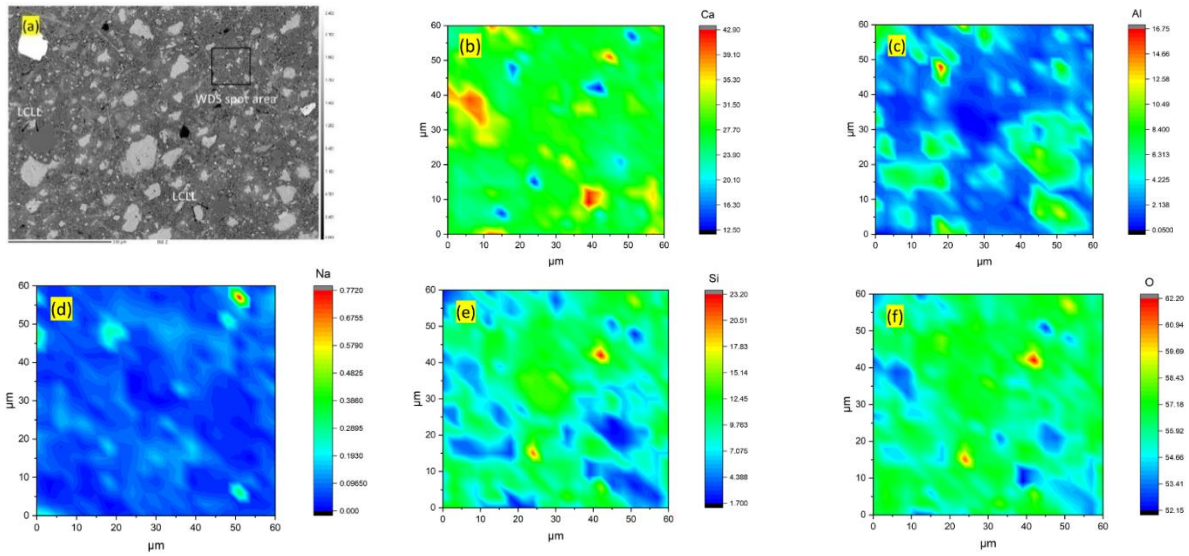

Figure 2-10. Quantitative WDS elemental mapping of 10LCLL sample at 28 days of curing with scale weight percentage for (a) BSE image, (b) calcium, (c) aluminum, (d) sodium, (e) silicon and (f) oxide.

Figure 2-11 presents the chemical clustering with 5 quantitative chemistry variables (Si/Ca, (Fe+Al)/Ca, S/Ca, Mg/Ca, Sum of Oxides (SOX). The cluster deconvolution analysis was carried out by a statistical most-likelihood algorithm which was used in previous work [67,220]. Such a method allows identifying the phases with a similar chemical structure by most-likelihood estimation of the aforementioned 5 quantitative chemistry variables [220]. That is, the identified cluster is a statistically recognizable phase or intermix of different phases.

It is well known that the microstructure of a hydrated cement is highly heterogenous and made of a complex intermix of several hydrated phases such as C-S-H, CH, E, as well as residual clinkers [220–222]. Table 2-3 and Table 2-4 present the estimated 6 clusters for control and 7 clusters for 10LCLL, respectively. In this section, we have used the vocabulary of previous works of Wilson et al. to describe the intermix phases which may compose a cluster [220], such as: (i) cluster #1 is Al-rich clinker (C_4AF, C_3A) intermix with C-S-H; (ii) cluster #2 is CH intermix with C-S-H; (iii) cluster #3 is E intermix with C-S-H; (iv) cluster #4 is a very small fraction of silicate clinkers (alite and belite); (v) cluster #5 «Others» is a minor phase which is not identified; (vi) cluster #6 is mostly C-S-H; (vii) cluster #7 is a intermix with mostly LCLL-ash particles.

As for cement microstructure, only cluster #6 can be considered as a mostly pure phase made of C-S-H, which has similar results of the referenced work [220]. The cluster #3 «Al-rich + C-S-H» has more

content in LCLL-ash system due to the formation of monocarboaluminate Mc products of which presence is confirmed by XRD results in Section 4.1.

Table 2-3. Results of the chemical clustering by quantitative chemistry from WDS for the control sample.

Cluster	Si/Ca (At.)	(Fe+Al)/Ca (At.)	S/Ca (At.)	Mg/Ca (At.)	SOX (Wt.)	π (%)	Predominant phases
#1	0.37 ± 0.16	0.41 ± 0.16	0.09 ± 0.03	0.13 ± 0.06	0.80 ± 0.06	19	Aluminate Mix
#2	0.41 ± 0.22	0.09 ± 0.04	0.06 ± 0.02	0.03 ± 0.01	0.70 ± 0.14	10	CH + C-S-H
#3	0.54 ± 0.11	0.21 ± 0.08	0.09 ± 0.03	0.07 ± 0.03	0.78 ± 0.04	30	Al-rich + C-S-H
#4	0.59 ± 0.12	0.11 ± 0.07	0.04 ± 0.03	0.18 ± 0.20	0.87 ± 0.07	4	Silicates Mix
#5	0.63 ± 0.22	0.24 ± 0.17	0.09 ± 0.02	0.02 ± 0.01	0.85 ± 0.07	2	Others
#6	0.65 ± 0.05	0.12 ± 0.03	0.08 ± 0.02	0.06 ± 0.03	0.78 ± 0.02	35	Mostly C-S-H

Table 2-4. Results of the chemical clustering by quantitative chemistry from WDS for the 10LCLL sample.

Cluster	Si/Ca (At.)	(Fe+Al)/Ca (At.)	S/Ca (At.)	Mg/Ca (At.)	SOX (Wt.)	π (%)	Predominant phases
#1	0.33 ± 0.14	0.48 ± 0.21	0.05 ± 0.03	0.13 ± 0.06	0.82 ± 0.06	12	Aluminate Mix
#2	0.34 ± 0.12	0.08 ± 0.04	0.05 ± 0.02	0.02 ± 0.01	0.71 ± 0.06	12	CH + C-S-H
#3	0.45 ± 0.13	0.26 ± 0.11	0.08 ± 0.02	0.07 ± 0.03	0.73 ± 0.03	36	Al-rich + C-S-H
#4	0.50 ± 0.2	0.56 ± 0.45	0.09 ± 0.06	0.46 ± 0.41	0.79 ± 0.06	3	Silicates Mix
#5	0.55 ± 0.17	0.06 ± 0.05	0.01 ± 0.01	0.02 ± 0.01	0.88 ± 0.08	6	Others
#6	0.58 ± 0.08	0.11 ± 0.03	0.07 ± 0.02	0.03 ± 0.01	0.73 ± 0.03	27	Mostly C-S-H
#7	0.92 ± 0.66	0.22 ± 0.15	0.06 ± 0.02	0.13 ± 0.02	0.77 ± 0.03	4	Mostly LCLL-ash

Figure 2-11 graphically plots the estimated clusters in terms of chemical mass ratios (Fe+Al)/Ca vs. Si/Ca (a.1, b.1), (Na+Al)/Ca vs. Si/Ca (a.2, b.2), Si/Ca vs. sum of oxides (a.3, b.3) for the 2 systems,

including control and 10LCLL. Clinker phases should have a sum of oxides equal to 1, while the sum of oxide of theoretical C-S-H is close to 0.7. It can be seen that the C-S-H phase (cluster #6) did not increase its aluminate content (Figure 2-11a.1 vs. b.1), which confirms that confirming no aluminum uptake by C-S-H [223]. However, the Ca/Si ratio of cluster #6 (mostly C-S-H) with 10LCLL system (1.72) is higher than that for the control system (1.53). The Ca/Si ratio is an important parameter of the C-S-H structure, but this shift is too small to evoke a C-S-H phase change [224–226]. In addition, unreacted LCLL-ash (cluster #7) can be found in LCLL-ash system. Figure 2-11 (b.3) shows the very high Si/Ca ratio of such cluster #7 as LCLL-ash is rich in Si and low in Ca content (Table 2-1). Notably, the C-S-H cluster #6 has similar values of (Fe+Al)/Ca for control and LCLL-ash systems (a.1 vs b.1), which hints that there was no aluminate uptake from C-S-H and no formation of C-A-S-H for such system.

2.7.5 Micromechanical properties by micro-indentation

Figure 2-12 shows the micro-indentation results of hardened pastes at 28 days, 56 days, 112 days of hydration. While the contact creep modulus (C) is related to the time-dependent deformation of a cement paste under sustained loading, the indentation modulus (M) and indentation hardness (H) are related to the elastic modulus and the compressive strength of cement pastes, respectively [227–229]. To make sure that the variation of micro indentation property is statistically acceptable, an analysis of variances (ANOVA) was carried out. Table 2-5 reports the results at different curing days, P-value with the normal distribution and the F-test with the Fisher—Snedecor distribution. These results are verified as P is much lower than the threshold $\alpha = 0.05$, while F is much greater than F_{crit}. Therefore, the observed effect of LCLL-ash on the indentation properties M and H is meaningful and statistically acceptable.

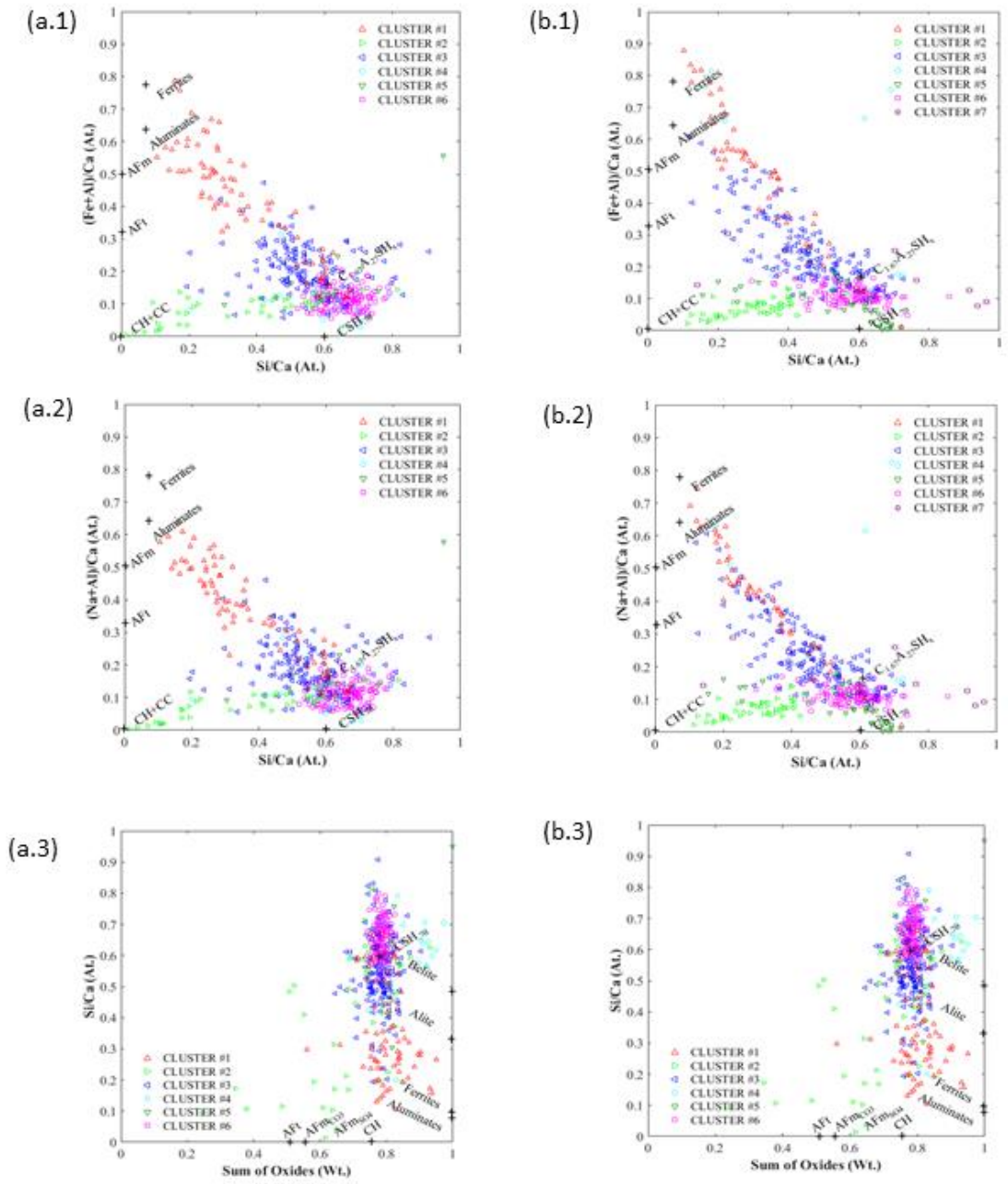

Figure 2-11. Statistical clustering analysis for the (a) Control and (b) 10LCLL in terms of (a.1-b.1) (Fe+Al)/Ca vs. Si/Ca; (a.2-b.2) (Na+Al)/Ca vs. Si/Ca and (a.2-c.2) Si/Ca vs. Sum of Oxides (SOX).

Table 2-5. ANOVA results on Indentation Modulus M, Hardness H with significant level α = 0.05. To reject the null hypothesis with confidence, P values must be smaller than 0.01, and F must be larger than F_{crit}.

Curing days	Indentation Modulus M		Indentation Hardness H		
	P	F	P	F	F_{crit}
28 days	3.39703E-57	90.37	1.52557E-35	50.32	2.39
56 days	7.35718E-71	170.96	3.84858E-44	89.78	2.62
112 days	3.43703E-57	123.37	1.72537E-35	70.34	2.40

As observed in Figure 2-12, the mechanical properties of the control sample increase with the hydration degree due to the formation of hydration products, mainly C-S-H and the reduction of porosity [230]. For cement with LCLL-ash samples, the same trend was also observed. The indentation properties of the 10LCLL sample (90% OPC+ 10% LCLL-ash) are comparable with those of the control sample. In the case of the 20LCLL sample, the micro-indentation properties are slightly reduced with respect to other systems. Compared to control, the indentation hardness H of 20LCLL sample at 28 days, 56 days and 112 days was reduced by a factor of 1.29, 1.15 and 1.10, respectively. As we have carried out the comparison of systems with the same water-to-binder ratio, this decrease may be attributed to the reduction of the water-to-cement ratio *w/c* ratio from 0.35 to 0.43 passing from control to 20LCLL, which might have caused a more porous cement paste with a negative effect on the strength [231]. Based on previous work on microindentation of cement paste, the increase in Hardness is due to an increase in the property of friction and cohesion of the material, which increases the compressive strength [228,232]. The creep compliance C is a powerful indicator of the basic creep of the cement paste as it correlates very well with the logarithmic creep compliance measured by macroscopic compressive creep tests over 1 year time as shown by several works published in the open literature [149,157]. The more the concrete creep compliance, the lower the concrete creep.

Figure 2-13 compares the H, M and C, respectively, for all the systems at different ages in terms of percentage variation with respect to the reference system (which is the cement paste without LCLL-ash at the same age). The mix-designs incorporating LCLL and calcium sulfate (10LCLL-1.25AH and 20LCLL-2.5AH) showed higher values of H and contact creep modulus C, compared to the reference samples at 28 days. Notably, the results of microindentation confirm the TGA results. Indeed, the

sample 10LCLL1.25AH, which was characterized by the highest amount of hydration products C-S-H and E at 28 days, also has the highest hardness H and lowest creep modulus C.

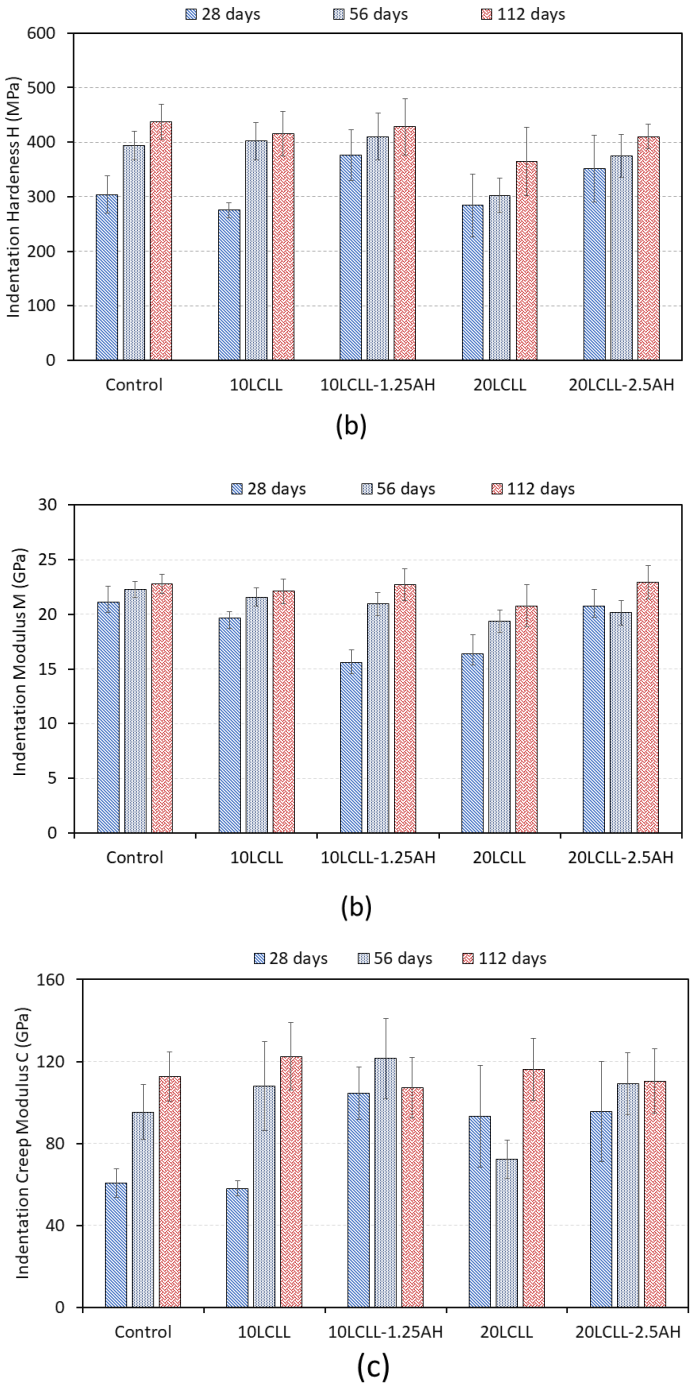

Figure 2-12. Micromechanical properties of cement pastes: (a) Indentation Hardness H; (b) Indentation Modulus M; and (c) Indentation Creep Modulus C.

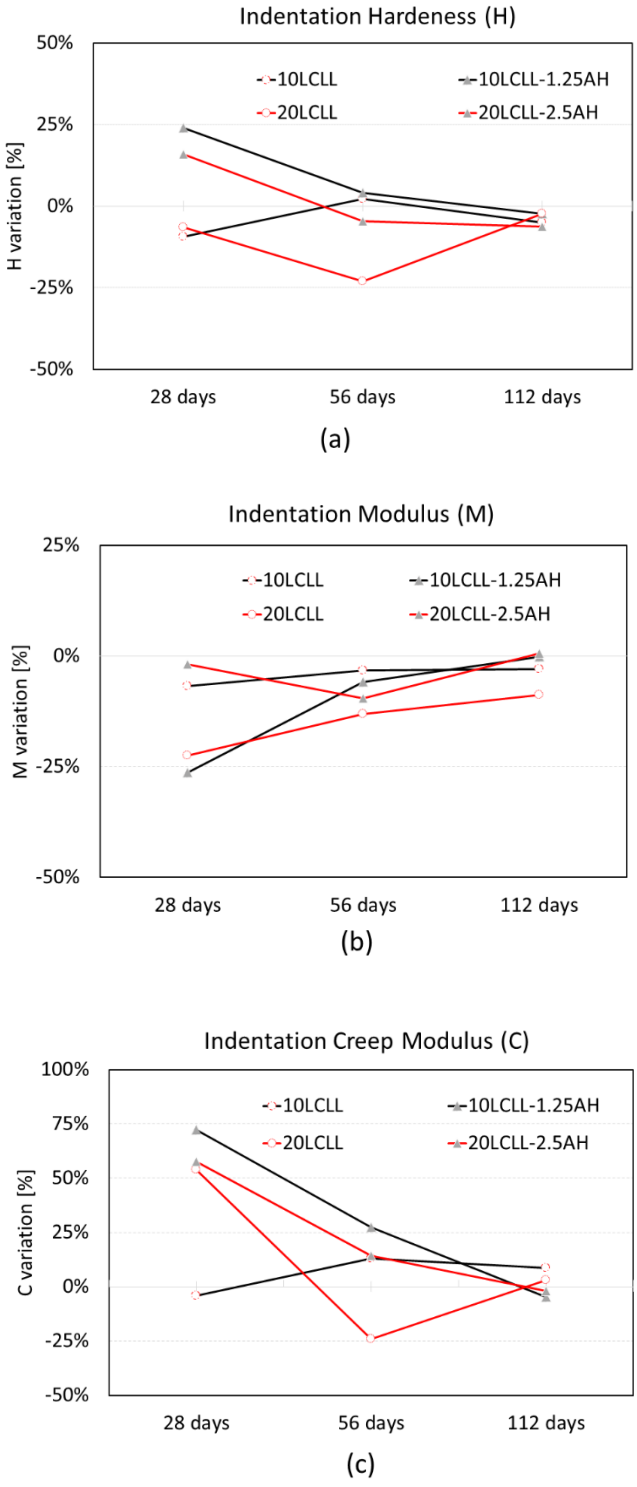

Figure 2-13. Normalized micromechanical properties to control sample: (a) Indentation Hardness H; (b) Indentation Modulus M; and (c) Indentation Creep Modulus C.

The possible reason is the increase of ettringite due to the presence of anhydrite (AH) which might have strengthened the cement paste microstructure. The increase of the content of ettringite due to LCLL-ash aluminate content at 28 days for the systems was also confirmed by XRD (Figure 2-5) and TGA (Figure 2-7). According to the results of Zajac et al. [214], the formation of ettringite increased concrete strength at early ages (less than 2 days), but the results from this search found that the addition of sulfate improved the strength of cement paste strength at later age of 28 days.

At a later stage, the enhancement of H and C of the systems with anhydrite was less important at 56 days with respect to the cement paste and even disappeared at 112 days (Figure 2-12). This may be attributed to the hydration process of cement in the reference control, which increased the hydrates product, resulting in a denser matrix.

2.8 Conclusion

By a multi-technique approach, this study investigates the microstructure of cement pastes with cement partially replaced by two industrial by-products of Aluminum production, LCLL-ash and a small amount of synthetic anhydrite. Based on the presented results, the following conclusions can be drawn:

- Based on XRD results, the microstructure of cement blended with LCLL-ash contains new hydrate products such as the hermicarboaluminate Hc at 7 days, which transforms into monocarbonaluminate Mc at 28 days. The latter appears chemically stable at 112 days as proven by XRD patterns. The ettringite peaks in cement pastes with LCLL-ash and anhydrite are more marked than in other systems. Moreover, unreacted LCLL-ash particles are visible.

- Based on TG/DTA results, the content of C-S-H by mass of cement increases by adding LCLL-ash, which is likely due to a filler and nucleation effect or the formation of aluminate-rich phases among C-S-H hydrates (e.g., Hc, Mc and E). The presence of new aluminate-rich phases was also confirmed by TG/DTA results.

- Based on SEM image analysis, the hardened blended cement pastes containing 10% LCLL-ash appeared as a denser microstructure than the one of control. The unreacted LCLL-ash particles are well visible in the BSE image, and the residual LCLL-ash particles seem to act as a filler inclusion embedded in the matrix of hydrated products.

- Based on WDS analysis and statistical clustering analysis, the phase with predominant C-S-H did not increase its aluminate content, confirming no aluminum uptake and a slight shift of the Ca/Si ratio was observed. This may be explained by an intermix of tiny LCLL-ash particle with C-S-H or a change of the silicate chain length.

- Based on micro-indentation, the indentation mechanical properties showed that it is possible to replace 10% of cement with LCLL-ash without affecting the mechanical property of the cement paste at different ages. The systems with LCLL-ash and anhydrite exhibit a clear enhancement of hardness H and creep modulus C at 28 days which is likely due to the presence of ettringite. The addition of sulfate (AH) led to an increase in the volume of hydrates (most likely ettringite), which caused a remarkable gain in strength. On the other hand, this effect was not found for cement paste systems without LCLL-ash, which hints at a limited filler effect of the fine particles of grinded LCLL-ash.

In the main conclusion, a cement paste blended with 10% LCLL-ash and 1.25% anhydrite seems a promising avenue to develop concrete with low carbon imprint by locally available industrial by-products. Further studies are required at the concrete level by considering the bond between the aggregate and the cement paste. The effect on the durability shall also be investigated, especially for alkali-silica reaction (ASR) due to the high content of alkalis in LCLL-ash [233,234]. Furthermore, nanoindentation techniques coupled with chemical analysis shall be used to disclose the high heterogeneity of cement paste microstructure with LCLL-ash [67,220].

Chapter 3. Investigation of Hydration of Cement Paste with Calcined Treated Spent Refractory Lining From The Primary Aluminum Smelters[3]

3.1 Résumé

Ces dernières années, l'utilisation de matériaux cimentaires supplémentaires pour remplacer le ciment dans le béton est le moyen le plus efficace de réduire les émissions de CO_2 de l'industrie du ciment. Les brasques usées (SPL) sont des sous-produits générés par la fonderie d'aluminium primaire. Après traitement par le procédé LCL&L, le SPL devient un sous-produit inerte, appelé LCLL-ash. Les LCLL-ash ont été broyées à la même taille que les particules de ciment et ensuite calcinées à haute température (800ºC et 1000ºC). Cet article présente une étude de l'effet de la substitution de 20% en masse de ciment par des LCLL-ash calcinées sur les caractéristiques d'hydratation des pâtes de ciment LCLL-ash calcinées. Les expériences réalisées comprennent la calorimétrie isotherme, l'analyse thermogravimétrique et la diffraction des rayons X. Les résultats seront discutés et comparés à ceux obtenus avec les pâtes de ciment calciné. Les résultats seront discutés et comparés au mélange de référence avec et sans LCLL-ash non traitées.

Mots clés: brasques usées traités, calcination, pâte de ciment, recyclage, cinétique d'hydratation.

3.2 Abstract

In recent years, using supplementary cementitious materials to replace cement in concrete is the most effective way to decrease CO_2 emissions of cement industry. Spent pot lining (SPL) is a by-product generated from the primary aluminum smelter. After treatment by LCL&L process, SPL becomes an inert by-product, which is called LCLL-ash. LCLL-ash was grinded as the fineness of cement and then calcinated at high temperatures (800ºC and 1000ºC). This paper presents a study on the effect of 20 wt% substitutions of cement by calcined LCLL-ash on the hydration characteristics of calcined LCLL-cement pastes. The experiments are performed, including isothermal calorimetry, thermogravimetric analysis, and X-ray diffraction. The results will discuss and compare to the reference mix with and without non-treated LCLL-ash.

[3] This chapter is in article format for sake of coherency, but it is not a journal article as it is a preliminary study

Keywords: cement paste, calcination, recycling, treated spent pot lining, hydration kinetic.

3.3 Introduction

Concrete is one of the most consumed materials in the world [1]. However, concrete industry is responsible for 5-8% of global carbon dioxide (CO_2) emissions, which is mainly contributed from the clinker production. In particular, the production of one ton of Portland clinkers can generate one tone of CO_2. Therefore, finding alternative materials for cement in concrete production has become the focus of many researchers in recent years. Several efforts on partial replacement of cement with industrial by-products or agricultural waste are one of the promising solutions to produce affordable concrete with less environmental impact, such as: fly ash [62], blast furnace slag [235], silica fume [236], rice husk ash [237]. The use of these by-products in concrete mixtures can be a viable solution to sustainable construction materials as well as to solve the problem of landfilling.

The primary aluminum production generates the industrial wastes, for example, spent pot lining (SPL) from electrolysis cells. SPL is considered as a hazardous material due to its leachable elements (fluoride and cyanide), but also due to its hydro reactivity creating explosive gases [199]. SPL can separate into parts (i) first cut- a carbon-rich fraction constituted of old cathode and (ii) second cut- mainly refractory brick part with non-carbon fraction. About 22 kg of SPL is generated per ton of aluminum produced. For Rio Tinto in Quebec, Canada, about 20 kt of SPL is cumulative per year [29]. In the early 1990s, Rio Tinto developed an innovative process - hydrometallurgical process - called Low Caustic Leaching and Liming (LCL&L) process in Jonquière, Quebec, Canada, to convert SPL into inert by-products. The plant treats 80 kt of SPL annually and has treated more than 700 kt of SPL since 2008. After treatment by LCL&L process, the refractory part of SPL becomes an inert non-hazardous material, which is called LCLL-ash. Approximately 10 kt per year of LCLL-ash are produced in this plant [92]. LCLL-ash has high content of silica and alumina of which can be used in concrete production.

Some of SCMs must be calcined before using to increase reactivity through amorphization. For example, metakaolin (MK) [238] is processed from kaolin clay—an available material in the earth's crust— by calcination at a temperature (650–800ºC). MK contains silica and alumina in an active form which can react with portlandite released from cement to make second C-S-H. Kannan et al.[239] found that the partial replacement of cement with MK enhanced the compressive strength of concrete, and

the optimum replacement level of OPC by MK was about 20 wt%. Several research has focused on improving the calcination process, particularly in terms of temperature and time optimization. It has been reported that the calcining temperature and time could directly influence the pozzolanic reactivity [240–242]. However, the calcining process influences not only the mineralogical composition of the materials but also the morphology and composition of the particles.

In a recent study, Brial et al. [243] studied the reactivity of LCLL-ash by Rilem R^3 tests compared to other SCMs. The results show that LCLL-ash has inert properties similar to quartz filler and retards the hydration of cement. Interestingly, calcination can improve the pozzolanic reaction of LCLL-ash, which increase the amorphous content from 6% to 75%.

Therefore, the aim of this study is to better understand the effect of calcined LCLL-ash at different calcining temperatures (800ºC and 1000ºC) on the hydration of cement paste systems. X-ray diffraction (XRD), thermogravimetric analysis (TGA) and isothermal calorimetry are employed.

3.4 Materials and methods

3.4.1 Materials and mix proportion

Portland cement type GU is used in this study. LCLL-ash was provided by the primary aluminum production. For the rest of this paper, LCLL-ash refers to LCLL. Before calcination, LCLL was grinded as the fineness of cement for 2 hours (donated as LCLL). We used the laboratory vibrating cup mill type Pulverized 9. Then, grinded LCLL is calcined at 800ºC (LCLL-800) and 1000ºC (LCLL-1000) in a muffle furnace for 2 hours, followed by a rapid air-cooling on a steel plate at room temperature. After that, calcined LCLL was re-grinded to separate agglomerate particles until d_{50} = 10 µm.

The chemical composition of all materials was measured by X-ray fluorescence, and the particle size distribution was measured using laser diffraction granulometry with isopropanol as a dispersant. The particle size distribution of all materials is given in Figure 3-1, while Table 3-1 shows the chemical composition and physical properties of cement, LCLL, and calcined LCLL. The mineralogical composition of cement, LCLL and two-calcined LCLL were measured by quantitative XRD as shown in Table 3-2. It can be seen that calcination of LCLL did not significantly affect its chemical composition but the LCLL's phase composition changed by decreasing the albite and quartz content and increasing nepheline content. Also, the loss of ignition reduces from 5% to 1% and the amorphous content increases for 6% to 34%.

Table 3-1. Chemical compositions and physical properties of granular materials used.

Materials	Cement	LCLL-ash	Calcined LCLL-ash
Chemical composition	(wt.%)	(wt.%)	(wt.%)
CaO,%	61.52	3.04	4.00
SiO_2,%	19.17	37.18	38.83
Al_2O_3,%	4.69	36.29	36.57
Fe_2O_3,%	3.61	7.36	8.59
MgO,%	2.40	0.38	0.39
SO_3,%	3.98	0.06	0.12
K_2O,%	1.06	0.77	0.79
Na_2O%	0.25	8.23	8.03
LOI,%	2.63	5.72	1.11
Amorphous content	-	5.90	74.90
Physical properties			
Specific gravity	3.09	2.72	2.72
Blaine surface area, m^2/kg	365	-	-
BET, m^2/kg	-	4.60	4.60
D50 (μ m)	13	20	20

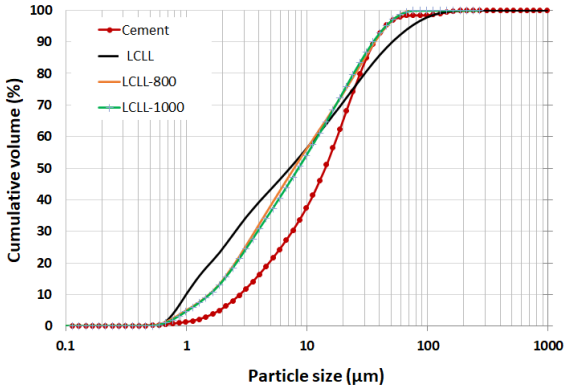

Figure 3-1. Particle size distribution measure by laser granulometry.

Table 3-2. Major mineralogical compositions of cement, LCLL and calcined LCLL.

Phase	Cement	LCLL	LCLL-800	LCLL-1000
C_3S	63.4	-	-	
C_2S	7.3	-	-	
C_3A	3.9	-	-	
C_4AF	13.0	-	-	
Quartz	0.1	6.7	4.5	1.6
Corundum	-	14.5	10.5	12.7
Albite	-	20.2	9.3	10.5
Nepheline	-	18.7	31.9	20.4
Anorthite	-	11.8	16.1	14.0
Graphite	-	6.9	2.1	3.0
Mullite	-	3.8	0.4	-
Hematite	-	2.6	-	
Magnetite	-	4.2	-	
Calcite	2.2	-	-	
Amorphous + Fe-rich phases	-	5.9	18.4	33.8

In this study, 20% in weight of cement is replaced by non-calcinated LCLL (LCLL) and two-calcined LCLL (LCLL-800 and LCLL-1000). The water-to-binder (binder = cement + LCLL) ratio is fixed at 0.485. Samples were remolded after 24h of casting and cured in the saturated lime solution until the tested day.

3.4.2 Methods

3.4.2.1 X-ray diffraction

X-ray Diffraction (XRD) was employed to identify crystalline phases of cement paste with LCLL with/without calcination. The measurements were carried out on samples cured at 7, 28 and 90 days. The sample preparation for XRD measurement is based on [145]. Firstly, the specimens were crushed and grinded using a mortar and a pestle. Then, the sample was immersed in 100 mL of isopropanol immediately after crushing for 15 min. Next, the crushed powders were dried for 10 min in a ventilated

oven at 40 ± 5°C. XRD measurements of the dried powders were done at room temperature using a Philips X'pert A.P.D. diffractometer, a Cu K∝ radiation. The analyses were performed within an angle range of 5-70° 2 thetas. The step width was set at 0.02, and the scan rate was 2°/min.

3.4.2.2 Isothermal calorimetry

To study the effect of calcined LCLL on hydration in blended cement paste, the isothermal calorimeter was employed by using means of I-Cal 2000 HPC. The pastes were prepared by hand-mixing for 2 min, followed by immediately injecting about 20 g of paste into the container to measure the rate of heat evolution at 23°C in 48 hours, according to ASTM C1702-17.

3.4.2.3 Thermogravimetric analysis

To investigate the hydration products of the paste systems at different curing days, the thermogravimetric analysis (TG) was carried out by using a Netzch simultaneous analyzer, model 449 F3 Jupiter. About 40 mg of finely ground powder was taken in a ceramic crucible without a lid. The heating rate was 20°C/min, from 50°C and 950°C. The test was done under argon gas at a flow rate of 50 mL/min.

3.5 Results and discussion

3.5.1 Effect of calcined LCLL on hydration products

Figure 3-2 illustrates the results of XRD patterns of paste cured at 7 days, 28 days and 90 days. The main crystalline phases in blended cement paste can be found, such as ettringite, ferrite, clinkers, and portlandite. The sodium aluminate oxide ($NaAlO_2$) at 7.9° 2θ and quartz at 26.4° 2θ in calcined LCLL (LCLL-C) systems is lower intensity than in systems without calcinating. In the system with LCLL and LCLL-C, the formation of carboaluminate is observed. The reference paste shows very small diffraction signal of calcium hemicarboaluminate hydrate (Hc) peak, and it is more obvious when 20 wt% LCLL is incorporated. This is attributed to the reactive alumina from LCLL, which can react with calcite in the binder to form Hc, as reported in reported of [72,214]. Moreover, the diffraction peak of Mc is generated at 90 days while remaining the Hc peak. This can conclude that Hc can convert into calcium monocarbonaluminate hydrate (Mc) during long-time curing, similar to results of [72]. This transformation is relatively related to the continuous dissolving of unreacted calcite from the binder, as addressed by other researchers [214,244]. However, this result is different from the same system with

20LCLL that observed the predominant Mc peak at all tested days [245]. This shows that LCLL particles are heterogeneous, leading to the change of chemical composition and hydrating products in cement paste systems.

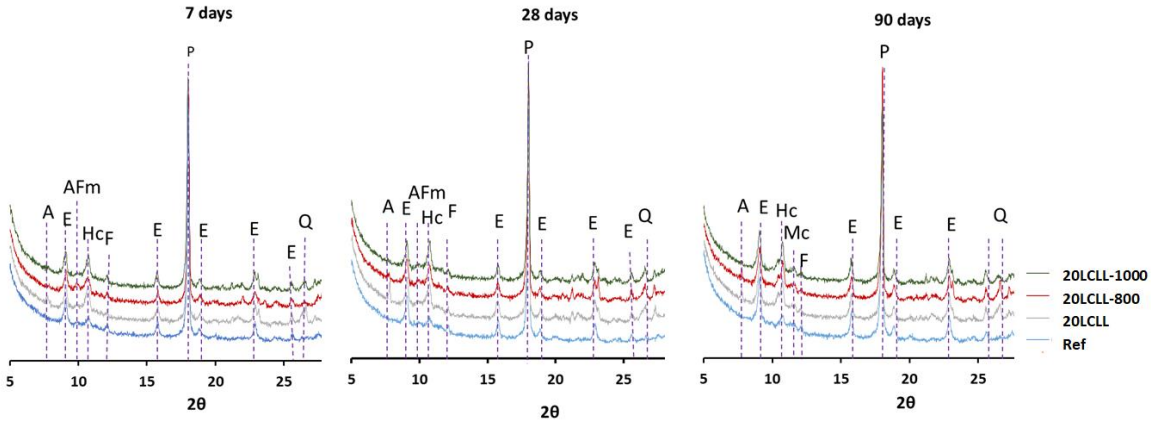

Figure 3-2. XRD patterns of all investigated mixes at (a) 7 days, (b) 28 days and (c) 90 days (A=Sodium aluminum hydration, E = ettringite, P = portlandite, Q = quartz, F=ferrite, Hc = hemicarboaluminate, Mc =monocarboaluminate).

3.5.2 Effect of calcined LCLL on the heat of hydration

The heat evolution and cumulative heat release of paste samples during the first 48h are shown in Figure 3-3. As a result of Figure 3-3a, the substitution of cement by LCLL delayed the reaction of alite. This phenomenon is more pronounced in the non-calcined LCLL system. Interestingly, for the system with LCLL, the second aluminate (C_3A) peak occurs after the main alite hydration peak, corresponding to the secondary formation of ettringite, as reported in [72,246]. Scrivener et al. [246] have reported that the retardation of the C_3A reaction is due to sulfate reaction and remains at around 15-18h. The reaction of C_3A can accelerate after the depletion of gypsum. This peak is only observed in cement paste with LCLL and this is attributed to the amorphous alumina phase from LCLL to form ettringite. Compared 20LCLL-800 and 20LCLL-1000 systems, Figure 3-3a shows that the rate of hydration in 20LCLL-1000 is lower than 20LCLL-800. It means that calcination at 800ºC can have more pozzolanic reaction.

Another observation that should be noticed is that a low broad peak can be seen between about 20h and 25h in the only sample with LCLL-C. This appears to correlate with the formation of hemicarbolauminate Hc phase, corresponding to results on XRD in section 3.4.1. This is due to the reactive alumina content in calcined LCLL, which reacts to calcite in the binder to form Hc [8,214,217].

The cumulative heat release is presented in Figure 3-3b. The heat of hydration in paste with LCLL system is lower than the reference due to the cement dilution effect. The systems with calcined LCLL (20LCLL-800 and 20LCLL-1000) react faster than the system with no-calcined LCLL for the first 18h. This is due to a small amount of LCLL-C acting as a nucleation agent, which enhances the hydration process of systems. Moreover, the total heat release of 20LCLL-C is lower than 20LCLL. It means that the calcinating did not significantly improve the pozzolanic reaction of LCLL.

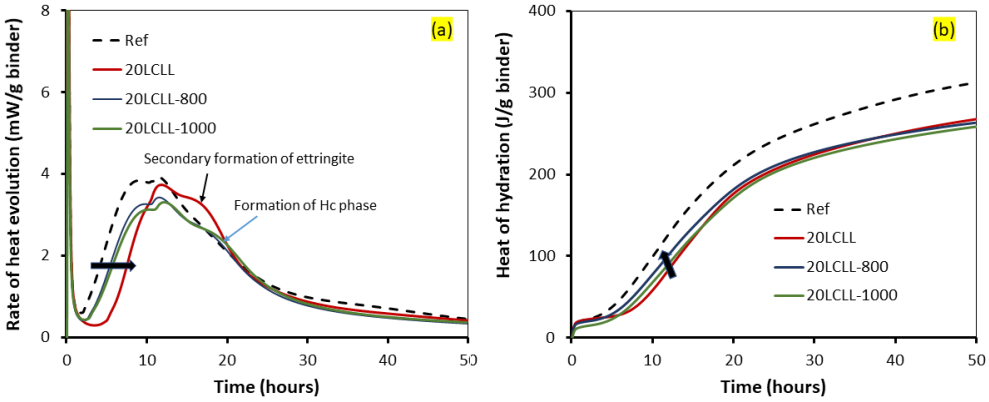

Figure 3-3. Heat of hydration of cement paste with no-calcined and calcined LCLL-ash at 48 hours.

3.5.3 Thermogravimetric analysis (TGA)

The TG and differential thermal analysis (DTG) of the hydrated LCLL-cement paste after curing at 7 days, 28 days and 90 days are shown in Figure 3-4 to 3-6. The DTG thermograms show the occurrence of four endothermic peaks at 100, 150, 400-500, 650-800ºC. The endothermic peaks located below 200ºC are mainly due to the dehydration of ettringite, AFm (Hc or Mc), and part of C-S-H, while the endothermic peak appears at 405-500ºC is due to the decomposition of $Ca(OH)_2$. The last endothermic peak located at 650-800ºC is due to the decomposition of $CaCO_3$.

From the TG curves, the amount of CH and hydrates contents can be calculated as the following equation [146,247]:

$$CH\,(\%) = (M_{405^\circ C} - M_{500^\circ C}) \times \frac{74}{18} \times 100 \qquad (3.1)$$

$$Hydrates\ (\%) = (M_{60^\circ C} - M_{405^\circ C}) \times 100 \qquad (3.2)$$

where $M_{60^\circ C}$, $M_{405^\circ C}$ and $M_{500^\circ C}$ is the percentage TG mass loss at 60°C, 405°C and 500°C, respectively, and 74/18 is the molar mass ratio between the CH and water.

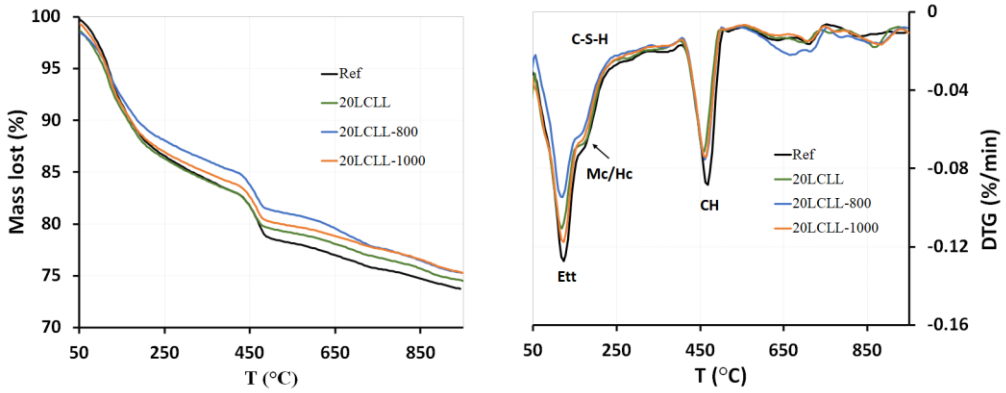

Figure 3-4. TG and DTG curves of all mixes at 7 days.

Figure 3-7 shows the CH and hydrates content, calculated by E.q3.1 and E.q3.2. The CH and hydrates content by total mass in LCLL-cement systems is lower than the reference systems, as directly related to the cement dilution. However, comparing 20LCLL and 20LCLL-C, the hydrate content by total mass in 20LCLL is higher than 20LCLL-C. It means that calcination seems not to enhance the pozzolanic reaction of LCLL-ash. This result corresponds to the isothermal calorimetry in section 3.4.1.

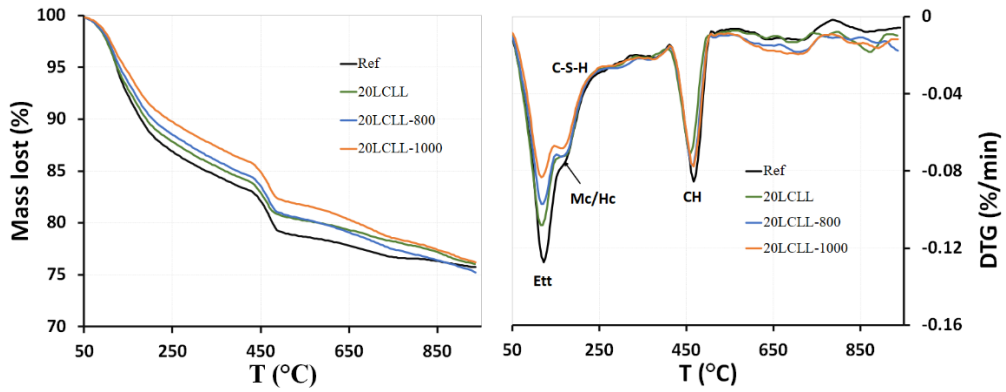

Figure 3-5. TG and DTG curves of all mixes at 28 days.

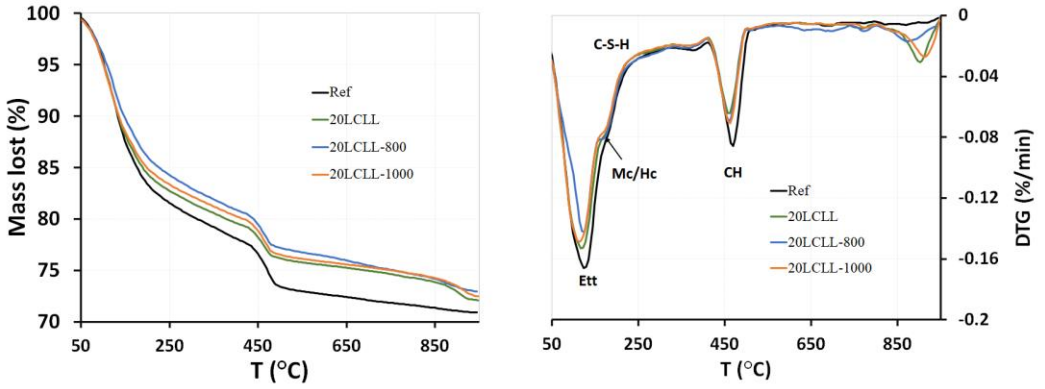

Figure 3-6. TG and DTG curves of all mixes at 90 days.

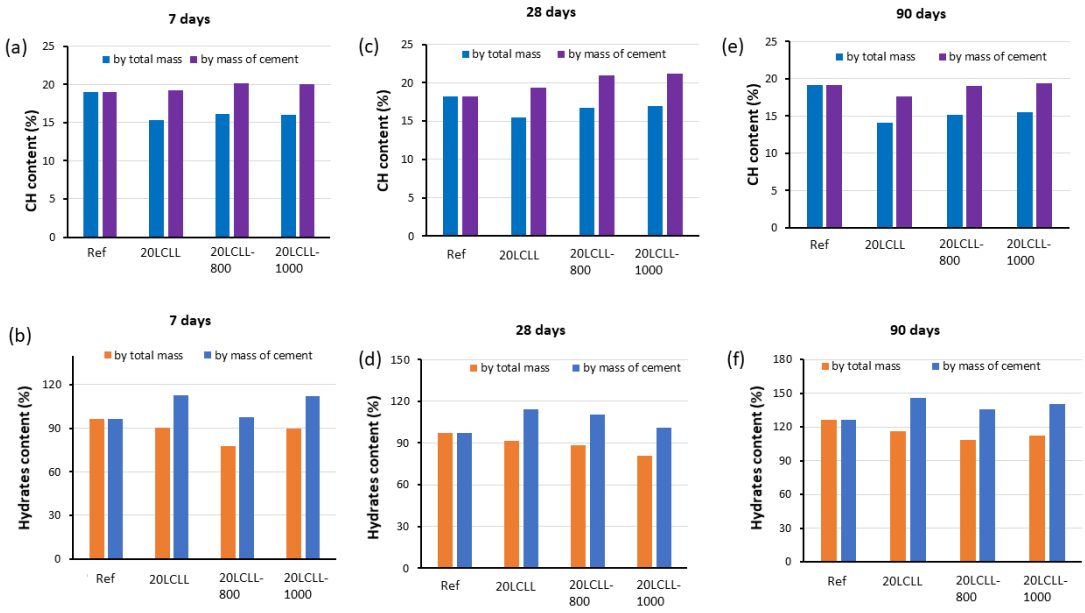

Figure 3-7. Hydrates and CH contents of cement pastes at (a-b) 7 days, (c-d) 28 days, and (e-f) 90 days.

3.6 Preliminary Conclusion

In this preliminary work, we start investigating the effect of calcined LCLL at different temperatures on hydration in the cement paste system. The following preliminary conclusions can be drawn based on the presented results:

- The replacement cement with LCLL changes the hydration products with the formation of hemicarboaluminate Hc besides the residual phases from LCLL particles.

- LCLL (calcined or non-calcined) particle delays the hydration of cement paste. The rate of hydration and the hydrates content in LCLL-C paste system is lower in LCLL paste system. It means that calcination LCLL does not improve the pozzolanic reaction.

Further studies need to be investigated, such as the compressive strength and durability of mortar and concrete with calcined LCLL. The heat treatment of LCLL is lower than clay in clinker production (1450ºC), but we need pre-treatment (grinding) before calcination. Thus, the efficiency of this solution should be considered and calculated.

Chapter 4. Understanding The Effect of Recycled Mineral Fillers on Ultra-High Performance Concretes

4.1 Résumé

Comme une partie considérable du ciment ne réagit pas dans le BFUP, le remplacement du ciment par des sous-produits industriels disponibles localement est une voie prometteuse pour favoriser la construction durable. Ce travail vise à réaliser une étude complète sur l'effet sur les BFUP à faible rapport eau/fines (w/f) du remplacement partiel du ciment par des fillers minéraux recyclées à partir de déchets industriels, comme le granite (GrP), le calcaire (LP) et post-consommé-le verre (GP).

Tout d'abord, des pâtes de ciment avec *w/f* = 0.2 ont été fabriquées en remplaçant partiellement la fumée de silice et le ciment Portland par différents pourcentages (0%, 20% et 40%) des fillers minéraux choisies. Les pâtes de ciment ont été caractérisés par plusieurs techniques, telles que la calorimétrie isotherme, l'analyse thermogravimétrique, le test de retrait endogène, le test de compression et le test de microindentation. Les principaux résultats montrent que la teneur optimale en fillers dépend du type de filler. En particulier, l'effet des fillers sur le retrait endogène varie considérablement, surtout au début de l'hydratation après la prise, selon le type de filler et le niveau de remplacement du liant. A l'échelle du béton, des mélanges de BFUP avec une teneur optimale en fillers minéraux ont été étudiés en termes de résistance à la compression et de résistivité électrique. Enfin, la formulation de BFUP permet de réduire le CO_2 en recyclant les déchets minéraux et constitue un matériau de construction prometteur pour les infrastructures civiles durables.

Mots clés: Matériaux cimentaires; fillers minéraux; sous-produits industriels; poudre de granite et de calcaire; poudre de verre; recyclage; béton fibré à ultra-hautes performances (BFUP); cinétique d'hydratation; retrait endogène; carbone incorporé.

4.2 Abstract

As a considerable part of cement remains unreacted in UHPC, replacing cement by locally available industrial by-products is a promising avenue for fostering sustainable construction. This works aims at carrying out a comprehensive study on the effect on UHPC with low water-to-fine (*w/f*) by partially replacing cement with mineral fillers recycled from industrial waste, such as granite (GrP), limestone (LP), and glass (GP).

Firstly, cement pastes with a ratio *w/f* = 0.2 were fabricated by partially replacing silica fume and cement with different percentages (0%, 20% and 40%) of the chosen mineral fillers. The cement paste samples were characterized by multiple techniques, such as isothermal calorimetry, thermogravimetric analysis, autogenous shrinkage test, compressive test, and microindentation test. As the main results, the optimum filler content was found to depend on the filler type. Notably, the effect of fillers on the autogenous shrinkage varies considerably, especially at the beginning of the hydration after setting, depending on the type of fillers and the binder replacement level. At the concrete scale, UHPC mix with optimal content of mineral fillers was studied in terms of compressive strength and electrical bulk resistivity. Finally, the UHPC formulation enables cutting CO_2 by recycling mineral wastes as a promising construction material for sustainable civil infrastructure.

Keywords: Cementitious materials; mineral fillers; industrial waste; granite and limestone powder; glass powder; recycling; ultra-high-performance concrete (UHPC); hydration kinetics; autogenous shrinkage, embodied carbon.

4.3 Introduction

Ultra-high-performance concrete (UHPC) is a new class of cement-based composites characterized by outstanding compressive strength and unprecedented durability [1]. In general, UHPCs are characterized by high cement content, e.g., in the range of 800–1200 kg/m^3, as well as a high dosage of silica fume (15–30% of cement content) [124,125], a very low water-to-cement (*w/c*) ratio of 0.18–0.33 [22,23,136], and a limited volume of fine aggregate (~50%). Moreover, a high dosage of high-range water-reducing admixtures (HRWRA) in the range of 1.4-2.4% by cement weight is employed to guarantee satisfactory workability [132]. As for structural applications, steel microfibers are added from 2% to 4% by volume to provide strain-hardening and low cracking under service [16].

UHPC technology is increasing acceptance in civil infrastructures for precast concrete elements, long-span footbridges and bridges, and bridge deck repairs and architectures with complex shapes [248–250]. Nonetheless, UHPC technology is today limited by the high construction cost associated with its raw materials, particularly mineral powders and steel fibers [127–130]. The latter may account for up to 50% of UHPC cost [129]. Owing to the fact that the concrete industry emits about 9% of global carbon dioxide CO_2 emission [1] and that a great amount of cement remains unreacted in UHPC, there is a strong interest in developing low-cement UHPC for building concrete structures with low volume

and embodied carbon. Given the very low water content in UHPC, only 45–60% of cement hydrates [22,23,136]. Consequently, the unhydrated cement plays the role of an expensive and high-CO_2 filler, thereby making UHPC less cost-effective. Thus, partially replacing cement with industrial by-products is one of the promising solutions to produce affordable UHPC with less environmental impact. This includes, UHPCs incorporating fly ash [173,174], slag [175–177], limestone powder [178,179], rice husk [33,180,181], granite powder [182,183] and glass powder [184,185].

Furthermore, existing UHPCs use a high content of silica fume with high surface area and pozzolanic activity to achieve high strength and durability. However, only about 20% of silica fume hydrates given the extremely low *w/c* environment [126]. While the use of silica fume in UHPC is intended for its filler and pozzolanic effects, the efficiency of the latter mechanism whereby calcium hydroxide (CH) from cement hydration is converted to secondary C-S-H gel, is questioned when the low *w/c* environment is not even sufficient for cement hydration to complete, not to mention that of silica fume. In fact, it was clearly shown that silica fume reduces the compressive strength of cement pastes at a water-to-cement ratio lower than 0.25 due to the lack of water in the mix to engender pozzolanic reactions [251]. With the increasing demand for silica fume, the partial replacement of silica fume by other SCM or mineral fillers would enable reducing the cost, and carbon footprint is imperative, particularly since silica fume has the further drawback of exacerbating autogenous shrinkage in UHPC [172].

Moreover, since that calcium hydroxide is mostly consumed by silica fume in UHPC with a very low *w/c* ratio, its availability for pozzolanic reactions of SCM might be much limited. Nevertheless, it was found that glass powder acts as a SCM in UHPC systems as it reacts just enough on the edges of the glass particles to enhance the bonds with cement hydrates [67,252]. From a mechanical standpoint, UHPC strength may be enhanced by the unreacted silica fume due to its extreme size (~0.1 μm) as it contributes to reducing the final porosity and increasing the packing density of the hydrates in the porous ITZ around mineral fillers and sand [253]. Thus, the micro-filler effect of silica fume allows for enhancing the overall mechanical properties and enhancement of durability [184,254].

Given that a significant portion of cement and silica fume in UHPC does not hydrate due to the very low *w/c*, it is legitimate to believe that the replacement of cement and silica fume with mineral fillers can enable developing low-CO_2 UHPCs. The filler effect of these materials enables replacing unhydrated cement and silica fume particles, while the low reactivity of these mineral fillers will enable attenuating autogenous shrinkage. Hajiesmaeili and Dénarié replaced cement up to 50% by limestone

fillers for developing ecological UHPC [255,256]. Li et al. [178] showed that it is possible to replace up 60% of cement with limestone in UHPC with compressive strength of 150 MPa without affecting workability. Finally, Bouchard et al.[257] developed UHPC with about 25% cement replaced by granite powders.

UHPC mixtures are characterized by autogenous shrinkage which mainly occurs in the first days after mixing [33,34]. The early-age autogenous shrinkage is caused by internal self-desiccation due to the hydration of cement and silica fume. As self-desiccation continues, water menisci are formed in the capillary pores and their surface tension increases, causing volume reduction. When these tensile forces exceed the tensile strength of UHPC which is growing with time, especially in the first week, early age cracks may occur [167]. Thus, autogenous shrinkage can cause a considerable potential at an early age micro-cracking which can affect the sough durability of UHPC or the esthetic texture for architectural applications [258]. The use of SCM and mineral fillers may strongly affect the autogenous shrinkage in a complex way depending on many parameters [259]. Ye et al. [33] showed that 20% replacement cement by rice husk ash (RHA) reduces 20% the autogenous shrinkage compared to the control sample, even the autogenous shrinkage of the RHA samples was further mitigated after 10 days. Hisseine et al. [172] reduced autogenous shrinkage of UHPC with glass powder by using nanocellulose filaments. Soliman et al.[168] reduced the shrinkage by replacing 12% volume of cement with wollastonite microfibers, resulting in the reduction in total shrinkage by about 16% compared to that of the control mixture at 7 days.

To foster the potential of low carbon UHPC with locally available mineral fillers which are recycled by industrial and post-consumer wastes, i.e., granite, limestone, and glass. This work has twofold objectives: (i) at the cement paste scale, to carry out a comprehensive study on the effect of on the key features of UHPC, such as hydration kinetics, autogenous shrinkage micromechanical properties; (ii) at the concrete scale, to study the effect of mineral fillers on UHPC compressive strength and electrical resistivity. Finally, research outcomes are expected to contribute to carbon imprints of concrete structures and better use of natural resources.

4.4 Materials and methods

4.4.1 Raw materials properties

Type General Use (GU) Portland Cement (CSA A3001) equivalent to Type III cement (ASTM C1157) and silica fume (SF) fulfilling the requirements of CAN/CSA A3000 specifications were used as a binder. Glass powder (GP), granite powder (GrP), and limestone powder (LP) were used as mineral fillers. The GrP is a solid waste material from the industrial stone industry and was obtained from a local supplier in Quebec. During the production of industrial stone, the cutting process generates significant waste of fine GrP with high silicate (SiO_2) content. The GP is obtained from post-consumer glass ground to a particle size closer to that of Portland cement. The LP used herein is generated from the cutting and polishing of coarse stone. All fillers were dried at 110°C for 24 hours prior to utilization in this project. The sand consists of natural sand (NS) with a maximum particle size (D_{max}) of 1.25 mm, a mean particle size (D_{50}) of 500 µm, and a specific gravity of 2.75. Steel fibers have an average length of 6 mm and an average diameter of 0.2 mm and have a nominal specific weight of 7800 kg/m^3.

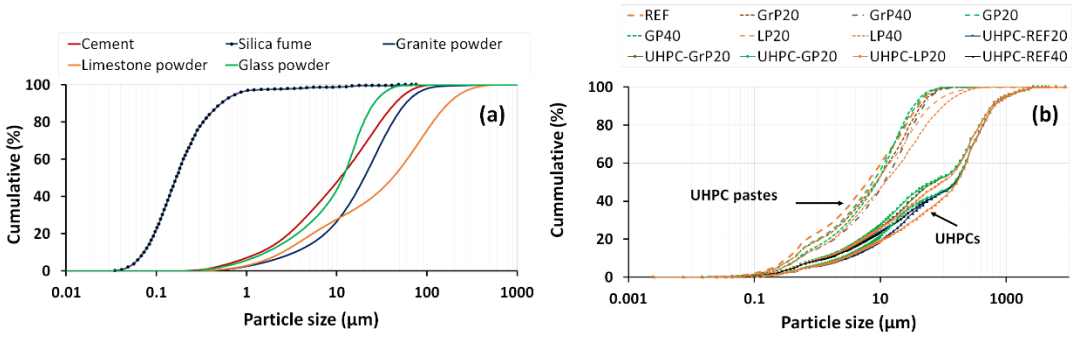

Figure 4-1. (a) PSD of the raw materials; (b) PSD of the powder mixtures for cement cement paste systems (without sand) and UHPC systems (with sands).

Table 4-1 presents the X-ray fluorescence (XRF)-based chemical properties of these materials measured as well as their physical properties. Figure 4-1 presents the particle size distributions for cement, SF, GrP, GP and LP, and cement pastes and mixtures, as measured using a Mastersizer 2000 laser granulometry by Malven. In addition, the particle size distribution of the densified SF after ultrasonic dispersion is presented.

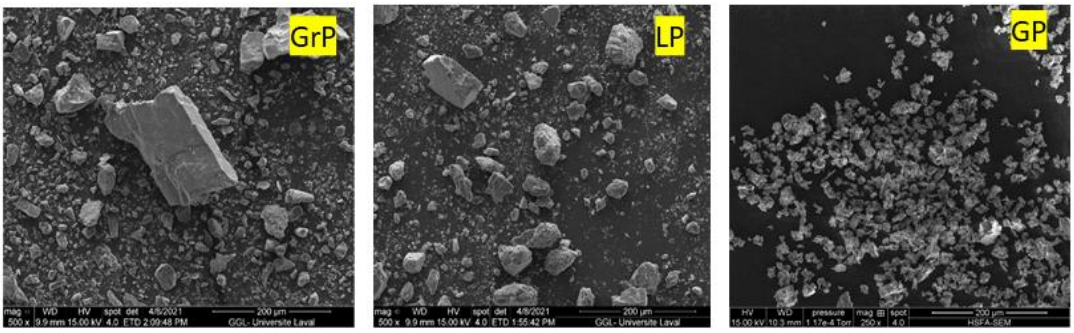

Figure 4-2. SEM images of the used materials.

Table 4-1. Chemical composition (percentage weight, Wt.%) and physical properties of PC, SF, GrP, GP and LP employed in this study.

Materials	PC	SF	GrP	GP	LP
CaO	61.3	0.40	1.25	11.3	51.2
Al_2O_3	4.4	0.11	13.4	1.5	0.08
SiO_2	19.7	99.8	72.9	74	5.2
Fe_2O_3	2.7	0.09	1.08	0.4	0.3
MgO	2.9	0.2	1.58	0.8	0.5
Na_2O	0.3	-	3.83	12.8	-
SO_3	4.0	-	0.06	-	-
K_2O	0.9	0.5	3.64	0.5	-
TiO_2	0.2	-	0.14	0.04	-
Loss on ignition	2.7	3.5	1.81	0.6	42.4
Specific gravity	3.09	2.20	2.74	2.53	2.75
Specific surface, BET (m^2/g)	445	20,000	-	-	-
D_{50} (µm)	9.6	0.1	20.1	11.6	40.8
D_{90} (µm)	44.3	1.0	58.2	25.9	172.5

Table 4-2. Mixture proportion (kg/m^3) of the cement paste systems.

Mix	PC	SF	GrP	GP	LP	SP	Water	*w/c*	*w/f*
Ref	1413	283	–	–	–	51	339	0.24	0.2
GrP10	1272	254	161	–	–	50	337	0.27	0.2
GrP20	1131	226	321	–	–	50	336	0.30	0.2
GrP30	989	198	482			50	334	0.34	0.2
GrP40	848	170	643	–	–	50	332	0.39	0.2
GP10	1272	254	–	148	–	50	335	0.26	0.2
GP20	1131	226	–	297	–	50	331	0.29	0.2
GP30	989	198		445		49	326	0.33	0.2
GP40	848	170	–	593	–	48	322	0.38	0.2
LP10	1272	254	–	–	162	51	338	0.27	0.2
LP20	1131	226	–	–	323	50	336	0.30	0.2
LP30	989	198			485	50	336	0.30	0.2
LP40	848	170	–	–	646	50	333	0.39	0.2

PC: Portland cement; SF: Silica fume, GrP: Granite powder, GP: Glass powder, LP: Limestone powder, *w/c*: water-to-cement ratio, *w/f*: water-to-fine ratio; fine = PC + SF + filler; filler = GrP or GP or LP

4.4.2 Mix proportions

To enable capturing the effect of mineral fillers on the hydration kinetics of UHPC, it was deemed necessary to conduct the assessment of hydration kinetics on the cement paste systems (without sand and fibers). In this study, the term fine (f) refers to the combination PC+SF+filler, whereby the filler can be either GrP, GP, or LP. The SF to cement ratio (SF/PC) is set to 20% by mass, while the water-to-fine ratio (*w/f*) was fixed at 0.20 by mass. For the paste systems, the substitution level of binder (PC+SF) by mineral additions ranges from 0 to 40 vol.% with an increment frequency of 10 vol.%. Later, these paste formulations with 20 vol.% and 40 vol.% were upscaled by integrating sand and steel fibers to produce UHPC. In both cases, UHPC mixes were designed following the absolute volume method—

utilizing the key components' proportions by volume instead of by mass is more reasonable and useful in mix design [20, 34]. In addition, superplasticizer (SP), with a specific gravity of 1.08 and a solid content of 28%, was added at 3% by mass of fine. Also, the micro-steel fibers were added at 2% by volume of mixture to final UHPC. Table 4-2 presents the mixture proportions of the paste systems, while Table 4-3 presents the proportions of final UHPC mixtures. It is worth noticing that the UHPC mixtures have a relatively high volume of fine aggregates for the economic and ecological purposes.

Table 4-3. Mixture proportion (kg/m^3) of final UHPC mixtures.

Mixtures	PC	SF	GrP	GP	LP	Sand	Water	Fiber	*w/c*	*w/f*
UHPC-Ref20	878	178	–	–	–	1052	211	156	0.24	0.2
UHPC-Ref40	757	151	–	–	–	1256	182	156	0.24	0.2
UHPC-GrP20	709	144	201	–	–	1061	211	156	0.30	0.2
UHPC-GP20	711	145	–	187	–	1064	208	156	0.29	0.2
UHPC-LP20	713	145	–	–	188	1071	210	156	0.29	0.2
UHPC-GrP40	457	91	346	–	–	1262	179	156	0.39	0.2
UHPC-GP40	459	92	–	321	–	1270	175	156	0.38	0.2
UHPC-LP40	456	92	–	–	348	1262	179	156	0.39	0.2

PC: Portland cement; SF: Silica fume, GrP: Granite powder, GP: Glass powder,
LP: Limestone powder, *w/c*: water-to-cement ratio, *w/f*: water-to-fine ratio; fine = PC + SF + filler;
filler = GrP or GP or LP

4.4.3 Batching and casting

The UHPCs were produced using Hobart mixer as the following sequence: (i) To achieve homogenous mixtures, all granular materials were initially dry-mixed at speed 1 for 5 minutes; (ii) From a pre-prepared suspension (of the mixing water and SP), 50% of the suspension was gradually added and mixing continued at speed 1 for 3 minutes; (iii) Upon stopping the mixer and scarping its sides and blades, the remaining 50% of the suspension (water + SP) was introduced then mixing continued at speed 2 for 2 min; (iv) For upscaling the initial paste systems to UHPC formulations, sand and steel fibers were added to the initial formulations. The mixing process followed the same sequence described

above except for an additional step of 2 min mixing at speed 2 once the steel fibers are gradually added to the batch at the end of step 3 above.

4.4.4 Tests and methods

4.4.4.1 Fresh cement paste properties

The workability was assessed using the flow table test in compliance with ASTM C1437. Statistic readings of three diameters for each mix were recorded at 120 seconds after slowly lifting the cone. The air content was measured in compliance with ASTM C185. The density of fresh concrete was measured as follows ASTM C138M.

4.4.4.2 Hydration reaction

Isothermal calorimetry

An isothermal calorimeter of type I-Cal 2000 HPC was employed to quantify the effect of different mineral fillers on the heat of hydration. Mixtures not containing neither sand nor steel fibers (as detailed in Table 4-2) were considered for this purpose. Directly after mixing, about 50 g of the fresh concrete mixture was poured into a sealed glass, which was then placed into the isothermal calorimeter. The instrument was set at a temperature of 23°C according to ASTM C1702-17. Reading continued for 48+ hours. Results were used to evaluate the effect of mineral fillers on the hydration kinetics of UHPC as well as to determine the degree of hydration.

Thermogravimetric analysis

Thermogravimetric analysis was conducted to evaluate the effect of different mineral fillers on the extent of hydrates (CH and C-S-H). A Netzch simultaneous analyzer (model 449 F3 Jupiter) was used to obtain the thermogravimetric (TG) and differential scanning calorimetry (DSC) curves of cement paste systems. For each test, about 40 mg of finely ground powder was taken in a ceramic crucible without a lid. Analyses were conducted at a heat ramp of 20°C/min from 50°C and 950°C. The test was performed under a nitrogen atmosphere at a flow rate of 50 mL/min. TGA results were then used to evaluate the amount of CH and C-S-H by the following equations [146,178]:

$$CH\,(\%) = \Delta WL_{CH}\,(\%)\,\mathrm{x}\;\frac{MW_{CH}}{MW_{H}}\,\mathrm{x}100\;(\%) \qquad (4.1)$$

$$C-S-H\,(\%) = \Delta WL_{C-S-H}\,(\%)\ \text{x}\ \frac{MW_{C-S-H}}{2.1MW_H}\,\text{x}100\ (\%) \tag{4.2}$$

where ΔWL_{CH} , ΔWL_{C-S-H} is the percentage TG mass loss during 400-500°C and 150-400°C, MW_{CH} , MW_{C-S-H} and MW_H are the molecular weight of CH, C-S-H gel, and water, respectively. It is noted that the exact boundaries for the temperature interval of CH are adapted based on the derivative curve (DTG). The stoichiometric amount of water in C-S-H gel is taken as 2.1 in Eq.2, as suggested by [261] due to some water of the 4 mol has already been lost below 150°C.

Double Danish Model

The assessment of heat of hydration by isothermal calorimetry is more efficient at early ages (first 48 hours). The technique has less sensitivity to heat release at long curing ages [262]. Therefore, the Double Danish Model, DDM [263] was used to predict the heat release beyond 48 hours. To do so, DDM parameters corresponding to the best fit (during the first 48 hours) between the experimental heat release and DDM-based heat release were estimated for all UHPCs. Using these DDM parameters, the heat releases up to 28 days (700+ hours) were estimated and used to determine the degree of hydration.

The DDM is an extension of the original Danish Model [264] where the heat of hydration is contributed by the cement alone. The DDM further considers the contribution of silica fume which has a phenomenal impact on the hydration of UHPC mixtures. The development of cumulative heat of hydration contributed by cement and silica fume can be estimated as follows:

$$H_T(t) = H_{T1}.e^{-(\frac{\tau_1}{t})^{\beta_1}} + H_{T2}.e^{-(\frac{\tau_2}{t})^{\beta_2}} \tag{4.3}$$

$$H_{T_\infty} = H_{T1} + H_{T2} \tag{4.4}$$

Where $H_T(t)$ is the profile of the cumulative heat of hydration in kJ/m^3, H_{T1} and H_{T2} are the heat of hydration of cement and silica fume at time τ_1 and τ_2 in hours, respectively, β_1 and β_2 are the hydration slope parameters of the cement and silica fume, and $H_{T\infty}$ is the asymptotic value of the cumulative heat of hydration of each mixture.

The degree of hydration at any time, $\alpha(t)$, then can be estimated by the following equation:

$$\alpha(t) = \frac{H_T(t)}{H_{T100\%}} \tag{4.5}$$

With $H_{T100\%}$ is the theoretical total potential heat of hydration release for full hydration of cement and silica fume. It is noted that the heat contributed by other components (e.g., SCMs) are negligible due to their documented slow reactivity at an early age. The heat release of cement and silica fume for full hydration are 452.3 kJ/kg [263,265] and 780 kJ/kg [263].

4.4.4.3 Autogenous shrinkage

The corrugated tube test (ASTM C1698) was utilized to measure the autogenous shrinkage of UHPCs. The length and diameter of the corrugated tube were approximately 430 mm and 29 mm, respectively. The fresh mixtures were poured into the tube and vibrated for 180 second. The test was conducted in a controlled environment (i.e., the temperature of 20 ± 2ºC and 55% RH). Test samples were then placed on a rigid frame equipped with a TRANS-TEK 350-000 displacement transducer. The length changes were recorded at 15 min intervals for 7 days. The setting time was determined based on ASTM C403. The measurements were carried out at room temperature with 55% of humidity. The final setting time was defined as “Time Zero” of autogenous shrinkage measurements.

4.4.4.4 Micromechanical properties

Microindentation is a powerful technique for statistically and rapidly probing the viscoelastic and strength property of a cement paste. Notably, such a technique allows for estimating the logarithmic rate of the basic creep of a cement paste in a few minutes instead of the several months required by macroscopic compression creep tests [227,266].

Prior to testing, the UHPC samples were carefully polished, following a procedure detailed in previous studies [151,266,267]. The specimen is cut into 3 mm thick slices. The latter were polished with coarse abrasive papers (240, 400, 600, 800 and 1200 of grid size) on a rotating table until the sample surface was horizontally leveled. Furthermore, oil-based diamond suspension (3 and 1 μm) was used as the final polishing process. Finally, the samples were cleaned by an ultrasonic bath in order to remove debris and suspensions lefts on the surface of the sample.

A typical P-h curve (Figure 4-3a) is constituted by a loading curve up to the maximum load Pmax, hold for a given time interval at Pmax, followed by an unloading curve. For this study, the Berkovich-type indenter—consisting of a three-sided pyramid with an equivalent cone semi-angle θ of 70.3º was used. Two mechanical properties can be extracted from the P-h curve: (i) the indentation Modulus $M = (S\pi^{0.5}) / (2\beta A_c)$ and (ii) the indentation Hardness $H = P_{max} / A_c$. Where Ac is the projected contact area and can be extrapolated from the indentation depth h through Oliver and Pharr's method [155]. The contact stiffness S=dP/dh is the slope measured during the initial stages of the unloading curve. The coefficient β accounts for the non-symmetrical shape of the indenter (β=1.034 for Berkovich indenter).

The indentation modulus, M, is related to the elastic Modulus, E, and Poisson's ration υ, of the isotropic material as follows: $M^{-1} = ((1-\upsilon^2)/E + (1-\upsilon_i^2)/E_i$. Where E_i and υ_i are the elastic modulus and the Poisson's ratio of the diamond tip, which are equal to 1141 GPa and 0.07, respectively; while E and υ are the Young modulus and the Poisson's ratio of the material, respectively. As for a creep microindentation test, the contact creep modulus C proposed by Vandamme and Ulm [157] which describes the logarithmic asymptote of the creep penetration depth $C = P_{max} / (2a_u x_1)$, where x_1 is term of the logarithmic penetration depth function $\Delta h(t) = x_1 \ln(t/\tau_H+1)$ which is employed to fit the creep curve of the holding period τ_H. This definition assumes that the radius of the contact area at unloading a_u is constant during holding, as experimentally verified with an error of approximately 5% [157].

The microindentation tests were carried out by using a CSM Indentation Tester. The maximum load applied in this study is 15 N, corresponding to the maximum depth of 30~35 μm. A grid of 10 x 10 microindentation tests with inter-distance of 400 μm was performed on cement pastes. The loading time and unloading time is 5 s, while the holding time at P=15 N is 60 s for the creep investigation (as shown in Figure 4-3b).

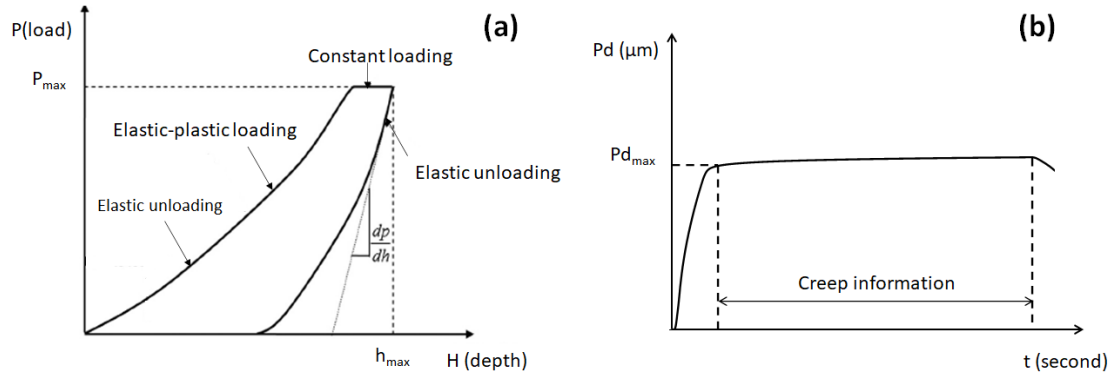

Figure 4-3. A schematic illustration of an indentation test in terms of (a) P-h curve, (b) P-t curve for a creep test.

4.4.4.5 Compressive strength

For both cement pastes systems and final UHPC mixtures, 50 mm cubic molds were used to prepare the sample for the assessment of the compressive strength (ASTM C109). The samples were demolded after 24 hours and then cured in an environmental control room with 20 ± 2ºC temperature and relative humidity (RH) > 95%. Testing was conducted at 7, 28 and 90 days using at least three samples, from which the mean value was used to designate the compressive strength. The test was carried out at a rate of 0.6 MPa/s. It is worth noticing that the means compressive strength converting factor between cube and cylinder specimen of UHPC with 1-2% fiber is about 0.95-0.99, as reported by [268,269]. It can also be expected a certain wall effect on the orientation of fibers as fibers of length 12 mm is 4.1 times smaller than the cube size.

4.4.4.6 Electrical resistivity

The electrical resistivity test is recently becoming popular to evaluate the durability properties of concrete since it is a rapid and non-destructive test and requires a minimal amount of equipment [270]. Electrical resistivity is a material property that indicates how easily an electrical charge moves through a material when an electric field is applied [270]. Hernandez et al.[271] evaluated the durability of the UHPC incorporating quartz and limestone fillers through an electrical resistivity test.

The electrical resistivity test using the uniaxial resistivity test method, which was measured on cubic samples without fibers at 7 days and 28 days of final UHPC-20% fillers by using the RCON device by Giatec at 1 kHZ. The measured resistance value Ω (denoted as ohm) was multiplied by the ratio of cross-sectional area-to-length m to determine the uniaxial resistivity (Ohm·m).

4.5 Results analysis and discussion

4.5.1 Fresh cement pastes properties

Figure 4-4. compares the fresh properties of developed UHPC mixtures in terms of spread (4a), air content (4b), unit weight (4c) and wet packing density (4d). Results indicated that the cement replacement with tested mineral fillers (GrP, LP, GP) affected the workability with a more pronounced effect at higher replacement levels Figure 4-4.a. A higher spread diameter was recorded in UHPCs-based paste with fillers as a direct consequence of the drop in the binder content (cement and silica fume) versus the increase in the effective water owing to the replacement of binder with fillers. Therefore, for the same *w/f* ratio of 0.20 in all UHPCs, there is higher effective water in cement pastes with fillers (e.g., a *w/c* of 0.39 in the case of the UHPCs with 40% filler content compared to a *w/c* of 0.24 in the reference UHPC). The considered mineral fillers increased mixture flowability for 2 reasons: (*i*) the reduced specific surface area of mineral fillers because of their relatively coarser particles (PSD depicted in Figure 2), and (*ii*) the low reactivity of mineral fillers, as addressed in the coming section (4.5.2). This trend was also observed by other researchers [182,183,185,272,273]. In particular, LP mineral fillers increase the workability the most, as found in previous work [178]. The air content is very low in all systems and not affected by the addition of mineral fillers. (Figure 4-4.b). However, LP slightly decreased the air content by increasing the replacement level. The contradictory effect on the air content reduction and increase of flowability is explained by the work of Li et al. [178] for which cement could be replaced up to 50% by LP without affecting strength and workability. They explained that LP acts as a mineral plasticizer which improves the fluidity of UHPC by the following factors: (ii) LP is characterized as a neutral surface with Ca^{2+} and CO_3^{2-} ions, and OH^- groups tend to localize over the Ca^{2+} surface, which contributes to electrostatic repulsion between particles [274,275]; (ii) LP has weaker adsorption ability than cement and micro-silica because of a lower solubility and lower surface charge, leading to reduced adsorption of polycarboxylic ethers molecules and consequently reduced superplasticizer saturation dosages [141]. Also, Figure 4-1 shows that LP is characterized by larger particles size than other fillers. Adding LP lead losing the compaction compared to the other fillers that air can entrap more easily.

Figure 4-4.c and d show the effect of fillers on the density and wet packing density calculated as aforementioned. The results may appear apparently contradictory, but the increase in packing density may not involve an increase in density if powder with higher density (cement ~3200 kg/m^3) is replaced

with powder with lower density (mineral fillers ~2700kg/m^3). The mineral fillers slightly increased the wet density of the systems in a similar fashion (i.e., reduced the density). In particular, GP mineral filler achieved the highest packing density for 40% addition.

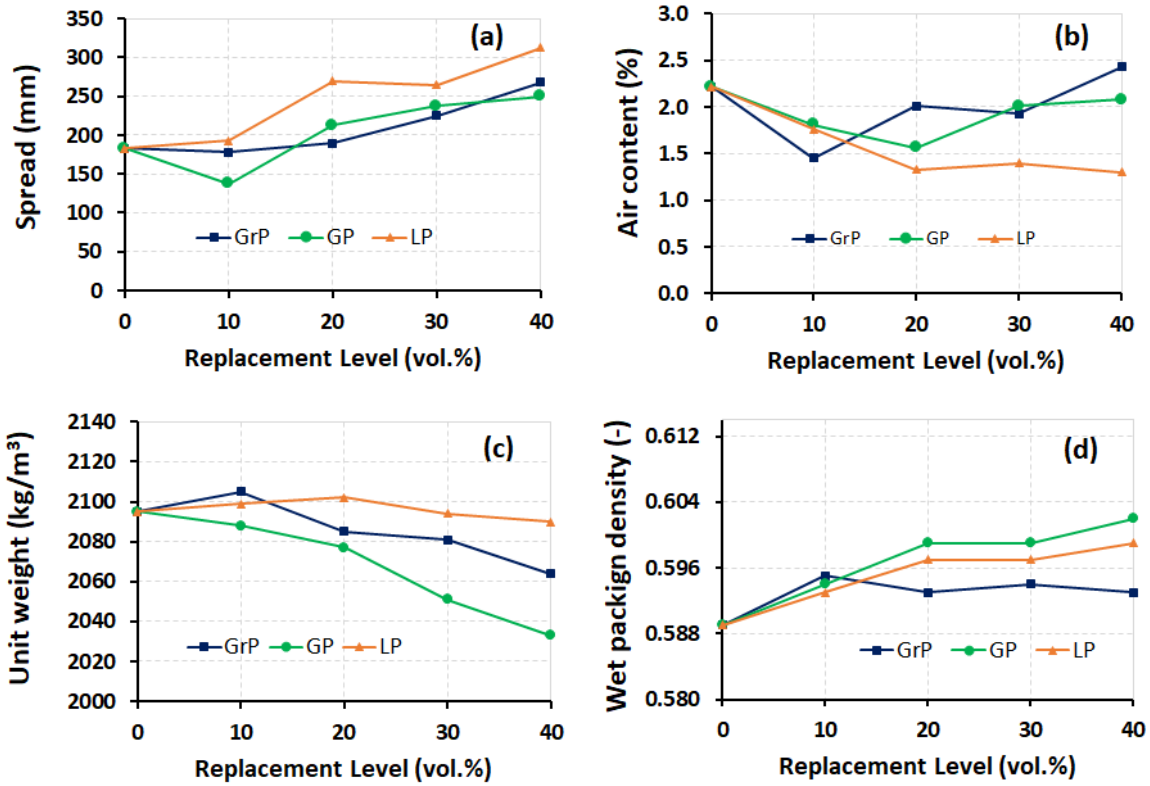

Figure 4-4. Effect of binder replacement level by mineral fillers on (a) spread; (b) air content; (c) unit weight; (d) wet packing density.

4.5.2 Hydration reaction

4.5.2.1. Isothermal calorimetry

Figure 4-5 presents the results of isothermal calorimetry for cement pastes with mineral fillers for the test duration of 48 hours. As can be seen, the studied mineral fillers affected the hydration kinetics. In particular, the hydration rate of UHPC decreased with an increase the mineral substitutions, as shown in Figure 4-5a. Moreover, 40% replacement level (GrP40, GP40 and LP40) remarkably delayed the hydration of cement as the heat-time curve was shifted on the right compared to the reference. The maximum peak value of heat flow of Ref, GrP40, GP40 and LP40 was achieved at the following time 20h, 24.5h, 26.6h and 26.4h, respectively. As we keep the same amount of superplasticizer as 3% of the mass of fines (cement, silica fume and filler), this caused a higher superplasticizer-to-binder ratio

in the systems with fillers, which could explain this retardation effect [141]. According to Jansen [276], the diffusion of Ca^{2+} ions was affected by the polymer adsorption on the nuclei or the anhydrous grain surfaces, which might prevent nuclei growth or lead to the dissolution of the anhydrous grains.

Figure 4-5c shows that the total heat of hydration of UHPC with mineral fillers decreased compared to the reference. This reduction is more pronounced in UHPC with 40% of replacement. This is directly related to the low reactivity of mineral fillers and the lower binder content (dilution effect). The lower cumulative heat of hydration can mitigate potential autogenous shrinkage, similar to the report of [34], as discussed in the next session 4.5.3.

Figure 4-5b and Figure 4-5d present the results of isothermal calorimetry normalized by a gram of cement. The normalized heat flow peak of the mixtures with the mineral additions is higher than that of the reference. The delayed hydration of cement is still observed in the curves with 40% substitution. Interestingly, UHPC-40% fillers exhibited a higher heat release than UHPC-20% fillers and the reference mixture. This can be explained by the following reasons: (i) the dilution of cement particles by filler particles in paste (*w/c* increase), which provides relative more space for the formation of hydrates of cement, and (ii) the fine particles sizes of mineral admixtures can provide additional sites for the nucleation of the hydration product (e.g., C-S-H gel) [76]. This conclusion is also confirmed by the result on TGA.

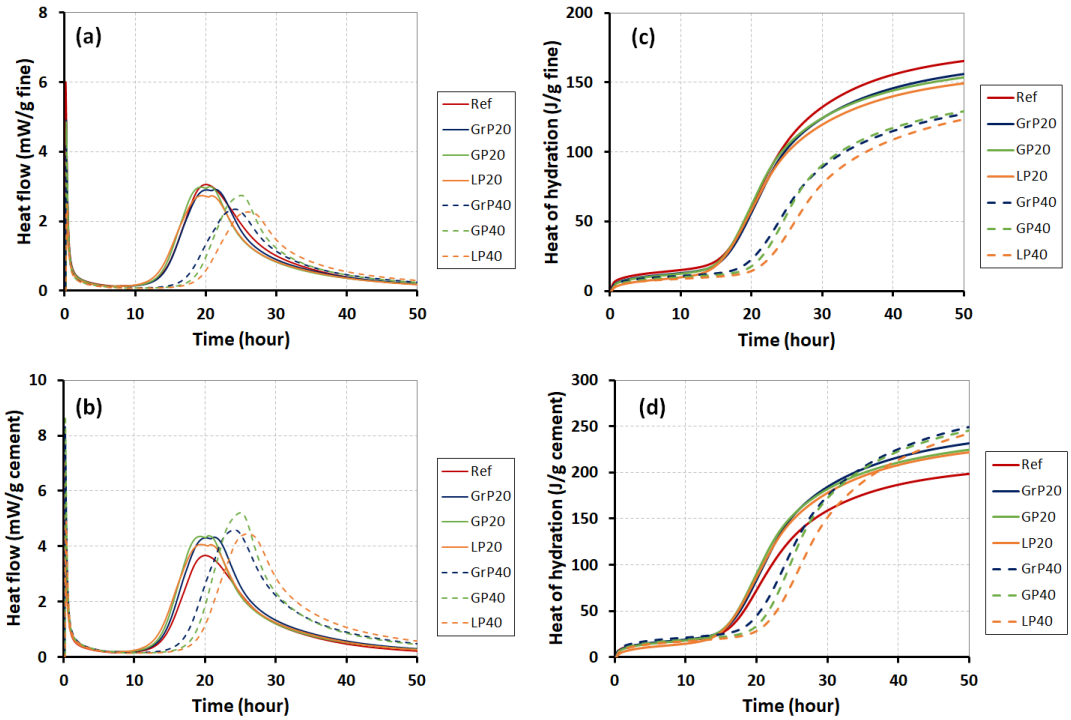

Figure 4-5. Isothermal calorimetry results of cement pastes with difference mineral fillers additions for 48 hours.

The normalized heat (Figure 4-5b and Figure 4-5d) of the mixtures with GP20 is similar to that with GrP20, which implies that the GP20 and GrP20 similarly affect cement hydration. By contrast, the effect is less pronounced for LP. This can be explained by the coarser particle size distribution of LP than other fillers, which slowed down the hydration process [78].

4.5.2.2. Thermalgravimetric analysis

Figure 4-6 shows thermogravimetric (TG) curves and derivative thermogravimetric (DTG) curves of cement paste with different mineral additions at 7 and 28 days. The hydrated cement paste showed a typical weight loss area related to the dehydration of ettringite at 110-130°C, the dehydration of C-S-H at 150-400°C, the dihydroxylation of CH between 400-500°C, and the decomposition of carbonate over 650°C.

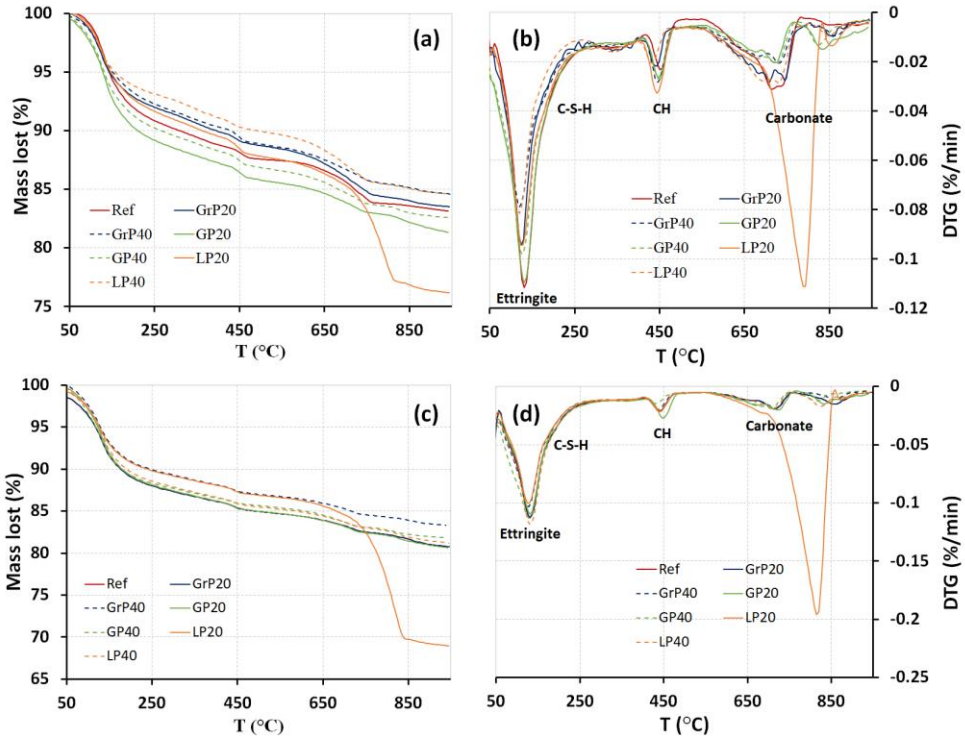

Figure 4-6. TG and DTG curves of UHPC mixtures at (a-b) 7 days and (c-d) 28 days.

To further determine the effect of mineral fillers on the hydration products of mixtures, Figure 4-7 compares the estimated amount of CH and C-S-H content based on Eq. 4.1 and Eq.4.1. In general, a filler effect on the cement hydration is clearly observed by the addition of mineral fillers [76] as the content of CH and C-S-H normalized by mass of binder increased by adding mineral fillers.

If we consider the content of CH and C-S-H normalized by total mass at 7 and 28 days (Figure 4-7), the content of CH and C-S-H of systems with mineral fillers is lower than those of the reference mixture at 28 days due to the dilution effect (lower cement content in the mixture). Considering the content of CH and C-S-H normalized by the total mass of the binder show a continuous increase in samples with higher fillers at both 7 and 28 days. This is more pronounced in samples with 40% of replacement level. For example, at 28 days, C-S-H content of the Ref sample is 42%, while GrP40, GP40 and LP40 have 60, 59, and 58%, respectively. This can be explained by two reasons: (i) the nucleation effect of fillers at an early age and (ii) increase *w/b* ratio in cement pastes with fillers, which can create more space to form hydrates phases. It means that the mineral fillers enhance the hydration degree of binder in UHPC systems, similar to the report [178]. This result corresponds to the result of the estimated degree of hydration in section 4.5.2.3.

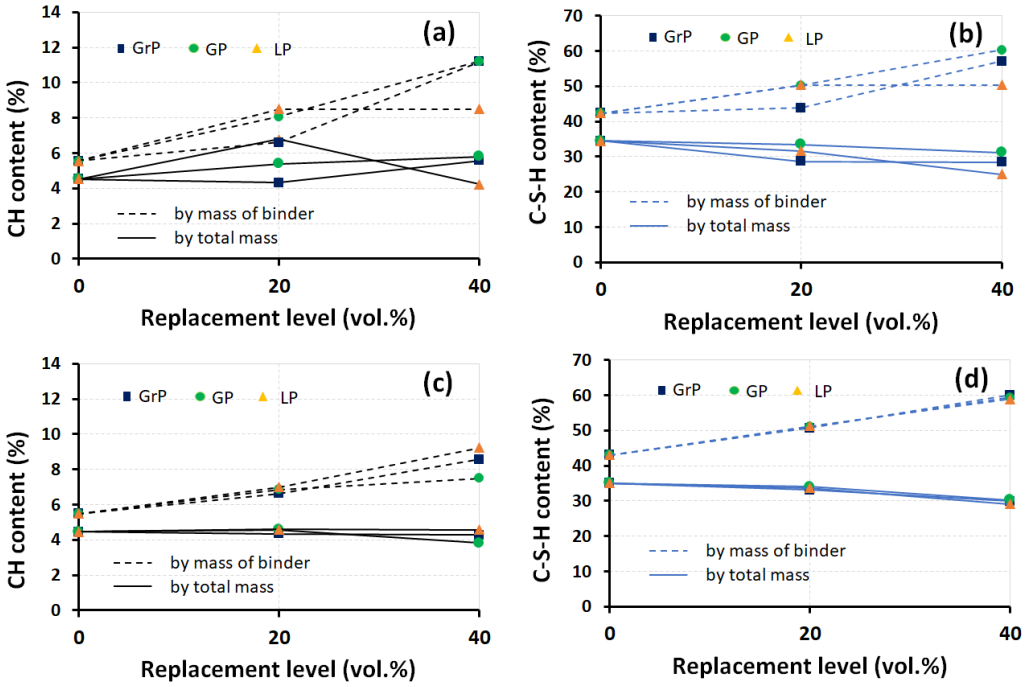

Figure 4-7. CH content and C-S-H content calculated from TG curves at (a-b) 7 days and (c-d) 28 days.

4.5.2.3. Estimated degree of hydration

As for an example, Figure 4-8 compares the measured heat release vs. time curve up to 48 hours (which is the calorimeter duration time) and the curve estimated by DDM model of for systems Ref, GrP20 and GrP40. The input parameters for DDM model are summarized in Table 4-4. The DDM parameters corresponding were identified by best fitting the experimental heat-time curves by DDM model during the first 48 hours (Figure 4-8a). This simplified model approach was applied by previous researchers [263] and allowed estimating the heat releases at a later time (e.g., up to 28 days in Figure 4-8d).

Table 4-4. Parameters of the DDM for developed mixtures.

Parameter	Units	Ref	GrP20	GrP40	GP20	GP40	LP20	LP40
H_{T1}	kJ/m³	215,000	2250,000	195,000	220,000	185,000	240,000	181,000
τ_1	hours	21,00	21,00	24,50	21,00	25,50	21,00	26,85
β_1	-	4,25	3,75	4,30	3,95	5,12	3,50	5,00
H_{T2}	kJ/m³	165,000	132,000	80,000	130,000	80,000	78,000	90,000
τ_2	hours	39,00	72,00	120,00	70,00	60,00	110,00	65,00
β_2	-	0,4	0,31	0,85	0,32	0,25	0,20	0,35
$H_T(t)$	kJ/m³	380,000	357,000	275,000	350,000	265,000	318,000	271,000

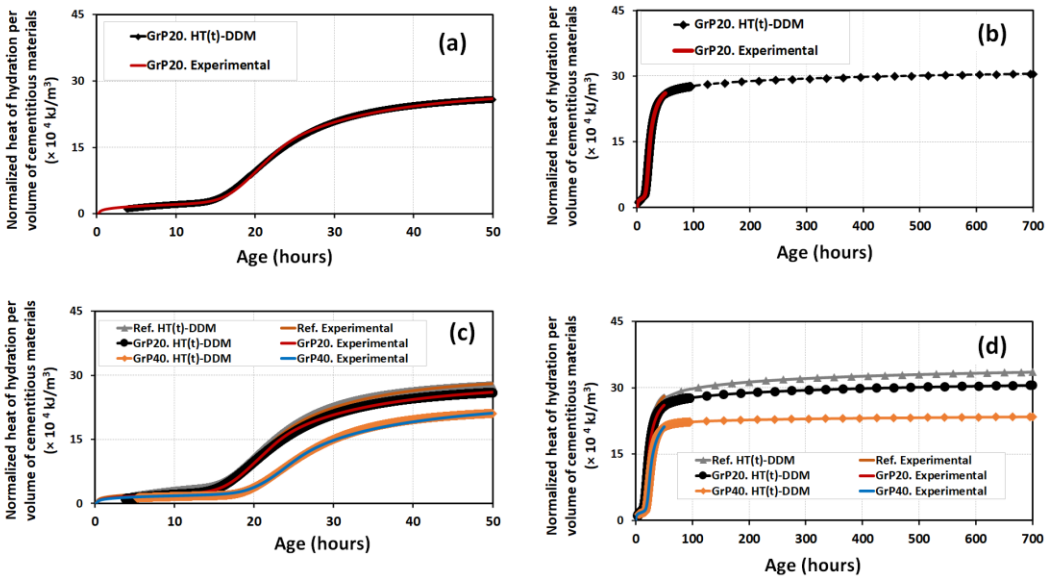

Figure 4-8. Normalized heat of hydration estimated from DDM model.

Another advantage of the simplified DDM model is that we can estimate the hydration degree $\alpha(t)$ [263]. The theoretical total potential heat of hydration and the estimated heat releases by DDM are then used to calculate the degree of hydration $\alpha(t)$ at any time for all UHPC mixtures as shown in Figure 4-9. The estimated $\alpha(t)$ of systems with mineral fillers were higher than that of the reference at all ages due to higher *w/b* in the mixture. This phenomenon is more pronounced in the mixtures with higher mineral filler replacement content. At 28 days (in Figure 4-10a), for example, $\alpha(t)$ value for

mixture Ref, GrP20 and GrP40 was 0.39, 0.44, and 0.45, respectively. The low water-to-cement ratio of the considered systems caused a maximum hydration degree that is lower than one, that is, the unreacted cement is present in the microstructure [277–279]. The estimated hydration degree is slightly lower than the theoretical values obtainable from Jensen model, which would be 0.44. 0.55, 0.71 [281]. The slight underestimation of the hydration degree can be explained by the choice of the heat release of cement and silica fume for full hydration are 452.3 kJ/kg [263,265] and 780 kJ/kg [263].

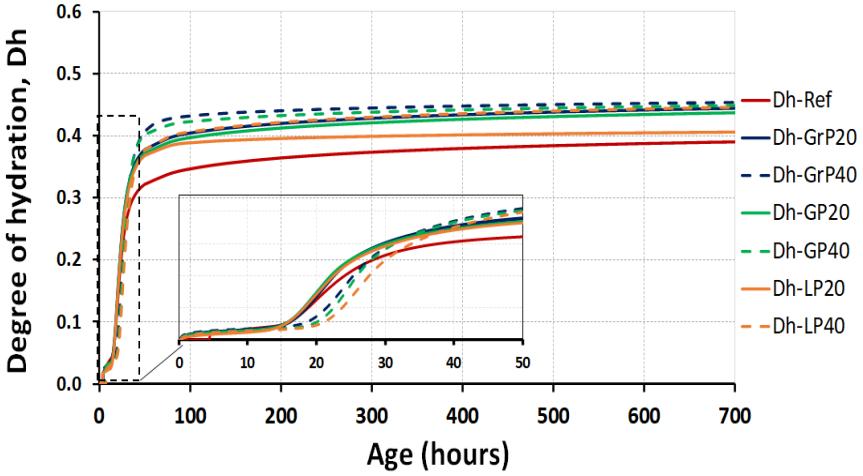

Figure 4-9. Degree of hydration of all mixtures up to 28 days.

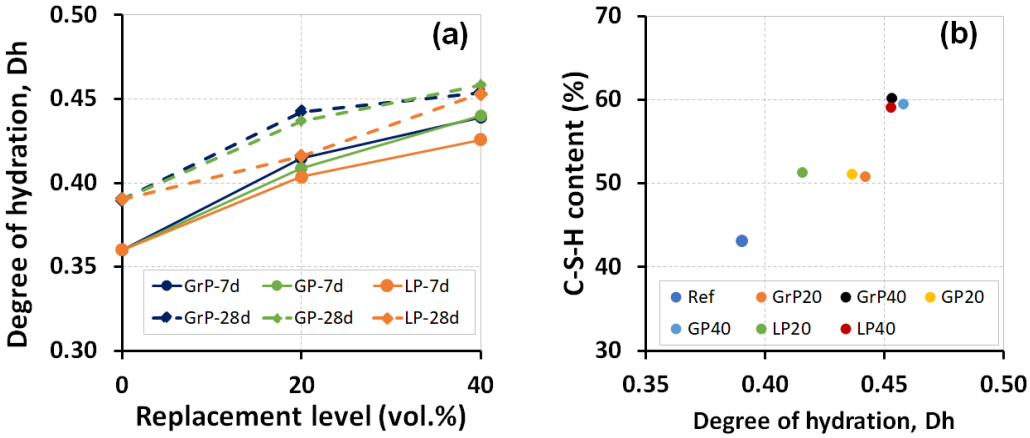

Figure 4-10. (a) Estimated maximum hydration degree at 7 days (Dh-7d) and 28 days (Dh-28d), and (b) Relationship between Dh-28d and C-S-H content normalized by mass of binder.

Figure 4-10a shows the relationship between hydration degree Dh at 28 days and the replacement level of mineral fillers. This confirms the previous discussion on the important filler effect on the cement hydration of the mineral fillers [76]. Figure 4-10b shows the relationship between C-S-H content calculated from TG curves in section 4.5.2.2 and the estimated degree of hydration at 28 days. It can

be found that the C-S-H content increase as Dh increases. This confirms the TGA methods and calorimeter are in agreement.

4.5.3 Autogenous shrinkage

Figure 4-11 presents the setting time and autogenous shrinkage of cement pastes with 20% and 40% of fillers. The shrinkage vs. time shows distinctive threefold kinetics [282]: (i) an important primary shrinkage which is due to precipitation-dissolution reactions at the very early age of cement hydration; (ii) a negligible swelling phase; (ii) an important secondary shrinkage due to capillary forces. Considering the shrinkage vs. time curves of Figure 4-11b, it is then possible to distinguish the primary shrinkage on the first day, which rapidly occurs from setting time to the inflection point, from the secondary shrinkage, which occurs gradually afterward. The rate of shrinkage in the first hours of the plastic phase is more important because of the hydration process (as detailed earlier in section 4.5.2.3).

Considering Figure 4-11 (a), the mixtures with GrP, GP and LP display evident setting retardation. The difference in setting time is likely due to the difference in the amount of superplasticizer [141] and silica fume [184,283] in the mixtures (see Table 4-2). The autogenous strain is zeroed at the final setting time for all mixtures. Considering Figure 4-11b, the shrinkage of systems was clearly affected by the type and amount of mineral filler. In general, the systems GrP20, GrP40 and LP20 exhibited a smaller autogenous shrinkage than the reference, which was reduced by 8%, 32% and 16%, respectively. This is due to the lower binder content by filler substitution, resulting in a higher *w/b* ratio – increasing internal relative humidity and less shrinkage. This is in agreement with a report by previous researchers [166,284,285].

On the other hand, the systems LP40, GP20 and GP40 increased the autogenous shrinkage of mixtures, which is 833, 821 and 1089 μm/m at 7 days, respectively. Notably, the autogenous shrinkage of UHPC-GP increased with the increase of GP content.

Figure 4-12 compares the effect of mineral fillers on the primary and secondary shrinkage of the systems. The primary shrinkage increases with the increase of the mineral filler with the only exception of granite powder, which is likely due to the fact that it is the most inert of the system (e.g., it does not affect the pore solution alkalinity as LP and GP). The higher autogenous shrinkage of systems GrP20, GrP40 and LP20 seem to mostly depend on the primary shrinkage. In particular, GP40 and LP40 exhibited a much greater primary shrinkage than that of the reference. On the contrary, the secondary

shrinkage reduced with the increase of the mineral filler. This hints that the mechanism of secondary creep is mainly due to the capillary surface tension in the tiny cement paste porosity.

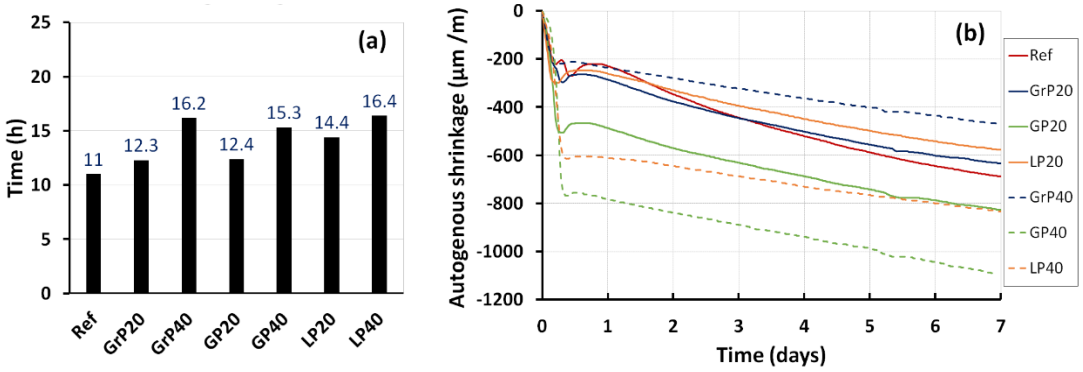

Figure 4-11. (a) Setting time and (b) Autogenous shrinkage of UHPC mixtures with mineral fillers.

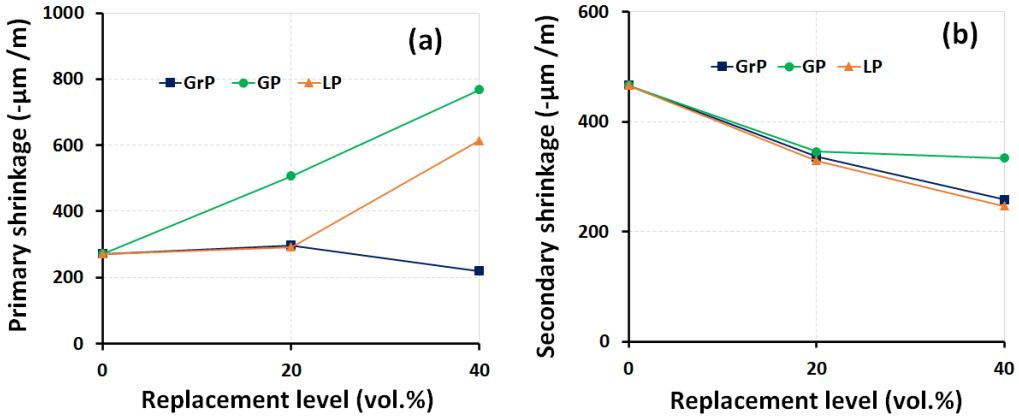

Figure 4-12. (a) Primary shrinkage and (b) secondary shrinkage of all tested mixtures.

Finally, it is possible to identify the relationship between autogenous shrinkage and the degree of hydration of the developed blended cement systems with mineral fillers. Figure 4-13 shows the relationship between autogenous shrinkage and degree of hydration. All the systems exhibit a similar S-shape relationship between hydration degree and autogenous shrinkage. Such a type of relationship is also helpful for modeling the risk of early-age cracking in UHPC structures [258]. In general, the systems GP20, GP40 and LP40 exhibited shrinkage-hydration degree curves with higher mean values. The systems with mineral fillers differ strongly in the primary shrinkage. This is strongly influenced by deformations occurring during the plastic phase (i.e., primary shrinkage), which may be related to the dissolution-precipitation reaction of C-S-H and ettringite. The effect of GP and LP on primary shrinkage may be explained by the filler effect [76] and by changing the alkalinity of the pore solution [179,286].

As for the secondary shrinkage, the reference system starts at an earlier hydration degree than all other systems with mineral fillers. The reason is that the *w/c* ratio of the reference system is the lowest value of 0.24, while the systems with mineral fillers have a *w/c* ratio ranging from 0.27 to 0.39, as summarized in Table 4-2.

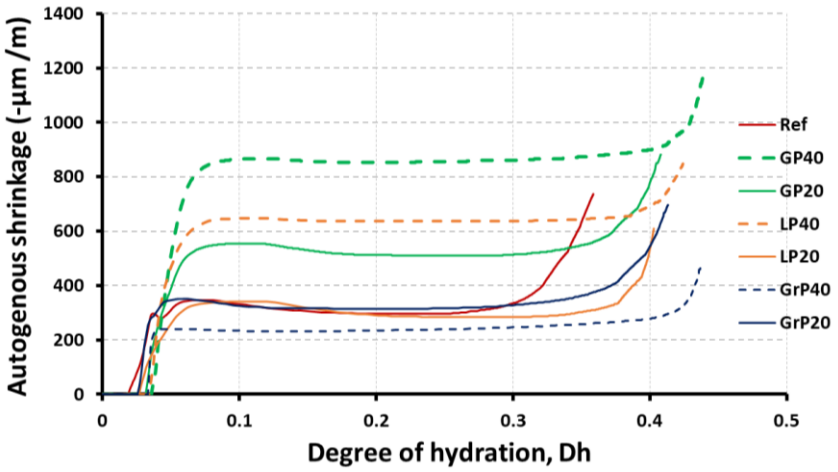

Figure 4-13. Relationship between autogenous shrinkage and hydration degree for the studied systems.

4.5.4 Mechanical properties

4.5.4.1. Compressive strength of cement pastes systems

Figure 4-14 presents the mean compressive strength of cement pastes at 7 and 28 days. As expected, the compressive strength increases over time due to the hydration process, which reduces the porosity.

The effect of the addition of mineral fillers on the compressive strength is similar for the different mineral fillers. At 7 days, the addition of 10% of mineral fillers does not reduce the compressive strength of the reference mix. For higher replacement level, the 7-day compressive strength reduces rather linearly with the mineral addition. The reduction of 7-day compressive strength is observed in all mixtures with 40% fillers, which is reduced by 19.4%, 14.1%, and 28.8% for the GrP40, GP40 and LP40, respectively. In general, for GrP and LP systems, the 7-day compressive strength reduces by about 8% for augmentation of 5% of mineral addition in the range from 10% to 40%. Notably, the 7-day compressive strength did not reduce for systems with GP up to 30%. This may be explained by a better filler effect of GP, providing more space for hydrates processing [9, 10], as having a closer the specific surface areas of GP with cement (as shown in Figure 4-1).

Interestingly, at 28 days, the systems with mineral fillers show equal or higher compressive strength than the reference system. It is possible to gain 15-20% of compressive strength by adding mineral fillers for all cement paste systems with w/f equal to 0.2. Notably, there seems to exist a different optimal replacement level for each mineral filler; that is, the peak of compressive strength is at 20%, 10% and 30% for GrP, GP and LP, respectively, with an increase by 16%, 19% and 9% compared to the reference mixture. In all cases, the binder (PC+SF) of the reference cement pastes with *w/c*=0.24 can be replaced by the considered mineral fillers up to 40% with out reduction in the compressive strength. Figure 4-15b, c and d show the SEM images of the microstructure of the systems at 1 year with 20% mineral fillers with respect to one of the references (Figure 4-15a). The replacement of the unreacted clinker by mineral fillers is visible.

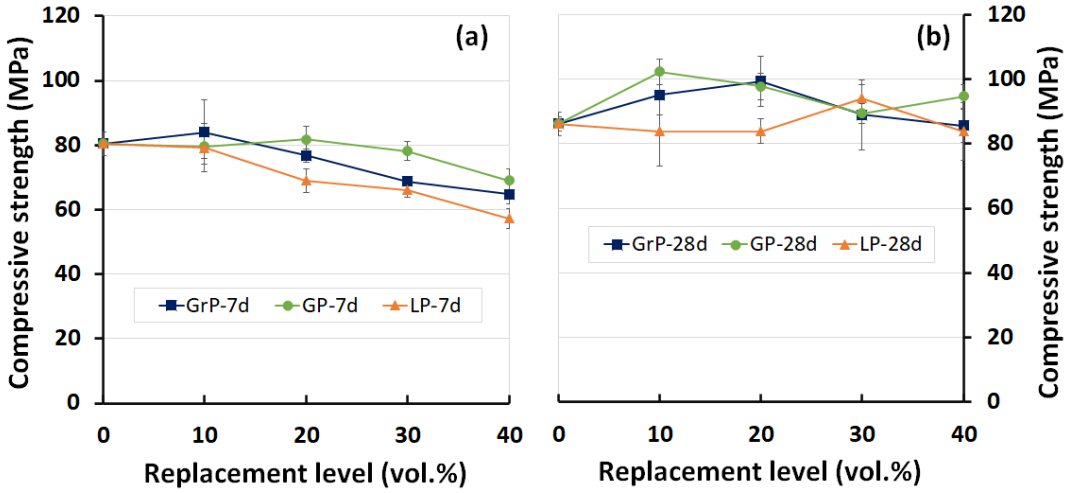

Figure 4-14. Compressive strength of cement pastes with different mineral additions at 7 days and 28 days of curing.

4.5.4.2. Micro-mechanical properties of cement paste systems

Figure 4-16a, and 15b show the micro-indentation results in terms of mean curves of load-penetration depth and mean curves of penetration depth-time for all systems, respectively. A higher penetration depth means a softer or more creep material. For instance, the LP40 has the highest penetration depth, resulting in the lowest microindentation properties.

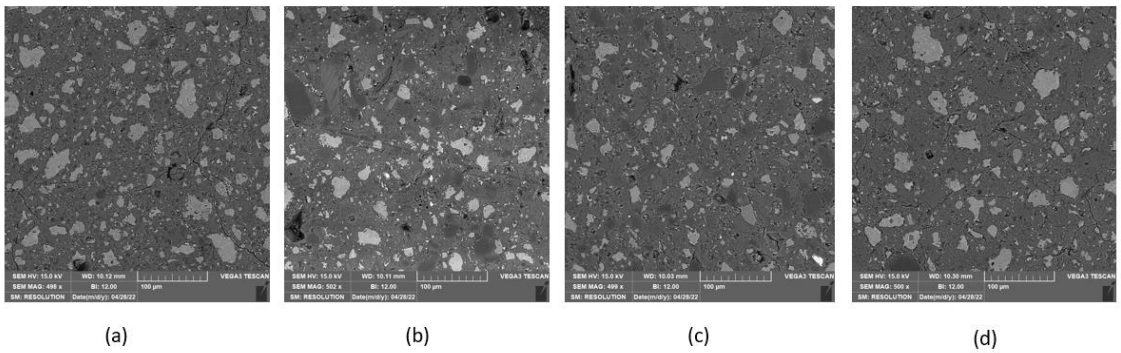

Figure 4-15. SEM images of the microstructure of the cement paste systems at 1 year: (a) Reference; (b) GP20; (c) GrP20; (d) LP20.

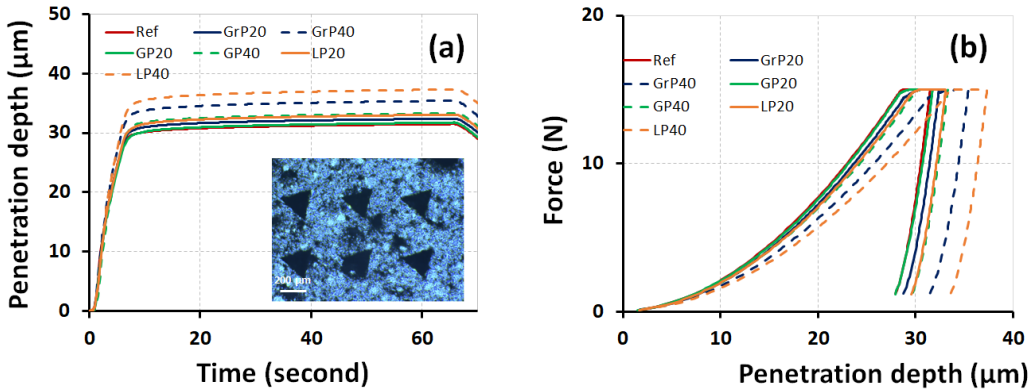

Figure 4-16. (a) The means h-t curves and (b) means F-h curves of all systems.

Figure 4-17 compares the mean microindentation properties H, M and C for all systems with an indication of the standard deviation. For all system, the values of H, M and C reduces with the increased volume of replacement of cement by the mineral fillers. This may be due to different reasons, such as (i) the *w/c* ratio of the cement paste increases with the increase of the filler content, which in turn increases the C-S-H gel porosity [287]; (ii) the filler particles are stiff, but they introduce a porous Interface Transition Zone [288,289]. For all those reasons, the mechanical property of the cement paste reduces with the increase of replacement of cement by a mineral filler system. Interestingly, the replacement of 20% cement with GrP and LP20 provided a strength closer to the reference. LP systems showed greater reduction as the coarser particle size may have affected the representation of the probed material probed by microindentation tests. The highest peak in hardness is the one with 20% of glass powder (GP) which is likely due to the pozzolanic reaction of glass after 1 year, which compensates for the lowest *w/c* of the cement paste [67].

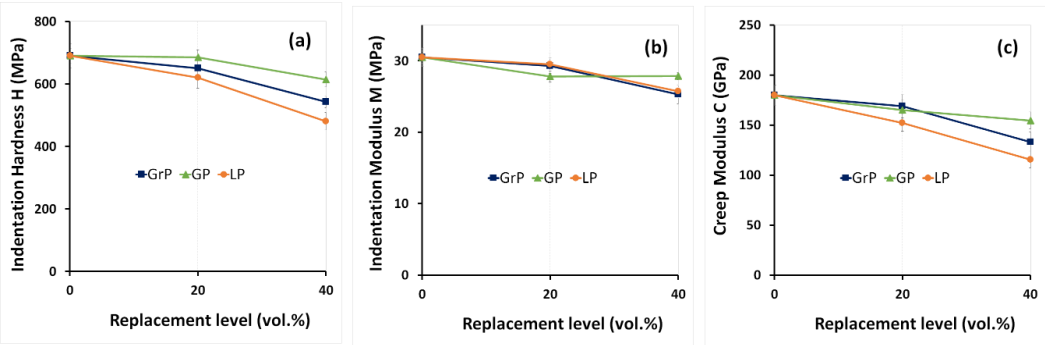

Figure 4-17. Microindentation properties of cement pastes at 1 year.

Table 4-5. Compressive strength of final UHPC incorporating fillers.

Replacement level (vol.%)	**Compressive strength, fc, (MPa)**							
	7 days				28 days			
	UHPC-Ref	UHPC-GrP	UHPC-GP	UHPC-LP	UHPC-Ref	UHPC-GrP	UHPC-GP	UHPC-LP
20	90±2.8	79±1.5	85±1.8	83±0.7	110±2.8	104±0.3	106±1.1	104±1.7
40	85±0.4	60±1.8	62±0.8	60±1.4	103±2.3	87±1.2	93±2.5	80±1.0

4.5.4.3. Compressive strength of UHPC systems

The compressive strength (fc) results at 7 days and 28 days of UHPC mixes with sand and fiber addition (Table 4-3) with substitution of 20% and 40% fillers are presented in Table 4-5. It is worth reminding that those UHPC systems have a relatively high volume of sand, which increases the ITZ zones and makes the need for cement paste with good bond property more important. As the main result, the mineral fillers slightly reduced the compressive strength of UHPCs. From Figure 4-18, the 7-day and 28-day compressive strength seem to linearly reduce with the replacement level of mineral fillers regardless of the type of mineral filler. As for the 28-day compressive strength, this reduction can be estimated by 6% and 23% for replacement levels of binder of 20% and 40% by mineral fillers, respectively. However, GP seems to exhibit a slightly improved compressive strength than GrP and LP due to the pozzolanic reaction of the glass particles, which increases the bond property [67]. This improvement in compressive strength of GP mixture is confirmed by other works [172,172]. The effect

of binder replacement by fillers on compressive strength at 7 days is greater, especially for a high volume of replacement. The importance of the ITZ zone in the UHPC systems is also confirmed by the recent work [253].

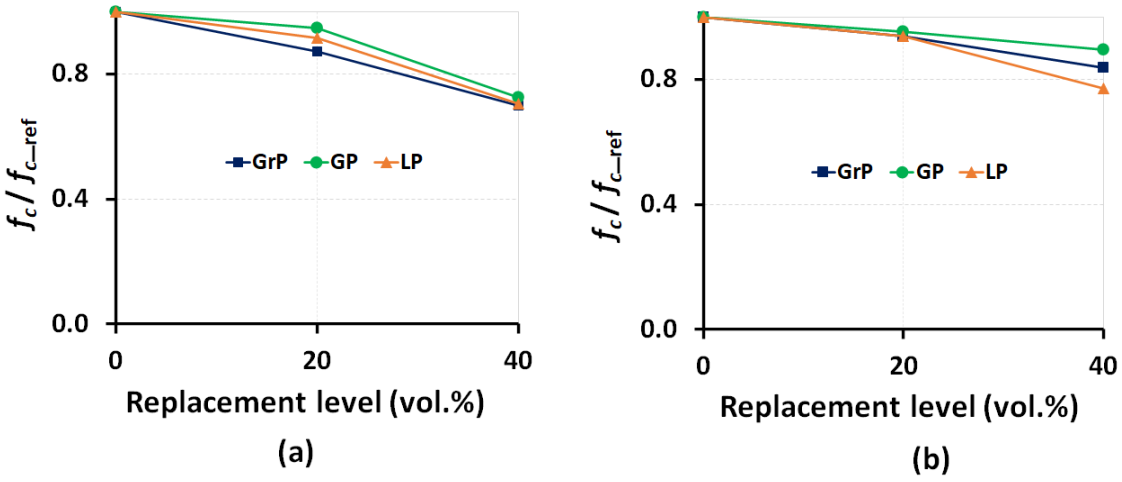

Figure 4-18. Relative the compressive strength of UHPC reference versus compressive strength of UHPC-fillers (a) 7 days and (b) 28 days.

4.5.4.4. Resistivity property of UHPC systems

To evaluate the durability of final UHPC mixtures (Table 4-3), uniaxial resistivity tests are carried out on the systems with a replacement level of 20%. Figure 4-19 shows the results in terms of the bulk electrical resistivity (BER) results of the UHPC systems with a 20% binder replacement level (without fiber) at 7 and 28 days. The threshold is employed to estimate the risk of chloride ion penetration that was established in AASHTO T 350 standard. The limits in terms of BER (High < 6, Moderate 6 ≤ 10.5, Low 10.5 ≤ 18.75, Very Low 18.75 ≤ 127, and Negligible > 127 Kohm·cm), were calculated through the procedure proposed by Morris et al. [290]. In Figure 4-19, BER increase over time due to the continuous hydration process. While the bulk resistivity of UHPC systems on all tested days is lower than that of the reference mixture, the chloride ion penetration in all designed UHPC mixtures is negligible. Those results are the first confirmation that the mineral fillers can partially replace binder in UHPC production without compromising the durability properties. This confirms the conclusions of Bentz on the effect of mineral fillers on the durability of concretes [291].

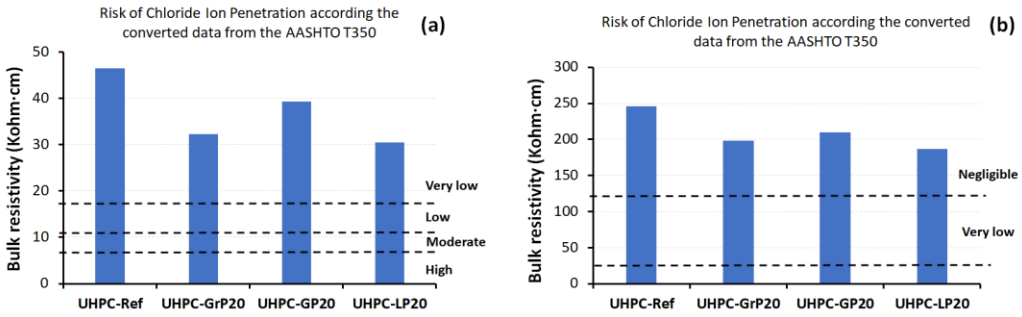

Figure 4-19. Uniaxial resistivity test results for UHPC with 20% fillers replacement at 7 days and 28 days.

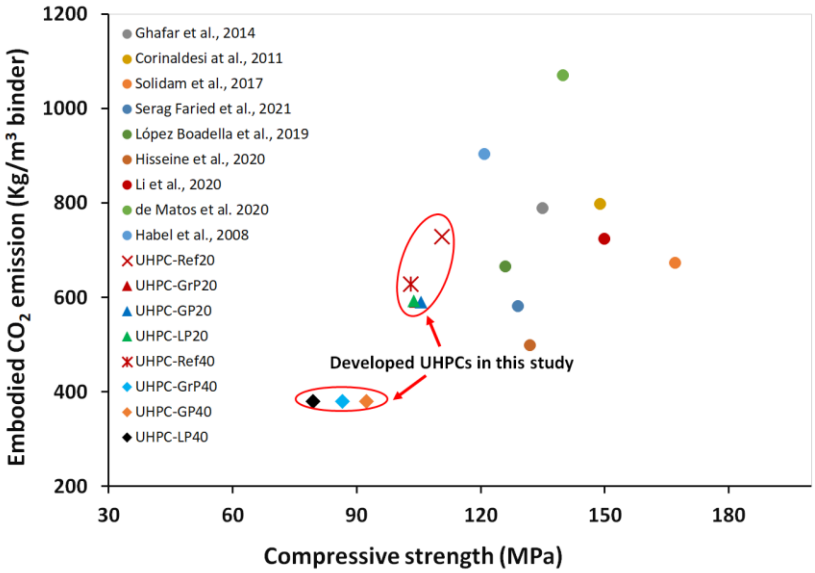

Figure 4-20. Comparison of UHPC mixes in terms of carbon emission and compressive strength.

4.5.5 Evaluation of carbon emission of studied UHPC mixtures

This section aims at provides a first-order estimation of the embodied CO_2 emission of the studied UHPC system in this research. The amount of CO_2 emission from cement and silica fume was assumed based on values reported in the open literature [292,293], as reported in 1 tone of cement and silica fume produce 0.83 and 0.0 tone of CO_2 emission, respectively. Figure 4-20 compares several UHPC mixtures published in open literature regarding the embodied carbon and 28-day compressive strength [172,178,180,294–299]. Although the UHPC mixes with higher compressive strength seem to exhibit more carbon emission, no clear trend between compressive strength and embodied carbon can be established. Indeed, the high compressive strength is not simply associated with a high binder content, but it is also related to packing density and quality of materials. For instance, compared to the Canadian UHPC developed by Habel et al. [299], the 120 MPa-compressive strength provide up to 900 Kg/m^3 of

CO_2 emission, while the developed UHPC with 20% filler in this research has 111 MPa and 729 kg/m^3 of CO_2 emission.

4.6 Conclusion

The present results provide a comprehensive study on the feasibility of replacing unreacted cements in UHPC mixes by comparing mineral fillers which are recycled wastes from local stone industry (granite powder GrP and limestone powder LP) or post-consumer waste (glass powder GP). In particular, the effect of replacing the binder up to 40% with the mineral fillers has been carried out at 2 scales: (i) cement pastes at a low water-to-fine (*w/f*) ratio of 0.2; (ii) at the UHPC scale, the previous cement pastes systems with the addition of sand and steel fibers. Based on the presented results, the following conclusions can be drawn:

- As for the fresh concrete property, the cement pastes systems with low *w/f* ratio and replacement levels of binder by mineral filers up to 40% exhibited improved workability and packing density.

- As for the hydration degree estimated by simple modeling of the calorimetry analysis, the cement pastes systems with mineral fillers increased the hydration degree due to the filler effect. The hydration degree at 28 days for mixture Ref, GrP20 and GrP40 was estimated to 0.39, 0.44, and 0.45, respectively. The replacement of binder of up to 40% with fillers delays hydration kinetics by 2-3 hours which may be favorable for casting at hot temperature. Among the considered mineral filler, GP provides a slightly higher hydration degree due to the pozzolanic activity.

- As for the TGA results, the cement pastes systems with mineral fillers increased the amount of CH and C-S-H produced by the binder due to a filler effect. Again, GP showed a slightly greater filler effect on the C-S-H content due to possible additional pozzolanic reaction.

- As for the autogenous shrinkage of cement paste systems, there was a strong dependency on the type of fillers and replacement levels. Notably, it was found that GrP20, GrP40, and LP20 exhibit a smaller autogenous shrinkage than the reference, which can reduce the risk of early age microcracking, which is particularly important for durability concerns and for architectural finishing quality.

- As for the compressive strength, the mineral fillers increased the 7-day and 28-day compressive strength. The optimal replacement level of each mineral filler was 20%, 10% and 30% for GrP, GP and LP, respectively, which increased by 16%, 19% and 9% compared to the reference mixture. That is, the mineral fillers increased the cement paste strength, in spite of the fact that the gel porosity increases as the *w/c* ratio increases with the replacement level of mineral fillers.

- As for the UHPC systems, the fine sands were added by 48-60% by solid volume. The replacement of binder with 40% mineral filler reduced the compressive strength by about 23%. In contrast, replacing up to 20% of binder with mineral fillers allows producing UHPC with a compressive strength close to that of the reference. Due to pozzolanic activity, GP showed a slightly greater compressive strength than other mineral fillers.

- As for the resistivity tests, all UHPCs mixtures with mineral filler exhibited resistivity which is very low at 7 days and negligible at 28 days. That confirms that the capillary porosity is very limited for UHPC with replacement of binder by mineral fillers up to 40%.

- Finally, the replacement of binder with available mineral fillers can significantly reduce the carbon footprint. As reported in previous studies, mineral fillers allow for reducing the embodied carbon below 500 kg/m^3 while keeping a very high compressive strength.

Further work should further optimize the UHPC mix design by increasing the particle packing density, e.g., by adding an intermediary powder (e.g., quartz) or by reducing the sand volumes. It could also be interesting to study finer-particle fillers for producing UHPC. Future studies shall investigate the flexural, tensile and durability properties which are needed in structural applications.

Chapter 5. Developing Sustainable Ultra-High-Performance Concrete with Aluminum Production Wastes

5.1 Résumé

Le béton fibré à ultra-hautes performances (BFUP) est une voie prometteuse pour favoriser les infrastructures civiles durables et résilientes. Comme ils sont souvent limités par leur coût élevé et la disponibilité limitée des matières premières locales, cette étude vise à concevoir une nouvelle conception de mélange de BFUP à teneur en ciment relativement faible en recyclant les brasques usées traités provenant de la production d'aluminium primaire, appelés LCLL-ash.

Tout d'abord, les mélanges de BFUP avec différentes teneurs en ciment remplacées par des poudres de LCLL-ash ont été développés au moyen de la méthode de compaction des particules. Ensuite, une caractérisation multi technique a été réalisée, telle que : les propriétés à l'état frais, l'analyse chimique par SEM et XRD, la calorimétrie, le retrait endogène, la résistance à la compression et la caractérisation par microindentation. Les résultats montrent que l'ajout de LCLL-ash retarde la cinétique d'hydratation, tout en réduisant légèrement la maniabilité et la résistance en compression. D'autre part, le remplacement de 12% du ciment par de la LCLL-ash réduit significativement le retrait endogène à 7 jours. Enfin, l'énergie et le carbone contenus dans le BFUP à base de LCLL-ash ont été évalués, ce qui confirme que cette méthode est prometteuse pour la production de BFUP durables à faible retrait.

Mots-clés: Retrait autogène, brasques usées traités, cinétique d'hydratation, microindentation, microstructure, fillers minérales, compaction particules, construction durable, BFUP.

5.2 Abstract

Ultra-high performance concretes (UHPC) are a promising avenue to foster sustainable and resilient civil infrastructures. As often limited by the high cost and limited availability of local raw materials, this study aims at engineering a novel UHPC mix design by recycling treated spent pot lining from primary Aluminum production, called LCLL-ash.

First, the UHPC mixtures with different cement content replaced by LCLL-ash powders were developed by means of the packing particle method. Then, a multi-technique characterization was carried out,

such as fresh concrete properties, SEM and XRD chemical analysis, calorimetry, autogenous shrinkage, compressive strength and microindentation characterization. Results show that the addition of LCLL-ash delays the hydration kinetics while slightly reducing the workability and the compressive strength. On the other hand, replacing 12% of cement with LCLL-ash significantly reduced the autogenous shrinkage at 7 days. Finally, the embodied energy and carbon of the developed LCLL-UHPC was assessed, confirming the promising avenue for producing sustainable UHPC with low shrinkage.

Keywords: Autogenous shrinkage; Aluminum production waste, Hydration kinetics; Microindentation; Microstructure; Mineral Fillers; Packing density; Sustainable construction; Ultra-high performance Concrete (UHPC).

5.3 Introduction

Ultra-High Performance Concrete (UHPC) is a relatively new class of concrete composites that provides a technological breakthrough for sustainable construction as it allows reducing the volume of the structural elements while significantly enhancing the durability [300,301]. Thus, UHPC outstanding mechanical properties allow reducing the use of construction materials. Similarly, UHPC superior durability enables extending the service life of concrete structures with an important reduction of maintenance costs, which is key in countries with severe environmental conditions [122,302]. In the last decades, several UHPC mixtures have been developed with an ultra-high compressive strength (usually greater than 120 MPa), a remarkable tensile strength (about 7-15 MPa) and toughness (about 1000 J/m^2) [302,303]. Typically, UHPC is composed of an optimized combination of mineral powders with high packing density, a very low water-to-cement (*w/c*) ratio, and high content of superplasticizers to ensure workability [31,122,304]. For structural applications, micro steel fibers are added at a volume content between 2 and 4% to provide tension hardening properties to enhance strain hardening and multiple cracking in tension, which in turns assures crack opening and durability in service [16,117,305]. As a result of the compacted matrix, UHPC exhibits a very low capillary porosity which confers impermeability to deteriorating agents, such as chlorides and sulfates [270,305]. Furthermore, UHPC mixture employs a relatively high volume of cement paste (~50%) with a fine aggregate of maximum diameter limited to a few millimeters. Thus, several commercial UHPC employ a significantly high volume of cement content, which comes with a significant embodied carbon level and environmental

impacts [306,307]. UHPC high cement content not only jeopardizes eco-efficiency, but also drives substantial autogenous shrinkage, a major handicap for UHPC.

Owing to its low-water content, the microstructure of UHPC is rich in unreacted clinker as the very low *w/c* ratio of limits the maximum hydration to about 50% [21–23]. Thus, partially replacing the unreacted clinker by supplementary cementitious materials (SCMs) or mineral fillers with a size similar to the one of the cement offers a means to reduce the cost and the carbon imprint of UHPC [87,308,309]. Note also that the use of a high amount of silica fume, which is usually in between 10 and 30% of cement mass in UHPC mixtures for enhancing ITZ zones of sand particles [310–312], may reduce the availability of Portlandite and then limit the pozzolanic reactivity of supplementary cementitious materials (SCMs). Thus, replacing the percentage of unreacted cement by SCMs or mineral fillers allows reducing embodied carbon of UHPC mainly due to the cement content.

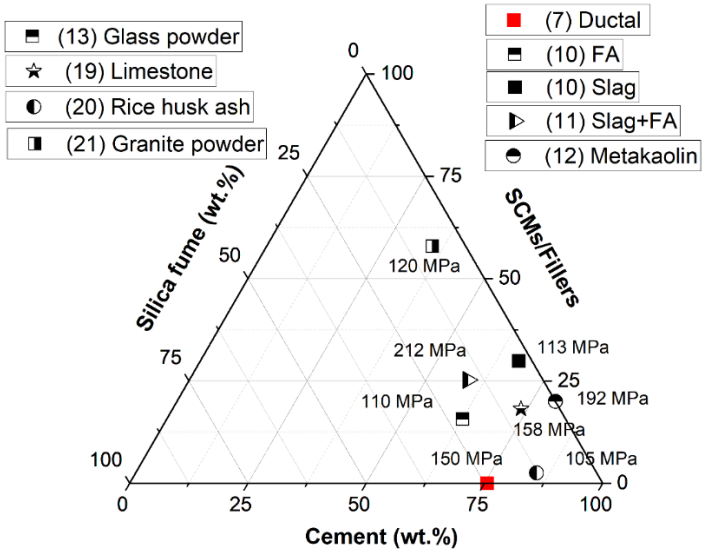

Figure 5-1. Ternary diagram of some ecological UHPC.

Following this direction, ecological UHPC mixtures have been recently developed worldwide by replacing cement with locally available SCMs or mineral fillers, such as limestone [32,178,313], rice hush [180], fly ash [313], ground granulated blast-furnace slag (GGBFS) [313,314], metakaolin [315], glass powder [185] and waste granite powder [293]. Table 5-1 compares the composition of fine powders (herein defined as the powders with a diameter less than 125 μm as proposed in [309]) of recently developed ecological UHPC mixtures within a ternary diagram with the percentage in masse

of the following raw materials: (i) cement; (ii) silica fume and (iii) SCMs or mineral fillers. As for a reference, UHPC is commercially available under the name Ductal® [304]. The average compressive strength is also indicated. The tendency of ecological UHPC to reduce cement and silica fume is evident. Several ecological UHPC replace more than 20wt.% of cement by SCM/Fillers while keeping a minimum amount of silica fume. Bouchard et al. [293] succeeded in replacing nearly 60% of cement by mineral fillers, such as limestone and granite powder. Moreover, since the initial construction cost is a major limiting factor for applications, the development of UHPC mixtures with locally available sources of SCM and mineral fillers is strongly worthwhile [316,317]. More in general, the successful implementation of eco-UHPC within a circular economy approach depends on the environmental cost of transport and possible pre-treatment [318].

The worldwide production of Aluminium is more than 60 million tons per year with China as the world's largest producer with 37 million tonnes, followed by India, Russia, and Canada [319,319]. The refinery processes used to produce aluminum generate about 2–2.5 tons of solid waste for every 1 ton of aluminum produced. This includes a small amount of waste rock, waste “red mud” and a small amount of other scrap and solid wastes. A significant industrial and hazardous waste of the aluminum industry is the spent pot lining (SPL) [29,320]. SPL is the most significant solid waste from smelting and the second-largest volume from the aluminum industry after bauxite residue. For instance, the company Rio Tinto in Canada generates approximately 35 kt of SPL per year, each ton of aluminum generating about 22 kg of SPL [29]. SPL can be classified into two types; the 1st cut is rich in carbonaceous materials, and the 2nd cut is rich in aluminum and silicon oxides. The former and the latter come from the cathode and refractory of the electrolytic cells, respectively. Pioneering research investigated the use of glass frit (GF) obtained by a pyro metallurgic treatment of SPL as alternative cementitious materials for normal concrete [201,321]. GF was used as a binder in concrete, and the materials were studied in terms of alkaline activation. The results demonstrated that concrete with cement partially replaced by GF exhibited enhanced durability against freezing-thawing, reduced chloride ion permeability, and low alkali-silica reaction related to control concrete [201]. A few decades ago, a hydrometallurgical process treatment called Low Caustic Leaching & Liming process (LCL&L) was developed to extract the toxic elements (i.e., cyanide and fluoride) and transform SPL into inert by-products. The refractory bricks (2nd cut), which are treated separately from the carbon part (1st cut), are herein called LCLL-ash [211]. For instance, about 20 kt of LCLL-ash per year can be produced at the SPL treatment plant in Jonquiere (Quebec) and can be reused in concrete production [29,322].

LCLL-ash is a fine powder with a mean granular size of about 20 μm, mainly composed of silica and alumina with a minor fraction of calcium, sodium, and iron. In a recent study, Brial et al. [211] evaluated the reactivity of LCLL-ash powder by the Rilem R^3 test. The results showed that the reactivity of LCLL-ash has negligible pozzolanic reactivity. However, the reactivity of LCLL-ash was improved by calcination, showing reactive properties closer to calcined clay [211]. Moreover, as a major drawback, hydro reactivity of LCLL-ash in the R^3 test condition was observed. The phase containing alumina from LCLL-ash can generate gases causing swelling of the cement paste [211]. To the authors' knowledge, no work yet has attempted to employ raw LCLL-ash powder as a filler in high or ultra-high-performance concretes.

One of the UHPC properties that strongly depend on replacing cement by SCMs or mineral fillers is the autogenous shrinkage. The latter is important in several UHPC applications where deformation constraints may cause early age microcracks that compromise the sought durability. Indeed, UHPC exhibits significant autogenous shrinkage at early age driven by the self-desiccation of capillary pores due to the cement hydration [323–325]. When the shrinkage deformation is restrained, internal tensile stress can build up with the risk of early-age cracking [258,326–328]. A recent benchmark on different commercial types of UHPCs showed that autogenous shrinkage strongly depends on several properties, including cement content, porosity systems, type of SCMs, etc. [302]. Therefore, replacing cement with mineral fillers, which can stiff UHPC mixtures at early, may be efficient means of reducing the risk of early-age micro-cracking UHPC [323,329]. Such microcracks may also be unacceptable for high-quality architectural applications [330].

This work aims at developing UHPC mixtures with LCLL-ash powder by taking advantage of their filler effect to enhance the competitiveness of UHPC in terms of cost and carbon imprint. Firstly, the CIPM model is applied to optimize the packing density of the mixture. Afterward, the effect of partially replacing the cement in UHPC mixtures with LCLL-ash was studied in terms of fresh properties, hydration kinetic, autogenous shrinkage, mechanical properties, and microstructure morphology. Moreover, microindentation investigation was employed to finely study the effect of the LCLL-Ash on the mechanical properties of the cement paste of the developed UHPC in which LCLL particles are embedded. Finally, the estimated embodied energy and carbon dioxide as well as the cost of the developed LCLL-UHPC confirmed the promising research direction.

Table 5-1.Chemical compositions and physical properties of granular materials used (n.a.=not available).

Materials	Cement	Silica fume	LCLL-ash	Limestone powder	Quartz powder
Chemical composition	(wt.%)	(wt.%)	(wt.%)	(wt.%)	(wt.%)
CaO,%	61.52	0.74	3.04	98.20	0.30
SiO_2,%	19.17	96.35	37.28	0.62	98.90
Al_2O_3,%	4.60	0.09	36.29	0.08	0.20
Fe_2O_3,%	3.61	0.41	7.36	0.32	0.30
MgO,%	2.40	0.57	0.38	0.49	0.02
SO_3,%	3.98	0.82	0.06	0.26	-
K_2O,%	1.06	-	0.77	-	-
Na_2O_{eq},%	0.25	-	8.23	-	-
LOI,%	2.63	3.50	5.72	42.4	-
Physical properties					
Specific gravity (g/cm^3)	3.09	2.26	2.72	2.65	2.65
Blaine surface area (m^2/kg)	365	n.a.	n.a.	n.a.	n.a.
BET (m^2/kg)	n.a.	2.62×10^4	4.60	n.a.	n.a.
Particle diameter, d_{10} (μm)	2.9	0.07	1.65	0.5	14.7
Mean particle diameter, d_{50} (μm)	13	0.16	22	1.7	105
Particle diameter, d_{90} (μm)	32	0.5	110	4.6	330

5.4 Materials and methods

5.4.1 Raw material properties

In this work, the following raw materials were employed: (i) a high early (HE) strength cement Type III (according to ASTM C150) with d_{50} of 13 μm; (ii) undensified silica fume with particle size of 0.1–1 μm provided by Silicon Quebec; (iii) quartz powder from industrial waste from crushing quartz into the sand in Quebec quarry, (iv) limestone filler under commercial name UF from Omnya, (v) and river sand with d_{50}= 485 μm as fine aggregate. LCLL-ash was provided by Rio Tinto Quebec and used as a cement substitution without any further treatment. Table 5-1 shows the chemical composition and physical properties of cement, silica fume, and LCLL-ash. The particle size distribution of the UHPC components is given in Figure 5-2. LCLL-ash has a dark-grey color, and the digital images and scanning electron

microscopic (SEM) images of LCLL-ash are presented in Figure 5-3. The X-ray diffraction analysis results of LCLL-ash is illustrated in Figure 5-4.

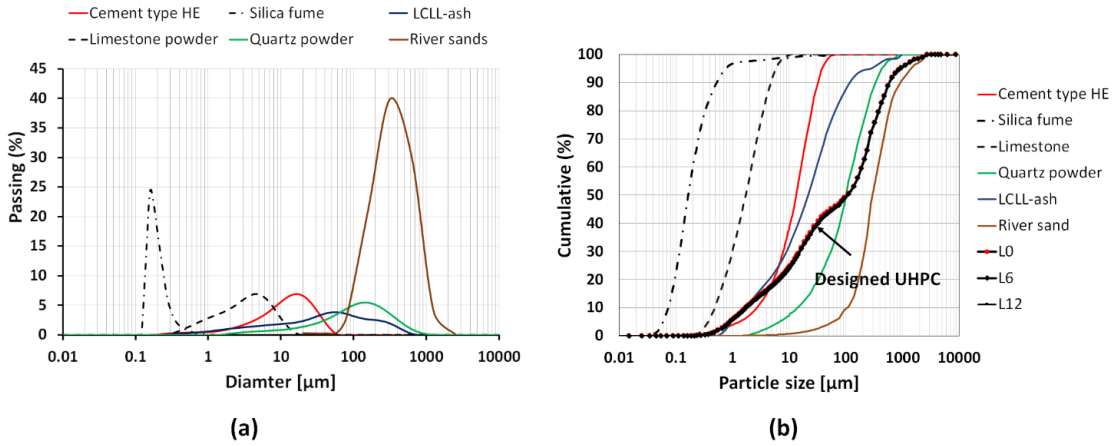

Figure 5-2. (a) Grading of the used materials and (b) cumulative particle size distribution.

Figure 5-3. (a) Digital image and (b) SEM image of LCLL-ash.

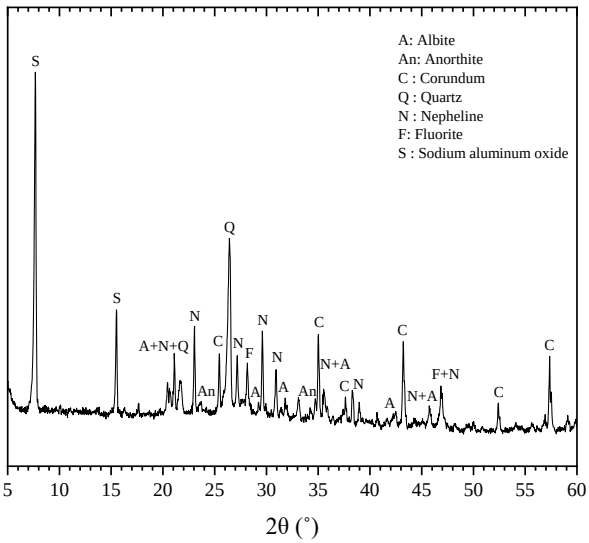

Figure 5-4. XRD pattern of LCLL-ash.

5.4.2 Mixture design

Key concepts for designing cementitious material are packing density and workability. In recent years, numerous models have been developed for concrete mixture proportioning by using the particle packing model. Among them, De Larrard [160] introduced the Compressible Packing Model (CPM) to optimize the packing density of cementitious material. Later, Fennis [31] developed the compaction-interaction packing model (CIPM), which includes interaction due to the surface forces like van der Waals forces for very fine particles (≤ 125 μm), which are necessary for UHPC. For instance, Hajiesmaeili et al. [100] applied the CIPM model to design Ultra High-Performance Fiber Reinforced Concrete with 50% clinker replacement by two limestone grades.

In this study, we employed the CIPM method. Firstly, the packing density of each employed powder with a maximum particle size smaller than 125 μm is determined in wet conditions by the mixing energy method [164]. To consider the interaction with cement particles and superplasticizer, the wet packing density of the powder mixed at different percentages of cement and superplasticizer is measured [31,331]. The wet packing density of the powder is then estimated from the asymptotic values for cement content tending to zero. The measurement of the wet packing density is divided into different steps (as shown in Figure 5-5), as followings: (i) A volume of 500 ml of dry powder is mixed for 60 s at low speed using a planetary mixer Hobart N-50 equipped with a flat beater; (ii) After 60 s, about 60-80% amount of premixed liquid (water and superplasticizer) is added to the mixer in 12-15 s, and mixing is continued up to 120 s; (iii) After 120 s, the mixer is stopped to hand-mixing with a soft silicone spatula

in order to prevent any agglomeration and to ensure homogeneity; (iv) The mixer is restarted at 180 s for 2 min; (v) The premixed solution is added gradually at a rate of 5 ml every 15 s using a self-dosing pipette. The liquid is added until the mixture loses all consistency, and the electrical consumption drops. It should be noted that a preliminary test was necessary to estimate the dosage of superplasticizer required in the liquid solution. The dosage was selected as the content of superplasticizer added during the test accounts for 3% by mass of cement when the maximum electrical consumption is reached, at the end of stage V. In practice, when the contents of superplasticizer at maximum peak consumption were recalculated at the end of the test, the values usually lied between 2.9 and 3.1%. The packing density α_t of each material can then be calculated as follows: $\alpha_t = V_P / (V_P + V_L)$ where V_P is the volume of powder, V_L is the total added liquid solution until reaching the maximum power consumption. As for the granular materials with a larger size than 125 μm (e.g., fine aggregates), the granular packing density is simply determined by the dry method (compact method). The test procedure as follows: filling a weight of materials w (known density) into a rigid steel container of known volume V_C. The packing density α_{exp} can calculate as follows: $\alpha_{exp} = V_{solid} / V_C$.

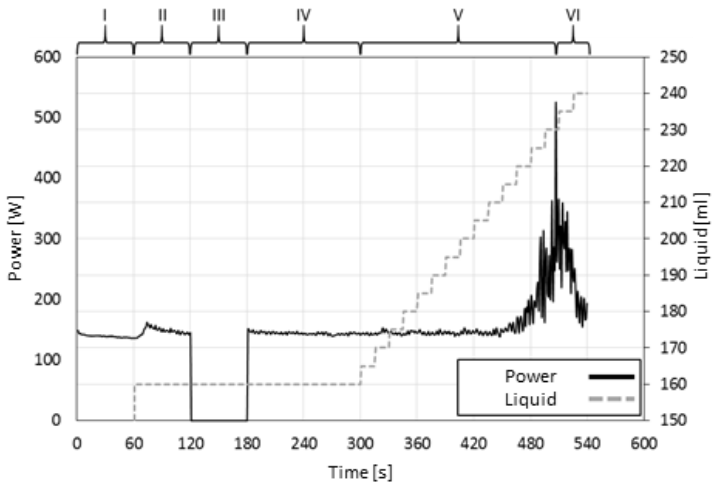

Figure 5-5. The power consumption during the addition of the solution.

Table 5-2. Packing density of individual material by experimental test and by CIPM.

Materials	$\alpha_{\exp}$	α_{CIPM}	Compaction index K
Cement type HE	0.613	0.612	10
Silica fume	0.480	0.478	6.7
Limestone powders	0.611	0.611	10
Quartz powders	0.568	0.63	10
LCLL-ash	0.573	0.547	10
River sand	0.599	0.614	4.1
(W_a =W_b =1, L_a = C_a =1.5, L_b = C_b = 0.2, suggested by Fennis [31])			

In order to consider the particle size distribution of the powders, the CIPM requires a virtual packing density β_i for each size class i for a certain compaction index K_i as model inputs. Therefore, a given material is divided into several size classes according to the known particle size distribution. It is suggested to divide materials into size classes with size ratios ranging from 0.5 to 0.9. Then, the virtual packing density β_i is calculated from the α_{exp} for a certain compaction index K_i. It is assumed that β_i of each material is constant for each sub-division size class. Afterward β_i is used as one input on the CIPM to optimize the packing density Φ of UHPC mixtures. For more detail, the authors recommended referring to the report of Fennis [31]. Table 5-2 shows the results of measured packing density and reversely calculated packing density from CIPM corresponding to compaction index K for each material used in this study.

5.4.3 Mixture proportioning and casting

The optimized proportion of UHPC mixtures is detailed in Table 5-3. The *w/b* ratio (binder defined as cement + silica fume) was fixed at 0.23. The substitution of cement by LCLL-ash was 6% and 12% by weight. Superplasticizer with a specific gravity of 1.08 and solid content of 29% was used in all mixtures. In addition, the micro-steel fibers (length of 13 mm and diameter of 0.2 mm) were added by 2% by total volume of mixture.

Table 5-3. Recipes of UHPC mixture designs and main characteristics.

Mixture composition (kg/m^3)	UHPC mixture		
	L0	L6	L12
Cement type HE	626	588	550
Silica fume	178	176	175
Limestone powder	85	84	84
LCLL-ash	0	43	85
Quartz powder	208	207	205
River sand	1081	1072	1064
Water	184	178	170
Superplasticizer	34	34	34
Water-to-cement ratio (*w/c*)	0.29	0.31	0.30
Water-to-binder ratio (*w/b*)	0.23	0.23	0.23
Water-to-fines ratio (*w/f*)	0.17	0.17	0.17
UltraFine-to-cement ratio (*uf/c*)	0.28	0.30	0.32
Cement paste volume	0.60	0.60	0.61
Superplasticizer-to-fine ratio (*sp/f*)	0.03	0.03	0.03
Measured packing	0.745	0.752	0.759
CIPM packing Φ	0.797	0.793	0.789

As for the mixing procedure, the dried cementitious materials (i.e., cement, silica fume, LCLL-ash, limestone powder, quartz powder, and fine aggregates) were mixed for 3 min at a slow speed using a planetary mixer. Then, about 80% of pre-prepared suspension (water mixing with superplasticizer) was added to the ingredients for 5 min, followed by the 20% remaining for 3 min at low speed. Subsequently, the steel fibers were added during 3 min of final mixing at high speed. The mixing was performed at room temperature (23°C).

5.4.4 Tests and methods

5.4.4.1 Fresh UHPC characterization

The flow characteristic of all mixtures was measured using a flow table test based on ASTM C1437. The dynamic flow of fresh UHPC was obtained after dropping the flow table 25 times in around 25 s. Two perpendicular spread diameters were determined for each mix.

The density of fresh concrete was measured as follows ASTM C138M. A cylindrical measurement tool (with a known volume) is necessary for this test. The fresh mixture was poured into the cylindrical tool in three layers. Each layer was compacted by vibration using the vibration table. The wet density of concrete was calculated by the weight of the concrete to the volume of the cylindrical measure. Then, the air content was measured based on ASTM C231.

5.4.4.2 Compressive strength of hardened concrete

UHPC mixtures were poured into 50 mm cube molds for the compressive strength test according to ASTM C39/C39 M 2010. After casting, the specimens were covered with a plastic sheet and demolded after 24h of casting. The two different curing regimes were employed in this study such as (i) a standard treatment (21 ± 2°C, Relative Humidity (RH) > 95%); (ii) a hot-water treatment (60°C, RH > 95%) for 48 hours applied at 1 day of age. The compressive strength of UHPC mixtures was determined as the average of three measurements at 7, 28, and 90 days. The test was carried out at a rate of 0.6 MPa/s. It is worth noticing that the means compressive strength converting factor between cube and cylinder specimen of UHPC with 1-2% fiber is about 0.95-0.99 as reported by [268,269]. Moreover, the fiber orientation may be affected by the wall effect as the fiber length (12 mm) is only about 4 times smaller than the cube size.

5.4.4.3 Crystalline phase analysis by X-ray diffraction (XRD)

X-ray Diffraction (XRD) was employed to identify crystalline phases of the cement paste, excluding aggregates and fibers. At 7 and 28 days of normal curing, samples were crushed and ground using a mortar and a pestle. Then, the sample was immersed in 100 mL of isopropanol immediately after crushing for 15 min. Next, the crushed powders were dried for 10 min in a ventilated oven at 40 ± 5°C. XRD measurements of the dried powders were done at room temperature using a Philips X'pert APD

diffractometer at a tube voltage of 40 kV, a tube current of 40 mA, and a Cu K∝ radiation. The analyses were performed within an angle range of 5-70° 2 thetas and a step width of 0.02.

5.4.4.4 Microstructure observations by scanning electron microscope (SEM)

The scanning electron microscope (SEM) technique was performed to study the microstructure of UHPC mixtures. Specimen were cut into 3 mm thick discs, which were surface polished as described in detail in [332]. The fraction sections and polished sections were examined using the Tescan Vega3 device at an accelerating voltage of 15 kV and a working distance of 15 mm. The UHPC specimens were examined at 28 days of curing.

5.4.4.5 Hydration reaction analysis by the isothermal calorimeter

Isothermal calorimetry

An isothermal calorimeter I-Cal 2000 HPC was employed to study the effect of LCLL-ash on the hydration in the UHPC matrix. Directly after mixing, about 140g of fresh pastes (without fiber) were poured into a sealed glass, which was then placed into the isothermal calorimeter. The instrument is set to a temperature of 23°C, based on ASTM C1702-17. After 72 hours, the measurement was stopped, and then the obtained results were normalized to the weight of the cement.

Double Danish Model

While the isothermal calorimetry accurately predicts the heat evolution for up to a few days (72 hours in this study), the technique is less sensitive to measuring the heat release at later curing ages [262]. To get more insight into the long-term hydration, a simplified hydration model introduced by Hansen and Pedersen [264] that considers the heat of hydration of cement was considered [263]. In particular, we employed a version called Double Danish Model (DDM) extended by Hafiz *et al.* [263] to predict the heat release from the hydration of cement and the pozzolanic reaction of silica fume. As a first-order approach, this simplified extended DDM allows estimating the maximum hydration degree of studied UHPC mixtures at a greater time than the duration of the calorimeter test. Based on DDM [263], the development of cumulative heat of hydration can be estimated from cement (subscript 1) and silica fume (subscript 2) as follows*:*

$$H_T(t) = H_{T1}.e^{-(\frac{\tau_1}{t})^{\beta_1}} + H_{T2}.e^{-(\frac{\tau_2}{t})^{\beta_2}} \quad (5.1)$$

where $H_T(t)$ is the development of cumulative heat of hydration in kJ/m^3, H_{T1} and H_{T2} are the heat hydration of cement and silica fume at time τ_1 and τ_2 in hours, respectively, β_1 and β_2 are the hydration slope parameters of the cement and silica fume, and $H_{T\infty} = H_{T1} + H_{T2}$ is the asymptotic value of the cumulative heat of hydration of the mixtures.

5.4.4.6 Autogenous shrinkage test

The autogenous shrinkage of cement pastes without steel fiber was measured based on ASTM C1698-19 standards. The length and diameter of the corrugated tube were approximately 430 mm and 29 mm, respectively. Directly after mixing, the fresh cement pastes were poured into a corrugated tube within about 2 min while applying vibration to avoid the air bubbles inside the tube. The mold was sealed to prevent moisture loss, and the samples were placed in an environmental chamber at a constant RH and temperature (23°C; 55% RH). Then the sample was placed on a rigid frame equipped with a TRANS-TEK 350-000 displacement transducer. The length changes were recorded every 15 min, and the measurements lasted up to 7 days from water addition at room temperature.

5.4.4.7 Microindentation test

Microindentation has become a powerful tool for investigating the viscoelastic property of cement pastes [149,227,333]. Before testing, 50 points from the surface of the specimen were selected manually only on the paste under optical microscopy of the CSM Instruments Indentation Tester. The maximum load P_{max} = 20 N corresponds to the maximum depth of about 30-35 μm was applied. Considering that the probed depth is about 10-20 times the penetration depth [334], this corresponds to an average probed volume of about 1 mm^3. To reduce the effect of sand heterogeneity on microindentation results, the indentation was carried out in the cement paste zone far from sand particles which were clearly visible by digital microscopic as the stage allows to precisely position the indentation spot with an accuracy of 1 μm [335].

The load was increased linearly from zero for 5 s, a holding time of 60 s, and unloading for 5 s. An indentation test consisted of establishing contact between a specimen and a tip of known geometry and then continuously measuring the change in indentation depth h as a function of increasing

indentation load *P*. The analysis of the *P*(*h*) curve proceeds by applying the continuum scale model [154] to assess the indentation properties (indentation hardness H and indentation modulus M), as defined by the following relations:

$$H \overset{def}{=} \frac{P_{\max}}{A_c} \tag{5.2}$$

$$M \overset{def}{=} \beta \frac{\sqrt{\pi}}{2} \frac{S}{\sqrt{A_c}} \tag{5.3}$$

where P_{max} is the maximum load applied, the coefficient β accounts for the non-symmetrical shape of the indenter, the projected area A_c of the indenter-sample contact depends on the contact depth h_c. As done on several works, the contact area A_c is estimated from h_{max} by the Oliver and Pharr method [155]. The contact stiffness S=d*P*/d*h* is the slope measured during the initial stage of the unloading curve. More detail of analysis results can find in [267,336].

One of the major advantage of microindentation is the ability of rapidly measuring the logarithmic basic creep of a cement paste [149,151,156]. For modeling indentation creep of cementitious materials, Vandamme et al. [151] proposed the logarithmic contact creep compliance equation as:

$$L(t) = \frac{1}{M(t)} = \frac{1}{M_0} + \frac{1}{C} \ln\left(1 + \frac{t}{\tau}\right) \tag{5.4}$$

where, C is the contact creep modulus C and τ is the characteristic time. The contact creep modulus (C) is further defined as follows [150,157]:

$$C = \frac{P_{\max}}{2x_1\sqrt{A_c / \pi}} \tag{5.5}$$

where x_1 can be estimated by fitting the increase of indentation depth Δh(t) under constant loading by $\Delta h(t)=x_1 ln(x_2 t+1)$.The contact creep modulus C allows assessing the logarithmic creep rate of a cement paste and can be reasonably used to predict long-term creep [157,227]. It is then possible to estimate the creep of the UHPC with sand from the value measured at the cement paste level by homogenization techniques [156]. If it is assumed that the cement paste makes a tight bond with the sand and that the sand does not creep, the creep modulus of the UHPC can be estimated from one of the cement pastes without sand as follows [157]:

$$C_{UHPC} = C\left(1 + 2\frac{f_s}{1 - f_s}\right) \tag{5.6}$$

where *fs* is the sand fraction, in this case, with f_s=40%, we can estimate that the overall creep modulus for UHPC is about 2.3 times the measured value C of the cement paste.

5.5 Results and discussion

5.5.1 Fresh concrete properties

Table 5-4 shows the fresh concrete properties of all UHPC mixtures in terms of spread diameter, wet density, and air content. The results indicate that LCLL-ash particles slightly reduced the flowability, particularly at LCLL-ash content of 12% in cement replacement. In addition, it was found in previous works that the high alkali content can significantly decrease mixture workability [337,338]. While LCLL-ash has low reactivity, it still can chemically bind with water to produce aluminate phases, such as sodium aluminum hydrates (A), as shown in the XRD analysis in section 5.5.2. The increase of air content on LCLL-UHPC is likely due to their lower packing density than the reference mixture. As for the wet density, it is observed to be slightly lower in mixtures with LCLL-ash consistency with the increased air content discussed above.

Table 5-4. Fresh concrete properties of all designed mixtures.

Mixtures	Spread (cm)	Wet density (kg/m^3)	Air content (%)
L0	20	2274	5.1
L6	19	2267	6.1
L12	17	2254	6.9

5.5.2 XRD patterns

Figure 5-6 shows the results of XRD analysis of designed UHPC mixtures cured at 7 and 28 days. The main crystalline phases in UHPC samples can be found, such as ettringite, ferrite, clinkers, and portlandite. Nevertheless, the ettringite peak intensity of L6 and L12 is significantly higher than that of L0 at 28 days. This is due to the reactive alumina and carbonate in LCLL-ash and its favorite to form more ettringite. Moreover, the quartz peak and sodium aluminum hydration peak presented in samples incorporating LCLL-ash particles especially increased their intensity with increased LCLL-ash content, similar to the report [245]. Interestingly, we could not observe the peak of carboaluminate phases (Mc,

Hc) which were found with the same LCLL-ash in normal concrete mixture at 2θ angles of 10.8 and 11.3 for hemicarboaluminate hydrate Hc and monocarbonaluminate hydrate Mc respectively [245].

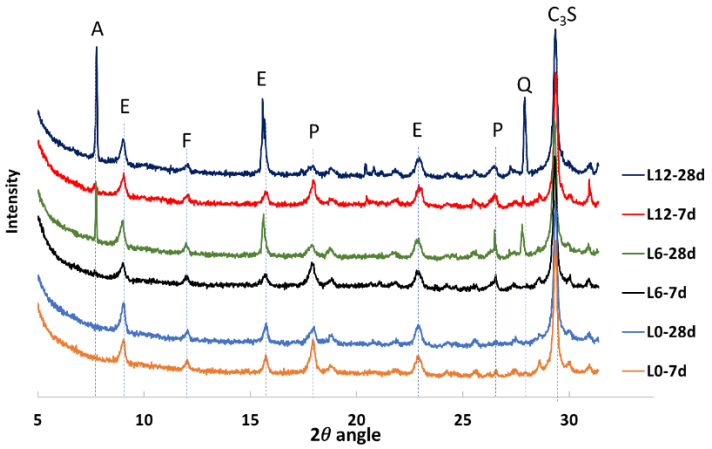

Figure 5-6. XRD pattern of cement paste at 7 days and 28 days: A=Sodium aluminum hydration, E = ettringite, C_3S = alite, P = portlandite, Q = quartz, F=ferrite.

5.5.3 Hydration kinetic

5.5.3.1. Isothermal calorimetry

Figure 5-7a and Figure 5-7b show the isothermal calorimetry results in terms of the heat release and the cumulative heat releases for the first 72 hours, respectively. The heat flow and the cumulative heat release were normalized per gram of cement. Figure 5-7a indicates 3 exothermic peaks. The 1st peak appears after a few minutes, resulting from the quick dissolution of free lime, gypsum, and the initial formation of ettringite [235]. However, this 1st peak did not completely capture the phenomenon because the mixing process was carried out outside the calorimetry. The 2nd peak was mainly associated with the hydration of alite (C_3S) [235,339]. As can be seen, LCLL-ash retarded the hydration of the mixture, and the mixture with LCLL-ash had a lower maximum of the prominent heat peak corresponding to hydration of C_3S. In other words, the time to reach the maximum hydration peak ΔT has been postponed by adding LCLL-ash particles. It appeared at 14h, 15h, and 18h for L0, L6, and L12, respectively. Several reasons can explain this: (i) the lower *w/c* ratio in the UHPC mixtures with LCLL-ash due to water taken by LCLL-ash to produce aluminate phases (see XRD analysis), resulting in the restriction of diffusion of Ca^{2+} and OH^- and delaying the hydration of the system [313,340,341], (ii) higher superplasticizer-to-cement ratio in the UHPC mixtures with LCLL-ash, which can lead retardation effect [141]. Moreover, the delay effect continuously increases with increased replacement

with LCLL-ash. The 3rd peak was related to the hydration of aluminate. This peak is more pronounced in the sample with 12% LCLL-ash, observed at 17.5 h. This could be due to the reaction of sulfate in cement with alumina in LCLL-ash to form ettringite [39]. This result corresponded to the XRD in the previous section 5.5.2.

The total heat released normalized to the mass of cement of L6 and L12 was lower than that of the system L0 (as shown in Figure 5-7b) due to the low activity of LCLL-ash and possibly the cement dilution effect as found in previous work [342].

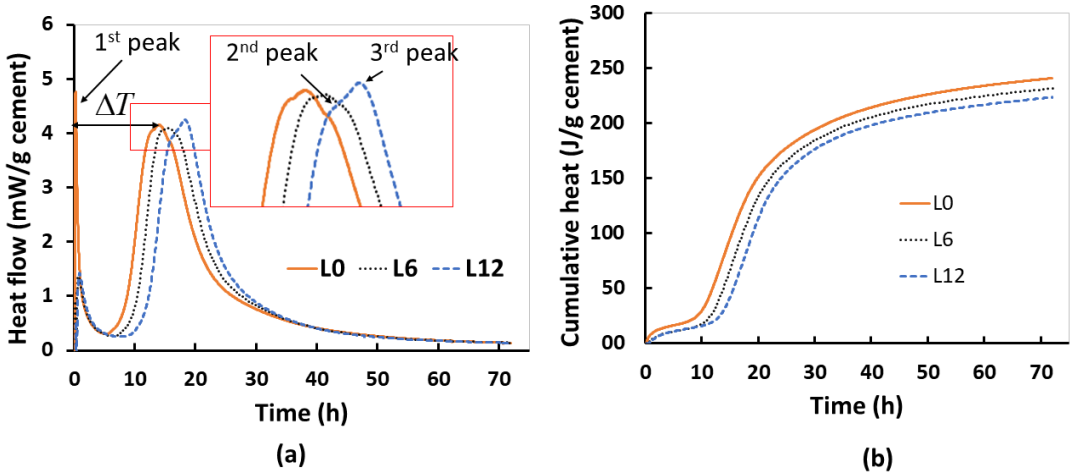

Figure 5-7. Isothermal calorimetry results: (a) normalized heat flow and (b) normalized cumulative heat for 72 hours.

The final setting time was estimated by the first derivative of the heat evolution curve as proposed by Hu at *al.* [343]. Figure 5-8 shows a typical plot of the first derivation d(q)/d(t) of the heat released rate curve from the original isothermal calorimetry test data. The time at which the first derivative dropped to zero was defined as the final setting time. The hydration rate reached the highest point at 13.8h, 15.4h, and 18.3h for L0, L6, and L12, respectively (as shown in Figure 5-8b). Based on such a definition, the final setting time of all investigated UHPC mixtures was significantly longer due to the use of a superplasticizer that might delay the cement hydration [141,344]. Moreover, the final setting time is increased by increasing the LCLL-ash content. This may be explained by two reasons: (i) the presence of high carbonaceous materials in LCLL-ash [345], and (ii) the high alkali content of LCLL-ash can delay the time of final setting [337].

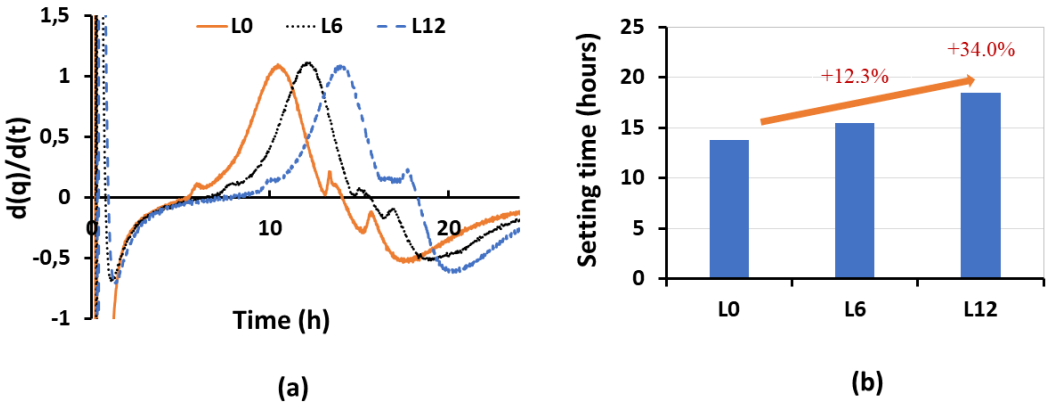

Figure 5-8. (a) Heat evolution rate curves d(q)/d(t) and (b) estimated final setting.

5.5.3.1 Double Danish Model

The aforementioned DDM model was employed to estimate the evolution of the degree of hydration from calorimeter results. Figure 5-9 presents the implementation of DDM for estimating the heat releases beyond the measurement period for the isothermal calorimetry. For that purpose, the heat releases of each UHPC mixture during the first 72 hours were normalized by the volume of cementitious materials (Figure 5-9a) —using the respective masse and unit weight of calorimetry test samples (section 5.5.3.1). As isothermal calorimetry is limited to 72 hours [262], the DDM [263] was used to predict the heat release beyond such a limited period. To do so, DDM parameters were identified by best fitting the experimental heat evolution during the first 72 hours (Figure 5-9b). The best-fitting parameters are summarised in Table 5-5. Figure 5-9c shows the satisfactory fit between the experimental heat release and the one simulated by DDM for all UHPCs. Using these DDM parameters, the heat release at 28 days was estimated and used to determine the degree of hydration at the age of other tests, presented in the next section 5.5.3.3.

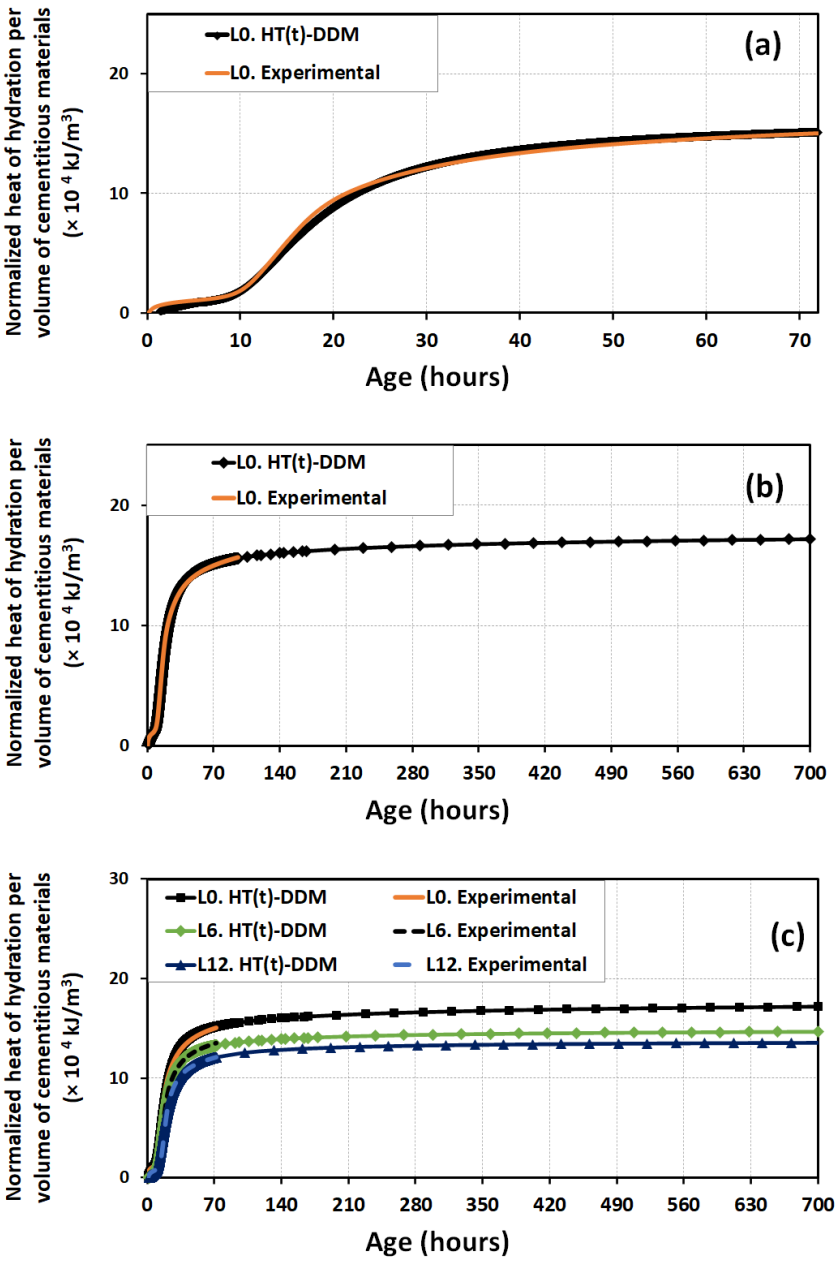

Figure 5-9. Comparison of the cumulative heat measured and simulated by DDM of the mixture L0 (a) at 72 hours (b) and up to 700 h. (c) Comparison of the cumulative heat measured and simulated by DDM up to 28 days of all developed mixtures.

Table 5-5. Parameters of the DDM for developed mixtures

Parameter	Units	L0	L6	L12
H_{T1}	kJ/m3	125,000	100,000	90,000
τ_1	hours	16,00	17,25	18,00
β_1	-	2,5	3,25	2,75
H_{T2}	kJ/m3	65,000	50,000	48,000
τ_2	hours	26,00	21,00	23,00
β_2	-	0,45	0,75	0,85
$H_T(t)$	kJ/m3	185,000	150,000	138,000

5.5.3.2 *The degree of hydration*

Using the heat releases estimated by the DDM detailed in section 5.5.3.2, the degree of hydration at any time t, $\alpha(t)$, can be defined as follows:

$$\alpha(t) \overset{def}{=} \frac{H_T(t)}{H_{T100\%}} \tag{5.7}$$

with $H_{T100\%}$ is the theoretical total potential heat of hydration release for full hydration of cement and silica fume. It is noted that the heat contributed by other components (e.g., SCMs) are negligible. The heat release of cement and silica fume for full hydration are 452.3 (kJ/kg) [263,265] and 780 (kJ/kg) [263]. The value of $H_{T100\%}$ for the different UHPC mixtures are presented in Table 5-6. Using these $H_{T100\%}$ values and the DDM-based heat releases, the degree of hydration $\alpha(t)$, for the different UHPC mixtures was estimated and presented in Figure 5-10.

The results of Figure 5-10 show that the estimated $\alpha(t)$ of LCLL-ash UHPCs were lower than that of the reference UHPC (L0) at all ages, as expected-given, the reduced cement content in LCLL-UHPC mixtures. At 28 days, for instance, $\alpha(t)$ the value for mixture L0 was 0.40 compared to 0.36 and 0.35 for L6 and L12, respectively. The observed lower value of $\alpha(t)$ in all UHPC mixtures (compared to $\alpha(t)$

ranges of 0.60-0.75 in conventional concrete [88,89]) is a direct implication of a very low *w/c* ratio. In the first few hours $\alpha(t)$ shows district differences between the reference and LCLL-ash mixtures. As elaborated in section 5.5.4, autogenous shrinkage in UHPC is strongly controlled by the deformations occurring during the plastic phase, also referred to as the primary shrinkage, where the rate of deformations is the highest due to the intensity of the hydration reactions.

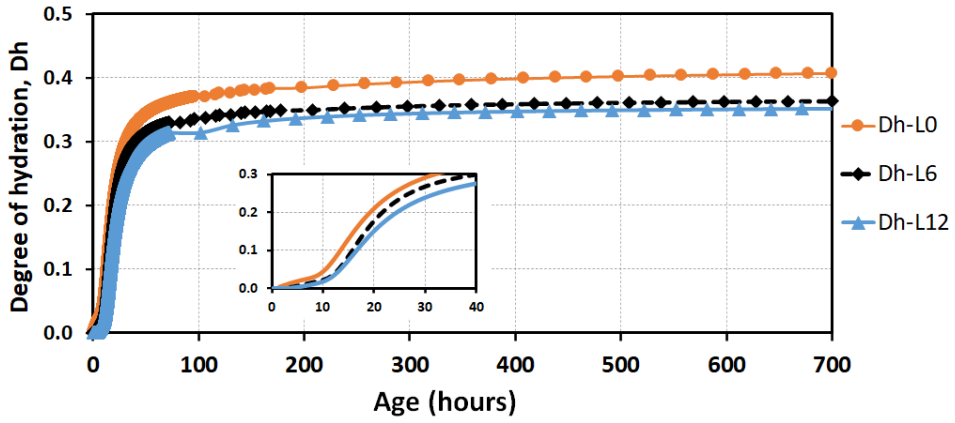

Figure 5-10. Degree of hydration of developed UHPC mixture from the cumulative heat of hydration curves from calorimetry tests at 72h and the one estimated by Double Danish Model up to 700h.

Table 5-6. Total potential heat release of the different UHPCs at full hydration, $H_{T100\%}$.

Mixtures	Total cement (Kg/m^3)	Heat release of cement for full hydration (kJ/kg) [263,265]	Total Silica fume (Kg/m^3)	Heat release of silica fume for full hydration, (kJ/kg) [263]	Total potential heat at full hydration, $H_{T100\%}$ (kJ/m^3)
L0	626	452	178	870	421,980
L6	588	452	176	780	403,232
L12	550	452	175	780	385,265

5.5.4 Early-age autogenous shrinkage

Concretes with a low *w/b* ratio may exhibit significant autogenous shrinkage with a risk of early-age cracking regardless of the curing conditions. Figure 5-11 shows the mean curves of the autogenous shrinkages of all the designed UHPC with different LCLL-ash dosages for 7 days. The test repeatability was satisfactory. Note that the time-zero (the final setting time) was conventionally chosen from the

inflection point of the (i.e., first derivative equal to zero) of the heat evolution as suggested by [343] (Figure 5-8.). In this work, we focus on autogenous shrinkage at an early age as the risk of cracking for UHPC structures occurs mainly during the first week when the UHPC strength is still growing [258]. Moreover, considering the results of autogenous shrinkage over 90 days for UHPC, the variation in the rate of shrinkage is practically constant after 3 days [346].

It may be interesting to quantify the main mechanisms separately at stake during the autogenous shrinkage at an early age. According to Baron [282], the early-age volumetric changes of cement comprises 4 phases, as shown in Figure 5-11, such as (i) The 1st phase (A-B), or the dormant period, occurs very shortly after placing the sample into the mold. The surface water layer is forming, and the duration of this period varies from 1-6 hours depending on the *w/c* ratio; (ii) The 2nd phase (B-C), or the primary shrinkage, is when the sample starts to shrink upon the evaporating of the surface water layer. This phase also coincides with the structuration of the hydrated system, thereby controlling the setting time. The maximum deformation at this phase depends mainly on the *w/c* ratio and the cement chemistry; (iii) The 3rd phase (C-D), or the swelling phase, often extents for several hours after primary shrinkage and its duration depends mainly on the gypsum content and the consequent precipitation of ettringite phase; (iv) The 4th phase (D-E), or secondary shrinkage, begins after the end of setting and ends when cement hydration stops. It should be noted that for concrete with a low *w/c* ratio, the rate of primary shrinkage is often much greater than that of the secondary shrinkage.

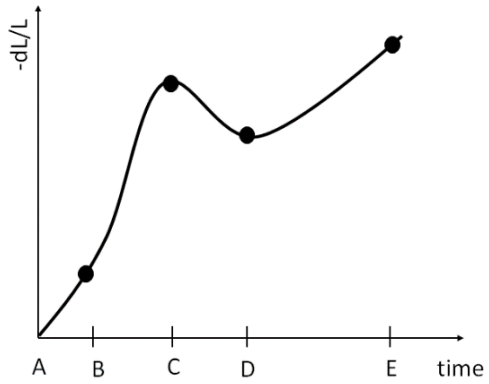

Figure 5-11. Shrinkage deformation of cement paste. It can divide into 4 phases: (A-B: dormant phase, B-C: primary phase, C-D: swelling phase, D-E: secondary phase).

As can be seen in Figure 5-12, the reference UHPC mixture exhibited relatively high autogenous shrinkage with comparable deformation ranges reported for UHPCs [34,342,347]. This trend can be

explained by the low *w/b* ratio and the high content of cement and silica fume, leading to self-desiccation—the driving force of autogenous shrinkage. Interestingly, results indicate that cement replacement with LCLL-ash decreased the autogenous shrinkage at an early age. There are two possible reasons: (i) the lower reactivity of LCLL-ash impedes the initial hydration process (as confirmed by the hydration kinetics in section 5.5.3.3); and (ii) the relatively higher water content in LCLL-UHPC allows for more water supply (or internal relative humidity) in the capillary pores and consequently reduces autogenous shrinkage [346]. Considering the phases of autogenous shrinkage discussed earlier (Figure 5-11), we can observe that the primary shrinkage showed a considerably higher rate (Figure 5-12a) and magnitude (Figure 5-12b) than the secondary shrinkage for all mixtures. Notably, both primary and secondary shrinkage was reduced by replacing cement by LCLL-ash.

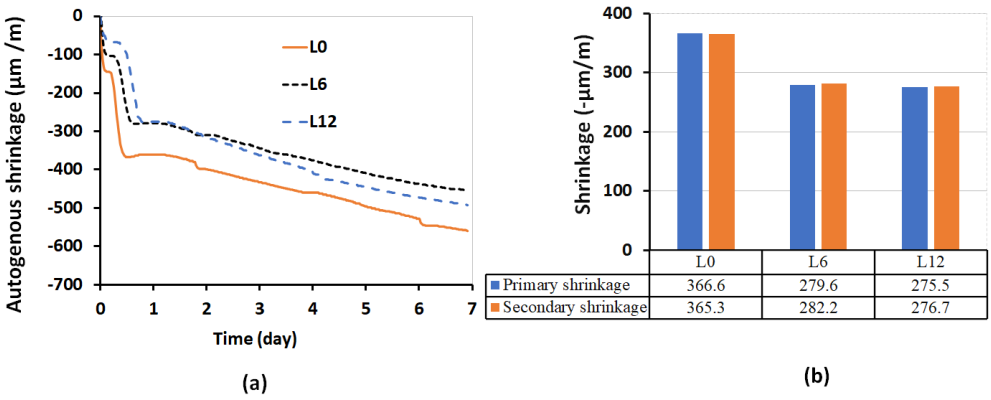

Figure 5-12. (a) Early-age autogenous shrinkage, and (b) primary and secondary shrinkage of the designed UHPC mixtures.

To capture the effect of hydration reaction on the autogenous deformations, the relationship between autogenous shrinkage ε_{sh} and the degree of hydration D_h was plotted in Figure 5-13 for the mean curves. For all UHPC mixtures, the trend shows 3 clear phases: (i) a rapid shrinkage growth with an exponential shape for a low degree of hydration between 0.05 and 0.15. This shrinkage is governed by chemical dissolution-precipitation reactions of cement and silica fume within the pore solution; (ii) a short dormant period with no effect of hydration degree on shrinkage for hydration between 0.15 and 0.25; (iii) a logarithmically increasing shrinkage for a very low increase of hydration degree from about 0.25-0.30 to 0.35-0.4 which were reached after about 7 days of the shrinkage test. Considering the triangular shape of the isotherm of UHPC for which a very small reduction of water can cause 50% variation of relative humidity [348], this shrinkage is due to the capillary suction induced in the capillary

porosity by a relatively small reaction. In general, for the same degree of hydration, the autogenous shrinkage is always smaller for UHPC systems with LCLL-ash particles. The autogenous shrinkage grows rapidly at an early age up to 7 days, and then increases logarithmically in time for a later age.

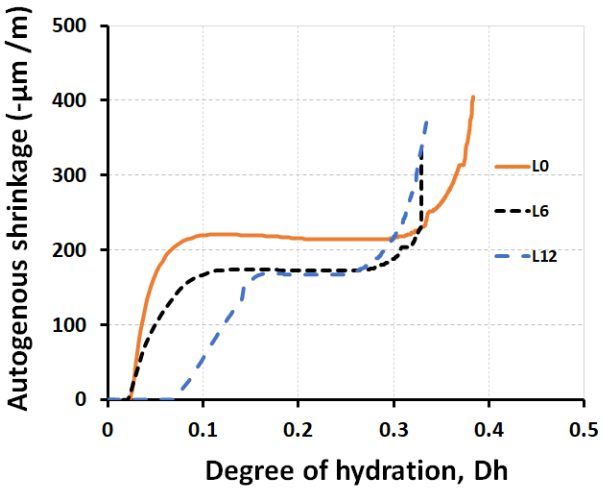

Figure 5-13. Relationship between autogenous shrinkage and degree of hydration at 7 days.

5.5.5 SEM microstructure observation

The possible effect of residual LCLL particles on the property of the cement paste matrix was verified by microindentation. Figure 5-14 shows the SEM image of all UHPC mixtures at 28-day of curing. A dense matrix can be observed in all designed UHPC mixtures. This is attributed to the high packing density granular of cementitious materials, which had a direct effect on the hydration reaction process and the microstructure formation [349]. Figure 5-15 shows the interfacial transition zone (ITZ) between matrix and aggregate of L12. The ITZ was very small and tiny as a direct consequence of the high granular packing density of the mixture. However, the residual LCLL-ash particles were still found in LCLL-UHPC samples. Figure 5-16 depicts a typical Backscatter image (BSE) of sample L12 (12% weight replacement cement by LCLL-ash). The microstructure of LCLL-ash particles can identify and distinguish by the EDS spot. For example, EDS spot 2 indicated the quartz particle while EDS spot 1 indicated LCLL-ash particles, nepheline, which contains sodium, aluminum, and silicon. Moreover, the grey value of unreacted LCLL-ash particles and quartz particles were very similar. Therefore, it can be a tackle for other analyses of BSE images. e.g., image analysis to estimate the degree of hydration.

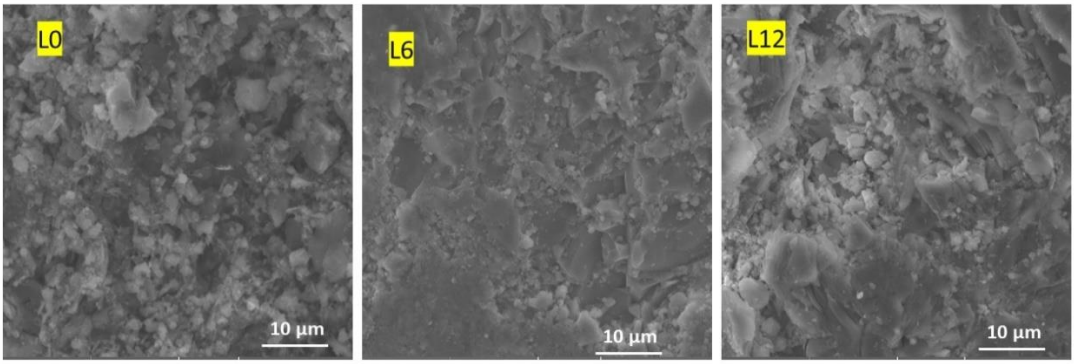

Figure 5-14. SEM images at 28 days of designed UHPC mixtures. A dense microstructure of designed UHPC mixtures is observed.

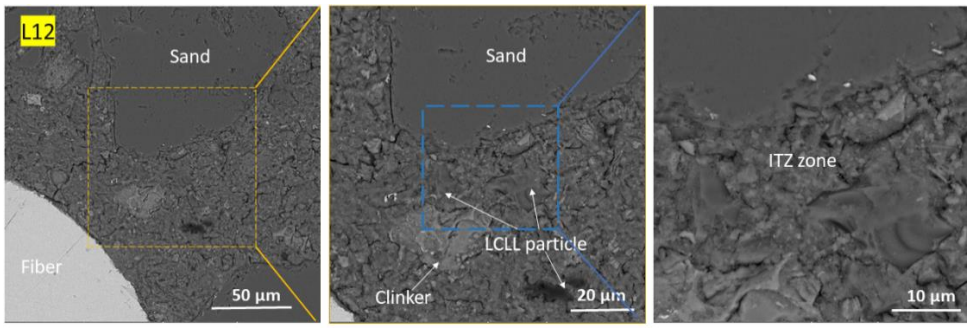

Figure 5-15. Backscatter image of 12% LCLL-ash replacement. This indicated that LCLL and unhydrated clinker are visible and the interfacial transition zone (ITZ) between sand and paste of designed UHPC is very tiny.

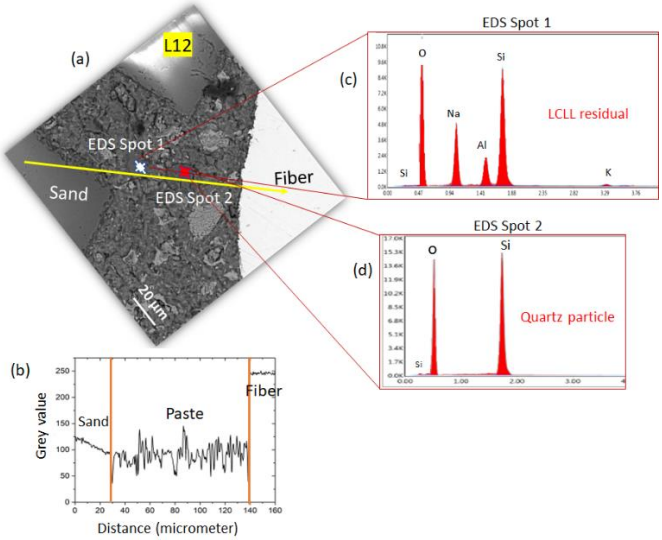

Figure 5-16. (a) Backscatter image with (b) the plot of grey value of the yellow line stretch from aggregate to fiber and (c,d) EDS spot analysis result. The grey values show that LCLL particles is closely to quartz powder while the EDS spots analysis enable to distinguish two particles.

5.5.6 Compressive strength

Figure 5-17 presents the compressive strength of the UHPC mixtures containing LCLL-ash by two curing regimes (hot curing and normal curing) at 7, 28, and 90 days. With normal curing (Figure 5-17a), the results show that LCLL-ash has no adverse effect on the strength of UHPC mixtures at 7 and 28 days. The compressive strength of L0, L6 and L12 at 28-day curing was 125 MPa, 123 MPa, and 121 MPa, respectively. However, the strength of UHPC incorporating LCLL-ash was slightly lower than that of reference at 90 days. This may be caused by the water taken in LCLL-ash, which simultaneously reduces the *w/c* ratio in the mixture with LCLL-ash.

For the hot water curing (Figure 5-17b), as expected, the compressive strength at 7 days of UHPC mixtures was significantly higher than that of samples cured under normal curing. This is in agreement with the growing tendency of compressive strength in UHPC in previous studies [350–352]. The application of thermal treatment enhances pozzolanic reaction. This results in more formation of hydration products, such as calcium silicate hydrate (C-S-H), filling the small pore and leading to denser microstructure and, consequently, to higher strength. It is noted that the strength at 7 days with hot water curing is closed to that of the 90 days of normal curing of the same mixture, which indicates that pre-treatment could bring some benefits to a structure that needs to reach a strength at a short time, such as pre-cast bridge session, jointing session, etc.

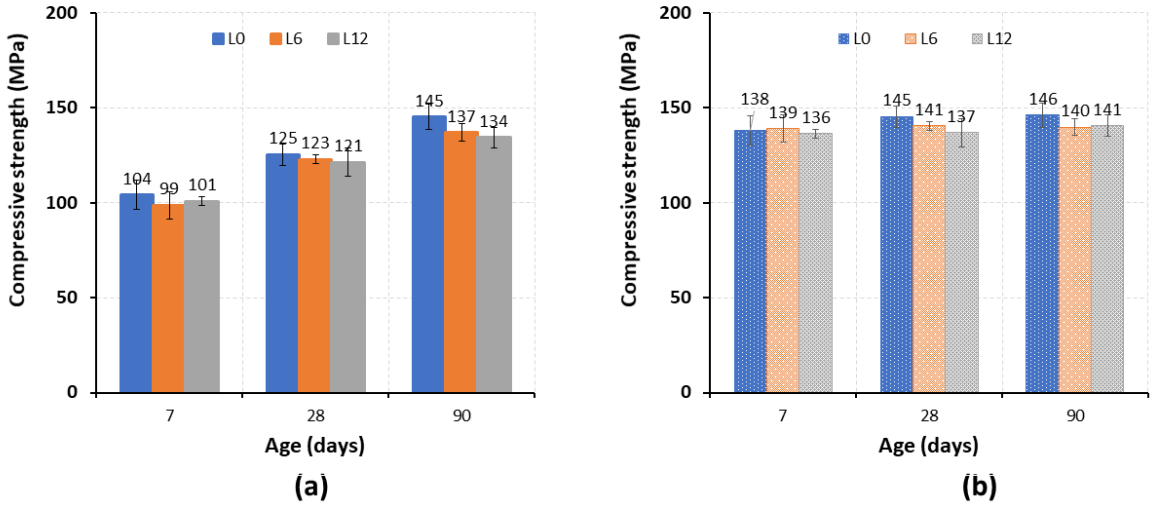

Figure 5-17.Compressive strength of designed UHPC mixtures (a) normal curing and (b) thermal curing.

5.5.7 Microindentation

Figure 5-18 summarizes the microindentation properties of designed UHPC mixtures at 28 days. The replacement of cement by LCLL-ash slightly reduced the elastic modulus of cement paste; that is, the elastic modulus E of systems L0, L6, and L12 were 46 GPa, 45 GPa, and 44 GPa, respectively. The hardness H of systems L0, L6, and L12 was 929 MPa, 908 MPa, and 901 MPa, respectively. In spite of the fact that the *w/c* ratio slightly increases for L6 and L12 systems with respect to the L0, the E-modulus and hardness H remain similar. This hints that the stiffening effect of the rigid filler particles has partially compensated for the increase of capillary porosity due to the *w/c* increase. In addition, this confirms that the ITZ bond between the cement paste and LCLL particles is not problematic. The dense interface around the sand and LCLL particles is visible in Figure 5-14. This result is consistent with the compressive strength measured at the same time of the indentation tests, i.e., 28 days, as shown in Figure 5-17

Moreover, sample L12 shows a slightly higher creep modulus C than the reference. Due to the fact that the creep mechanisms occur at a small scale, the creep deformation may be reduced by the stiffening effect of the tiny LCLL-ash particles. Compared to other works on micro-indentation tests on cement paste with a similar *w/c* ratio [266], the *E* and *H* values look greater than those measured on cement paste with a similar *w/c* ratio. This is probably attributed to the presence of quartz powder and fine limestone stiffening and strengthening the cement paste of the three systems (L0, L6, and L12).

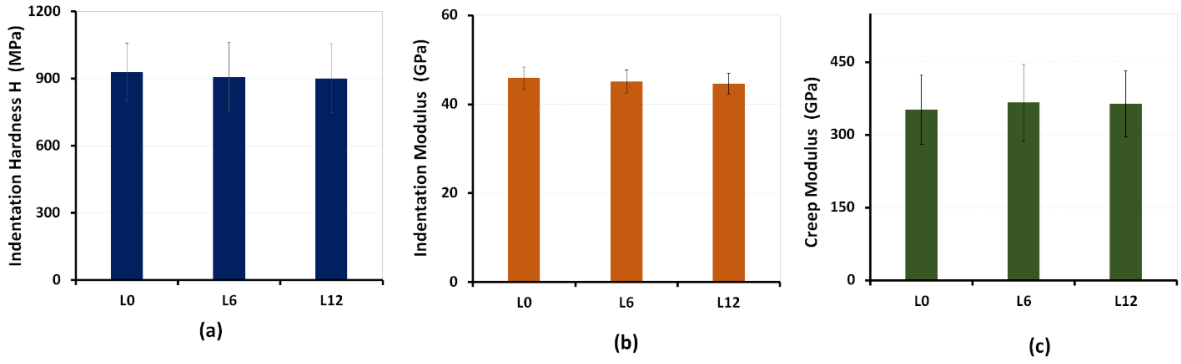

Figure 5-18. (a) Indentation Hardness H, (b) Indentation Elastic Modulus E and (c) Indentation Creep Modulus C of the designed UHPC mixtures at 28 days.

Due to the dispersion of results, an analysis of variance (ANOVA) was carried out to verify the elastic modulus and creep modulus of UHPC mixtures with LCLL-ash. Table 5-7 shows two analyses — P-value with the normal distribution and the F-test with Fisher-Snedecor distribution. From the results in

Table 5-7, P-value is much lower than the threshold α = 0.05, and F is smaller than F_{crit}. This confirms that the null hypothesis is acceptable, and the comparison of mean values of H, E and C is statistically meaningful.

Table 5-7. ANOVA on Indentation hardness H, Indentation Elastic Modulus E and Indentation Creep Modulus C with significance level α= 0.05.

Testing conditions	ANOVA parameters	Indentation Hardness H		Indentation Elastic Modulus E		Creep Modulus C		F_{crit}
		P	F	P	F	P	F	
28 days of curing	0%, 6%, 12% of replacement	0.34	1.21	0.17	1.81	0.38	0.96	3.05

5.5.8 Eco-Efficiency assessment

As for the hypothesis, Table 5-8 summarizes the cost, embodied energy (EE), and embodied carbon (E_{CO2}) of the raw materials based on reference values available in the open literature. Although such data may be limited to certain geographical zones, those values are herein employed for a preliminary comparison. It is worthy to note that the cost, EE, and the E_{CO2} of LCLL-ash and quartz powder were assumed as zero in this study since they were considered as waste materials.

Table 5-8. Cost, embodied energy and embodied carbon of the raw materials.

Items	Cost [$/ton]	Embodied Energy (EE) [MJ/kg]	Embodied CO_2 (E_{CO2}) [$kgCO_2$ /kg]	References
Cement	220	4.73	0.83	[300,353–356]
Silica fume	450	0	0	[353–355]
Limestone	160	0	0	42
Quartz powder*	560	2.12	0.023	[353,357,358]
Natural sand	14	0.06	0.0026	[300,301,358]
LCLL-ash*	0	0	0	
Steel fibers	10,000	20.56	1.45	[301,354,355]
Superplasticizer	3,800	18.30	0.72	[301,354,355,359]

In the previous studies, different efficiency index has been proposed to compare UHPC mixtures in terms of different properties such as slump, strength, etc. In the context of this work, we developed an efficiency index (EI) which is conventionally defined as considering 3 aspects: cost, embedded energy (EE), and embodied carbon (E_{CO2}). The efficiency index was defined as the following equation:

$$EI = w_1 \frac{\text{Cost}_{\text{ref}} - \text{Cost}}{\text{Cost}_{\text{ref}}} + w_2 \frac{\text{EE}_{\text{ref}} - \text{EE}}{\text{EE}_{\text{ref}}} + w_3 \frac{\text{E}_{CO2ref} - \text{E}_{CO2}}{\text{E}_{CO2ref}} \quad (18)$$

As the first approach, the efficiency index can be estimated assuming the equal importance weight of the three parameters (cost, EE and E_{CO2}): such as $w_1 = w_2 = w_3 = 33.33\%$. Table 5-9 compares the cost, EE, E_{CO2}, and EI of the developed UHPC mixtures. Compared to the reference UHPC, cement replacement with 6% and 12% LCLL-ash contributed to reducing cost, EE and E_{CO2}. Relative to the reference L0, L12 allowed reducing the EE and E_{CO2} by 6% and 10%, respectively. This resulted in an improvement in overall EI of 9%. Furthermore, we can compare the cost, EE, and E_{CO2} of the developed LCLL-UHPC with a reference UHPC which is commercially available under the commercial name of Ductal®. Based on the mix design prescribed in the FHWA report [304] and the data of the raw materials presented in Table 5-8. The EI, cost, EE, and E_{CO2} are calculated in Table 5-9. As compared to Ductal®, L12 formulation without fiber consists of a reduction from 620 $KgCO_2/m^3$ to 485 $KgCO_2/m^3$, which is about 22%, with a difference in EI index of about 32%.

Table 5-9. Cost, EE, E_{CO2}, and EI of all designed mixtures.

		L0	L6	L12	Commercial UHPC [304]
With fibers	Cost [$/m^3]	1931	1922	1913	2067
	EE [MJ/m^3]	6896	6716	6536	7628
	E_{CO2} [kg/m^3]	774	742	711	846
	EI (%)	-	+2%	+5%	-9%
Without fibers	Cost [$/m^3]	371	362	353	507
	EE [MJ/m^3]	3689	3509	3329	4420
	E_{CO2} [kg/m^3]	548	516	485	620
	EI (%)	-	+4%	+9%	-23%

For the sake of comparison, Figure 5-19 compares the developed LCLL-UHPC with other UHPC formulations which are available in the open literature [34,178,184,296,297,329,360–365]. Figure 5-19a presents the E_{CO2} versus compressive strength, while Figure 5-19b illustrates the cost versus EE. The Cost, EE, and E_{CO2} are normalized per cement for producing 1 m^3 of UHPC mix. The LCLL-UHPC formulations satisfy the 120 MPa target while offering lower cost, EE, and E_{CO2}, thereby fostering the EI. These results confirm the promising direction in using LCLL-ash for ecological UHPCs recycling locally available mineral fillers.

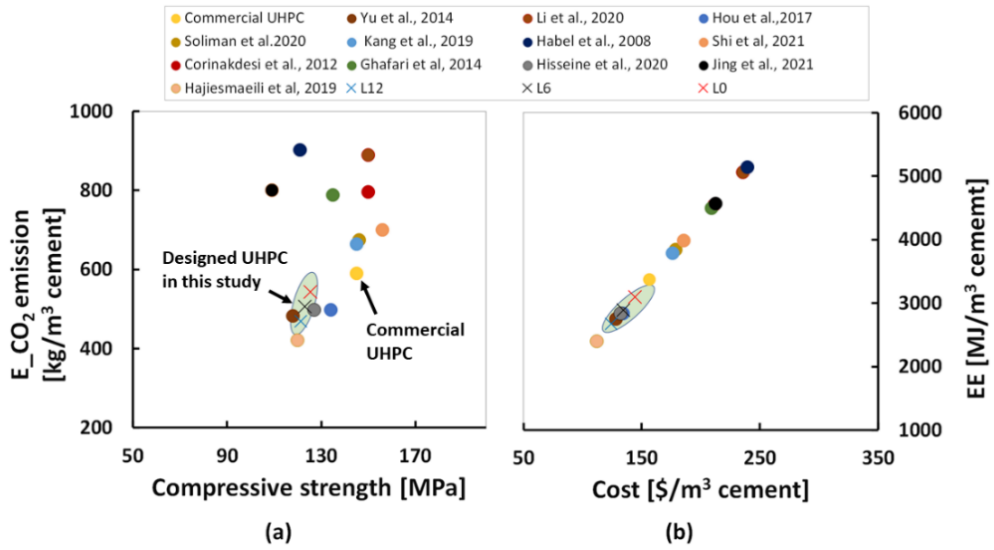

Figure 5-19. Ecological evaluation of the designed UHPC compared to other UHPC mixtures in literature. (a) plot compressive strength vs. E_{CO2} emission, (b) plot cost vs. EE.

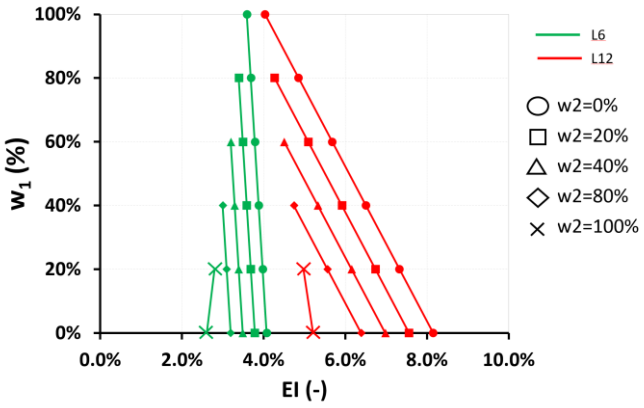

Figure 5-20. Estimation of the efficiency index for different weights w_1 and w_2 for the two systems L6 (green line) and L12 (red line).

To further generalize, Figure 5-20shows the effect of choosing different weights for the selection criteria (w_1=0-100% for cost, w_2=0-100% for embodied energy and w_3=1-w_2-w_3 for embodied carbon). For instance, if the choice is only based on cost (w_1=100%, w_2=0, w_3=0), the EI is about 4% for the L6 and L12 systems with a small difference of 0.4%. If the choice is based only on embodied carbon (w_1=0, w_2=0, w_3=100%), the EI difference between the 2 systems is more important, i.e., L12 implies an increase of EI from 4.1% to 8.2%. All intermediary cases will depend on the importance of the chosen criteria.

5.6 Conclusion

This work aims at developing an ultra-high-performance concrete (UHPC) that recycles the waste of Aluminium production, which is a chemically treated SPL in the form of LCLL-ash. Based on a wide experimental campaign, the following specific conclusions can be drawn:

- Optimized LCLL-UHPC mixtures with mineral fillers (quartz, limestone, LCLL-ash) and SCM (silica fume) were obtained at a packing density by the Compaction-Interaction Packing Model (CIPM).

- The replacement of cement by LCLL-ash reduced the spread flow, which is likely due to the high alkali content of LCLL-ash. Furthermore, the LCLL-ash acted as a retarder, delaying the cement hydration by 2–3 hours. Consequently, the setting time was also longer. Therefore, it may be limited to applications where the strength gains in a short time.

- It was possible to estimate the hydration degree at a longer time by a simplified Double Danish model (DDM), which fits the time-evolution of the heat of hydration as measured by an isothermal calorimeter test. The estimated degree of hydration of LCLL-UHPC was lower than that of the reference mixture. This is due to the limited pozzolanic reaction of LCLL-ash and a possible dilution effect.

- The replacement of cement with LCLL-ash by 6% and 12% reduced the early autogenous shrinkage of UHPC, which reduces the risk of cracking. By coupling DDM estimation of hydration degree and the autogenous shrinkage with the same time zero, it was possible to estimate the distinctive relationship between autogenous shrinkage and hydration degree for the UHPC-LCLL systems. Notably, the shrinkage of LCLL-UHPC exhibited a non-linear

dependency on the degree of hydration with two clear phases, such as a primary phase governed by chemical dissolution-precipitation reaction, followed by a secondary shrinkage governed by capillary suction.

- The compressive strength at 28 days of LCLL-UHPC was greater than 120 MPa. The replacement of cement by LCLL very slightly reduced the compressive strength. As for the effect of heat treatment for prefabrication purposes, the compressive strength of the designed UHPC at 7 days of heat curing is comparable to that at 91 days of conventional curing. Although the w/c and the air content were slightly increased for the LCLL-UHPC systems, microindentation tests confirmed that the cement paste matrix is not weakened by LCLL-ash particles. This confirms a satisfactory bond between LCLL particles and cement paste.

- The addition of LCLL-ash in UHPC reduced the embodied energy by up to 8% in UHPCs with 2% of steel fibers and by up to 12% for the UHPC without steel fibers. Compared with commercially available UHPC, the developed LCLL-UHPC mixtures exhibit low embodied carbon with a difference of 11% and 20% with and without considering fibers, respectively.

The presented results demonstrate the feasibility of producing LCLL-UHPC with significantly reduced autogenous shrinkage at an early age and a lower carbon footprint. LCLL-UHPC may contribute to the cost-saving toward the sustainability of the concrete industry while reducing landfill disposal in countries dealing with waste from Aluminium production. Future studies shall investigate the effect of grinding LCLL powders to further increase the cement replacement amount by LCLL. Also, the effect of LCLL-ash on other mechanical properties, such as flexural and tensile strength, as well as the durability properties shall be investigated.

Conclusion and future work

Concluding remarks

This thesis presented the feasibility of recycling the treated by-product from primary aluminum smelters —LCLL-ash— into concrete mixtures. Based on the literature review, there were few works on the use of treated SPL in developing green concrete [321], while the use of LCLL-ash was completed unexplored. In this thesis, I first investigated the effect of LCLL-ash on concrete properties and its microstructure. In some mixtures, a small amount of synthetic anhydrite (another by-product related to the aluminum industry) was added. After that, the effect of calcined LCLL-ash (LCLL-C) at 800ºC and 1000ºC on the hydration of the LCLL-C-cement paste system was carried out. Before replacement cement by LCLL-ash and LCLL-C, they were grinded as the fineness of cement. Fostering to develop of low carbon concrete, the study aimed to better understand the effect of mineral fillers on the cement paste systems and the upscale to UHPC mixtures. These mineral fillers are locally industrial by-products (granite and limestone powder) and post-consumer glass (glass powder) in Quebec, which act as mineral fillers. The development of Ecological-UHPC incorporating LCLL-ash was carried out. The particle packing of LCLL-UHPC mixtures was optimized by the compaction-interaction packing model (CIPM). It was possible to replace cement with LCLL-ash by 6% and 12% in mass percentage. The effect on the fresh concrete properties, hydration kinetics, microstructure, and compression strength were implemented. The cost, embedded energy and embodied CO_2 of developed LCLL-UHPC were also assessed. Hence, the main concluding remarks are summarized as follows:

- We discovered that LCLL-ash modified the hydrates products of LCLL-cement system. Particularly, AFm-CO_3 phase, e.g., hermicarboaluminate Hc that was formed at 7 days and transformed into monocarbonaluminate Mc at 28 days and stability at a long time. The system containing anhydrite observed broader ettringite peaks than those of control and cement with LCLL-ash systems. The presence of such new aluminate-rich phases was also confirmed by TGA result;

- Unreacted LCLL-ash particles were still found in the paste systems as observed by XRD and SEM. However, the content of C-S-H by mass of cement, calculated by TG curves, increased by adding LCLL-ash, which is likely due to a nucleation effect or the formation of aluminate-rich phases among C-S-H hydrates;

- Based on WDS analysis and statistical clustering analysis, the phase with predominant C-S-H did not increase its aluminate content confirming any aluminum uptake, and a slight shift of the Ca/Si ratio was observed. This was explained by an intermix of tiny LCLL-ash particles with C-S-H or a change of the silicate chain length;

- The indentation properties showed that it was possible to replace 10% of cement mass by LCLL-ash without affecting the mechanical property of the cement paste at the different ages (28, 56 and 112days). Interestingly, the systems with LCLL-ash and anhydrite exhibit a clear enhancement of hardness H and creep compliance C at 28 days which is likely due to the presence of ettringite. The addition of anhydrite led to an increase of the volume of hydrates (most likely ettringite), which caused a remarkable gain in strength;

- The calcined LCL-ash changed the hydrate products, similar to non-calcined LCLL-ash. The delayed hydration rate was observed in both systems with LCLL-ash and LCLL-C due to high alkalis content. The hydrate content estimated from TG curves in LCLL-C-cement system was lower than LCLL-cement and the reference. It means that calcination did not improve the pozzolanic reaction of LCLL-ash in this study;

- As for cement paste systems at very low w/f = 0.2, all the considered mineral fillers (GrP, GP, LP) obtained from industrial stone waste and post-consumer waste of Quebec improved the workability of the cement pastes systems. This trend is more pronounced with filler levels up to 40% of binder replacement;

- The use of mineral fillers in replacing 40% of the binder delays hydration kinetics by 2-3 hours. The cement pastes systems with mineral fillers improved the hydration degree due to the filler impact, as measured by a simple model called Double Danish model (DDM) [263] for the calorimetry analysis. Remarkably, GP exhibited a slightly higher hydration degree than the other systems with other mineral fillers due to its pozzolanic reaction;

- The type of mineral fillers and binder replacement levels had a considerable influence on the autogenous shrinkage of cement paste systems. The presented results showed that GrP20, GrP40, and LP20 had lower autogenous shrinkage than the reference, of which was reduced by 8%, 32% and 16%, respectively. This can help to reduce the risk of early

age microcracking. It was also possible to identify the relationship between shrinkage and degree of hydration, which allows easily distinguish primary and secondary shrinkage of all study systems and be employed in structural modeling of UHPC risk of cracking [258];

- The enhancement of compressive strength of cement pastes depended on the type and replacing levels of mineral fillers. In particular, for GrP, GP, and LP, the optimal mineral filler replacement levels were 20%, 10%, and 30%, respectively, which increased by 16%, 19%, and 9% when compared to the reference;

- For UHPC mixtures, by substituting mineral fillers for up to 20% of the binder, the compressive strength of UHPC was comparably related to the reference. However, replacing the binder with 40% mineral filler reduced the compressive strength by around 23% due to the relatively high volume of fine aggregates. In addition, compared to the previous studies, substituting cement by mineral fillers allow for a reduction in embodied carbon below 500 kg/m^3 while maintaining a high compressive strength;

- Preliminary mixes of ecological-UHPC incorporating LCLL-ash as a mineral filler were developed. LCLL-ash did not do any treatment before adding concrete to optimize the cost and energy consumption for concrete production. LCLL-UHPC mixtures were designed using the CIPM model with the cement substitution up to 12% by mass;

- LCLL-ash reduced the spread flow and delayed the cement hydration of LCLL-UHPC mixtures. Consequently, the setting time was also longer. Therefore, it may be limited to applications where the strength gains in a short time.

- Double Danish Model was applied to estimate the degree of hydration Dh of UHPC with LCLL-ash based on the heat of hydration from calorimetry up to 48 hours. The result showed that Dh of LCLL-UHPC has lower than Dh of reference. This is related to the limited pozzolanic reaction of LCLL-ash and the lower cement content in LCLL-UHPCs.

- The replacement of cement with LCLL-ash reduced by 25% the autogenous shrinkage of UHPC mixture at 7 days. This will likely reduce the risk of the early-age cracking of UHPC structural, or architectural elements subjected to constrained deformations;

- The compressive strength of LCLL-UHPCs was slightly lower than the reference mixture. However, it still gained 120 MPa after 28 days of curing. The effect of heat treatment was also investigated for prefabrication purposes. The compressive strength of the designed UHPC at 7 days of heat curing is comparable to that at 91 days of conventional curing.

- Compared with commercially available UHPC, the developed LCLL-UHPC mixtures exhibited low embodied carbon with a difference of 11% and 20% with and without considering fibers, respectively.

The main important results of this thesis can be summarized as follows:

1. The feasibility of concrete with about 10% of mass of cement replaced by LCLL-ash was verified. In particular, the microstructure of 10LCLL sample was enhanced by adding 1.25% synthetic anhydrite—another by-product from aluminum sector.

2. Different sources of mineral fillers recycled by industrial stone waste and post-consumer waste, such as granite powders, limestone powders and glass powders, can be efficiently used for replacing the unreacted part of the binders in cement paste at a very low water-to-fine ratio. All the considered mineral fillers, which were employed to replace cement up to 40%, increased the workability, while GP showed a slightly higher degree of hydration and GrP the lowest autogenous shrinkage.

3. LCLL-ash allows replacing the unreacted part of the cement in UHPC mixtures by acting as mineral fillers. Based on the particle packing model was applied to optimize and design LCLL-UHPC. The results indicate that the UHPC with cement replaced by fillers recycled by aluminum smelters of Quebec was successfully developed, which has the 120 MPa compressive strength and reduced autogenous shrinkage.

Future work

Further work is needed to link the microstructure properties with the macroscopic properties of systems with LCLL-ash, which will be a key for further engineering of such composite systems. Upscale to the concrete level and study the bond between the aggregate and the cement paste can employ. The effect on the durability shall also be investigated, especially for alkali-silica reaction (ASR) due to the high content of alkalis in LCLL-ash [233,234].

Future works are needed to further study the effect of calcination of LCLL by considering further temperature and process variables. For calcined LCLL-ash, the cement paste systems with different substitution levels of cement with LCLL-C can study (e.g., 5%, 10%, 15%...) in terms of hydration kinetics, microstructure, and mechanical properties. Afterward, it could be interesting to upscale these cement pastes to concrete. Life cycle assessment shall be assessed since the lower calcination temperature of LCLL-ash than clinker, but the pre-treatment of LCLL-ash (dried and ground) can affect the efficiency of this calcination solution.

Future works shall further optimize UHPC-LCLL mixtures. For instance, the use of calcinated LCLL or grinded particle size of LCLL-ash may be explored in UHPC formulations. The particle size closer to cement can increase the replacement level, improve the workability, and enhance the strength of UHPC. The flexural and tensile properties of LCLL-UHPC mixtures are needed to investigate. In addition, the durability properties of this newly developed UHPC were also examined, including freeze-thaw, salt scaling and chloride permeability. Moreover, the cement and silica fume content of these LCLL-UHPC can also reduce, for example, by changing the type of cement (e.g., high-strength cement, low-alkali cement) and silica fume (e.g., nano-silica). Also, LCLL-UHPC could be installed and tested on deteriorated existing bridges as an overlay to analyze its efficiency in construction. Furthermore, this UHPC should be tested in aggressive environments as in cold-snowy weather.

Future works at a smaller scale should investigate the properties of the complex chemical phases composing concrete with LCLL and UHPC-LCLL mixtures. For instance, even though it was not completed, we have started to work on the coupling of Nanoindentation and Quantitative Energy Dispersion Spectroscopy (NI-QEDS) method to study the chemo-mechanical properties of each hydrates phases of cement paste with LCLL-ash (calcined and non-calcined). We are developing this method as shown in . The smallest nano indenter named Alemnis. We installed Alemnis inside the SEM chamber. The controlling systems of Alemnis, which are connected to the software, is located outside of SEM chamber. The sample holder is able to rotate 360º by the orientation stage. It means that after indenting, the sample can rotate under the X-ray beam to perform the chemistry analysis in the same indenter's location. The advantage of this nanoindenter is that the position accuracy between 2 indents is very small, approximately 0.01 µm, as shown in and , which allows mechanical testing points which have been previously selected by Sem and chemically analyzed by EDX. This new method

will enable to finely disclose the chemo-mechanical properties of the microstructure phases composing, such as carbo-aluminates phase, herein Mc and Hc, and possible C-A-S-H.

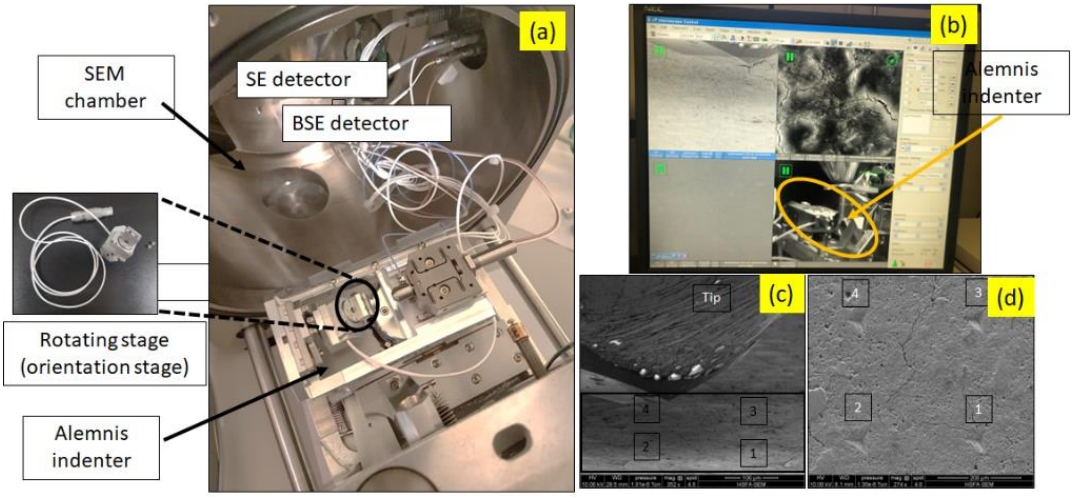

A coupled Nanoindentation and Quantitative Energy Dispersion Spectroscopy.

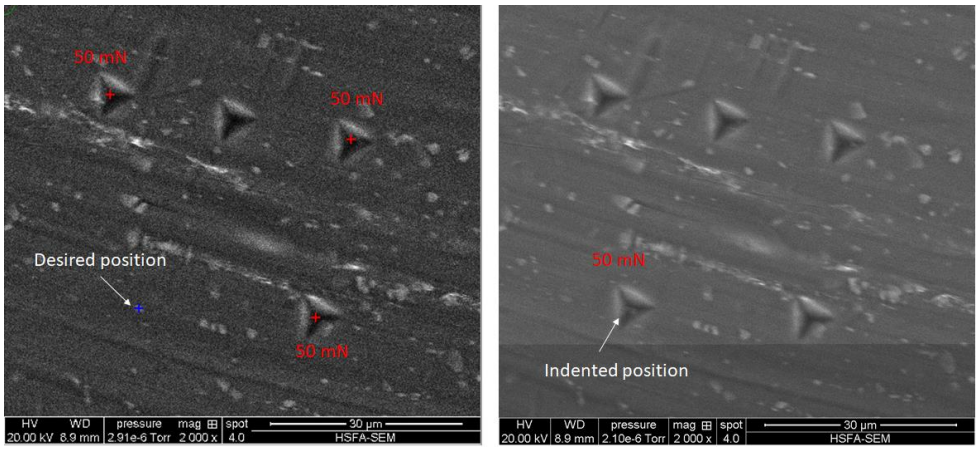

Some test results on the aluminum sample. As can be seen, the indented location is very closed to the desired one.

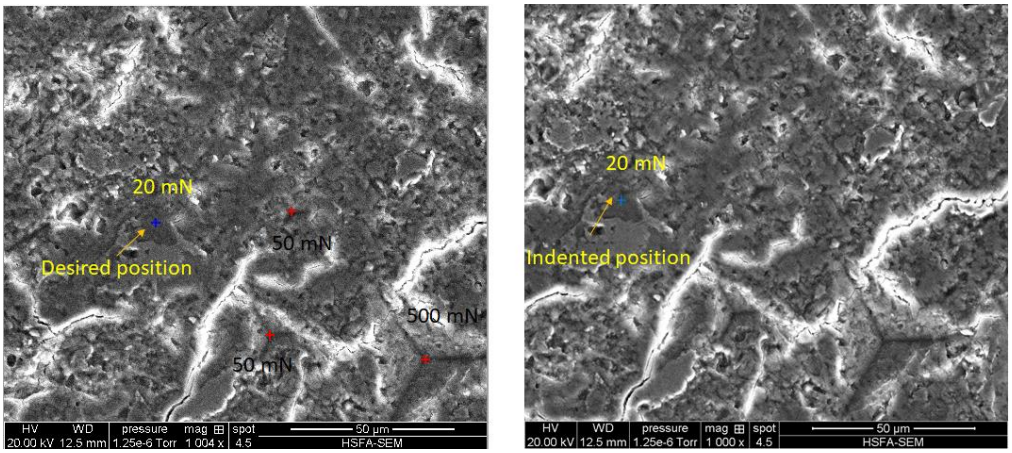

Some test results on cement paste. Few nanometers error between the desired and indented position is observed.

References

[1] R.M. Andrew, Global CO2 emissions from cement production, (2018) 23.

[2] E. Worrell, L. Price, N. Martin, C. Hendriks, L.O. Meida, Carbon Dioxide Emissions from the Global Cement Industry, Annu. Rev. Energy Environ. 26 (2001) 303–329. https://doi.org/10.1146/annurev.energy.26.1.303.

[3] P.J.M. Monteiro, S.A. Miller, A. Horvath, Towards sustainable concrete, Nat. Mater. 16 (2017) 698–699. https://doi.org/10.1038/nmat4930.

[4] J. Park, S. Tae, T. Kim, Life cycle CO2 assessment of concrete by compressive strength on construction site in Korea, Renew. Sustain. Energy Rev. 16 (2012) 2940–2946.

[5] P.-C. Aitcin, S. Mindess, Sustainability of Concrete, CRC Press, London, 2014. https://doi.org/10.1201/9781482266696.

[6] S. Mindess, Developments in the Formulation and Reinforcement of Concrete, Woodhead Publishing, 2019.

[7] B. Lothenbach, K. Scrivener, R.D. Hooton, Supplementary cementitious materials, Cem. Concr. Res. 41 (2011) 1244–1256. https://doi.org/10.1016/j.cemconres.2010.12.001.

[8] B. Lothenbach, G. Le Saout, E. Gallucci, K. Scrivener, Influence of limestone on the hydration of Portland cements, Cem. Concr. Res. 38 (2008) 848–860. https://doi.org/10.1016/j.cemconres.2008.01.002.

[9] M.C.G. Juenger, R. Siddique, Recent advances in understanding the role of supplementary cementitious materials in concrete, Cem. Concr. Res. 78 (2015) 71–80. https://doi.org/10/f7w7gv.

[10] J. Skibsted, R. Snellings, Reactivity of supplementary cementitious materials (SCMs) in cement blends, Cem. Concr. Res. 124 (2019). https://doi.org/10.1016/j.cemconres.2019.105799.

[11] S. Kosmatka, B. Kerkhoff, W. Panarese, Design and Control of Concrete Mixtures, 2002.

[12] CEMBUREAU, The European Cement Association Activity Report, (2011).

[13] K.Scrivener, Issues in sustainability in cements and concrete, (2012) 47–50.

[14] E. and C.C. Canada, Coal phase-out: the Powering Past Coal Alliance, (2017). https://www.canada.ca/en/services/environment/weather/climatechange/canada-international-action/coal-phase-out.html (accessed September 28, 2021).

[15] Z. Haber, I. De la Varga, B. Graybeal, Properties and Behavior of UHPC-Class Materials, 2018.

[16] J.-P. Charron, E. Denarié, E. Brühwiler, Permeability of ultra high performance fiber reinforced concretes (UHPFRC) under high stresses, Mater. Struct. 40 (2007) 269–277. https://doi.org/10/c4963f.

[17] B. Aarup, UHPC Joints-Not Just for Bridges, in: 2019.

[18] O. Babarinde, N. Farzana, D. Kuruppuarachchi, Use of UHPC Jackets in Coastal Bridge Piles, (n.d.) 10.

[19] N. Bertola, P. Schiltz, E. Denarié, E. Brühwiler, A Review of the Use of UHPFRC in Bridge Rehabilitation and New Construction in Switzerland, Front. Built Environ. 7 (2021) 769686. https://doi.org/10/gnm4vs.

[20] B. Graybeal, E. Brühwiler, B.-S. Kim, F. Toutlemonde, Y.L. Voo, A. Zaghi, International perspective on UHPC in bridge engineering, J. Bridge Eng. 25 (2020) 04020094.

[21] W. Huang, H. Kazemi-Kamyab, W. Sun, K. Scrivener, Effect of replacement of silica fume with calcined clay on the hydration and microstructural development of eco-UHPFRC, Mater. Des. 121 (2017) 36–46. https://doi.org/10.1016/j.matdes.2017.02.052.

[22] A. Korpa, T. Kowald, R. Trettin, Phase development in normal and ultra high performance cementitious systems by quantitative X-ray analysis and thermoanalytical methods, Cem. Concr. Res. 39 (2009) 69–76. https://doi.org/10.1016/j.cemconres.2008.11.003.
[23] R. Yu, P. Spiesz, H.J.H. Brouwers, Mix design and properties assessment of Ultra-High Performance Fibre Reinforced Concrete (UHPFRC), Cem. Concr. Res. 56 (2014) 29–39. https://doi.org/10.1016/j.cemconres.2013.11.002.
[24] I. Rustad, K.H. Karstensen, K.E. Ødegrd, Disposal options for spent potlining, in: G.R. Woolley, J.J.J.M. Goumans, P.J. Wainwright (Eds.), Waste Manag. Ser., Elsevier, 2000: pp. 617–632. http://www.sciencedirect.com/science/article/pii/S0713274300800720 (accessed October 10, 2018).
[25] G. Holywell, R. Breault, An Overview of Useful Methods to Treat, Recover, or Recycle Spent Potlining, JOM. 65 (2013) 1441–1451. https://doi.org/10/gfhwkq.
[26] F.M. Kimmerle, J.-L. Bernier, V.K. Kasireddy, G. Holywell, Chemical Revovery from Spent PotLining, Miner. Met. Materilas Soc. (1993) 671–685.
[27] S. Broek, H.A. Øye, Fundamentals of Managing Spent Potlining (SPL), Trav. 46 Proc. 35th Int. ICSOBA Conf. (2018) 817–834.
[28] H.A. Øye, Discussion of Industrial Spent Pot Lining Treatment, in: Proc. 35th Int. ICSOBA Conf., Hamburg, Germany, 2017: pp. 2–5.
[29] L. Birry, S. Leclerc, S. Poirier, The LCL&L Process: A Sustainable Solution for the Treatment and Recycling of Spent Potlining, in: E. Williams (Ed.), Light Met. 2016, Springer International Publishing, Cham, 2016: pp. 467–471. https://doi.org/10.1007/978-3-319-48251-4_77.
[30] F.. Kimmerle, V. Kasireddy, J.. Tellier, SPL treatment by the LCL&L process: Pilot study of two-stage leaching, Light Met. (2001).
[31] Fennis S.A.A.M, Design of Ecological Concrete by Particle Packing Optimization, Delft University of Technology, 2008.
[32] A. Hajiesmaeili, E. Denarié, Next generation UHPFRC for sustainable structural applications, in: DSCS 2018 2nd Int. Workshop Durab. Sustain. Concr. Struct., 2018.
[33] G. Ye, N. Tuan, Mitigation of autogenous shrinkage of ultra-high performance concrete by rice husk ash, Kuei Suan Jen Hsueh PaoJournal Chin. Ceram. Soc. 40 (2012) 212–216.
[34] E. Ghafari, S.A. Ghahari, H. Costa, E. Júlio, A. Portugal, L. Durães, Effect of supplementary cementitious materials on autogenous shrinkage of ultra-high performance concrete, Constr. Build. Mater. 127 (2016) 43–48. https://doi.org/10.1016/j.conbuildmat.2016.09.123.
[35] H.A. Heinemann, Historic Concrete: From Concrete Repair to Concrete Conservation, (2013). https://repository.tudelft.nl/islandora/object/uuid%3A987fafd0-cd76-4230-be0e-be8843cae08e (accessed March 21, 2022).
[36] I.B.& M. Inc, Concrete Planet: The Strange And Fascinating Story Of The World's Most Common Man-made Material, Indigo.Ca. (n.d.). https://www.chapters.indigo.ca/en-ca/books/concrete-planet-the-strange-and/9781616144814-item.html (accessed March 21, 2022).
[37] C. Shi, Z. Wu, J. Xiao, D. Wang, Z. Huang, Z. Fang, A review on ultra high performance concrete: Part I. Raw materials and mixture design, Constr. Build. Mater. 101 (2015) 741–751. https://doi.org/10.1016/j.conbuildmat.2015.10.088.
[38] T. Guenet, UN MODÈLE NUMÉRIQUE POUR STRUCTURES EN BÉTON FIBRÉ À ULTRA-HAUTES PERFORMANCES : PRISE EN COMPTE DE L'ORIENTATION DES FIBRES PAR UNE APPROCHE D'ENDOMMAGEMENT MICROMÉCANIQUE, (n.d.) 154.
[39] Taylor, Cement Chemistry, (1990).

[40] I. Odler, 6 - Hydration, Setting and Hardening of Portland Cement, in: P.C. Hewlett (Ed.), Leas Chem. Cem. Concr. Fourth Ed., Butterworth-Heinemann, Oxford, 1998: pp. 241–297. https://doi.org/10.1016/B978-075066256-7/50018-7.
[41] H.F.W. Taylor, Cement chemistry, 2nd ed, T. Telford, London, 1997.
[42] G.C. Bye, Portland Cement: Composition, Production and Properties, Thomas Telford, 1999.
[43] D. Bentz, A three-dimensional cement hydration and microstructure program. I. Hydration rate, heat of hydration and chemical shrinkage, 1995.
[44] W. Kurdowski, Hydration of Clinker Phases, in: W. Kurdowski (Ed.), Cem. Concr. Chem., Springer Netherlands, Dordrecht, 2014: pp. 129–203. https://doi.org/10.1007/978-94-007-7945-7_3.
[45] S. CHATTERJI, J. JEFFERY, Studies of Early Stages of Paste Hydration of Cement Compounds, I, J. Am. Ceram. Soc. 45 (2006) 536–543. https://doi.org/10.1111/j.1151-2916.1962.tb11053.x.
[46] K. Van Breugel, Simulation of hydration and formation of structure in hardening cement-based materials, (1991). https://repository.tudelft.nl/islandora/object/uuid%3A2f8a3f72-1a25-4aa6-bc25-872df6fa32d4 (accessed March 12, 2022).
[47] S. Mindess, J.F. Young, Concrete, Prentice-Hall, Englewood Cliffs, N.J., 1981.
[48] H.M. Jennings, Refinements to colloid model of C-S-H in cement: CM-II, Cem. Concr. Res. 38 (2008) 275–289. https://doi.org/10.1016/j.cemconres.2007.10.006.
[49] F.W. Locher, Erstarren von Zement: Reaktion und Gefiigeentwicklung, Zem. Kalk Gips 10, 435–442., (1976).
[50] F. Avet, E. Boehm-Courjault, K. Scrivener, Investigation of C-A-S-H composition, morphology and density in Limestone Calcined Clay Cement (LC3), Cem. Concr. Res. 115 (2019) 70–79. https://doi.org/10.1016/j.cemconres.2018.10.011.
[51] E. L'Hôpital, B. Lothenbach, G. Le Saout, D. Kulik, K. Scrivener, Incorporation of aluminium in calcium-silicate-hydrates, Cem. Concr. Res. 75 (2015) 91–103. https://doi.org/10.1016/j.cemconres.2015.04.007.
[52] O. Ozcelik, C. White, Nanoscale Charge Balancing Mechanism in Alkali Substituted Calcium-Silicate-Hydrate Gels, J. Phys. Chem. Lett. 7 (2016). https://doi.org/10.1021/acs.jpclett.6b02233.
[53] K.L. Scrivener, Backscattered electron imaging of cementitious microstructures: understanding and quantification, Cem. Concr. Compos. 26 (2004) 935–945. https://doi.org/10/bfbdxh.
[54] I.G. Richardson, G.W. Groves, Microstructure and microanalysis of hardened ordinary Portland cement pastes, J. Mater. Sci. 28 (1993) 265–277. https://doi.org/10.1007/BF00349061.
[55] I.G. Richardson, Tobermorite/jennite- and tobermorite/calcium hydroxide-based models for the structure of C-S-H: applicability to hardened pastes of tricalcium silicate, β-dicalcium silicate, Portland cement, and blends of Portland cement with blast-furnace slag, metakaolin, or silica fume, Cem. Concr. Res. 34 (2004) 1733–1777. https://doi.org/10/b9q5r4.
[56] J. Rossen, Composition and morphology of C-A-S-H in pastes of alite and cement blended with supplementary cementitious materials, 2014. https://doi.org/10.5075/epfl-thesis-6294.
[57] H.M. Jennings, A model for the microstructure of calcium silicate hydrate in cement paste, Cem. Concr. Res. 30 (2000). https://doi.org/10.1016/S0008-8846(99)00209-4.
[58] A. Bazzoni, Study of early hydration mechanisms of cement by means of electron microscopy, EPFL, 2014. https://doi.org/10.5075/epfl-thesis-6296.
[59] Index - Petrographic Methods of Examining Hardened Concrete: A Petrographic Manual, July 2006 - FHWA-HRT-04-150, (n.d.).

https://www.fhwa.dot.gov/publications/research/infrastructure/pavements/pccp/04150/ (accessed March 14, 2022).
[60] J.E. Rossen, K.L. Scrivener, Optimization of SEM-EDS to determine the C–A–S–H composition in matured cement paste samples, Mater. Charact. 123 (2017) 294–306. https://doi.org/10/f9n2kt.
[61] P.T. Durdziński, M. Ben Haha, M. Zajac, K.L. Scrivener, Phase assemblage of composite cements, Cem. Concr. Res. 99 (2017) 172–182. https://doi.org/10.1016/j.cemconres.2017.05.009.
[62] F. Deschner, F. Winnefeld, B. Lothenbach, S. Seufert, P. Schwesig, S. Dittrich, F. Goetz-Neunhoeffer, J. Neubauer, Hydration of Portland cement with high replacement by siliceous fly ash, Cem. Concr. Res. 42 (2012) 1389–1400. https://doi.org/10.1016/j.cemconres.2012.06.009.
[63] W. Wilson, L. Sorelli, S. Krishnan, S. Bishnoi, A. Tagnit-Hamou, Micro-Chemo-Mechanical Characterization of a Limestone-Calcinated-Clay Cement Paste by Statistical Nanoindentation and Quantitative SEM-EDS, in: F. Martirena, A. Favier, K. Scrivener (Eds.), Calcined Clays Sustain. Concr., Springer Netherlands, 2018: pp. 494–499.
[64] M. Antoni, J. Rossen, F. Martirena, K. Scrivener, Cement substitution by a combination of metakaolin and limestone, Cem. Concr. Res. 42 (2012) 1579–1589. https://doi.org/10.1016/j.cemconres.2012.09.006.
[65] I.G. Richardson, The nature of C-S-H in hardened cements, Cem. Concr. Res. 29 (1999) 1131–1147. https://doi.org/10.1016/S0008-8846(99)00168-4.
[66] M.D. Jackson, S.R. Chae, S.R. Mulcahy, C. Meral, R. Taylor, P. Li, A.-H. Emwas, J. Moon, S. Yoon, G. Vola, H.-R. Wenk, P.J.M. Monteiro, Unlocking the secrets of Al-tobermorite in Roman seawater concrete†, Am. Mineral. 98 (2013) 1669–1687. https://doi.org/10.2138/am.2013.4484.
[67] W. Wilson, L. Sorelli, A. Tagnit-Hamou, Unveiling micro-chemo-mechanical properties of C–(A)–S–H and other phases in blended-cement pastes, Cem. Concr. Res. 107 (2018) 317–336. https://doi.org/10/gdhsr7.
[68] D. Damidot, S. Stronach, A. Kindness, M. Atkins, F.P. Glasser, Thermodynamic investigation of the CaO□Al2O3□CaCO3□H2O closed system at 25°C and the influence of Na2O, Cem. Concr. Res. 24 (1994) 563–572. https://doi.org/10.1016/0008-8846(94)90145-7.
[69] V.L. Bonavetti, V.F. Rahhal, E.F. Irassar, Studies on the carboaluminate formation in limestone filler-blended cements, Cem. Concr. Res. 31 (2001) 853–859. https://doi.org/10.1016/S0008-8846(01)00491-4.
[70] T. Matschei, B. Lothenbach, F.P. Glasser, The AFm phase in Portland cement, Cem. Concr. Res. 37 (2007) 118–130. https://doi.org/10.1016/j.cemconres.2006.10.010.
[71] K. De Weerdt, M.B. Haha, G. Le Saout, K.O. Kjellsen, H. Justnes, B. Lothenbach, Hydration mechanisms of ternary Portland cements containing limestone powder and fly ash, Cem. Concr. Res. 41 (2011) 279–291. https://doi.org/10.1016/j.cemconres.2010.11.014.
[72] Y. Wang, Z. Shui, L. Wang, X. Gao, Y. Huang, Q. Song, K. Liu, Alumina-rich pozzolan modification on Portland-limestone cement concrete: Hydration kinetics, formation of hydrates and long-term performance evolution, Constr. Build. Mater. 258 (2020) 119712. https://doi.org/10.1016/j.conbuildmat.2020.119712.
[73] Y. Wang, Z. Shui, X. Gao, R. Yu, Y. Huang, S. Cheng, Understanding the chloride binding and diffusion behaviors of marine concrete based on Portland limestone cement-alumina enriched pozzolans, Constr. Build. Mater. 198 (2019) 207–217. https://doi.org/10.1016/j.conbuildmat.2018.11.270.

[74] F. Zunino, K. Scrivener, Microstructural developments of limestone calcined clay cement (LC3) pastes after long-term (3 years) hydration, Cem. Concr. Res. 153 (2022) 106693. https://doi.org/10.1016/j.cemconres.2021.106693.
[75] F. Zunino, K. Scrivener, The hydration of limestone calcined clay cement (LC3) studied by in-situ X-Ray diffraction, 2018. https://doi.org/10.13140/RG.2.2.21725.74729.
[76] E. Berodier, K. Scrivener, Understanding the Filler Effect on the Nucleation and Growth of C-S-H, J. Am. Ceram. Soc. 97 (2014) 3764–3773. https://doi.org/10/f6rrjs.
[77] P. Lawrence, M. Cyr, E. Ringot, Mineral admixtures in mortars, Cem. Concr. Res. - CEM CONCR RES. 33 (2003) 1939–1947. https://doi.org/10.1016/S0008-8846(03)00183-2.
[78] T. Oey, A. Kumar, J.W. Bullard, N. Neithalath, G. Sant, The Filler Effect: The Influence of Filler Content and Surface Area on Cementitious Reaction Rates, J. Am. Ceram. Soc. 96 (2013) 1978–1990. https://doi.org/10.1111/jace.12264.
[79] Z. Zhang, Q. Wang, M. Zhang, Z. Huang, S. Zhuang, A new understanding of the effect of filler minerals on the precipitation of synthetic C–S–H, J. Mater. Sci. 55 (2020) 16455–16469. https://doi.org/10.1007/s10853-020-05185-2.
[80] K. Abdelli, T. Mahfoud, R. Belarbi, M.N. Oudjit, Influence of the pozzolanic reactivity of the Blast Furnace Slag (BFS) and metakaolin on mortars, Energy Procedia. 139 (2017) 224–229. https://doi.org/10.1016/j.egypro.2017.11.200.
[81] J. Pera, A. Wolde, M. Chabannet, Hydraulic activity of slags obtained by vitrification of wastes, ACI Mater. J. NovDec. 93 (1996) 613–618.
[82] P. Duan, Z. Shui, W. Chen, C. Shen, Effects of metakaolin, silica fume and slag on pore structure, interfacial transition zone and compressive strength of concrete, Constr. Build. Mater. 44 (2013) 1–6. https://doi.org/10.1016/j.conbuildmat.2013.02.075.
[83] R. Madandoust, M.M. Ranjbar, H.A. Moghadam, S.Y. Mousavi, Mechanical properties and durability assessment of rice husk ash concrete, Biosyst. Eng. 110 (2011) 144–152. https://doi.org/10.1016/j.biosystemseng.2011.07.009.
[84] M. Schneider, M. Romer, M. Tschudin, H. Bolio, Sustainable cement production—present and future, Cem. Concr. Res. 41 (2011) 642–650. https://doi.org/10.1016/j.cemconres.2011.03.019.
[85] UN Environment, K.L. Scrivener, V.M. John, E.M. Gartner, Eco-efficient cements: Potential economically viable solutions for a low-CO2 cement-based materials industry, Cem. Concr. Res. 114 (2018) 2–26. https://doi.org/10.1016/j.cemconres.2018.03.015.
[86] D. Bentz, J.T. Conway, Computer modeling of the replacement of “coarse” cement particles by inert fillers in low w/c ratio concretes: Hydration and strength, Cem. Concr. Res. 31 (2001) 503–506. https://doi.org/10.1016/S0008-8846(01)00456-2.
[87] D.P. Bentz, Replacement of “coarse” cement particles by inert fillers in low w/c ratio concretes: II. Experimental validation, Cem. Concr. Res. 35 (2005) 185–188.
[88] D.P. Bentz, E.F. Irassar, B.E. Bucher, W.J. Weiss, Limestone fillers conserve cement; Part 1: an analysis based on Powers’ model, Concr. Int. 31 (2009) 41–46.
[89] D. Bentz, E. Irassar, B.E. Bucher, W. Weiss, Limestone Fillers Conserve Cement Part 2: Durability Issues and the Effects of Limestone Fineness on Mixtures, Concr. Int. 31 (2009) 35–39.
[90] D. Bentz, M. Peltz, Reducing Thermal and Autogenous Shrinkage Contributions to Early-Age Cracking, Aci Mater. J. 105 (2008) 414–420.
[91] I.V. Flores, F. Fraiz, R.A. Lopes Junior, M.C. Bagatini, Evaluation of spent pot lining (SPL) as an alternative carbonaceous material in ironmaking processes, J. Mater. Res. Technol. (2017). https://doi.org/10/gfgng5.

[92] The SPL Waste Management Challenge in Primary Aluminum, Light Met. Age Mag. (2021). https://www.lightmetalage.com/news/industry-news/smelting/the-spl-waste-management-challenge-in-primary-aluminum/ (accessed April 4, 2022).
[93] International Aluminium Institute. Global Mass Flow Mode, (2018).
[94] X. Zhao, L. Ma, Hazardous waste treatment for spent pot liner, IOP Conf. Ser. Earth Environ. Sci. 108 (2018) 042023. https://doi.org/10.1088/1755-1315/108/4/042023.
[95] L. Birry, S. Leclerc, S. Poirier, the Lcl & L Process : a Sustainable Solution for the Treatment and Recycling of Spent Potlining, (2016) 467–472.
[96] J.-F. Batoz, M. Behloul, UHPFRC development on the last two decades: an overview, in: Fr. Marseille UHPFRC Conf., Marseille, 2009.
[97] F. de Larrard, T. Sedran, Optimization of ultra-high-performance concrete by the use of a packing model, Cem. Concr. Res. 24 (1994) 997–1009.
[98] J. Resplendino, F. Toulemonde, Designing and Building with UHPFRC, John Wiley & Sons, 2013.
[99] P. Richard, M.H. Cheyrezy, Reactive powder concretes with high ductility and 200-800 MPa compressive strength, Spec. Publ. 144 (1994) 507–518.
[100] P. Rossi, High performance multimodal fiber reinforced cement composites (HPMFRCC): the LCPC experience, ACI Mater. J. 94 (1997) 478–483.
[101] P. Acker, M. Behloul, Ductal® technology: A large spectrum of properties, a wide range of applications, in: Proc Int Symp UHPC Kassel Ger., 2004: pp. 11–23.
[102] U. Maeder, I. Lallemant-Gamboa, J. Chaignon, J.-P. Lombard, Ceracem, a new high performance concrete: characterisations and applications, in: First Int. Symp. Ultra High Perform. Concr. Kassel, 2004: pp. 59–68.
[103] H. Musha, H. Ohkuma, T. Kitamura, Innovative UFC structures in Japan, Newsletter. (2016).
[104] J. Resplendino, State of the art of design and construction of UHPFRC structures in France, Proc. Hipermat. (2012) 27–41.
[105] J. Resplendino, F. Toutlemonde, The UHPFRC revolution in structural design and construction, Newsletter. (2015).
[106] AFGC/SETRA, Ultra-high performance fibre-reinforced concretes - Recommendations, Interim Recomm. AFGC Publ. Fr. (2013). http://www.afgc.asso.fr/index.php/publications/41-publications/documents-scientifiques-et-techniques/37-documents-scientifiques-et-techniques-edition-afgc.
[107] K. Wille, A.E. Naaman, G.J. Parra-Montesinos, Ultra-High Performance Concrete with Compressive Strength Exceeding 150 MPa (22 ksi): A Simpler Way., ACI Mater. J. 108 (2011).
[108] B. Graybeal, F. Baby, Development of Direct Tension Test Method for Ultra-High-Performance Fiber-Reinforced Concrete, ACI Mater. J. 110 (2013) 177–186.
[109] G. Chanvillard, S. Rigaud, Complete characterization of tensile properties of Ductal® UHPFRC according to the French recommendations, High Perform. Fiber Reinf. Cem. Compos. HPFRCC4 Rilem Proc. PRO. 30 (2003) 21–34.
[110] S.-T. Kang, Y. Lee, Y.-D. Park, J.-K. Kim, Tensile fracture properties of an Ultra High Performance Fiber Reinforced Concrete (UHPFRC) with steel fiber, Compos. Struct. 92 (2010) 61–71.
[111] O. Millon, W. Riedel, K. Thoma, E. Fehling, M. Nöldgen, Fiber-reinforced ultra-high performance concrete under tensile loads, in: 9th Int. Conf. Mech. Behav. Mater. Dyn. Load. DYMAT, 2009: pp. 671–677.

[112] K. Wille, S. El-Tawil, A.E. Naaman, Properties of strain hardening ultra high performance fiber reinforced concrete (UHP-FRC) under direct tensile loading, Cem. Concr. Compos. 48 (2014) 53–66.
[113] K. Wille, A.E. Naaman, Fracture energy of UHPFRC under direct tensile loading, in: Fram.-7 Int. Conf. Jeju Korea, 2010.
[114] J.-P. Charron, E. Denarié, E. Brühwiler, Permeability of ultra high performance fiber reinforced concretes (UHPFRC) under high stresses, Mater. Struct. 40 (2007) 269–277.
[115] Guillaume Blais-Dufou, David Conciatori, Luca Sorelli, Dominique Corvez, Modified Chloride Migration test on UHPFRC samples, 9th RILEM Int. Symp. Fiber Reinf. Concr. BEFIB 2016 Vanc. Can. 19 - 21 Sept. 2016. (2016).
[116] M. Thomas, B. Green, E. O'Neal, V. Perry, S. Hayman, A. Hossack, Marine performance of UHPC at Treat Island, in: 2012: pp. 365–370.
[117] E. Denarié, E. Brühwiler, Strain-hardening Ultra-high Performance Fibre Reinforced Concrete: Deformability versus Strength Optimization, Restor. Build. Monum. 17 (2011) 397–410. https://doi.org/10/gkmwqz.
[118] Ductal, (2016). http://www.ductal.com/fr.
[119] O. Mishra, S.P. Singh, An overview of microstructural and material properties of ultra-high-performance concrete, J. Sustain. Cem.-Based Mater. 8 (2019) 97–143. https://doi.org/10.1080/21650373.2018.1564398.
[120] M. Schmidt, E. Fehling, eds., Ultra high performance concrete (UHPC): proceedings of the International Symposium on Ultra High Performance Concrete, Kassel, Germany, September 13-15, 2004, Kassel University Press, Kassel, 2004.
[121] P. Aitcin, Cements of yesterday and today Concrete of tomorrow, (2000). https://doi.org/10.1016/S0008-8846(00)00365-3.
[122] E. Ghafari, M. Arezoumandi, H. Costa, E. Júlio, Influence of nano-silica addition on durability of UHPC, Constr. Build. Mater. 94 (2015) 181–188. https://doi.org/10.1016/j.conbuildmat.2015.07.009.
[123] A. Hermann, E.A. Langaro, S.H.L.D. Silva, N.S. Klein, Particle packing of cement and silica fume in pastes using an analytical model, Rev. IBRACON Estrut. E Mater. 9 (2016) 48–65. https://doi.org/10.1590/S1983-41952016000100004.
[124] K. Wille, S. El-Tawil, A.E. Naaman, Properties of strain hardening ultra high performance fiber reinforced concrete (UHP-FRC) under direct tensile loading, Cem. Concr. Compos. 48 (2014) 53–66. https://doi.org/10.1016/j.cemconcomp.2013.12.015.
[125] A. Arora, M. Aguayo, H. Hansen, C. Castro, E. Federspiel, B. Mobasher, N. Neithalath, Microstructural packing- and rheology-based binder selection and characterization for Ultra-high Performance Concrete (UHPC), Cem. Concr. Res. 103 (2018) 179–190. https://doi.org/10.1016/j.cemconres.2017.10.013.
[126] V. Waller, RELATIONS ENTRE COMPOSITION DES BETONS, EXOTHERMIE EN COURS DE PRISE ET RESISTANCE EN COMPRESSION, 1999.
[127] R. Zhong, K. Wille, R. Viegas, Material efficiency in the design of UHPC paste from a life cycle point of view, Constr. Build. Mater. 160 (2018) 505–513. https://doi.org/10.1016/j.conbuildmat.2017.11.049.
[128] A. Alsalman, C.N. Dang, J.R. Martí-Vargas, W. Micah Hale, Mixture-proportioning of economical UHPC mixtures, J. Build. Eng. 27 (2020) 100970. https://doi.org/10.1016/j.jobe.2019.100970.
[129] H.A. Shah, Q. Yuan, N. Photwichai, Use of materials to lower the cost of ultra-high-performance concrete – A review, Constr. Build. Mater. 327 (2022) 127045. https://doi.org/10.1016/j.conbuildmat.2022.127045.

[130] S. Abbas, M.L. Nehdi, M.A. Saleem, Ultra-High Performance Concrete: Mechanical Performance, Durability, Sustainability and Implementation Challenges, Int. J. Concr. Struct. Mater. 10 (2016) 271–295. https://doi.org/10.1007/s40069-016-0157-4.
[131] P.K. Mehta, P.J.M. Monteiro, Concrete: microstructure, properties, and materials, 3rd ed, McGraw-Hill, New York, 2006.
[132] K. Wille, A. Naaman, G. Parra-Montesinos, Ultra-High Performance Concrete with Compressive Strength Exceeding 150 MPa (22 ksi): A Simpler Way, ACI Mater. J. 108 (2011) 46–54.
[133] P. Rossi, Development of new cement composite materials for construction, Proc. Inst. Mech. Eng. Part -J. Mater.-Des. Appl. - PROC INST MECH ENG -J MATER. 219 (2005) 67–74. https://doi.org/10.1243/146442005X10193.
[134] P. Richard, M. Cheyrezy, Composition of reactive powder concretes, Cem. Concr. Res. 25 (1995) 1501–1511. https://doi.org/10/c95grc.
[135] A. Imam, K.K. Sharma, V. Kumar, N. Singh, A. Imam, K.K. Sharma, V. Kumar, N. Singh, A review study on sustainable development of ultra high-performance concrete, AIMS Mater. Sci. 9 (2022) 9–35. https://doi.org/10.3934/matersci.2022002.
[136] W. Huang, H. Kazemi-Kamyab, W. Sun, K. Scrivener, Effect of replacement of silica fume with calcined clay on the hydration and microstructural development of eco-UHPFRC, Mater. Des. 121 (2017) 36–46. https://doi.org/10.1016/j.matdes.2017.02.052.
[137] R. Flatt, I. Schober, 7 - Superplasticizers and the rheology of concrete, in: N. Roussel (Ed.), Underst. Rheol. Concr., Woodhead Publishing, 2012: pp. 144–208. https://doi.org/10.1533/9780857095282.2.144.
[138] C.-Z. Li, N.-Q. Feng, Y.-D. Li, R.-J. Chen, Effects of polyethlene oxide chains on the performance of polycarboxylate-type water-reducers, Cem. Concr. Res. 35 (2005) 867–873. https://doi.org/10.1016/j.cemconres.2004.04.031.
[139] Y. Li, C. Yang, Y. Zhang, J. Zheng, H. Guo, M. Lu, Study on dispersion, adsorption and flow retaining behaviors of cement mortars with TPEG-type polyether kind polycarboxylate superplasticizers, Constr. Build. Mater. 64 (2014) 324–332. https://doi.org/10.1016/j.conbuildmat.2014.04.050.
[140] Y. Zhang, X. Kong, Correlations of the dispersing capability of NSF and PCE types of superplasticizer and their impacts on cement hydration with the adsorption in fresh cement pastes, Cem. Concr. Res. 69 (2015). https://doi.org/10.1016/j.cemconres.2014.11.009.
[141] P.P. Li, Q.L. Yu, H.J.H. Brouwers, Effect of PCE-type superplasticizer on early-age behaviour of ultra-high performance concrete (UHPC), Constr. Build. Mater. 153 (2017) 740–750. https://doi.org/10.1016/j.conbuildmat.2017.07.145.
[142] E. Fehling, M. Schmidt, J. Walraven, T. Leutbecher, S. Fröhlich, Ultra-High Performance Concrete UHPC, 2014. http://onlinelibrary.wiley.com/book/10.1002/9783433604076.
[143] J. Ma, M. Orgass, F. Dehn, D. Schmidt, N.V. Tue, Comparative investigations on ultra-high performance concrete with and without coarse aggregates, in: Proc. Int. Symp. Ultra High Perform. Concr. Ger., 2004: pp. 205–212.
[144] P. Richard, M. Cheyrezy, Composition of reactive powder concretes, Cem. Concr. Res. 25 (1995) 1501–1511.
[145] K. Scrivener, R. Snellings, B. Lothenbach, A Practical Guide to Microstructural Analysis of Cementitious Materials, CRC Press, 2016.
[146] J. Jain, N. Neithalath, Analysis of calcium leaching behavior of plain and modified cement pastes in pure water, Cem. Concr. Compos. 31 (2009) 176–185. https://doi.org/10.1016/j.cemconcomp.2009.01.003.

[147] J. Goldstein, D.E. Newbury, D.C. Joy, C.E. Lyman, P. Echlin, E. Lifshin, L. Sawyer, J.R. Michael, Scanning Electron Microscopy and X-Ray Microanalysis: Third Edition, 3rd ed., Springer US, 2003. https://doi.org/10.1007/978-1-4615-0215-9.
[148] J. Vanzo, A nanochemomechanical investigation of carbonated cement paste, (2010).
[149] J. Frech-Baronet, L. Sorelli, J.-P. Charron, New evidences on the effect of the internal relative humidity on the creep and relaxation behaviour of a cement paste by micro-indentation techniques, Cem. Concr. Res. 91 (2017) 39–51. https://doi.org/10/f9hpsq.
[150] Y. Wei, S. Liang, X. Gao, Indentation creep of cementitious materials: Experimental investigation from nano to micro length scales, Constr. Build. Mater. 143 (2017) 222–233. https://doi.org/10/ggkmkj.
[151] M. Vandamme, F.-J. Ulm, Nanoindentation investigation of creep properties of calcium silicate hydrates, Cem. Concr. Res. 52 (2013) 38–52. https://doi.org/10/f5f4zk.
[152] F.-J. Ulm, M. Vandamme, C. Bobko, J.A. Ortega, K. Tai, C. Ortiz, Statistical Indentation Techniques for Hydrated Nanocomposites: Concrete, Bone, and Shale, J. Am. Ceram. Soc. 90 (2007) 2677–2692. https://doi.org/10/czhw6g.
[153] F.-J. Ulm, M. Vandamme, H.M. Jennings, J. Vanzo, M. Bentivegna, K.J. Krakowiak, G. Constantinides, C.P. Bobko, K.J. Van Vliet, Does microstructure matter for statistical nanoindentation techniques?, Cem. Concr. Compos. 32 (2010) 92–99. https://doi.org/10/cq28qh.
[154] M. Miller, C. Bobko, M. Vandamme, F.-J. Ulm, Surface roughness criteria for cement paste nanoindentation, Cem. Concr. Res. 38 (2008) 467–476. https://doi.org/10/bpc9km.
[155] W.C. Oliver, G.M. Pharr, An improved technique for determining hardness and elastic modulus using load and displacement sensing indentation experiments, J. Mater. Res. 7 (1992) 1564–1583. https://doi.org/10/bdv47f.
[156] J. Baronet, L. Sorelli, J.-P. Charron, M. Vandamme, J. Sanahuja, A two-time-scale method to quickly characterize the logarithmic basic creep of concrete by combining microindentation and Uniaxial Compression Creep Tests., Cem. Concr. Compos. (2021).
[157] M. Vandamme, The nanogranular origin of concrete creep : a nanoindentation investigation of microstructure and fundamental properties of calcium-silicate-hydrates, (2008).
[158] F. de Larrard, T. Sedran, Optimization of ultra-high-performance concrete by the use of a packing model, Cem. Concr. Res. 24 (1994) 997–1009. https://doi.org/10/czwwbv.
[159] A.K.H. Kwan, C.F. Mora, Effects of various shape parameters on packing of aggregate particles, Mag. Concr. Res. 53 (2001) 91–100. https://doi.org/10.1680/macr.2001.53.2.91.
[160] F. de Larrard, Concrete mixture proportioning: a scientific approach, (1999).
[161] F. de Larrard, T. Sedran, Mixture-proportioning of high-performance concrete, Cem. Concr. Res. 32 (2002) 1699–1704. https://doi.org/10.1016/S0008-8846(02)00861-X.
[162] T. Stovall, F. de Larrard, M. Buil, Linear packing density model of grain mixtures, Powder Technol. 48 (1986) 1–12. https://doi.org/10.1016/0032-5910(86)80058-4.
[163] F. S.A.A.M, Design of Ecological Concrete by Particle Packing Optimization, (2008).
[164] Marquardt I, Determination of the composition of self-compacting concretes on the basis of the water requirements of the constituent materials – presentation of a new mix concept, Betonw. Fert. – BFT. No.11 (2002) pp.22-30.
[165] A. Radocea, Autogenous volume change of concrete at very early age, Mag. Concr. Res. 50 (1998) 107–113. https://doi.org/10.1680/macr.1998.50.2.107.
[166] E. Tazawa, S. Miyazawa, Experimental study on mechanism of autogenous shrinkage of concrete, Cem. Concr. Res. 25 (1995) 1633–1638. https://doi.org/10.1016/0008-8846(95)00159-X.

[167] D.-Y. Yoo, S. Kim, M.-J. Kim, Comparative shrinkage behavior of ultra-high-performance fiber-reinforced concrete under ambient and heat curing conditions, Constr. Build. Mater. 162 (2018) 406–419. https://doi.org/10.1016/j.conbuildmat.2017.12.029.
[168] A.M. Soliman, M.L. Nehdi, Effect of Natural Wollastonite Microfibers on Early-Age Behavior of UHPC, J. Mater. Civ. Eng. 24 (2012) 816–824. https://doi.org/10.1061/(ASCE)MT.1943-5533.0000473.
[169] A.M. Soliman, M.L. Nehdi, Effects of shrinkage reducing admixture and wollastonite microfiber on early-age behavior of ultra-high performance concrete, Cem. Concr. Compos. 46 (2014) 81–89. https://doi.org/10.1016/j.cemconcomp.2013.11.008.
[170] A.M. Soliman, M.L. Nehdi, Effect of partially hydrated cementitious materials and superabsorbent polymer on early-age shrinkage of UHPC, Constr. Build. Mater. 41 (2013) 270–275. https://doi.org/10.1016/j.conbuildmat.2012.12.008.
[171] H.K. Lee, K.M. Lee, B.G. Kim, Autogenous shrinkage of high-performance concrete containing fly ash, Mag. Concr. Res. 55 (2003) 507–515. https://doi.org/10.1680/macr.2003.55.6.507.
[172] O.A. Hisseine, N.A. Soliman, B. Tolnai, A. Tagnit-Hamou, Nano-engineered ultra-high performance concrete for controlled autogenous shrinkage using nanocellulose, Cem. Concr. Res. 137 (2020) 106217. https://doi.org/10.1016/j.cemconres.2020.106217.
[173] I. Ferdosian, A. Camões, M. Ribeiro, High-volume fly ash paste for developing ultra-high performance concrete (UHPC), Ciênc. Tecnol. Mater. 29 (2017) e157–e161. https://doi.org/10.1016/j.ctmat.2016.10.001.
[174] M.A. Bahedh, M.S. Jaafar, Ultra high-performance concrete utilizing fly ash as cement replacement under autoclaving technique, Case Stud. Constr. Mater. 9 (2018) e00202. https://doi.org/10.1016/j.cscm.2018.e00202.
[175] R. Yang, R. Yu, Z. Shui, X. Gao, X. Xiao, X. Zhang, Y. Wang, Y. He, Low carbon design of an Ultra-High Performance Concrete (UHPC) incorporating phosphorous slag, J. Clean. Prod. 240 (2019) 118157. https://doi.org/10.1016/j.jclepro.2019.118157.
[176] T. Ahmed, M. Elchalakani, A. Karrech, M.S. Mohamed Ali, L. Guo, Development of ECO-UHPC with very-low-C3A cement and ground granulated blast-furnace slag, Constr. Build. Mater. 284 (2021) 122787. https://doi.org/10.1016/j.conbuildmat.2021.122787.
[177] Z. He, S. Du, D. Chen, Microstructure of ultra high performance concrete containing lithium slag, J. Hazard. Mater. 353 (2018) 35–43. https://doi.org/10.1016/j.jhazmat.2018.03.063.
[178] P.P. Li, H.J.H. Brouwers, W. Chen, Q. Yu, Optimization and characterization of high-volume limestone powder in sustainable ultra-high performance concrete, Constr. Build. Mater. 242 (2020) 118112. https://doi.org/10.1016/j.conbuildmat.2020.118112.
[179] W. Huang, H. Kazemi-Kamyab, W. Sun, K. Scrivener, Effect of cement substitution by limestone on the hydration and microstructural development of ultra-high performance concrete (UHPC), Cem. Concr. Compos. 77 (2017) 86–101. https://doi.org/10.1016/j.cemconcomp.2016.12.009.
[180] A.S. Faried, S.A. Mostafa, B.A. Tayeh, T.A. Tawfik, The effect of using nano rice husk ash of different burning degrees on ultra-high-performance concrete properties, Constr. Build. Mater. 290 (2021) 123279. https://doi.org/10.1016/j.conbuildmat.2021.123279.
[181] N. Van Tuan, G. Ye, K. van Breugel, A.L.A. Fraaij, D.D. Bui, The study of using rice husk ash to produce ultra high performance concrete, Constr. Build. Mater. 25 (2011) 2030–2035. https://doi.org/10.1016/j.conbuildmat.2010.11.046.
[182] Í. Boadella, F. Lopez Gayarre, J. González, J. Gómez-Soberón, C. López-Colina Pérez, M. López, J. Brito, The Influence of Granite Cutting Waste on The Properties of Ultra-High Performance Concrete, Materials. 12 (2019) 634. https://doi.org/10.3390/ma12040634.

[183] H. Zhang, T. Ji, B. He, L. He, Performance of ultra-high performance concrete (UHPC) with cement partially replaced by ground granite powder (GGP) under different curing conditions, Constr. Build. Mater. 213 (2019) 469–482. https://doi.org/10.1016/j.conbuildmat.2019.04.058.
[184] N. Soliman, A. Tagnit-Hamou, Partial substitution of silica fume with fine glass powder in UHPC: Filling the micro gap, Constr. Build. Mater. 139 (2017) 374–383. https://doi.org/10.1016/j.conbuildmat.2017.02.084.
[185] N.A. Soliman, A. Tagnit-Hamou, Development of ultra-high-performance concrete using glass powder – Towards ecofriendly concrete, Constr. Build. Mater. 125 (2016) 600–612. https://doi.org/10.1016/j.conbuildmat.2016.08.073.
[186] K.L. Scrivener, Options for the future of cement, Indian Concr J. 88 (2014) 11–21.
[187] R.P. Khatri, V. Sirivivatnanon, W. Gross, Effect of different supplementary cementitious materials on mechanical properties of high performance concrete, Cem. Concr. Res. 25 (1995) 209–220. https://doi.org/10/b6f9nt.
[188] M.B. Haha, K. De Weerdt, B. Lothenbach, Quantification of the degree of reaction of fly ash, Cem. Concr. Res. 40 (2010) 1620–1629. https://doi.org/10/fv37rm.
[189] V. Kocaba, E. Gallucci, K.L. Scrivener, Methods for determination of degree of reaction of slag in blended cement pastes, Cem. Concr. Res. 42 (2012) 511–525. https://doi.org/10/fzhz7r.
[190] S. Feng, P. Wang, X. Liu, SEM-backscattered electron imaging and image processing for evaluation of unhydrated cement volume fraction in slag blended Portland cement pastes, J. Wuhan Univ. Technol.-Mater Sci Ed. 28 (2013) 968–972. https://doi.org/10/ggkzth.
[191] K. Scrivener, F. Martirena, S. Bishnoi, S. Maity, Calcined clay limestone cements (LC 3), Cem. Concr. Res. (2017).
[192] SINTEF Building and Infrastructure, Norway, H. Justnes, How SCMs Improve Concrete Durability – A Fundamental View, in: 2016: pp. 25–46. https://doi.org/10/ghj8hp.
[193] A.K. Saha, M.N.N. Khan, P.K. Sarker, F.A. Shaikh, A. Pramanik, The ASR mechanism of reactive aggregates in concrete and its mitigation by fly ash: A critical review, Constr. Build. Mater. 171 (2018) 743–758.
[194] A. Adesina, S. Das, Influence of glass powder on the durability properties of engineered cementitious composites, Constr. Build. Mater. 242 (2020) 118199.
[195] M.T. de Grazia, H. Deda, L.F. Sanchez, The influence of the binder type & aggregate nature on the electrical resistivity of conventional concrete, J. Build. Eng. 43 (2021) 102540.
[196] J. Camiletti, A.M. Soliman, M.L. Nehdi, Effect of nano-calcium carbonate on early-age properties of ultra-high-performance concrete, Mag. Concr. Res. 65 (2013) 297–307.
[197] The Greenest Aluminium in the World, (n.d.). https://www.investquebec.com/international/en/industries/aluminum/the-greenest-aluminum-in-the-world.html (accessed September 28, 2021).
[198] M.A. Jawi, C.-M. Chow, S. Pujari, M. Pan, T. Kulkarni, M. Mahmoud, H. Akasha, S. Abdulla, Environmental Benefits of Using Spent Pot Lining (SPL) in Cement Production, in: 2020. https://doi.org/10.1007/978-3-030-36408-3_172.
[199] H.A. Øye, Discussion of Industrial Spent Pot Lining Treatment, (n.d.) 8.
[200] A. Al-Maqbali, S. Feroz, G. Ram, H. Al-Dhamri, Feasibility Study on Spent Pot Lining (SPL) as Raw Material in Cement Manufacture Process, (2016) 10.
[201] S. Laldji, A. Tagnit-Hamou, Glass frit for concrete structures: a new, alternative cementitious material, Can. J. Civ. Eng. 34 (2007) 793–802. https://doi.org/10/bk2m68.
[202] V. Gomes, P.Z. Drumond, J.O.P. Neto, A.R. Lira, Co-Processing at Cement Plant of Spent Potlining from the Aluminum Industry, in: A. Tomsett, J. Johnson (Eds.), Essent. Read. Light

Met. Vol. 4 Electrode Technol. Alum. Prod., Springer International Publishing, Cham, 2016: pp. 1057–1063. https://doi.org/10.1007/978-3-319-48200-2_142.
[203] I. Fernandes, M.A.T.M. Broekmans, Alkali–Silica Reactions: An Overview. Part I, Metallogr. Microstruct. Anal. 2 (2013). https://doi.org/10/gjg854.
[204] G. Fares, Nouveau systèmecimentaire: casde la Frittede verre(New CementitiousSystem: the case of Glass Frit)., (2008).
[205] S. Laldji, A. Phithaksounthone, A. Tagnit-Hamou, Synergistic Effect between Glass Frit and Blast-Furnace Slag, ACI Mater. J. 107 (2010) 75–79.
[206] V. Brial, H. Tran, C. Ouellet-Plamondon, L. Sorelli, D. Conciatori, Evaluation of the reactivity of treated spent pot lining from primary aluminum production as cementitious materials, Resour. Conserv. Recycl. (2021).
[207] F. Avet, R. Snellings, A. Alujas, K. Scrivener, Development of a New Rapid, Relevant and Reliable (R3) Testing Method to Evaluate the Pozzolanic Reactivity of Calcined Clays, in: K. Scrivener, A. Favier (Eds.), Calcined Clays Sustain. Concr., Springer Netherlands, Dordrecht, 2015: pp. 539–544. https://doi.org/10/gh75fg.
[208] Maubert, F., Le gypse et l'anhydrite, (1987).
[209] U. Environment, K.L. Scrivener, V.M. John, E.M. Gartner, Eco-efficient cements: Potential economically viable solutions for a low-CO2 cement-based materials industry, Cem. Concr. Res. 114 (2018) 2–26. https://doi.org/10/dbmc.
[210] T.H. Adams, Fly Ash Use in Concrete Increases Slightly As Overall Coal Ash Recycling Rate Declines, (n.d.) 5.
[211] V. Brial, H. Tran, L. Sorelli, D. Conciatori, C.M. Ouellet-Plamondon, Evaluation of the reactivity of treated spent pot lining from primary aluminum production as cementitious materials, Resour. Conserv. Recycl. 170 (2021) 105584. https://doi.org/10.1016/j.resconrec.2021.105584.
[212] X. Wang, A.B. Eberhardt, K.L. Scrivener, E. Gallucci, Assessing Early Age Properties Of Cementitious Systems By Water-Isopropanol Replacement, in: 2014.
[213] The suitability of solvent exchange techniques for studying the pore structure of hardened cement paste | M.D.A. Thomas, ResearchGate. (n.d.).
[214] M. Zajac, A. Rossberg, G. Le Saout, B. Lothenbach, Influence of limestone and anhydrite on the hydration of Portland cements, Cem. Concr. Compos. 46 (2014) 99–108. https://doi.org/10/ggrbdh.
[215] I. Soroka, M. Abayneh, Effect of gypsum on properties and internal structure of PC paste, Cem. Concr. Res. 16 (1986) 495–504. https://doi.org/10/c4trfm.
[216] P. Feng, C. Miao, J. Bullard, Factors Influencing the Stability of AFm and AFt in the Ca - Al - S - O - H System at 25 ° C, J. Am. Ceram. Soc. 99 (2015) n/a-n/a. https://doi.org/10/f8frnf.
[217] T. Matschei, B. Lothenbach, F.P. Glasser, The AFm phase in Portland cement, Cem. Concr. Res. 37 (2007) 118–130. https://doi.org/10/dxh5jn.
[218] M. Antoni, J. Rossen, F. Martirena, K. Scrivener, Cement substitution by a combination of metakaolin and limestone, Cem. Concr. Res. 42 (2012) 1579–1589. https://doi.org/10/ghdfsw.
[219] P. Lura, O.M. Jensen, J. Weiss, Cracking in cement paste induced by autogenous shrinkage, Mater. Struct. 42 (2009) 1089–1099. https://doi.org/10/cxhm3d.
[220] W. Wilson, L. Sorelli, A. Tagnit-Hamou, Automated coupling of NanoIndentation and Quantitative Energy-Dispersive Spectroscopy (NI-QEDS): A comprehensive method to disclose the micro-chemo-mechanical properties of cement pastes, Cem. Concr. Res. 103 (2018) 49–65. https://doi.org/10/gcwq6m.

[221] K.L. Scrivener, H.H. Patel, P.L. Pratt, L.J. Parrott, Analysis of Phases in Cement Paste using Backscattered Electron Images, Methanol Adsorption and Thermogravimetric Analysis, MRS Online Proc. Libr. Arch. 85 (1986). https://doi.org/10/b59fc9.
[222] K.L. Scrivener, P.L. Pratt, Backscattered Electron Images Of Polished Cement Sections In The Scanning Electron Microscope, Proc. Int. Conf. Cem. Microsc. (1984) 145–155.
[223] E. L'Hôpital, B. Lothenbach, D.A. Kulik, K. Scrivener, Influence of calcium to silica ratio on aluminium uptake in calcium silicate hydrate, Cem. Concr. Res. 85 (2016) 111–121. https://doi.org/10/f8txjs.
[224] R.A. Alizadeh, Nanostructure and engineering properties of basic and modified calcium-silicate-hydrate systems, University of Ottawa (Canada), 2009.
[225] R. Shahsavari, M.J. Buehler, R.J.-M. Pellenq, F.-J. Ulm, First-principles study of elastic constants and interlayer interactions of complex hydrated oxides: Case study of tobermorite and jennite, J. Am. Ceram. Soc. 92 (2009) 2323–2330.
[226] L. Sorelli, D. Vallée, A.R. Alizadeh, J. Beaudoin, N. Randall, Disclosing the mechanical properties of green calcium-silicate-hydrates by statistical nanoindentation techniques, in: Adv. Mater. Res., Trans Tech Publ, 2012: pp. 544–549.
[227] Q. Zhang, R. Le Roy, M. Vandamme, B. Zuber, Long-term creep properties of cementitious materials: Comparing microindentation testing with macroscopic uniaxial compressive testing, Cem. Concr. Res. 58 (2014) 89–98. https://doi.org/10/gg3w35.
[228] C.P. Bobko, B. Gathier, J.A. Ortega, F.-J. Ulm, L. Borges, Y.N. Abousleiman, The nanogranular origin of friction and cohesion in shale—a strength homogenization approach to interpretation of nanoindentation results, Int. J. Numer. Anal. Methods Geomech. 35 (2011) 1854–1876.
[229] A.C. Fischer-Cripps, Nanoindentation Springer, N. Y. (2004).
[230] S. Diamond, The microstructure of cement paste and concrete—a visual primer, Cem. Concr. Compos. 26 (2004) 919–933. https://doi.org/10/bkmvfx.
[231] R. Talero, C. Pedrajas, M. González, C. Aramburo, A. Blázquez, V. Rahhal, Role of the filler on Portland cement hydration at very early ages: Rheological behaviour of their fresh cement pastes, Constr. Build. Mater. 151 (2017) 939–949. https://doi.org/10/ghn3w9.
[232] S. Cariou, F.-J. Ulm, L. Dormieux, Hardness–packing density scaling relations for cohesive-frictional porous materials, J. Mech. Phys. Solids. 56 (2008) 924–952.
[233] G. Vijayakumar, H. Vishaliny, D. Govindarajulu, Studies on Glass Powder as Partial Replacement of Cement in Concrete Production, Undefined. (2013). https://www.semanticscholar.org/paper/Studies-on-Glass-Powder-as-Partial-Replacement-of-Vijayakumar-Vishaliny/e9e5846be36aa3c3b76f428b848492f25ba89b2b (accessed October 18, 2021).
[234] F. Rajabipour, H. Maraghechi, G. Fischer, Investigating the Alkali Silica Reaction of Recycled Glass Aggregates in Concrete Materials, J. Mater. Civ. Eng. - J MATER Civ. ENG. 22 (2010). https://doi.org/10/cgrpm3.
[235] M. Boháč, M. Palou, R. Novotný, J. Másilko, D. Všianský, T. Staněk, Investigation on early hydration of ternary Portland cement-blast-furnace slag–metakaolin blends, Constr. Build. Mater. 64 (2014) 333–341. https://doi.org/10.1016/j.conbuildmat.2014.04.018.
[236] H. Sasanipour, F. Aslani, Effect of specimen shape, silica fume, and curing age on durability properties of self-compacting concrete incorporating coarse recycled concrete aggregates, Constr. Build. Mater. 228 (2019) 117054. https://doi.org/10.1016/j.conbuildmat.2019.117054.
[237] N. Van Tuan, G. Ye, K. van Breugel, A.L.A. Fraaij, D.D. Bui, The study of using rice husk ash to produce ultra high performance concrete, Constr. Build. Mater. 25 (2011) 2030–2035. https://doi.org/10.1016/j.conbuildmat.2010.11.046.

[238] H. El-Diadamony, A.A. Amer, T.M. Sokkary, S. El-Hoseny, Hydration and characteristics of metakaolin pozzolanic cement pastes, HBRC J. 14 (2018) 150–158. https://doi.org/10/gfpkjw.
[239] Kannan, Mechanical and transport properties in ternary blended self compacting concrete with metakaolin and fly ash, (2012). https://doi.org/10.9790/1684-0242231.
[240] M. Canut, S. Miller, M. Jolnæs, Calcined Clay: Process Impact on the Reactivity and Color, in: S. Bishnoi (Ed.), Calcined Clays Sustain. Concr., Springer, Singapore, 2020: pp. 163–167. https://doi.org/10.1007/978-981-15-2806-4_19.
[241] B.B. Sabir, S. Wild, J. Bai, Metakaolin and calcined clays as pozzolans for concrete: a review, Cem. Concr. Compos. 23 (2001) 441–454.
[242] M. Murat, Hydration reaction and hardening of calcined clays and related minerals. I. Preliminary investigation on metakaolinite, (1983). https://doi.org/10.1016/0008-8846(83)90109-6.
[243] V. Brial, H. Tran, L. Sorelli, D. Conciatori, C. Ouellet-Plamondon, Evaluation of the reactivity of treated spent pot lining from primary aluminum production as cementitious materials, Resour. Conserv. Recycl. 170 (2021) 105584. https://doi.org/10.1016/j.resconrec.2021.105584.
[244] K. De Weerdt, K.O. Kjellsen, E. Sellevold, H. Justnes, Synergy between fly ash and limestone powder in ternary cements, Cem. Concr. Compos. 33 (2011) 30–38. https://doi.org/10.1016/j.cemconcomp.2010.09.006.
[245] H. Tran, V. Brial, D. Conciatori, C. Ouellet-Plamondon, L. Sorelli, Microstructure Characterization of Cement Pastes with Mineral Fillers Recycled from Aluminum Production By-products, J. Elsevier Cem. Concr. Compos. (under review) (n.d.).
[246] K.L. Scrivener, P. Juilland, P.J.M. Monteiro, Advances in understanding hydration of Portland cement, Cem. Concr. Res. 78 (2015) 38–56. https://doi.org/10.1016/j.cemconres.2015.05.025.
[247] P.R. de Matos, R.D. Sakata, P.J.P. Gleize, J. de Brito, W.L. Repette, Eco-friendly ultra-high performance cement pastes produced with quarry wastes as alternative fillers, J. Clean. Prod. 269 (2020) 122308. https://doi.org/10.1016/j.jclepro.2020.122308.
[248] L. Teng, M. Valipour, K.H. Khayat, Design and performance of low shrinkage UHPC for thin bonded bridge deck overlay, Cem. Concr. Compos. 118 (2021) 103953. https://doi.org/10.1016/j.cemconcomp.2021.103953.
[249] G. Habert, E. Denarié, A. Sajna, P. Rossi, Lowering the global warming impact of bridge rehabilitations by using Ultra High Performance Fibre Reinforced Concretes, Cem. Amp Concr. Compos. 38 (2013) 1. https://doi.org/10.1016/j.cemconcomp.2012.11.008.
[250] B. Graybeal, Development of Non-Proprietary Ultra-High Performance Concrete for Use in the Highway Bridge Sector : TechBrief, Undefined. (2013).
[251] H.A. Toutanji, T. El-Korchi, The influence of silica fume on the compressive strength of cement paste and mortar, Cem. Concr. Res. 25 (1995) 1591–1602.
[252] A. Tagnit-Hamou, N. Soliman, A. Omran, Green Ultra-High Performance Glass Concrete, in: Proc. First Int. Interact. Symp. UHPC, Iowa State University, Des Moines, Iowa, USA, 2016. https://doi.org/10/gft8p7.
[253] G. Hernández-Carrillo, A. Durán-Herrera, A. Tagnit-Hamou, Optimization of Ultra-High-Performance Concrete Using Soft and Hard Inert Fillers (Limestone and Quartz)., ACI Mater. J. 119 (2022).
[254] V. Srivastava, R. Kumar, V. Agarwal, P. Mehta, Effect of Silica Fume on Workability and Compressive Strength of OPC Concrete, 3 (2015) 32–35. https://doi.org/10.13074/jent.2014.09.143086.
[255] A. Hajiesmaeili, Next generation synthetic fibers UHPFRC for sustainable structural applications, EPFL, 2019.

[256] A. Hajiesmaeili, F. Pittau, E. Denarié, G. Habert, Life cycle analysis of strengthening existing RC structures with R-PE-UHPFRC, Sustainability. 11 (2019) 6923.
[257] D. Bouchard, L. Sorelli, Development of High-Performance Concrete using Recycled Granite Powders, Constr. Build. Mater. (2022).
[258] L. Sorelli, R. Davila, F.-J. Ulm, V. Perry, P. Seibert, Risk Analysis of Early-Age Cracking in UHPC Structures, in: Kassel, Germany, 2008: pp. 331–338.
[259] Z. Haber, I. De La Varga, J.F. Munoz, B.A. Graybeal, UHPC Overlays for Highway Bridge Decks: Bond Behavior, Durability, and Structural Performance, in: Iowa State University Digital Press, 2019.
[260] H.J.H. Brouwers, H.J. Radix, Self-Compacting Concrete: Theoretical and experimental study, Cem. Concr. Res. 35 (2005) 2116–2136. https://doi.org/10.1016/j.cemconres.2005.06.002.
[261] H.F.W. Taylor, Cement chemistry, 2nd ed, T. Telford, London, 1997.
[262] Y. Cao, P. Zavaterri, J. Youngblood, R. Moon, J. Weiss, The influence of cellulose nanocrystal additions on the performance of cement paste, Cem. Concr. Compos. 56 (2015) 73–83. https://doi.org/10.1016/j.cemconcomp.2014.11.008.
[263] M.A. Hafiz, J. Skibsted, E. Denarié, Influence of low curing temperatures on the tensile response of low clinker strain hardening UHPFRC under full restraint, Cem. Concr. Res. 128 (2020) 105940. https://doi.org/10.1016/j.cemconres.2019.105940.
[264] F.. Hansen, E.J. Pedersen, Maturity computer for controlled curing and hardening of concrete, Nord Betong 1. (1977) 21–25.
[265] A. Kamen, Comportement au jeune âge et différé d'un BFUP écrouissant sous les effets thermomécaniques, EPFL, 2007. https://doi.org/10.5075/epfl-thesis-3827.
[266] J. Baronet, L. Sorelli, Z. Chen, A closer look at the temperature effect on basic creep of cement pastes by microindentation, Constr. Build. Mater. 258 (2020). https://doi.org/10.1016/j.conbuildmat.2020.119455.
[267] L. Sorelli, G. Constantinides, F.-J. Ulm, F. Toutlemonde, The nano-mechanical signature of Ultra High Performance Concrete by statistical nanoindentation techniques, Cem. Concr. Res. (2008) 10.
[268] Y. Kusumawardaningsih, E. Fehling, M. Ismail, UHPC Compressive Strength Test Specimens: Cylinder or Cube?, Procedia Eng. 125 (2015) 1076–1080. https://doi.org/10.1016/j.proeng.2015.11.165.
[269] N.M. Sudarshan, T.C. Rao, Experimental Investigation of UHPFRC Cube and Cylinder Compression Test at Elevated Temperature, Open J. Civ. Eng. 07 (2017) 282–296. https://doi.org/10.4236/ojce.2017.72018.
[270] R.P. Spragg, B.A. Graybeal, N. Saladi, L. Montanari, I. De la Varga, Electrical Resistivity Testing to Rapidly Assess The Durability of UHPC-Class Materials [techbrief], United States. Federal Highway Administration. Office of Research …, 2022.
[271] G. Hernandez, A. Durán-Herrera, A. Tagnit-Hamou, Optimization of Ultra-High-Performance Concrete by Use of Soft and Hard Inert Fillers (Limestone and Quartz), ACI Mater. J. 119 (2022). https://doi.org/10.14359/51734222.
[272] W. Zhu, J.C. Gibbs, Use of different limestone and chalk powders in self-compacting concrete, Cem. Concr. Res. 35 (2005) 1457–1462. https://doi.org/10.1016/j.cemconres.2004.07.001.
[273] C. Wang, C. Yang, F. Liu, C. Wan, X. Pu, Preparation of Ultra-High Performance Concrete with common technology and materials, Cem. Concr. Compos. 34 (2012) 538–544. https://doi.org/10.1016/j.cemconcomp.2011.11.005.
[274] W. Sekkal, A. Zaoui, Nanoscale Analysis of the Morphology and Surface Stability of Calcium Carbonate Polymorphs, Sci. Rep. 3 (2013) 1587. https://doi.org/10.1038/srep01587.

[275] D. Bentz, C. Ferraris, S. Jones, D. Lootens, F. Zunino, Limestone and Silica Powder Replacements for Cement: Early-Age Performance, Cem. Concr. Compos. 78 (2017). https://doi.org/10.1016/j.cemconcomp.2017.01.001.
[276] D. Jansen, J. Neubauer, F. Goetz-Neunhoeffer, R. Haerzschel, W.-D. Hergeth, Change in reaction kinetics of a Portland cement caused by a superplasticizer — Calculation of heat flow curves from XRD data, Cem. Concr. Res. 42 (2012) 327–332.
[277] G. Fagerlund, Chemically bound water as measure of degree of hydration: method and potential errors, Undefined. (2009). https://www.semanticscholar.org/paper/Chemically-bound-water-as-measure-of-degree-of-and-Fagerlund/a7a95ca6f66e144fd6f20e0922dcbaf69b111203 (accessed April 12, 2022).
[278] S.E. Chidiac, M. Shafikhani, Cement degree of hydration in mortar and concrete, J. Therm. Anal. Calorim. 138 (2019) 2305–2313. https://doi.org/10.1007/s10973-019-08800-w.
[279] D.P. Bentz, E.F. Irassar, B.E. Bucher, W.J. Weiss, Limestone fillers conserve cement; Part 1: an analysis based on Powers' model, Concr. Int. 31 (2009) 41–46.
[280] M. Mouret, A. Bascoul, G. Escadeillas, Study of the Degree of Hydration of Concrete by Means of Image Analysis and Chemically Bound Water, Adv. Cem. Based Mater. 6 (1997) 7. https://doi.org/10/ggkmkh.
[281] P. Lura, O.M. Jensen, K. van Breugel, Autogenous shrinkage in high-performance cement paste: An evaluation of basic mechanisms, Cem. Concr. Res. 33 (2003) 223–232. https://doi.org/10/bhn568.
[282] Baron J., Fissuration du béton par hydratation localement différée du ciment, (1971).
[283] M. Alkaysi, S. El-Tawil, Z. Liu, W. Hansen, Effects of silica powder and cement type on durability of ultra high performance concrete (UHPC), Cem. Concr. Compos. 66 (2016) 47–56. https://doi.org/10/gc4pgb.
[284] A. Itim, K. Ezziane, E.-H. Kadri, Compressive strength and shrinkage of mortar containing various amounts of mineral additions, Constr. Build. Mater. 25 (2011) 3603–3609. https://doi.org/10.1016/j.conbuildmat.2011.03.055.
[285] P. Turcry, A. Loukili, L. Barcelo, J.M. Casabonne, Can the maturity concept be used to separate the autogenous shrinkage and thermal deformation of a cement paste at early age?, Cem. Concr. Res. 32 (2002) 1443–1450. https://doi.org/10.1016/S0008-8846(02)00800-1.
[286] P.P. Li, H.J.H. Brouwers, W. Chen, Q. Yu, Optimization and characterization of high-volume limestone powder in sustainable ultra-high performance concrete, Constr. Build. Mater. 242 (2020) 118112.
[287] P.K. Mehta, D. Manmohan, Pore size distribution and permeability of hardened cement paste. 7e Congrès international de la Chimie des ciments, Paris, 1980.
[288] B. Bourdette, E. Ringot, J.P. Ollivier, Modelling of the transition zone porosity, Cem. Concr. Res. 25 (1995) 741–751.
[289] K.L. Scrivener, A.K. Crumbie, P. Laugesen, The Interfacial Transition Zone (ITZ) Between Cement Paste and Aggregate in Concrete, Interface Sci. 12 (2004) 411–421. https://doi.org/10/fbpdwb.
[290] W. Morris, E.I. Moreno, A.A. Sagüés, Practical evaluation of resistivity of concrete in test cylinders using a Wenner array probe, Cem. Concr. Res. 26 (1996) 1779–1787. https://doi.org/10.1016/S0008-8846(96)00175-5.
[291] D.P. Bentz, E.F. Irassar, B.E. Bucher, W.J. Weiss, Limestone fillers conserve cement; part 2: durability issues and the effects of limestone fineness on mixtures, Concr. Int. 31 (2009) 35–39.

[292] Y. Shi, G. Long, C. Ma, Y. Xie, J. He, Design and preparation of ultra-high performance concrete with low environmental impact, J. Clean. Prod. 214 (2019) 633–643. https://doi.org/10.1016/j.jclepro.2018.12.318.
[293] D. Bouchard, T. Sanchez, L. Sorelli, D. Conciatori, Development of Eco-Efficient UHPC and UHPFRC by Recycling Granite Waste Powder (GWP), in: 2022: pp. 903–914. https://doi.org/10.1007/978-3-030-83719-8_77.
[294] P.R. de Matos, R.D. Sakata, P.J.P. Gleize, J. de Brito, W.L. Repette, Eco-friendly ultra-high performance cement pastes produced with quarry wastes as alternative fillers, J. Clean. Prod. 269 (2020) 122308. https://doi.org/10.1016/j.jclepro.2020.122308.
[295] Í. López Boadella, F. López Gayarre, J. Suárez González, J.M. Gómez-Soberón, C. López-Colina Pérez, M. Serrano López, J. de Brito, The Influence of Granite Cutting Waste on The Properties of Ultra-High Performance Concrete, Mater. Basel Switz. 12 (2019) E634. https://doi.org/10.3390/ma12040634.
[296] E. Ghafari, H. Costa, E. Júlio, A. Portugal, L. Durães, The effect of nanosilica addition on flowability, strength and transport properties of ultra high performance concrete, Mater. Des. 59 (2014) 1–9.
[297] V. Corinaldesi, G. Moriconi, Mechanical and thermal evaluation of Ultra High Performance Fiber Reinforced Concretes for engineering applications, Constr. Build. Mater. 26 (2012) 289–294. https://doi.org/10.1016/j.conbuildmat.2011.06.023.
[298] N. Soliman, A. Tagnit-Hamou, Using Particle Packing and Statistical Approach to Optimize Eco-Efficient Ultra-High-Performance Concrete, ACI Mater. J. 114 (2017). https://doi.org/10.14359/51701001.
[299] K. Habel, J.-P. Charron, S. Braike, R.D. Hooton, P. Gauvreau, B. Massicotte, Ultra-high performance fibre reinforced concrete mix design in central Canada, Can. J. Civ. Eng. 35 (2008) 217–224. https://doi.org/10.1139/L07-114.
[300] G. Habert, E. Denarié, A. Sajna, P. Rossi, Lowering the global warming impact of bridge rehabilitations by using Ultra High Performance Fibre Reinforced Concretes, Cem. Amp Concr. Compos. 38 (2013) 1. https://doi.org/10.1016/j.cemconcomp.2012.11.008.
[301] W. Meng, Design and performance of cost-effective ultra-high performance concrete for prefabricated elements, (n.d.) 269.
[302] Z.B. Haber, I. De la Varga, B.A. Graybeal, B. Nakashoji, R. El-Helou, Properties and behavior of UHPC-class materials, United States. Federal Highway Administration. Office of Infrastructure …, 2018.
[303] S. Abbas, M.L. Nehdi, M.A. Saleem, Ultra-High Performance Concrete: Mechanical Performance, Durability, Sustainability and Implementation Challenges, Int. J. Concr. Struct. Mater. 10 (2016) 271–295. https://doi.org/10.1007/s40069-016-0157-4.
[304] B.A. Graybeal, Material Property Characterization of Ultra-High Performance Concrete, 2006. https://trid.trb.org/view.aspx?id=798080.
[305] J. Provete Vincler, B. Majidi, T. Sanchez, D. Conciatori, L. Sorelli, Analysis of UHPFRC Steel Fiber Corrosions in Accelerated Migration Tests, (2018) 18.
[306] L. Scrivener K., M. John V., M. Gartner.E, Eco-efficient cements: Potential economically viable solutions for a low-CO2 cement-based materials industry, (2016).
[307] E. Gartner, Scientific and societal issues involved in developing sustainable cements, in: Role Cem. Sci. Sustain. Dev. Proc. Int. Symp. Held Univ. Dundee Scotl. UK 3–4 Sept. 2003, Thomas Telford Publishing, 2003: pp. 445–458.

[308] N. Randl, T. Steiner, S. Ofner, E. Baumgartner, T. Mészöly, Development of UHPC mixtures from an ecological point of view, Constr. Build. Mater. 67 (2014) 373–378. https://doi.org/10/gdvns7.
[309] E. Denarié, ARCHE D06-Recommendations for the tailoring of UHPFRC recipes for rehabilitation, MCS/EU, 2009.
[310] G. Hernández-Carrillo, A. Durán-Herrera, A. Tagnit-Hamou, Optimization of Ultra-High-Performance Concrete Using Soft and Hard Inert Fillers (Limestone and Quartz)., ACI Mater. J. 119 (2022).
[311] P.-C. Aïtcin, S. Mindess, Sustainability of concrete, CRC Press, 2011.
[312] A.E. Naaman, K. Wille, The path to ultra-high performance fiber reinforced concrete (UHP-FRC): five decades of progress, in: 2012: pp. 3–13.
[313] R. Yu, P. Spiesz, H.J.H. Brouwers, Development of an eco-friendly Ultra-High Performance Concrete (UHPC) with efficient cement and mineral admixtures uses, Cem. Concr. Compos. 55 (2015) 383–394. https://doi.org/10.1016/j.cemconcomp.2014.09.024.
[314] H. Yazıcı, M. Yardımcı, S. Aydin, A. Karabulut, Mechanical properties of reactive powder concrete containing mineral admixtures under different curing regimes, Constr. Build. Mater. 23 (2009) 1223–1231. https://doi.org/10.1016/j.conbuildmat.2008.08.003.
[315] A. Tafraoui, G. Escadeillas, S. Lebaili, T. Vidal, Metakaolin in the formulation of UHPC, Constr. Build. Mater. 23 (2009) 669–674. https://doi.org/10.1016/j.conbuildmat.2008.02.018.
[316] A. Alsalman, C.N. Dang, J.R. Martí-Vargas, W.M. Hale, Mixture-proportioning of economical UHPC mixtures, J. Build. Eng. 27 (2020) 100970.
[317] B. Graybeal, Development of Non-Proprietary Ultra-High Performance Concrete for Use in the Highway Bridge Sector, Turn.-Fairbank Highw. Res. Cent. Fed. Highw. Adm. (2013).
[318] J. Deschamps, B. Simon, A. Tagnit-Hamou, B. Amor, Is open-loop recycling the lowest preference in a circular economy? Answering through LCA of glass powder in concrete, J. Clean. Prod. 185 (2018) 14–22.
[319] A. Tabereaux, The SPL waste management challenge in primary aluminum, Light Met. Age March. 16 (2021).
[320] Broek, S., Øye, H.A., Fundamentals of Managing Spent Potlining (SPL), Trav 46 Proc 585 35th Int. (2018) 817–834.
[321] G. Fares, Nouveau système cimentaire: cas de la fritte de verre = New cementitious system : the case of glass frit., Library and Archives Canada = Bibliothèque et Archives Canada, 2010.
[322] P.B. Personnet, Treatment and reuse of spent pot lining, an industrial application in a cement kiln, (1999) 8.
[323] L. Wu, N. Farzadnia, C. Shi, Z. Zhang, H. Wang, Autogenous shrinkage of high performance concrete: A review, Constr. Build. Mater. 149 (2017) 62–75. https://doi.org/10.1016/j.conbuildmat.2017.05.064.
[324] T. Xie, C. Fang, M. Ali, P. Visintin, Characterizations of autogenous and drying shrinkage of ultra-high performance concrete (UHPC): An experimental study, Cem. Concr. Compos. 91 (2018). https://doi.org/10.1016/j.cemconcomp.2018.05.009.
[325] Ç. Yalçınkaya, H. Yazıcı, Effects of ambient temperature and relative humidity on early-age shrinkage of UHPC with high-volume mineral admixtures, Constr. Build. Mater. 144 (2017) 252–259. https://doi.org/10.1016/j.conbuildmat.2017.03.198.
[326] M.A. Hafiz, A. Hajiesmaeili, E. Denarié, Tensile response of low clinker UHPFRC subjected to fully restrained shrinkage, Cem. Concr. Res. 124 (2019) 105804.

[327] D.-Y. Yoo, J.-J. Park, S.-W. Kim, Y.-S. Yoon, Influence of ring size on the restrained shrinkage behavior of ultra high performance fiber reinforced concrete, Mater. Struct. 47 (2014) 1161–1174. https://doi.org/10.1617/s11527-013-0119-0.
[328] H.R. Sobuz, P. Visintin, M.S. Mohamed Ali, M. Singh, M.C. Griffith, A.H. Sheikh, Manufacturing ultra-high performance concrete utilising conventional materials and production methods, Constr. Build. Mater. 111 (2016) 251–261. https://doi.org/10.1016/j.conbuildmat.2016.02.102.
[329] T. Lu, Z. Li, H. Huang, Effect of Supplementary Materials on the Autogenous Shrinkage of Cement Paste, Materials. 13 (2020). https://doi.org/10.3390/ma13153367.
[330] S. Aubry, P. Bompas, B. Vaudeville, D. Corvez, T. Lagrange, P. Mazzacane, A. Brizou, A UHPFRC cladding challenge: the fondation Louis Vuitton pour la création" Iceberg, Newsletter. (2016).
[331] Dénarié Emmanuel, The generalized CIPM derivation, (2016).
[332] J.J. Chen, L. Sorelli, M. Vandamme, F.-J. Ulm, G. Chanvillard, A Coupled Nanoindentation/SEM-EDS Study on Low Water/Cement Ratio Portland Cement Paste: Evidence for C–S–H/Ca(OH)2 Nanocomposites, J. Am. Ceram. Soc. 93 (2010) 1484–1493. https://doi.org/10/d99t6f.
[333] D.-T. Nguyen, R. Alizadeh, J.J. Beaudoin, L. Raki, Microindentation creep of secondary hydrated cement phases and C–S–H, Mater. Struct. 46 (2013) 1519–1525.
[334] M. Vandamme, C.A. Tweedie, G. Constantinides, F.-J. Ulm, K.J. Van Vliet, Quantifying plasticity-independent creep compliance and relaxation of viscoelastoplastic materials under contact loading, J. Mater. Res. 27 (2012) 302–312.
[335] L. Sorelli, J. Frech-Baronet, J.-P. Charron, Creep Behavior of Cement Paste, Mortar, and Concrete: The Role of Relative Humidity and Interface Porosity, (2015) 296–305. https://doi.org/10.1061/9780784479346.034.
[336] W. Wilson, L. Sorelli, A. Tagnit-Hamou, Automated coupling of NanoIndentation and Quantitative Energy-Dispersive Spectroscopy (NI-QEDS): A comprehensive method to disclose the micro-chemo-mechanical properties of cement pastes, Cem. Concr. Res. 103 (2018) 49–65. https://doi.org/10/gcwq6m.
[337] Z. li, K. Afshinnia, P. Rangaraju, Effect of alkali content of cement on properties of high performance cementitious mortar, Constr. Build. Mater. 102 (2016) 631–639. https://doi.org/10.1016/j.conbuildmat.2015.10.110.
[338] I. Jawed, J. Skalny, Alkalies in cement: A review: II. Effects of alkalies on hydration and performance of Portland cement, Cem. Concr. Res. 8 (1978) 37–51. https://doi.org/10.1016/0008-8846(78)90056-X.
[339] J.W. Bullard, H.M. Jennings, R.A. Livingston, A. Nonat, G.W. Scherer, J.S. Schweitzer, K.L. Scrivener, J.J. Thomas, Mechanisms of cement hydration, Cem. Concr. Res. 41 (2011) 1208–1223. https://doi.org/10.1016/j.cemconres.2010.09.011.
[340] K. Wesche, ed., Fly Ash in Concrete: Properties and performance, CRC Press, London, 2014. https://doi.org/10.1201/9781482267051.
[341] C. Shi, D. Wang, L. Wu, Z. Wu, The hydration and microstructure of ultra high-strength concrete with cement–silica fume–slag binder, Cem. Concr. Compos. 61 (2015) 44–52. https://doi.org/10.1016/j.cemconcomp.2015.04.013.
[342] X. Wang, R. Yu, Z. Shui, Z. Zhao, Q. Song, B. Yang, D. Fan, Development of a novel cleaner construction product: Ultra-high performance concrete incorporating lead-zinc tailings, J. Clean. Prod. 196 (2018) 172–182. https://doi.org/10.1016/j.jclepro.2018.06.058.
[343] J. Hu, Z. Ge, K. Wang, Influence of cement fineness and water-to-cement ratio on mortar early-age heat of hydration and set times, Constr. Build. Mater. 50 (n.d.) 657–663.

[344] M.-H. Zhang, K. Sisomphon, T.S. Ng, D.J. Sun, Effect of superplasticizers on workability retention and initial setting time of cement pastes, Constr. Build. Mater. 9 (2010) 1700–1707. https://doi.org/10.1016/j.conbuildmat.2010.02.021.
[345] D.K. Dutta, D. Bordoloi, P.C. Borthakur, Hydration of portland cement clinker in the presence of carbonaceous materials, Cem. Concr. Res. 25 (1995) 1095–1102. https://doi.org/10.1016/0008-8846(95)00104-K.
[346] H. Ousmane Ahmat, N. Soliman, B. Tolnai, A. Tagnit-Hamou, Nano-engineered ultra-high performance concrete for controlled autogenous shrinkage using nanocellulose, Cem. Concr. Res. Volume 137 (2020) 106217. https://doi.org/10.1016/j.cemconres.2020.106217.
[347] S. Meddah, A. Tagnit-Hamou, Pore Structure of Concrete with Mineral Admixtures and its Effect on Self-desiccation Shrinkage, ACI Mater. J. V. 106 (2009) 241–250.
[348] An Experimental Study on the Sorption in UHPFRC: Adaptation of the DVS Measurement Procedure, in: n.d.
[349] F. Lange, H. Mörtel, V. Rudert, Dense packing of cement pastes and resulting consequences on mortar properties, Cem. Concr. Res. 27 (1997) 1481–1488. https://doi.org/10.1016/S0008-8846(97)00189-0.
[350] D. Mostofinejad, M.R. Nikoo, S.A. Hosseini, Determination of optimized mix design and curing conditions of reactive powder concrete (RPC), Constr. Build. Mater. 123 (2016) 754–767. https://doi.org/10/ggmxgh.
[351] Z. Mo, X. Gao, A. Su, Mechanical performances and microstructures of metakaolin contained UHPC matrix under steam curing conditions, Constr. Build. Mater. (2020) 121112. https://doi.org/10/ghgn9f.
[352] K. Tan, J. Zhu, Influences of steam and autoclave curing on the strength and chloride permeability of high strength concrete, Mater. Struct. 50 (2016) 56. https://doi.org/10/gjz27v.
[353] N. Soliman, A. Tagnit-Hamou, Using glass sand as an alternative for quartz sand in UHPC, Constr. Build. Mater. 145 (2017) 243–252. https://doi.org/10.1016/j.conbuildmat.2017.03.187.
[354] B. Chiaia, A.P. Fantilli, A. Guerini, G. Volpatti, D. Zampini, Eco-mechanical index for structural concrete, Constr. Build. Mater. 67 (2014) 386–392. https://doi.org/10.1016/j.conbuildmat.2013.12.090.
[355] Y. Shi, G. Long, C. Ma, Y. Xie, J. He, Design and preparation of ultra-high performance concrete with low environmental impact, J. Clean. Prod. 214 (2019) 633–643. https://doi.org/10/gjjwpr.
[356] G. Long, Y. Gao, Y. Xie, Designing more sustainable and greener self-compacting concrete, Constr. Build. Mater. 84 (2015) 301–306. https://doi.org/10.1016/j.conbuildmat.2015.02.072.
[357] H. Mueller, M. Haist, M. Vogel, J.S. Moffatt, Design Approach and Properties of a New Generation of Sustainable Structural Concretes, Undefined. (2018). /paper/Design-Approach-and-Properties-of-a-New-Generation-Mueller-Haist/56680572bd441df8f936cbbf84176f2f57909587 (accessed March 24, 2021).
[358] M. Rajczakowska, L. Nilsson, K. Habermehl-Cwirzen, H. Hedlund, A. Cwirzen, Does a High Amount of Unhydrated Portland Cement Ensure an Effective Autogenous Self-Healing of Mortar?, Materials. 12 (2019). https://doi.org/10/gjbzdt.
[359] W. Huang, H. Kazemi-Kamyab, W. Sun, K. Scrivener, Effect of cement substitution by limestone on the hydration and microstructural development of ultra-high performance concrete (UHPC), Cem. Concr. Compos. 77 (2016). https://doi.org/10.1016/j.cemconcomp.2016.12.009.
[360] K. Habel, M. Viviani, E. Denarié, E. Brühwiler, Development of the mechanical properties of an Ultra-High Performance Fiber Reinforced Concrete (UHPFRC), Cem. Concr. Res. 36 (2006) 1362–1370. https://doi.org/10.1016/j.cemconres.2006.03.009.

[361] D. Hou, D. Wu, X. Wang, S. Gao, R. Yu, M. Li, P. Wang, Y. Wang, Sustainable use of red mud in ultra-high performance concrete (UHPC): Design and performance evaluation, Cem. Concr. Compos. 115 (2021) 103862. https://doi.org/10.1016/j.cemconcomp.2020.103862.
[362] T. Makita, E. Brühwiler, Tensile fatigue behaviour of Ultra-High Performance Fibre Reinforced Concrete combined with steel rebars (R-UHPFRC), Int. J. Fatigue. 59 (2014) 145–152. https://doi.org/10.1016/j.ijfatigue.2013.09.004.
[363] A. Hajiesmaeili, F. Pittau, E. Denarié, G. Habert, Life Cycle Analysis of Strengthening Existing RC Structures with R-PE-UHPFRC, Sustainability. 11 (2019). https://doi.org/10.3390/su11246923.
[364] Y. Shi, G. Long, X. Zen, Y. Xie, T. Shang, Design of binder system of eco-efficient UHPC based on physical packing and chemical effect optimization, Constr. Build. Mater. 274 (2021) 121382. https://doi.org/10.1016/j.conbuildmat.2020.121382.
[365] R. Jing, Y. Liu, P. Yan, Uncovering the effect of fly ash cenospheres on the macroscopic properties and microstructure of ultra high-performance concrete (UHPC), Constr. Build. Mater. 286 (2021) 122977. https://doi.org/10.1016/j.conbuildmat.2021.122977.